ATLAS NOTE

May 14, 2012

Search for new phenomena with mono-jet plus missing transverse energy signature in pp collisions at $\sqrt{s}$ = 7 TeV with the ATLAS detector

J. Abdallah[1], H. Beauchemin[2], D. Berge[3], P. Calfayan[4], V. Giangiobbe[1], N. Kanaya[5],
M. Kaneda[3], S. Kazama[5], M. Martinez[1], S. Poddar[6], R. Pöttgen[7], R. Rezvani[8], V. Rossetti[1],
N. Ryder[9], P. Savard[8], D. Salek[3], and N. Zhou[10]

[1]Universitat Autónoma de Barcelona
[2]Tufts University
[3]CERN
[4]Ludwig-Maximilians-Universität München
[5]Tokyo University
[6]Ruprecht-Karls-Universität Heidelberg
[7]Johannes Gutenberg-Universität, Mainz
[8]University of Toronto
[9]University of Oxford
[10]University of California, Irvine

Abstract

A search for a high-energy jet in combination with large missing transverse energy is performed in proton-proton collisions at $\sqrt{s}$ = 7 TeV with the ATLAS experiment at the Large Hadron Collider (LHC) at CERN. Four kinematic regions are explored in a model independent way using a dataset corresponding to an integrated luminosity of 4.7 fb^{-1} recorded in 2011. No excess of data over the expectation from the Standard Model is oberved, and limits are set for a range of model interpretations.

Contents

1 Introduction

The production of an energetic jet in association with large missing transverse energy is predicted by various theories beyond the Standard Model. Previous ATLAS analyses performed the search for new physics in the mono-jet final state [1]. This document describes the update of these analyses using the complete 2011 dataset, collected in proton-proton collision at a center-of-mass energy of $\sqrt{s} = 7$ TeV.

The sensitivity of the analysis largely depends on the precision reached by the estimation of the background from the Standard Model. Therefore, a data-driven approach has been developed to determine the contribution of the electroweak processes. It relies on control regions consisting in the production of W and Z bosons followed by their leptonic decays (τ excluded).

Furthermore, the definition of the signal region has been arranged in order to test additional theoretical interpretations in addition to the model of Large Extra Dimensions (LED) previously tested in References [1]. In this note, current ATLAS limits on the production of ADD (Arkani-Hamed, Dimopoulos, and Dvali) Gravitons [2] are updated, and interpreted as lower bound on the associated fundamental Planck scale as function of a number of extra dimensions. Furthermore, the pair-production of WIMPs with an energetic jet from initial state radiation is investigated.

The note is organized as follows. The Data and simulated samples considered in the analysis are described in Section 2. The cuts used to select mono-jet event candidates are detailed in Section 3, while Section 4 focuses on the study of the trigger chosen to collect the Data. The determination of the contribution from the Standard Model is largely explained in Sections 5 to 10, before providing the experimental results in Section 11. Finally, the theoretical interpretations in terms of Graviton production or pair-production of WIMPs are presented in Section 12.

2 Data and simulated samples

All the samples used in this analysis are Standard Model or SUSY D3PDs originating from official AOD productions, with production tags p833 and p832, respectively.

2.1 Data sample

The raw Data samples used in this analysis were recorded by the ATLAS detector over the period 22$^{\text{nd}}$ March 2011 – 30$^{\text{th}}$ October 2011, corresponding to runs 178044 to 191933 (data-taking periods B2 – M10). Period C was excluded due to reduced $\sqrt{s}$. Over this period the peak instantaneous luminosity increased from 1.3×10^{30} to 3.6×10^{33} cm^{-2}s^{-1} and the peak mean number of interactions per bunch crossing increased from 2.6 to 17.5.

The recorded raw Data corresponds to an integrated luminosity of 5.25 fb^{-1}, falling to 4.7 fb^{-1} after the application of the basic data quality requirements defined in the Good Run List of the SUSY working group[1]. The uncertainty on the luminosity is 3.9%.

Events from the JetTauEtmiss stream triggered with a unprescaled calorimeter-based $E_{\text{T}}^{\text{miss}}$ trigger are utilized to select mono-jet candidates and to define control regions based on events with muons. The integrated luminosity estimated in each data period with a $E_{\text{T}}^{\text{miss}}$ trigger can be found in Table 10. Control regions relying on events with electrons are making use of the Egamma stream together with electron triggers.

2.2 Simulated samples

All simulated samples used in the analysis have been produced using the Athena release 17 (mc11c). Pile-up is included in the simulation to model the average pile-up in 4 periods of the Data, namely periods B-D, E-H, I-K, and L-M. In addition, the largest backgrounds of the analysis are determined with a data-driven method for which correction factors are obtained from ratios of simulated samples, thus reducing the potential effect of a wrong modelisation of pile-up. As a result, no pile-up reweighting has been applied to simulated samples. For instance, the signal acceptance of the ADD signal with 4 extra dimensions and a scale of 2.5 TeV varied by only 0.12% after applying the recommended procedure of pile-up re-weighting.

Tables 1, 2, 3, 4, 5 provide all the simulated samples that have been used to model the background from the Standard Model, together with the associated Monte Carlo generators.

Signal samples were generated using the `ExoGraviton_i` generator [3] and passed to the fast detector simulation (AtlFast II) and reconstruction. Parton showering and hadronisation were performed by PYTHIA with the ATLAS MC11c tuning and MRST LO** PDF set[2]. Table 6 shows the production cross-sections of signal samples for different (δ, M_D) phase space points[3] with a p_T cut of 80 GeV at the generator level. The M_D values chosen to generate the samples are the ones nearest to the latest published M_D limits [arXiv:1106.5327]. Table 6 lists the names and cross-sections of some of the generated samples. Additional samples with a modification in the level of Initial and Final State Radiations (ISR/FSR), different PDF sets, and choices of Q^2 have been generated at Truth level to study the systematic uncertainties due to ISR/FSR, PDF, and renormalisation and factorisation scales.

---

[1] The official GRL for 2011 data for Moriond2012 (data11_7TeV.periodAllYear_DetStatus-v36-pro10_CoolRunQuery-00-04-08_Susy.xml) is used.

[2] The PDF re-weighting tool is used to get the corresponding CTEQ6.6 signal acceptances and cross-sections.

[3] The complete table of cross-sections can be found at: `https://twiki.cern.ch/twiki/bin/viewauth/Atlas/ADDGraviton`

Sample ID	Name	Generator	Cross Section [pb]	k–factor	N_{gen}
107680	WenuNp0_pt20	Alpgen Jimmy	6932	1.1955	3458883
107681	WenuNp1_pt20	Alpgen Jimmy	1305	1.1955	2499645
107682	WenuNp2_pt20	Alpgen Jimmy	378	1.1955	3768632
107683	WenuNp3_pt20	Alpgen Jimmy	101.9	1.1955	1008947
107684	WenuNp4_pt20	Alpgen Jimmy	25.7	1.1955	250000
144018	WenuNp5_excl_pt20	Alpgen Jimmy	5.81	1.1955	979197
144022	WenuNp6_pt20	Alpgen Jimmy	1.55	1.1955	144998
144196	WenuNp1_pt20_susyfilt	Alpgen Jimmy	7.38	1.1955	180899
144197	WenuNp2_pt20_susyfilt	Alpgen Jimmy	6.24	1.1955	134998
144198	WenuNp3_pt20_susyfilt	Alpgen Jimmy	3.47	1.1955	139999
144199	WenuNp4_pt20_susyfilt	Alpgen Jimmy	1.45	1.1955	75000
107690	WmunuNp0_pt20	Alpgen Jimmy	6932	1.1955	3462942
107691	WmunuNp1_pt20	Alpgen Jimmy	1305	1.1955	2499593
107692	WmunuNp2_pt20	Alpgen Jimmy	378	1.1955	3768737
107693	WmunuNp3_pt20	Alpgen Jimmy	101.9	1.1955	1008446
107694	WmunuNp4_pt20	Alpgen Jimmy	25.7	1.1955	254950
144019	WmunuNp5_excl_pt20	Alpgen Jimmy	5.82	1.1955	979794
144023	WmunuNp6_pt20	Alpgen Jimmy	1.54	1.1955	144999
144200	WmunuNp1_pt20_susyfilt	Alpgen Jimmy	7.08	1.1955	171000
144201	WmunuNp2_pt20_susyfilt	Alpgen Jimmy	6.14	1.1955	139900
144202	WmunuNp3_pt20_susyfilt	Alpgen Jimmy	3.42	1.1955	139899
144203	WmunuNp4_pt20_susyfilt	Alpgen Jimmy	1.44	1.1955	70000
107700	WtaunuNp0_pt20	Alpgen Jimmy	6932	1.1955	3418296
107701	WtaunuNp1_pt20	Alpgen Jimmy	1305	1.1955	2499194
107702	WtaunuNp2_pt20	Alpgen Jimmy	378	1.1955	3750986
107703	WtaunuNp3_pt20	Alpgen Jimmy	101.9	1.1955	1009946
107704	WtaunuNp4_pt20	Alpgen Jimmy	25.7	1.1955	249998
107705	WtaunuNp5_excl_pt20	Alpgen Jimmy	5.82	1.1955	989595
144024	WtaunuNp6_pt20	Alpgen Jimmy	1.54	1.1955	149999
144204	WtaunuNp1_pt20_susyfilt	Alpgen Jimmy	10.9	1.1955	265000
144205	WtaunuNp2_pt20_susyfilt	Alpgen Jimmy	9.25	1.1955	204999
144206	WtaunuNp3_pt20_susyfilt	Alpgen Jimmy	5.10	1.1955	209900
144207	WtaunuNp4_pt20_susyfilt	Alpgen Jimmy	2.10	1.1955	104999

Table 1: Vector boson + jet Monte Carlo samples used in the mono-jet analyses including cross section times branching ratio, the k–factors and the number of generated events of the sample. The k–factors are the NNLO/LO scaling factors used to scale the overall cross-section for $W \to l\nu$ to the total NNLO inclusive cross section.

WIMP signal samples were produced using a MadGraph5 implementation interfaced to Pythia (cf. Section 12.2 for more details about the simulated process). The signal processes calculated with Mad-Graph are $pp \to \chi\chi\, j$ and $pp \to \chi\chi\, j\, j$ with a lead parton cut of 80 GeV, the Pythia parton shower and hadronization is added on top of these using MLM matching and a matching-scale parameter setting of $QCUT = 80$ GeV. For some of the generated samples the event statistics in the large $E_{\text{T}}^{\text{miss}}$ regime were augmented by additional samples with lead-parton cut at 300 GeV. Sample numbers and cross

177 sections are given in Table 7. As for ADD truth samples for estimating systematic uncertainties were
178 produced privately. These were produced varying α_s in Pythia, the MLM matching scale parameter, and
179 the event-by-event factorisation and renormalisation scale (in MadGraph itself).

Sample ID	Name	Generator	Cross Section [pb]	k–factor	N_{gen}
107650	ZeeNp0_pt20	Alpgen Jimmy	669.6	1.24345	6617284
107651	ZeeNp1_pt20	Alpgen Jimmy	134.6	1.24345	1334897
107652	ZeeNp2_pt20	Alpgen Jimmy	40.65	1.24345	809999
107653	ZeeNp3_pt20	Alpgen Jimmy	11.26	1.24345	220000
107654	ZeeNp4_pt20	Alpgen Jimmy	2.84	1.24345	60000
107655	ZeeNp5_pt20	Alpgen Jimmy	0.76	1.24345	20000
116250	ZeeNp0_Mll10to40_pt20	Alpgen Jimmy	3054.7	1.24345	994949
116251	ZeeNp1_Mll10to40_pt20	Alpgen Jimmy	84.9	1.24345	299998
116252	ZeeNp2_Mll10to40_pt20	Alpgen Jimmy	41.2	1.24345	939946
116253	ZeeNp3_Mll10to40_pt20	Alpgen Jimmy	8.35	1.24345	149998
116254	ZeeNp4_Mll10to40_pt20	Alpgen Jimmy	1.85	1.24345	40000
116255	ZeeNp5_Mll10to40_pt20	Alpgen Jimmy	0.46	1.24345	10000
107660	ZmumuNp0_pt20	Alpgen Jimmy	669.6	1.24345	6615230
107661	ZmumuNp1_pt20	Alpgen Jimmy	134.6	1.24345	1334296
107662	ZmumuNp2_pt20	Alpgen Jimmy	40.65	1.24345	404947
107663	ZmumuNp3_pt20	Alpgen Jimmy	11.26	1.24345	110000
107664	ZmumuNp4_pt20	Alpgen Jimmy	2.84	1.24345	30000
107665	ZmumuNp5_pt20	Alpgen Jimmy	0.76	1.24345	10000
116260	ZmumuNp0_Mll10to40_pt20	Alpgen Jimmy	3054.9	1.24345	999849
116261	ZmumuNp1_Mll10to40_pt20	Alpgen Jimmy	84.78	1.24345	300000
116262	ZmumuNp2_Mll10to40_pt20	Alpgen Jimmy	41.13	1.24345	999995
116263	ZmumuNp3_Mll10to40_pt20	Alpgen Jimmy	8.34	1.24345	150000
116264	ZmumuNp4_Mll10to40_pt20	Alpgen Jimmy	1.87	1.24345	39999
116265	ZmumuNp5_Mll10to40_pt20	Alpgen Jimmy	0.46	1.24345	10000
107670	ZtautauNp0_pt20	Alpgen Jimmy	669.6	1.24345	10613179
107671	ZtautauNp1_pt20	Alpgen Jimmy	134.6	1.24345	3334137
107672	ZtautauNp2_pt20	Alpgen Jimmy	40.65	1.24345	1004847
107673	ZtautauNp3_pt20	Alpgen Jimmy	11.26	1.24345	509847
107674	ZtautauNp4_pt20	Alpgen Jimmy	2.84	1.24345	144999
107675	ZtautauNp5_pt20	Alpgen Jimmy	0.76	1.24345	45000
116940	ZtautauNp0_Mll10to40_pt20	Alpgen Jimmy	3054.8	1.24345	41500
116941	ZtautauNp1_Mll10to40_pt20	Alpgen Jimmy	84.88	1.24345	79950
116942	ZtautauNp2_Mll10to40_pt20	Alpgen Jimmy	41.28	1.24345	34500
116943	ZtautauNp3_Mll10to40_pt20	Alpgen Jimmy	8.35	1.24345	15000
116944	ZtautauNp4_Mll10to40_pt20	Alpgen Jimmy	1.83	1.24345	5000
116945	ZtautauNp5_Mll10to40_pt20	Alpgen Jimmy	0.46	1.24345	2000
107710	ZnunuNp0_pt20	Alpgen Jimmy	39.62	1.2604	54949
107711	ZnunuNp1_pt20	Alpgen Jimmy	451.5	1.2604	909848
107712	ZnunuNp2_pt20	Alpgen Jimmy	196.5	1.2604	169899
107713	ZnunuNp3_pt20	Alpgen Jimmy	59.89	1.2604	144999
107714	ZnunuNp4_pt20	Alpgen Jimmy	15.51	1.2604	309899
144017	ZnunuNp5_excl_pt20	Alpgen Jimmy	3.57	1.2604	185000
144021	ZnunuNp6_pt20	Alpgen Jimmy	0.92	1.2604	114999
144192	ZnunuNp1_pt20_susyfilt	Alpgen Jimmy	12.86	1.2604	499898
144193	ZnunuNp2_pt20_susyfilt	Alpgen Jimmy	10.14	1.2604	399999
144194	ZnunuNp3_pt20_susyfilt	Alpgen Jimmy	5.40	1.2604	299998
144195	ZnunuNp4_pt20_susyfilt	Alpgen Jimmy	2.18	1.2604	184998

Table 2: Vector boson + jet Monte Carlo samples used in the mono-jet analyses including cross section times branching ratio, the k–factors and the number of generated events of the sample. The k–factors are the NNLO/LO scaling factors used to scale the overall cross-section for $Z \to \nu\bar{\nu}$ and $Z \to l^+l^-$ to the total NNLO inclusive cross section.

Sample ID	Name	Generator	Cross Section [pb]	k–factor	N_{gen}
105200	T1	MC@NLO Jimmy	90.6		14983835
105204	TTbar_FullHad	MC@NLO Jimmy	76.2		1198875
105500	Wt	Acer MC	15.74		994897
117360	st_tchan_enu	Acer MC	6.97		999295
117361	st_tchan_munu	Acer MC	6.97		999948
117362	st_tchan_taunu	Acer MC	6.97		998995
117363	st_schan_enu	Acer MC	0.5		199899
117364	st_schan_munu	Acer MC	0.5		199850
117365	st_schan_taunu	Acer MC	0.5		200000
108346	st_Wt	MC@NLO Jimmy	14.37		899694
108340	st_tchan_enu	MC@NLO Jimmy	6.83		299998
108341	st_tchan_munu	MC@NLO Jimmy	6.82		299999
108342	st_tchan_taunu	MC@NLO Jimmy	6.81		299999
108343	st_schan_enu	MC@NLO Jimmy	0.46		299948
108344	st_schan_munu	MC@NLO Jimmy	0.46		299998
108345	st_schan_taunu	MC@NLO Jimmy	0.46		299899

Table 3: Top Monte Carlo samples used in the mono-jet analyses including cross section times branching ratio, the k–factors and the number of generated events of the sample. The k–factors are the NNLO/LO scaling factors used to scale the overall cross-section to the total NNLO inclusive cross section. AcerMC and MC@NLO simulations of single top processes provided similar results for this analysis.

Sample ID	Name	Generator	Cross Section [pb]	N_{gen}
125950	Ztoee2JetsEW2JetsQCD15GeVM40	Sherpa	0.447	199999
125951	Ztomm2JetsEW2JetsQCD15GeVM40	Sherpa	0.446	181200
125952	Ztott2JetsEW2JetsQCD15GeVM40	Sherpa	0.444	199899
125956	Ztoee2JetsEW2JetsQCD15GeVM7to40	Sherpa	0.477	100000
125957	Ztomm2JetsEW2JetsQCD15GeVM7to40	Sherpa	0.477	100000
125958	Ztott2JetsEW2JetsQCD15GeVM7to40	Sherpa	0.469	99900
128810	WWlnulnu	Sherpa	2.983	1999697
128811	WZlllnu	Sherpa	0.362	299950
128812	WZlllnuLowMass	Sherpa	1.021	299949
128813	ZZllll	Sherpa	0.267	100000
128814	ZZllnn	Sherpa	0.238	349900
143062	WZlnnn	Sherpa	0.719	100000
143063	WZqqnn	Sherpa	1.425	99900
143064	Wtolnu2JetsEW1JetQCD	Sherpa	24.54	99900
143065	Ztonunu2JetsEW1JetQCD	Sherpa	1.337	99999

Table 4: Diboson processes Monte Carlo samples used in the mono-jet analyses including cross section times branching ratio and the number of generated events of the sample.

Sample ID	Name	Generator	Cross Section [pb]	N_{gen}
105009	J0 jetjet	Pythia	$9860 \cdot 10^6$	999997
105010	J1 jetjet	Pythia	$678 \cdot 10^6$	999993
105011	J2 jetjet	Pythia	$41.0 \cdot 10^6$	999999
105012	J3 jetjet	Pythia	$2.19 \cdot 10^6$	999992
105013	J4 jetjet	Pythia	$87.7 \cdot 10^3$	989992
105014	J5 jetjet	Pythia	2350	999987
105015	J6 jetjet	Pythia	33.6	999974
105016	J7 jetjet	Pythia	0.137	998955
105017	J8 jetjet	Pythia	$6.2 \cdot 10^{-6}$	998948

Table 5: QCD processes Monte Carlo samples used in the mono-jet analyses including cross section times branching ratio and the number of generated events of the sample.

Sample ID	Name	cross-section [pb]
145318	qqbar-delta2_MD_3500	0.09149
145319	qg-delta2_MD_3500	0.9751
145320	gg-delta2_MD_3500	1.159
145333	qqbar-delta3_MD_2500	0.1972
145334	qg-delta3_MD_2500	1.153
145335	gg-delta3_MD_2500	1.379
145342	qqbar-delta4_MD_2500	0.1262
145343	qg-delta4_MD_2500	0.4804
145344	gg-delta4_MD_2500	0.5877
145351	qqbar-delta5_MD_2500	0.08668
145352	qg-delta5_MD_2500	0.2447
145353	gg-delta5_MD_2500	0.3098
145360	qqbar-delta6_MD_2500	0.06143
145361	qg-delta6_MD_2500	0.1419
145362	gg-delta6_MD_2500	0.185

Table 6: ADD signal samples for various (δ, M_D) phase space points, with p_T cut = 80 GeV at the generator level. CTEQ6.6 cross-sections are quoted.

Sample ID	Operator	WIMP mass	Lead-parton cut (GeV)	Cross-section (fb)
144960	D1	10	80	5.16e-06
144964	D1	50	80	4.21e-06
144968	D1	100	80	2.80e-06
144972	D1	200	80	1.11e-06
144961	D5	10	80	380.64
144965	D5	50	80	373.56
144969	D5	100	80	338.13
144973	D5	200	80	254.25
144976	D1	10	300	1.19e-07
144978	D1	50	300	1.07e-07
144980	D1	100	300	8.79e-08
144982	D1	200	300	4.64e-08
144977	D5	10	300	23.12
144979	D5	50	300	22.78
144981	D5	100	300	22.18
144983	D5	200	300	18.87
144962	D9	10	80	90.00
144966	D9	50	80	68.63
144970	D9	100	80	64.69
144974	D9	200	80	41.29
144963	D11	10	80	246.54
144967	D11	50	80	233.99
144971	D11	100	80	189.21
144975	D11	200	80	134.39

Table 7: WIMP signal samples used to produce limits.

3 Event selection

The event selection for the analysis of the complete 2011 dataset has been updated in comparison with that of the previous publication [1].

The number of signal regions has been increased from three to four for a better coverage of the increased size of the dataset.

Moreover, the veto on the second jet has been dropped and a third jet is now vetoed. This modification is motivated by the size of the systematic uncertainty due to ISR/FSR levels in the signal samples. In the previous analysis this contribution turned out to be almost dominating the signal uncertainty, reaching up to 13%. Since not vetoing events with a second but a third jet reduced this contribution to only 2%, the decision was taken to allow events with a second jet. To keep the QCD multi-jet contribution under control, events in which the second jet and the missing transverse energy are aligned in ϕ are excluded.

In addition, a tighter veto on charged leptons is now applied in the event selection, as it includes leptons with a larger acceptance. Although performance groups provide identification efficiencies for both electrons and muons with p_T as low as 7 GeV, only the lower p_T threshold of the muon veto has been brought down to such a low value. In the case of the electrons, a conservative lower p_T threshold of 20 GeV is used to avoid vetoing on events with radiatons of high-p_T jets faking electrons. Besides, electrons within cracks as well as segment-tagged muons up to $|\eta| < 2.5$ are now considered in the definition of the veto.

3.1 Preselection

The event preselection includes the following requirements:

- GRL: $data11\_7TeV.periodAllYear\_DetS tatus-v36-pro10\_CoolRunQuery-00-04-08\_S usy.xml$

- Trigger (emulated on top of a looser trigger for the early data periods): $EF\_xe60\_verytight\_noMu$

- At least one reconstructed primary vertex with a minimum of two tracks

- Cleaning cuts defined using Athena release 16 are applied on all jets with at least 20 GeV transverse momentum in the full η range. The leading jet is required to pass a charge and electromagnetic fraction cut of 0.02 and 0.1 respectively, and the *LArError* flag shall not be equal to 2

- Jets are reconstructed with the AntiKt4 algorithm and calibrated using *EMJES* coefficients. Leading jets are required to be central within $|\eta| < 2.0$. The other jets are further considered if their transverse momentum exceeds 30 GeV and if they fulfill $|\eta| < 4.5$.

- The *LocHadTopo* flavour of missing transverse momentum is used

- To account for the intermittent LAr hole the smart veto developed by the SUSY group is applied: events are vetoed if a jet that points to the LAr hole is aligned with the missing ET direction in the transverse plane

3.2 Signal regions

In order to select monojet final states, the final kinematic cuts comprises tight cuts on the transverse momentum of the leading jet and on the missing transverse energy. An event veto on charged leptons and on the number of jets (N_{jets}) are applied. In addition, a cut on the difference of azimuthal angle between the sub-leading jet (jet_2) and the missing transverse energy is also imposed:

219 • $\Delta\phi(E_T^{\text{miss}}, jet_2) > 0.5$

220 • Not more than two jets with a transverse momentum above 30 GeV

221 • Events that contain at least one electron or muon passing the following loose quality cuts are ve-
222   toed:

Loose electrons:

· $p_T > 20$ GeV and $|\eta_{cl}| < 2.47$

· MediumPP

· author $\in \{1, 3\}$

· exclude BadClusElectron

· keep electrons in cracks

223 · No overlap removal with jets

Loose muons:

· $p_T > 7$ GeV and $|\eta| < 2.5$

· StacoCombined or Segment-tagged
(author $\in \{6, 7\}$)

· Isolated p_T-cone20< 1.8 GeV

· Matched to inner detector track fulfilling
MCP quality cuts

224 • Four signal regions defined by symmetric cuts on the leading jet transverse momentum and the
225   missing transverse energy, with the following lower threshold (in GeV): 120, 220, 350, and 500.

226   In the following, the mono-jet signal regions (SR) including all these cuts are referred to signal
227 regions 1 to 4 for lower threshold on E_T^{miss} (leading jet transverse momentum) from 120 to 500 GeV.
228 Table 8 summarizes the four inclusive signal regions of the analysis.

Signal regions	SR 1	SR 2	SR 3	SR 4
Common cuts	Preselection cuts + lepton veto + $\Delta\phi(E_T^{\text{miss}}, jet_2) > 0.5 + N_{jets} < 3$			
Dedicated cuts	$p_T^{jet_1} > 120$ GeV $E_T^{\text{miss}} > 120$ GeV	$p_T^{jet_1} > 220$ GeV $E_T^{\text{miss}} > 220$ GeV	$p_T^{jet_1} > 350$ GeV $E_T^{\text{miss}} > 350$ GeV	$p_T^{jet_1} > 500$ GeV $E_T^{\text{miss}} > 500$ GeV

Table 8: Definition of the four inclusive signal regions (SR) of the analysis.

4 E_T^{miss} Trigger

4.1 Definition and associated integrated luminosity

The lowest unprescaled calorimeter-based E_T^{miss} trigger EF_xe60_verytight_noMu, activated in the last few periods of 2011 data-taking, is used in this analysis. Details about the implementation of the E_T^{miss} trigger can be found in Reference [4].

This trigger chain has the following thresholds (no cuts are applied on muons):

- $E_T^{\mathrm{miss}}(L1) > 50\,\mathrm{GeV}$

- $E_T^{\mathrm{miss}}(L2) > 55\,\mathrm{GeV}$

- $E_T^{\mathrm{miss}}(EF) > 60\,\mathrm{GeV}$

As EF_xe60_verytight_noMu was inactive for periods B-I, a lower threshold trigger, EF_xe60_noMu, is used along with an additional cut on the $E_T^{\mathrm{miss}}(L2)$ in order to emulate EF_xe60_verytight_noMu. For the first three runs of period J, the trigger EF_xe60_tight_noMu is utilized with the same emulation, since EF_xe60_noMu was prescaled out and EF_xe60_verytight_noMu inactive. Table 9 summarizes the triggers considered in each period and Table 10 provides the associated integrated luminosities.

Period	Trigger and requirement
B to I	EF_xe60_noMu and $L2_{Met} > 55\,\mathrm{GeV}$
J (186516, 186532, 186533)	EF_xe60_tight_noMu and $L2_{Met} > 55\,\mathrm{GeV}$
J (from 186533 excluded) to M	EF_xe60_verytight_noMu

Table 9: Trigger and additional requirements considered for the different periods of data taking.

Period	Run range	Luminosity (pb^{-1})	Trigger considered
B	178044 - 178109	11.73	EF_xe60_noMu
D	179710 - 180481	166.33	EF_xe60_noMu
E	180614 - 180776	48.65	EF_xe60_noMu
F	182013 - 182519	132.35	EF_xe60_noMu
G	182726 - 183462	507.53	EF_xe60_noMu
H	183544 - 184169	259.50	EF_xe60_noMu
I	185353 - 186493	338.39	EF_xe60_noMu
J	186516 - 186533	20.76	EF_xe60_tight_noMu
J	186669 - 186755	204.90	EF_xe60_verytight_noMu
K	186873 - 187815	590.10	EF_xe60_verytight_noMu
L	188921 - 190343	1403.68	EF_xe60_verytight_noMu
M	190608 - 191933	1019.73	EF_xe60_verytight_noMu
Total	178044 - 191933	4703.65	

Table 10: Integrated luminosity and associated trigger for the different periods of data taking. A total integrated luminosity of 4.7 pb^{-1} is calculated for the complete dataset, using the list of good runs specified in Section 3.

4.2 Efficiency in Data and simulation

To determine the trigger efficiency, a Data sample consisting of events triggered by EF_mu18_medium is used. These events are required to survive the cuts on jets and E_T^{miss} as defined in signal region 1 (see Table 8), and must include one reconstructed staco muon satisfying the following criteria:

- $p_T > 20$ GeV and $|\eta| < 2.4$

- *isCombined* requirements

- isolation cut : $p_T$cone20 < 1.8 GeV

- quality: tight and track quality

The Muon stream, corresponding to 4.5 fb^{-1} integrated luminosity, is used to collect this data sample. Datasets before and after the LAr hole problem are combined, as no significant difference in trigger efficiencies between the two is found.

Figure 1 shows the efficiency as a function of the offline reconstructed E_T^{miss} [4]. The trigger efficiency turn-on curve measured in data is compared to that from pile-up reweighted MC11c $W \rightarrow \mu\nu$ samples simulated with the ALPGEN generator. The Monte Carlo events are required to pass the same event selection cuts mentioned above. Trigger efficiencies in each bin of E_T^{miss} are summaried in Table 11. The effect of pile-up reweighting on the calculation of the simulated trigger efficiency is found to be negligible.

The efficiency of the trigger EF_xe60_verytight_noMu is computed using the Bayesian method. Trigger efficiencies derived from data and from the reweighted simulated samples agree within 1%. This difference is taken as a systematic uncertainty.

E_T^{miss} [GeV]	Efficiency in Data	Efficiency in MC
120 - 130	0.979 ± 0.002	0.971 ± 0.002
130 - 140	0.987 ± 0.001	0.983 ± 0.002
140 - 150	0.991 ± 0.001	0.990 ± 0.002
150 - 160	0.996 ± 0.001	0.997 ± 0.001
160 - 170	0.994 ± 0.001	0.998 ± 0.001

Table 11: EF_xe60_verytight_noMu efficiency in bins of E_T^{miss}, obtained from 2011 data and $W \rightarrow \mu\nu$ (ALPGEN) MC11c sample.

To investigate correlations between the leading jet transverse momentum and the E_T^{miss} trigger efficiency, efficiencies are studied for various leading jet p_T cuts. The cuts used are 60 ,90, and 120 GeV for MC, and 90 and 120 GeV for data. The trigger efficiency shows a strong dependency on the leading jet p_T cut, as shown in Figure 2. This behaviour is further investigated by studying the distribution of the Level-1 E_T^{miss} significance (XS), defined as:

$$ XS = \frac{E_T^{miss}}{0.5 \sqrt{SUME_T}} $$

.

Figure 3 shows the XS distribution for various leading jet p_T cuts in data and simulation. Higher cuts on the leading jet p_T result in higher XS, and hence a smaller contribution of the stochastic term to the E_T^{miss} resolution. This improvement in the resolution leads to higher efficiencies.

---

[4]The same reconstructed E_T^{miss} mentioned in the object definition section, Sec. 3, with no muon correction.
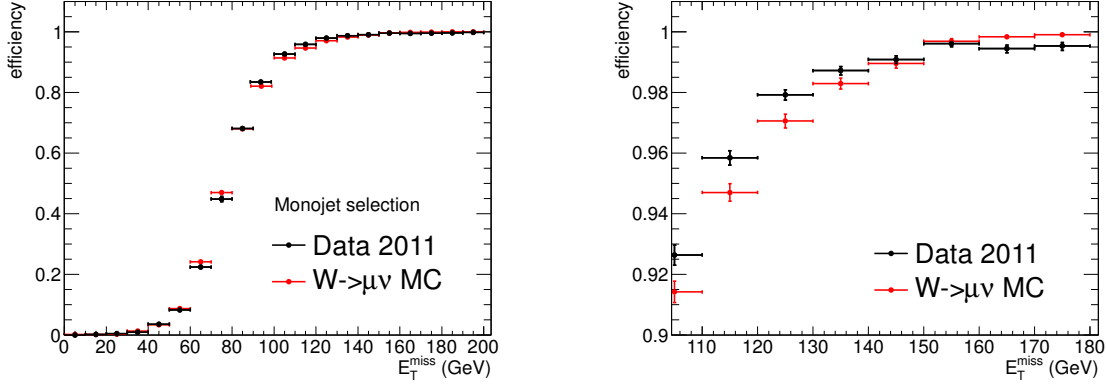
Figure 1: EF_xe60_verytight_noMu trigger efficiency as a function of E_T^{miss} on $W \rightarrow \mu\nu + jet$ data events (black). The turn-on curve from data (Black) is compared to the one from $W \rightarrow \mu\nu$ MonteCarlo (Red). On the right, a zoomed view of the left plot is shown.

A combined jet+E_T^{miss} is also studied. Due to non-trivial correlations between jet p_T and E_T^{miss} explained above, the determination of the efficiency becomes more difficult for such trigger. Also, due to the different calibrations of the trigger-based E_T^{miss} (at the electromagnetic energy scale) and the offline reconstructed jets (at the hadronic energy scale), an additional source of systematic uncertainty due to the Jet Energy Scale (JES) should be considered. Furthermore, the improvement in the trigger acceptance (the number of $Z \rightarrow \nu\nu$ (ALPGEN) events passing the monojet selection cuts) is less than 1% using the jet+E_T^{miss} trigger, as is shown in Figure 4; the difference between the acceptance of a E_T^{miss} trigger and a jet+E_T^{miss} trigger is within the statistical error of the events.

Due to the reasons mentioned above, the E_T^{miss}-only trigger is chosen for this analysis.
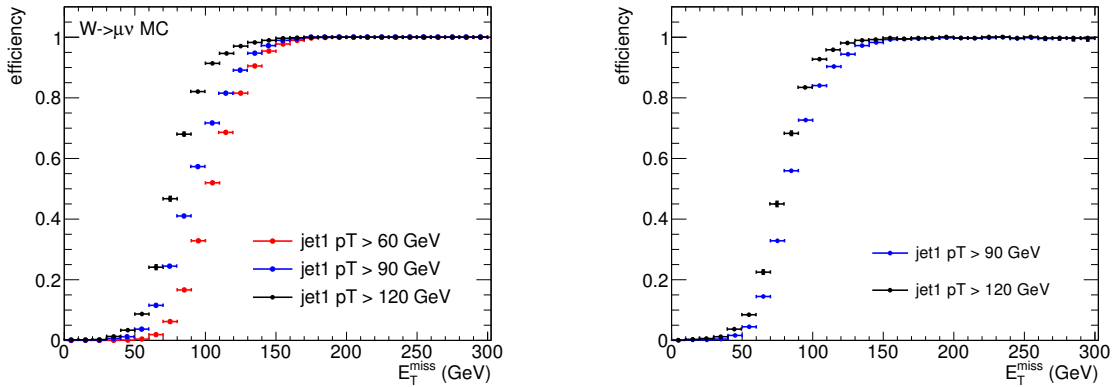
Figure 2: EF_xe60_verytight_noMu efficiency as a function of E_T^{miss} for varyious leading jet p_T cuts in $W \rightarrow \mu\nu$ MonteCarlo (left) and Data (right)

4.3 Trigger efficiency and pile-up

The trigger efficiency may also depend on pile-up. Therefore, a study quantifying effects of pile-up is necessary in order to correctly evaluate the final systematic uncertainty on the trigger efficiency. The
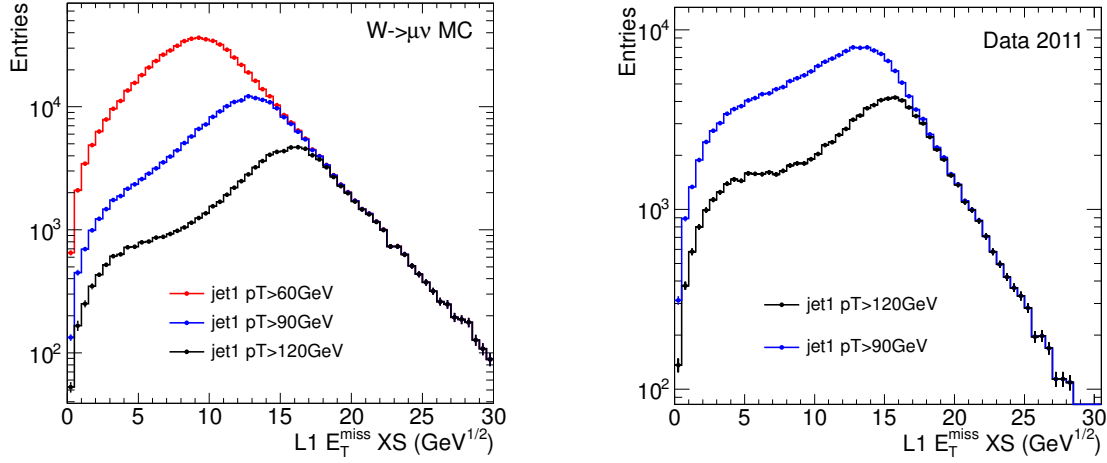
Figure 3: Level1 E_T^{miss} significance (MET XS) for varyious leading jet p_T cuts in MonteCarlo (left) and Data (right)
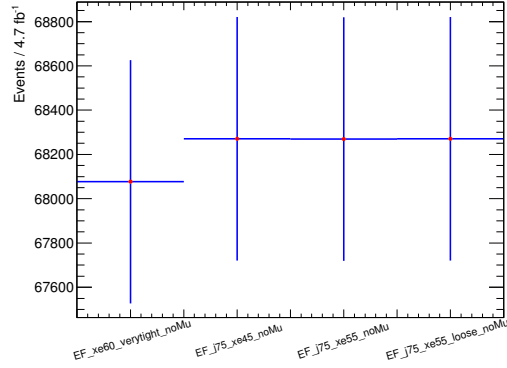
Figure 4: Number of $Z \rightarrow \nu\nu$ (ALPGEN) events after the low p_T monojet selection uts, as a function of different triggers.

pile-up studies in this section are performed on both data and $W \rightarrow \mu\nu$ Monte Carlo using the following event selection, which is a simplified version of the analysis selection cuts with an inverted muon veto.

- GRL

- muon trigger *EF_mu18* up to the period H, *EF_mu18_medium* from period I on

- At least one reconstructed primary vertex with a minimum of two tracks

- Release 17 medium cleaning cuts [5], a cut on *larError* flag, smart LAr hole veto

- Electron veto

- Inverted muon veto

- At least one *staco* muon with $p_T > 40\,\text{GeV}$

- Leading jet of $p_T > 120\,\text{GeV}$ and $|\eta| < 2.8$
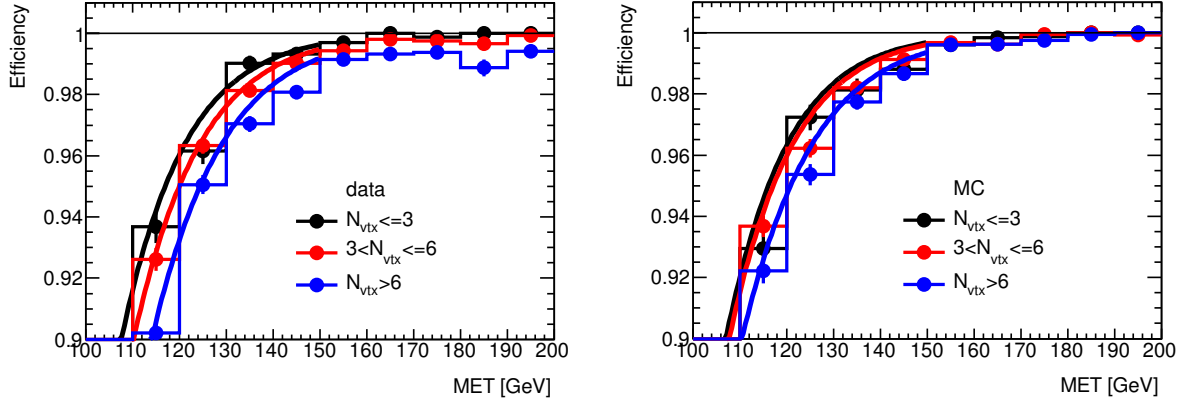
Figure 5: Trigger efficiency in different bins of number of primary vertices in data and $W \rightarrow \mu\nu$ Monte Carlo. The turn-on curves are fitted with a Fermi function.

	data	Monte Carlo
$N_{\text{vtx}} \leq 3$	0.960 ± 0.007	0.963 ± 0.008
$3 < N_{\text{vtx}} \leq 6$	0.950 ± 0.005	0.960 ± 0.005
$N_{\text{vtx}} > 6$	0.932 ± 0.007	0.947 ± 0.007

Table 12: Trigger efficiency in different bins of number of primary vertices in data and $W \rightarrow \mu\nu$ Monte Carlo. The values of the fitted turn-on curves at $MET = 120\,$GeV are given.

294 The effect of in-time pile-up can be studied by looking at the trigger efficiency in the events with
295 different amount of interactions per bunch crossing. The number of interactions per bunch crossing
296 is correlated with the number of reconstructed primary vertices N_{vtx}. Therefore, we choose to evalu-
297 ate the trigger efficiency for $N_{\text{vtx}} \leq 3$, $3 < N_{\text{vtx}} \leq 6$ and $N_{\text{vtx}} > 6$. The trigger turn-on curves for
298 *EF_xe60_veryTight_noMu* in these cases are displayed in Figure 5. The curves are fitted with a Fermi
299 function $y = \frac{1}{1+e^{Ax+B}}$, and the values of this function at $MET = 120\,$GeV are listed in Table 12. From the
300 differences between the efficiencies, we evaluate the systematic effect of the in-time pile-up as $\sim 1\%$.

301 The impact of out-of-time pile-up on the trigger efficiency is studied with the help of the bunch
302 position in the bunch train. We would like to see how do the neighbouring bunch crossings influence
303 the measured trigger efficiency. The readout window of the LAr calorimeter is $500\,$ns and the bunch
304 spacing in 2011 data is $50\,$ns. Therefore, the trigger turn-on is evaluated for the first 10 bunch crossings
305 in the bunch train, last 10 and the remaining bunch crossings in the middle. The turn-on curves for these
306 cases can be seen in Figure 6. The curves are fitted with a Fermi function, and the values of the fits at
307 $MET = 120\,$GeV are given in Table 13. The differences of the observed values quantify the systematic
308 uncertainty on the trigger efficiency coming from the out-of-time pile-up. This uncertainty is observed
309 to be less than 1%[5].

---

[5]In general, the initial part of the bunch trains has higher pile-up than the rest. Therefore, this study does not only show the effect of the out-of-time pile-up, and the resulting number has to be understood as an upper limit on the out-of-time pile-up systematics.
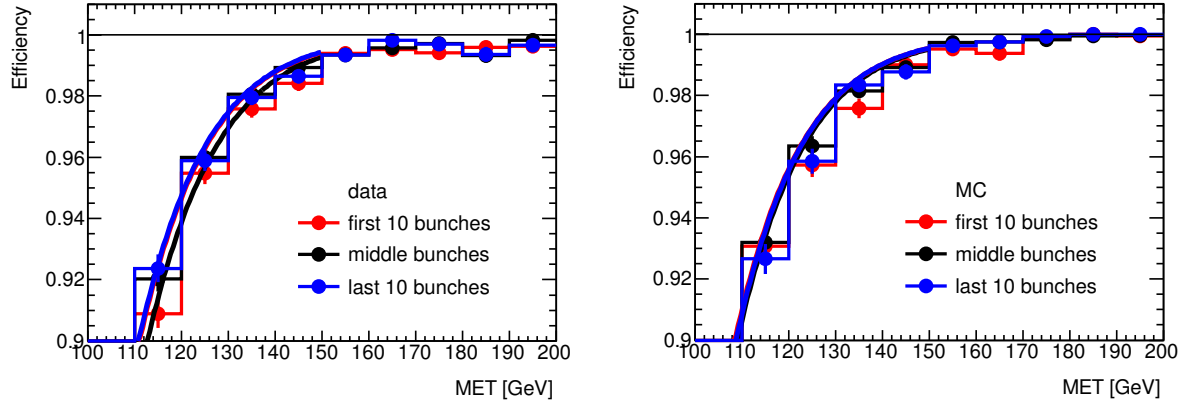
Figure 6: Trigger efficiency depending on the bunch position in the bunch train in data and $W \rightarrow \mu\nu$ Monte Carlo. The turn-on curves are fitted with a Fermi function.

	data	Monte Carlo
first 10 bunches	0.939 ± 0.007	0.954 + −0.007
middle bunches	0.947 ± 0.006	0.956 + −0.006
last 10 bunches	0.947 ± 0.007	0.956 + −0.007

Table 13: Trigger efficiency depending on the bunch position in the bunch train in data and $W \rightarrow \mu\nu$ Monte Carlo. The values of the fitted turn-on curves at $MET = 120\,\text{GeV}$ are given.

5   Strategy for the determination of the background from the Standard Model

5.1   Introduction

The mono-jet final state can originate from several processes of the Standard Model. The following sources are distinguished:

- The electroweak background from the W and Z bosons production in association with jets, and followed by their leptonic decays.

- The background originating from top pairs (t$\bar{\text{t}}$), single-top, and di-bosons productions

- The QCD multi-jet background

- The background from non-collision events

The contributions from t$\bar{\text{t}}$, single-top and di-bosons are determined from simulation, using the samples and normalizations described in Section 2. These backgrounds only contribute to about 1% of the total Standard Model monojet prediction. All the other backgrounds considered are estimated using a data-driven approach to minimize the dependence of the prediction on the modeling of QCD effects (PDF, renormalization scale, etc) and detector effects (Jet energy scale and resolution, Missing transverse momentum scale and resolution, pile-up, etc) that might not be well understood for highly energetic regions of monojet events.

The largest source of background from the Standard Model is Z+Jets events where the Z boson decays to a pair of neutrinos, and W+Jets events where the W bosons decays to a lepton which escapes the dedicated veto. A particular treatment has been made to determine the prediction of these processes.

5.2   The electroweak background

The estimation of the W/Z electroweak backgrounds is obtained from control regions with Z+Jets or with W+jets data events where the selected boson decays to an electron or a muon that can be well identified, and where the jets fulfill the same requirements as in the signal regions. Hence, to each signal region defined in Section 3 corresponds four orthogonal control regions, one mainly composed of W+jets events where the W bosons decay to muon, one for W+jets events with the W bosons decaying to electron, one for Z+jets events with the Z bosons decaying to a pair of muons, and, the last control region consists of Z+jets events where the Z bosons decay to a pair of electrons.

This method reduces the large systematic uncertainties due to the modeling of jet quantities, because of applying the same jet selections in both the control and signal regions, using well identified Z+jets events, to model the Z+jets background to monojet events, and well identified W+jets events to model the jet distribution of the W+jets events in the signal region. In such method there is no need to have a precise estimate of the absolute W+jets and Z+jets cross sections, or to assume any relative k-factor between various W+jets and Z+jets contributions to monojet events, as well-identified Z+jets events are used to model Z+jets backgrounds and similarly for Ws. The precision of the method therefore relies on how well we model the difference in the impact of the lepton between the signal and the control regions, as well as the background to W+jets and Z+jets control region events (because the Z+jets control region is used to predict the number of Z+jets events in the signal region, and not the full signal region background). Standard Model measurements of W and Z events have already shown accurate modeling of lepton acceptances and efficiencies as well as precise background estimate to W and Z events. Similar studies can be used in the present analysis.

351 The presence of leptons in the events of the control regions is responsible for small differences in
352 the E_T^{miss} and the number of jets (N_{jets}) distributions between these control regions and the the signal
353 region. Simulations are used to estimate these effects. For example, in order to get the E_T^{miss} distribution
354 of $Z(\rightarrow \nu\nu)$+jets events from $Z(\rightarrow \ell\ell)$+jets events, the energy of the leptons originating from the the
355 Z boson has to be removed from the reconstructed E_T^{miss} quantity. In the particular case of a control
356 region based on events with muons, the E_T^{miss} is only very slightly affected by the presence of the muons
357 since muons only interact as minimum ionizing particles with the material of the calorimeter, and a
358 purely calorimeter-based E_T^{miss} reconstruction is considered in this analysis. Using simulations to model
359 the effects of muons on the E_T^{miss} distribution will therefore not result in large uncertainties because the
360 effect itself is very small.

361 Sections 6, 7, and 8 present data-driven determinations of the electroweak backgrounds. Sections 6
362 and 7 perform differential pseudo cross section measurements of W+jets and Z+jets productions in ex-
363 clusive control regions. Different corrections are then applied to translate the measurements to the signal
364 region (see Section 5.2.1 for details). Section 8 takes a more inclusive and simpler approach where
365 control regions are defined after reverting the lepton veto requirements applied in the selection criteria.
366 Inclusive electron and muon control regions are defined using events with at least one electron or muon
367 in the final state. In addition, more exclusive control regions with Ws and Zs in the final state are then
368 defined applying a transverse mass cut and selecting dilepton events within the Z mass peak, respectively.
369 Bin-by-bin transfer factor, as extracted from simulation, are then built to translate in one single step, the
370 measured distributions in the control regions to the signal region (see Section 5.2.2 for details).

371 Despite high correlations between events in the different approaches, the two methods are sufficiently
372 different and allow a very powerful cross check of each other.

373 ### 5.2.1 Method based on pseudo cross section measurements

374 In order to obtain the data-driven prediction of $Z(\rightarrow \nu\nu) + jets$ in the signal region ($N_{Z(\rightarrow \nu\nu)+jets}^{DD,SR}$) from
375 $Z(\rightarrow \ell\ell) + jets$ events selected in the control region (ℓ referring to electrons or to muons), we need to
376 apply the three following corrections:

377 • A subtraction of the Standard Model background (N_{bkg}) to the selected candidate events in the
378   control region in order to have a pure $Z(\rightarrow \ell\ell) + jets$ sample;

379 • A transfer function (T_ℓ) that account for the charge lepton acceptance and efficiency of the control
380   region selections, as well as for the difference in the impact of the lepton between the signal and
381   the control regions;

382 • The efficiency ratio of the trigger used in the signal and the control regions (R_{trig}).

From these three corrections, the prediction for the number of monojet events expected from Z+jets
events where the Z boson decays to a pair of neutrinos is given by:

$$N_{Z(\rightarrow \nu\nu)+jets}^{DD,SR} = (N_{Z(\rightarrow \ell\ell)+jets}^{Data} - N_{bkg}) \times T_\ell \times R_{trig} \tag{1}$$

383 This formula assumes that the same good run list has been used in both the control and the signal
384 regions, in order to ensure a perfect cancellation of the luminosity corrections. Because of the leptons
385 acceptance and efficiencies, the amount of background in the control region and the distortion of the
386 hadronic E_T^{miss} distribution by the presence of the lepton in the control regions can vary as a function of
387 the vector boson transverse momentum (which correspond to the E_T^{miss} in $Z(\rightarrow \nu\nu) + jets$ events). These
388 correction factors are binned as a function of the E_T^{miss} distribution on which we cut to select various
389 signal regions. Such correction therefore modifies both the shape and the normalization of the E_T^{miss}

390 distribution obtained in the control region to obtain the proper $Z(\to \nu\nu) + jets$ prediction in the signal
391 region.

392   A priori, these three correction factors are obtained from simulation. However, these correction
393 factors can further be decomposed into corrections that can only be obtained from simulation and cor-
394 rections that can be extracted from data. For example, Standard Model W and Z measurements indicated
395 that while the electroweak background contribution to $Z(\to \ell\ell) + jets$ events in our control region can
396 be modeled reasonably well by simulations, the QCD background must be predicted from data. We
397 can therefore decompose the background correction factor (N_{bkg}) into an electroweak component that
398 can be obtained from Monte Carlo (N_{ewk}) and a QCD component N_{QCD} estimated from data. Simi-
399 larly, the transfer function can be decomposed into a lepton efficiency factor that can be estimated using
400 data-driven technique well-established in the ATLAS collaboration, a simulation factor correcting for the
401 detector and kinematic acceptance of the lepton selections defining the control region, and another factor
402 obtained from simulation which accounts for the impact of the lepton on the E_T^{miss} and N_{jets} distributions
403 extracted from the control region. Data to Monte Carlo efficiency scale factors have been shown to be
404 as high as 5% by the various ATLAS performance group. Using such data-driven correction factors
405 therefore considerably improves the precision of the estimate by not fully relying on simulation or the
406 various lepton corrections. The other advantage of further decomposition of the factor presented above
407 is that by correcting first for background, efficiencies and acceptance, we thus obtain results that can be
408 compared to pseudo-cross section measurements of Z+jets and W+jets processes, i.e. cross section after
409 full lepton correction but before jet unfolding. This helps to give additional confidence on the validity of
410 the prediction.

411   In Sections 6 and 7, this method is applied to muon and electron control regions to obtain predictions
412 for the $Z(\to \nu\nu) + jets$ background following the above procedure. The three correction factors presented
413 above are further decomposed when a sub-factor can be extracted from data. The $W(\to \ell\nu) + jets$ back-
414 ground to monojet events is obtained similarly. Finally, in order to cross check the prediction obtained
415 from $Z(\to \ell\ell) + jets$ events, $W(\to \ell\nu) + jets$ control region events are also used, separately, to obtain
416 a prediction for the $Z(\to \nu\nu) + jets$ background to monojet events. While the systematic uncertainty on
417 such prediction will typically be higher than the one obtained from $Z(\to \ell\ell) + jets$ (different jet mo-
418 mentum, different E_T^{miss} distribution, different k-factors, etc), the statistical uncertainty will be smaller,
419 which could be a real advantage in very high kinematic regions. Results will later be compared. All
420 these correction factors are summarized in the equations below:

$$N_{Z(\to \nu\nu)+jets}^{DD,SR} = \frac{N_{Z(\to \ell\ell)+jets}^{Data} - N_{QCD}}{A_\ell \times \epsilon_\ell \times \epsilon_\ell^{trig} \times \mathcal{L}_\ell} \times (1 - f_{EW}) \times \frac{N_{Z(\to \nu\nu)+jets}^{SR}}{N_{Z(\to \ell\ell)+jets}} \times \epsilon_{E_T^{miss}}^{trig} \times \mathcal{L}_{E_T^{miss}} \tag{2}$$

$$N_{Z(\to \nu\nu)+jets}^{DD,SR} = \frac{N_{W(\to \ell\nu)+jets}^{Data} - N_{QCD}}{A_\ell \times \epsilon_\ell \times \epsilon_W \times \epsilon_\ell^{trig} \times \mathcal{L}_\ell} \times (1 - f_{EW}) \times \frac{N_{Z(\to \nu\nu)+jets}^{SR}}{N_{W(\to \ell\nu)+jets}} \times \epsilon_{E_T^{miss}}^{trig} \times \mathcal{L}_{E_T^{miss}} \tag{3}$$

$$N_{Z(\to \ell\ell)+jets}^{DD,SR} = \frac{N_{Z(\to \ell\ell)+jets}^{Data} - N_{QCD}}{A_\ell \times \epsilon_\ell \times \epsilon_\ell^{trig} \times \mathcal{L}_\ell} \times (1 - f_{EW}) \times \epsilon_{E_T^{miss}}^{trig} \times \mathcal{L}_{E_T^{miss}} \times T(\ell) \tag{4}$$

$$N_{W(\to \ell\nu)+jets}^{DD,SR} = \frac{N_{W(\to \ell\nu)+jets}^{Data} - N_{QCD}}{A_\ell \times \epsilon_\ell \times \epsilon_W \times \epsilon_\ell^{trig} \times \mathcal{L}_\ell} \times (1 - f_{EW}) \times \epsilon_{E_T^{miss}}^{trig} \times \mathcal{L}_{E_T^{miss}} \times T(\ell) \tag{5}$$

421   where:

422   • $N_X^{DD,SR}$ the data-driven determination of the process X in the signal region

423   • N_X^{Data} and N_{QCD} are the number of Data and QCD events in the control region X, respectively

- A_ℓ and ϵ_ℓ are the lepton acceptance (from simulation) and identification efficiency (from Data), respectively

- ϵ_ℓ^{trig} and $\mathcal{L}_{lep}$ are the lepton trigger efficiency (from Data) and the corresponding luminosity, for the lepton control region considered

- $\epsilon_{E_{\mathrm{T}}^{\mathrm{miss}}}^{trig}$ and $\mathcal{L}_{met}$ are the $E_{\mathrm{T}}^{\mathrm{miss}}$ trigger efficiency (from Data) and the corresponding luminosity, for the signal region

- ϵ_W is the simulated efficiency for the W boson specific selection cuts

- f_{EW} is the electroweak background fraction defined by the ratio of simulated electroweak events except that of the control region process over all simulated electroweak events

- $\frac{N_{Z(\to \nu\nu)+jets}^{SR}}{N_{Z(\to \ell\ell)+jets}}$ is the ratio of simulated $Z(\to \nu\nu) + jets$ events in the signal region over simulated $Z(\to \ell\ell) + jets$ events with the full lepton phase space. This term includes the ratio of branching fractions $\frac{\mathrm{Br}(Z\to\nu\nu)}{\mathrm{Br}(Z\to\ell\ell)}$, and the difference in topology between the decays $Z(\to \nu\nu) + jets$ and $Z(\to \ell\ell) + jets$

- $\frac{N_{Z(\to \nu\nu)+jets}^{SR}}{N_{W(\to \ell\nu)+jets}}$ is the ratio of simulated $Z(\to \nu\nu) + jets$ events in the signal region over simulated $W(\to \ell\nu) + jets$ events with the full lepton phase space. This term includes the ratio of branching fractions $\frac{\mathrm{Br}(Z\to\nu\nu)}{\mathrm{Br}(Z\to\ell\ell)}$, the ratio $R_{W/Z+jets}^\sigma$ of the W+jets cross section over that of Z+jets, and the difference in topology between the decays $Z(\to \nu\nu) + jets$ and $W(\to \ell\nu) + jets$

- $T(\ell)$ is a transfer factor that includes the probability that $W + jets$ or $Z + jets$ events in the signal region survive the lepton veto requirement, but also the difference of phase space between the target process and the full lepton phase space of $W + jets$ or $Z + jets$ events (depending on the control region considered)

In summary, the main idea is first to select a W or a Z boson in Data using dedicated cuts and background removal, and then to correct for these cuts with correction factors, which provides a pseudo cross section of the boson (it is corrected for the lepton acceptance but not for the jets). The next step is to normalize to the luminosity of the signal region (has no impact on the precision of the measurement as the luminosity in the signal region is the same, but allows for intermediate pseudo-cross section validation). Finally, the last correction factors allow to convert the $E_{\mathrm{T}}^{\mathrm{miss}}$ and N_{jet} distributions obtained in the control region after lepton selection correction to what they should be in the signal region where no leptons interfere with the hadronic activity measurement. Such factors can also eventually correct cross section differences between the two processes.

A particularity of this method is that it provides a total of four measurements of $Z(\to \nu\nu) + jets$ in the signal region, using control regions based on the electron and muon leptonic decays of the W or Z boson.

5.2.2 Method based on an overall transfer factor

The method described in Section 8 defines the control regions by reverting the lepton vetoes and selecting either inclusive lepton (electron or muon) samples, or more exclusive Ws and Zs samples after applying an additional transverse mass cut and selecting events with dileptons in the final state state, respectively. Therefore, three different control regions are constructed: inclusive-lepton, exclusive Ws, and exclusive Zs. After subtracting non-EWK background contributions from QCD, top and dibosons processes in the control regions, bin-by-bin transfer factors are then defined separately for each EWK sub-process and for each of the measured distributions.

As an example, in the case of the $Z(\to \nu\nu) + jets$ process, its constribution to the signal region in a given bin of a given distribution $N(Z(\to \nu\nu) + jets)_{signal}$ would be determined using the inclusive muon control region according to

$$N(Z(\to \nu\nu) + jets)_{signal} = (N^{data}_{\mu,control} - N^{background}_{\mu,control}) \times \frac{N^{MC}(Z(\to \nu\nu) + jets)_{signal}}{N^{MC}_{\mu,control}} \qquad (6)$$

where $N^{data}_{\mu,control}$ denotes the observed events in data in the control region, $N^{background}_{\mu,control}$ is the non-EWK background, $N^{MC}(Z(\to \nu\nu) + jets)_{signal}$ is the number of $Z(\to \nu\nu) + jets$ simulated events as determined by the simulation in the signal region, and $N^{MC}_{\mu,control}$ is the predicted MC events in the muon inclusive sample formed by a mixture of W+jets and Z+jets dominated by the W+jets contribution. Similarly, the $N(Z(\to \nu\nu) + jets)_{signal}$ contribution can be determined using exclusive Ws and Zs control samples in data according to

$$N(Z(\to \nu\nu) + jets)_{signal} = (N^{data}_{W\to\mu\nu,control} - N^{background}_{W,control}) \times \frac{N^{MC}(Z(\to \nu\nu) + jets)_{signal}}{N^{MC}_{W\to\mu\nu,control}} \qquad (7)$$

and

$$N(Z(\to \nu\nu) + jets)_{signal} = (N^{data}_{Z\to\mu\mu,control} - N^{background}_{Z,control}) \times \frac{N^{MC}(Z(\to \nu\nu) + jets)_{signal}}{N^{MC}_{Z\to\mu\mu,control}}, \qquad (8)$$

respectively, where now $N^{data}_{W\to\mu\nu,control}$ ($N^{data}_{Z\to\mu\mu,control}$) and $N^{MC}_{W\to\mu\nu,control}$ ($N^{MC}_{Z\to\mu\mu,control}$) denote the number of $W \to \mu\nu$ ($Z \to \mu\mu$) candidates in data and MC in the control region. Therefore, in each control sample, the transfer factors for each process are simply defined as the ratio of simulated events for the process in the signal region over the total number of simulated events in the control region. In this way the transfer factors include in a single step all effects related to lepton acceptance and efficiency and take as input the predicted branching ratios for the W and Z decays into leptons. The use of the three control samples (inclusive, Ws and Zs) gives confidence that the transfer factors determined from MC simulation are understood.

6   Data-driven electroweak background determination from a muon control region

6.1   Introduction

In this section, a data-driven method for determining each of the W/Z electroweak backgrounds in the mono-jet signal regions is presented. Two control regions are considered, based on the processes: $Z(\to \mu\mu)$+jets and $W(\to \mu\nu)$+jets.

The W-based control region is used to derive $Z(\to \nu\nu)$+jets, $W(\to \tau\nu)$+jets, and $W(\to \mu\nu)$+jets in the signal region. Similarly, the Z-based control region is employed to determine $Z(\to \nu\nu)$+jets, $Z(\to \tau\tau)$+jets, and $Z(\to \mu\mu)$+jets in the signal region.

To select events in the $Z(\to \mu\mu)$+jets and $W(\to \mu\nu)$+jets control regions, the same trigger as in the signal region is utilized. Since it is a calorimeter-based trigger, the W/Z decays into muons are not highly reduced. The advantage lies in the fact that it simplifies Equations 3 and 4 (Section 5), and avoids additional systematic uncertainties.

To each control region a set of correction factors is applied to recover the full lepton phase space, after which another set of correction factors is used to get the final estimation for each of the target electroweak backgrounds in a mono-jet signal region. For each of the correction factors, closure tests based on simulation are done to validate them. Even if not mentioned, all the correction factors are applied bin-by-bin to the control regions (as function of the E_T^{miss}), and are calculated with respect to the mono-jet selection cuts. In the following, the complete procedure is explained in detail.

6.2   Muon reconstruction efficiencies

The same "good muon" definition is considered to select the $Z(\to \mu\mu)$+jets and $W(\to \mu\nu)$+jets control regions:

- staco combined

- $p_T > 20$ GeV and $|\eta| < 2.4$

- Isolation cut : ptcone20 < 1.8 GeV, where ptcone20 is the p_T sum of all the tracks in a cone of radius 0.2 around the muon track

- z distance of the muon with respect to the primary vertex lower than 10 mm

- Matched inner detector track fulfilling the recommendion of the Muon Combined Performance group [6]

In order to correct control region events for the muon selection, the muon reconstruction efficiencies are required. The Scale Factor defined by the ratio of the reconstruction efficiency in Data over that in simulation is provided by the Muon Combined Performance group. The efficiency in simulation has therefore been computed in such a way to be multiplied by the scale factors to obtain the efficiency in Data.

The muon reconstruction efficiencies in simulation have been derived by matching a truth muon to a reconstructed muon in η and ϕ, with $\Delta R = \sqrt{\eta^2 + \phi^2} < 0.05$, and using $Z\mu\mu$ events simulated with PYTHIA. The same binning in regions of η and ϕ as that used by the Muon Combined Performance group has been used. The muon reconstruction efficiency is flat in p_T from 7 GeV onwards, but not the muon isolation efficiency. Reconstruction and isolation efficiencies have therefore been calculated separately. The muon isolation efficiency is estimated as function of the muon p_T and with respect to a reconstructed muon. Figure 7 represents the good muon reconstruction and isolation efficiencies.

Not reviewed, for internal circulation only
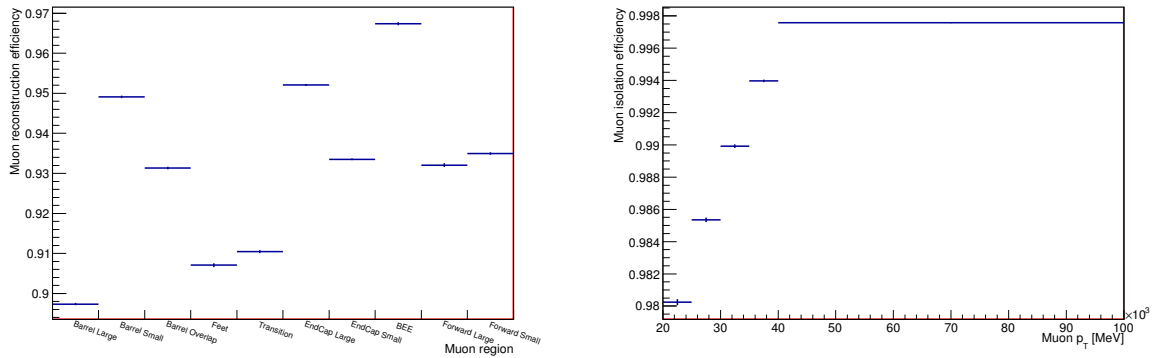
Figure 7: Left: Good muon reconstruction efficiency in simulation as function of the muon region (average = 93.44 ± 0.01%). Right: Good muon isolation efficiency in simulation with respect to a reconstructed muon, and as function of the muon p_T (average = 99.3%).

The muon reconstruction and isolation efficiencies have also been computed for muons fulfill the muon veto quality (defined in Section 3). Figure 8 represents the reconstruction and isolation efficiencies of the muons satisfying the quality cuts used in the muon veto definition (loose muons defined in Section 3).
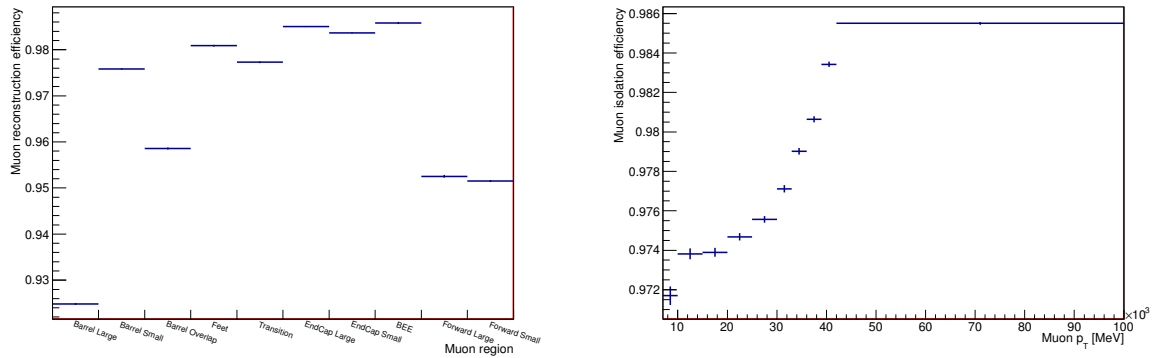
Figure 8: Left: Veto muon reconstruction efficiency in simulation as function of the muon region (average = 96.4 ± 0.01%). Right: Veto muon isolation efficiency in simulation with respect to a reconstructed muon, and as function of the muon p_T (average = 98.0%).

In the following, ϵ_{reco} refers to the product of the reconstruction and isolation efficiencies.

6.3   Z($\mu\mu$) control region

Events that enter the Z($\mu\mu$) control region are required to pass the following criteria:

- Exactly two good muons

- All the signal region cuts on the jets and E_T^{miss}, as well as the lepton veto (except the selected muons)

- $66 < \frac{m_{\mu\mu}}{\text{GeV}} < 116$ with $m_{\mu\mu}$ the invariant mass computed from the four vetors of the two selected muons (in order to limit the contamination from γ^*)

Simplifying the equations of Section 5.2.1, the total number of Z($\nu\nu$), Z($\mu\mu$), and Z($\tau\tau$) events in the signal region can be written as:

$$N^{DD,SR}_{Z(\to \nu\nu)+jets} = \frac{N^{Data}_{Z(\to \mu\mu)+jets}}{A_\mu \times \epsilon_{\mu_1} \times \epsilon_{\mu_2} \times} \times (1 - f_{EW}) \times \frac{N^{SR}_{Z(\to \nu\nu)+jets}}{N_{Z(\to \mu\mu)+jets}} \quad (9)$$

$$N^{DD,SR}_{Z(\to \tau\tau)+jets} = \frac{N^{Data}_{Z(\to \mu\mu)+jets}}{A_\mu \times \epsilon_{\mu_1} \times \epsilon_{\mu_2}} \times (1 - f_{EW}) \times T(\bar{t}) \quad (10)$$

$$N^{DD,SR}_{Z(\to \mu\mu)+jets} = \frac{N^{Data}_{Z(\to \mu\mu)+jets}}{A_\mu \times \epsilon_{\mu_1} \times \epsilon_{\mu_2}} \times (1 - f_{EW}) \times T(\not\mu) \quad (11)$$

where $N_{Z(\to \mu\mu)+jets}$ is the total number of simulated events in the Z control region with the full muon phase space, and after requiring the invariant mass constructed from the truth four vectors of the two muons from Z to be within the mass window of the Z. Here "Full lepton phase space" refers to the phase space after the mono-jet selection cuts except the muon veto (i.e., cuts on the jets and the E_T^{miss}, electron veto, and veto on any muon not from the Z decay).

Since the Z($\mu\mu$) control region depends on mono-jet signal region cuts, there are as many control regions as mono-jet signal regions, as listed in Table 14.

Control regions	CR 1	CR 2	CR 3	CR 4
Common cuts	Preselection cuts + $\Delta\phi(E_T^{miss}, jet_2) > 0.5 + N_{jets} < 3$ + exactly 2 good muons + lepton veto (except on good muons) + $66 < \frac{m_{\mu\mu}}{\text{GeV}} < 116$			
Dedicated cuts	$p_T^{jet_1} > 120$ GeV $E_T^{miss} > 120$ GeV	$p_T^{jet_1} > 220$ GeV $E_T^{miss} > 220$ GeV	$p_T^{jet_1} > 350$ GeV $E_T^{miss} > 350$ GeV	$p_T^{jet_1} > 500$ GeV $E_T^{miss} > 500$ GeV

Table 14: Definition of the four Z($\mu\mu$) exclusive control regions (CR).

Backgrounds to this control region consist of the electroweak and QCD multi-jet events. The electroweak background is estimated using simulation while the QCD background is negligible in this channel. The background is composed of (in percentage of simulated Z($\mu\mu$) events in CR1): $t\bar{t}$ + single top (1.1%), di-bosons (0.8%), and Z($\tau\tau$) (0.1%) events.

In CR1, CR2, CR3 and CR4, a total of 4803, 445, 45, and 6 Z($\mu\mu$) candidate events are selected in Data, respectively. The background contamination is stable at nearly 2%.

Figure 9 shows kinematic distributions of the two good muons and of the leading jet in the control region corresponding to the first signal region. Only shapes are compared, since the simulation is normalized to Data by scaling the simulated W and Z contributions. For these plots (CR1), W and Z simulated events were thus scaled by 0.93. Good agreements between Data and simulation are observed.

6.3.1 Correction factors to get the full lepton phase space

First the electroweak background to the control region is removed by multiplying (bin by bin) $N^{Data}_{Z(\to \mu\mu)+jets}$ by $(1 - f_{EW})$, where f_{EW} is defined as:

$$f_{EW} = \frac{N^{CR}(\text{All EW channels except Z}(\mu\mu))}{N^{CR}(\text{Total EW})} \quad (12)$$
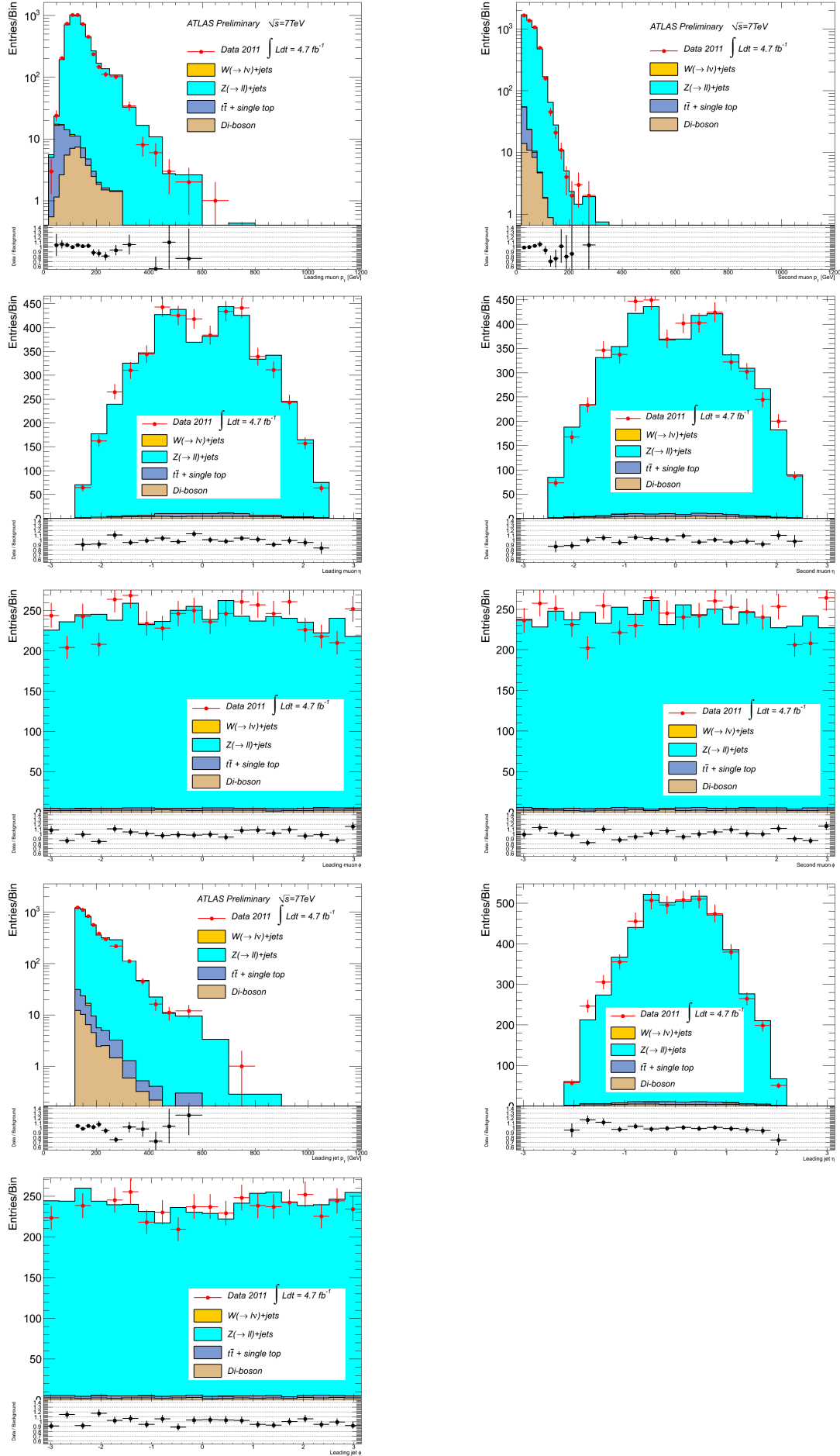
Figure 9: (top left to bottom right) first and second muons p_T, η, and ϕ, leading jet p_T, η, and ϕ.

556 with N being the number of simulated events. A background contamination of 2% is found. Table 15
557 includes the values of (1-f_{EW}) in each Z($\mu\mu$) control region.

558

559 The muon acceptance (in p_T and η) and the muon reconstruction efficiencies are required as correc-
560 tion factors to recover the full lepton phase space.

561 The muon acceptance is calculated from simulation and is defined by the number of events with
562 two reconstructed muons passing the cuts $p_T > 20$ GeV, $|\eta| < 2.4$ and $66 < \frac{m_{\mu\mu}}{\text{GeV}} < 116$ over the number
563 of events for which the invariant mass reconstructed from the truth four vectors of the two muons is
564 included in the Z boson mass window. The condition on the truth invariant mass is required to limit the
565 contamination from γ^*. The same cut is placed on the simulated Z($\rightarrow \mu\mu$)+ *jets* events at the denominator
566 of the correction factor of Equation 13, so that after combining the latter with the acceptance correction,
567 the efficiency of this cut is canceled. The muon acceptance in the control region relative to the first bin of
568 signal region is shown in Fig 10. Table 16 provides the average values for the acceptance in all control
569 regions.
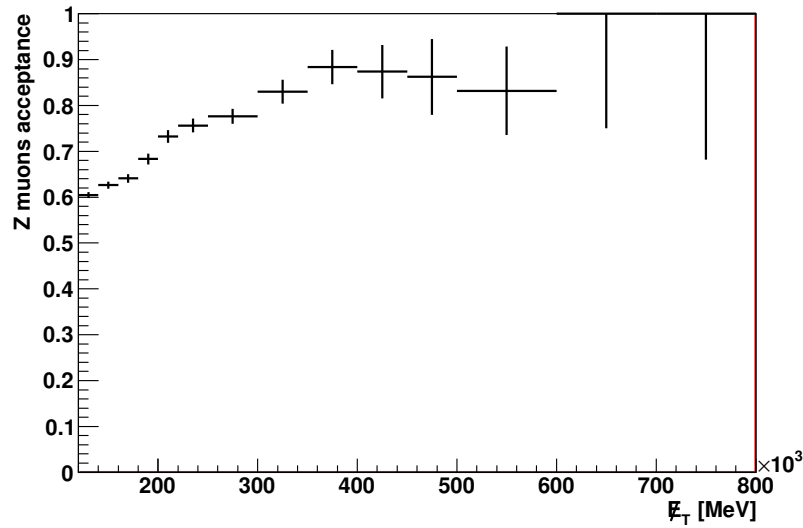
Figure 10: Z($\mu\mu$) muon acceptance in the first control region.

Control regions	(1-f_{EW}) (%)
CR 1	98.0 ± 0.1
CR 2	98.6 ± 0.1
CR 3	98.4 ± 0.3
CR 4	97.7 ± 1.0

Table 15: (1-f_{EW}) in each Z($\mu\mu$) control region, with f_{EW} calculated as ratio of integrals (uncertainties are statistical).

Control regions	Acceptance (%)
CR 1	65.25 ± 0.37
CR 2	79.27 ± 1.06
CR 3	86.36 ± 2.99
CR 4	85.00 ± 7.98

Table 16: Average values of the muon acceptance corrections in each Z($\mu\mu$) control region (uncertainties are statistical).

6.3.2 Z($\nu\nu$) correction factors

The full lepton phase space of Z($\mu\mu$) is used to estimate the Z($\nu\nu$) contribution to the signal region, using the additional factor:

$$\frac{N^{SR}_{Z(\rightarrow\nu\nu)+jets}}{N_{Z(\rightarrow\mu\mu)+jets}} \tag{13}$$

This correction factor includes the branching ratio of Z($\nu\nu$) to Z($\mu\mu$) after mono-jet cuts, and the differences in the event topologies. Table 17 provides its values as a ratio of integrals, for each control region, while Figure 11 shows it in the first control region.

Control regions	$\frac{N^{SR}_{Z(\rightarrow\nu\nu)+jets}}{N_{Z(\rightarrow\mu\mu)+jets}}$
CR 1	7.24 ± 0.03
CR 2	7.69 ± 0.15
CR 3	8.56 ± 0.57
CR 4	8.49 ± 1.53

Table 17: $\frac{N^{SR}_{Z(\rightarrow\nu\nu)+jets}}{N_{Z(\rightarrow\mu\mu)+jets}}$ (ratio of integrals) in each Z($\mu\mu$) control regions (uncertainties are statistical).
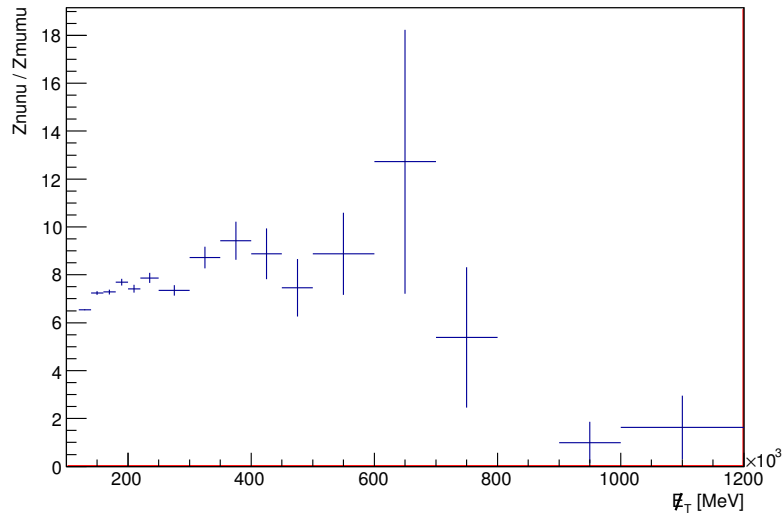
Figure 11: Correction factor $\frac{N^{SR}_{Z(\rightarrow\nu\nu)+jets}}{N_{Z(\rightarrow\mu\mu)+jets}}$ for the first control region.

6.3.3 Z($\tau\tau$) correction factors

The Z($\tau\tau$) background in the mono-jet signal region is determined by applying the following factor to the full lepton phase space of Z($\mu\mu$):

$$T(\not{E}) = \frac{N^{SR}_{Z(\rightarrow\tau\tau)+jets)}}{N_{Z(\rightarrow\mu\mu)+jets}} \tag{14}$$

579   This factor corrects for the differences in both the rate and the event topology between $Z(\mu\mu)$ and
580 $Z(\tau\tau)$ events. Table 18 lists the value of this factor as a ratio of integrals, for each control region.
581 Figure 12 shows this factor in the first control region.
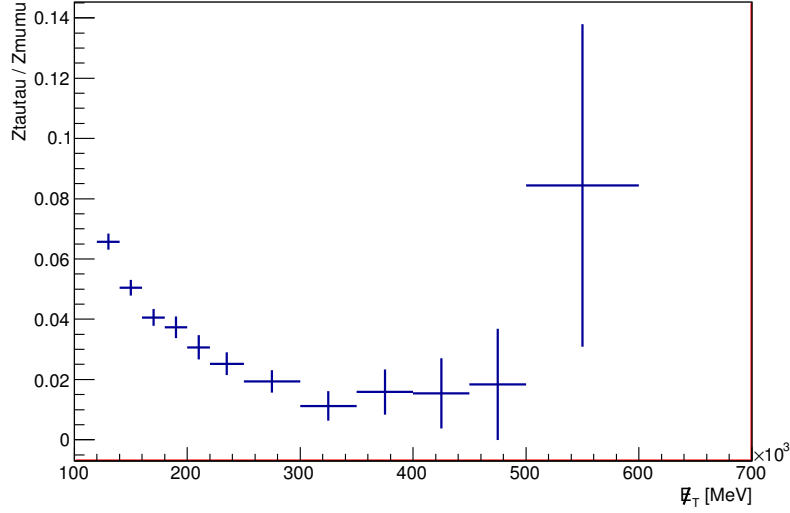
Figure 12: Correction factor $\frac{N^{SR}_{Z(\to\tau\tau)+jets}}{N_{Z(\to\mu\mu)+jets}}$ for the first control region.

Control regions	$\dfrac{N^{SR}_{Z(\to\tau\tau)+jets}}{N_{Z(\to\mu\mu)+jets}}$
CR 1	0.048 ± 0.001
CR 2	0.022 ± 0.003
CR 3	0.024 ± 0.009
CR 4	0.012 ± 0.012

Table 18: $\frac{N^{SR}_{Z(\to\tau\tau)+jets}}{N_{Z(\to\mu\mu)+jets}}$ (ratio of integrals) in each $Z(\mu\mu)$ control region (Uncertainties are statistical).

6.3.4   Z($\mu\mu$) correction factors

583 The $Z(\mu\mu)$ background in the signal region is obtained by applying the factor $T(\mu)$ (as defined in Equa-
584 tion 15) to the full lepton phase space of $Z(\mu\mu)$. Table 19 lists the values of $T(\mu)$ as a ratio of integrals,
585 in each control region. Figure 13 represents it in CR1.

$$T(\mu) = \frac{N^{SR}_{Z(\to\mu\mu)+jets)}}{N_{Z(\to\mu\mu)+jets}} \tag{15}$$

6.3.5   Closure tests

587 In order to check the validity of the correction factors used to correct the control regions, closure tests
588 are performed using simulated samples. Figure 14 compares the $Z(\nu\nu)$ distribution in the signal region
589 (obtained from $Z(\nu\nu)$ simulation) to the one obtained using the $Z(\mu\mu)$ control region.

Control regions	$\frac{N^{SR}_{Z(\to\mu\mu)+jets}}{N_{Z(\to\mu\mu)+jets}}$
CR 1	0.0232 ± 0.0003
CR 2	0.0120 ± 0.0005
CR 3	0.0068 ± 0.0009
CR 4	0.0152 ± 0.0052

Table 19: $\frac{N^{SR}_{Z(\to\mu\mu)+jets}}{N_{Z(\to\mu\mu)+jets}}$ (ratio of integrals) in each $Z(\mu\mu)$ control region (uncertainties are statistical).
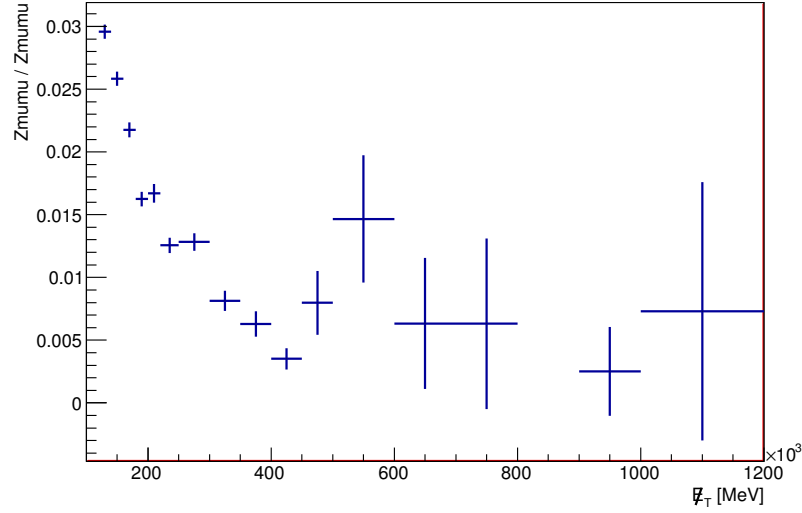
Figure 13: Correction factor $\frac{N^{SR}_{Z(\to\mu\mu)+jets}}{N_{Z(\to\mu\mu)+jets}}$ for the first control region.
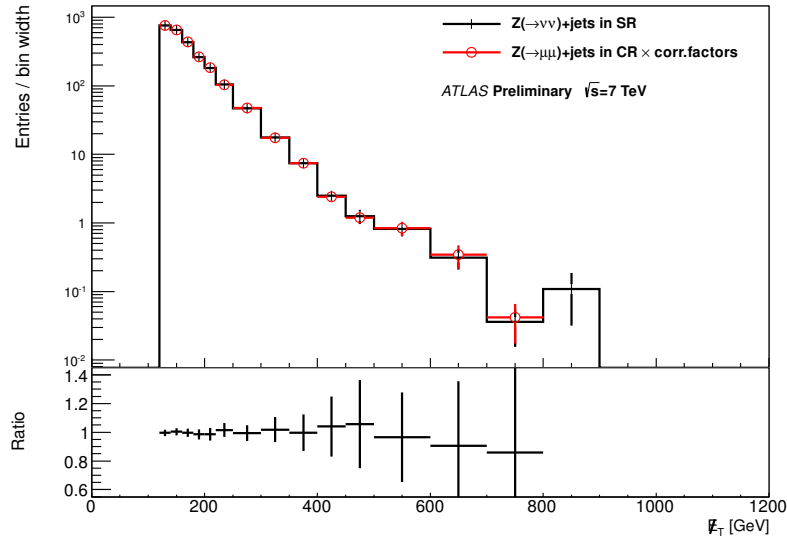
Figure 14: Closure test for $Z(\nu\nu)$+jets in signal region, obtained from the Z control region.

6.4 W($\mu\nu$) control region

Events that enter the W($\mu\nu$) control region are required to pass the following criteria:

- Exactly one good muon

- All the signal region cuts on the jets and E_T^{miss}, as well as the lepton veto (except the selected muon)

- A E_T^{miss} (corrected for the selected muon) larger than 25 GeV

- A transverse mass m_T above 40 GeV, with $m_T = \sqrt{2 \times p_T^\mu \times E_T^{miss} \times [1 - \cos \Delta\phi(\mu, E_T^{miss})]}$

The cuts on the transverse mass and on the E_T^{miss} (corrected for the selected muon) are applied in order to purify the W control region.

Referring to the equations of Section 5.2.1, the data-driven prediction of Z($\nu\nu$), W($\tau\nu$), and W($\mu\nu$) are:

$$N_{Z(\to\nu\nu)+jets}^{DD,SR} = \frac{N_{W(\to\mu\nu)+jets}^{Data}}{A_\mu \times \epsilon_\mu \times \epsilon_W} \times (1 - f_{EW}) \times \frac{N_{Z(\to\nu\nu)+jets}^{SR}}{N_{W(\to\mu\nu)+jets}} \tag{16}$$

$$N_{W(\to\tau\nu)+jets}^{DD,SR} = \frac{N_{W(\to\mu\nu)+jets}^{Data}}{A_\mu \times \epsilon_\mu \times \epsilon_W} \times (1 - f_{EW}) \times T(\not{t}) \tag{17}$$

$$N_{W(\to\mu\nu)+jets}^{DD,SR} = \frac{N_{W(\to\mu\nu)+jets}^{Data}}{A_\mu \times \epsilon_\mu \times \epsilon_W} \times (1 - f_{EW}) \times T(\not{\mu}) \tag{18}$$

where $N_{W(\to\mu\nu)+jets}$ is the total number of simulated events in the W control region with the full lepton phase space.

As in the case of the Z($\mu\mu$) control region, four W($\mu\nu$) exclusive control regions are defined according to the four mono-jet signal regions. A summary is available in Table 20.

Control regions	CR 1	CR 2	CR 3	CR 4
Common cuts	Preselection cuts + $\Delta\phi(E_T^{miss}, jet_2) > 0.5$ + $N_{jets} < 3$			
	+ exactly 1 good muon + lepton veto (except on the good muon) + $m_T > 40$ GeV			
Dedicated cuts	$p_T^{jet_1} > 120$ GeV $E_T^{miss} > 120$ GeV	$p_T^{jet_1} > 220$ GeV $E_T^{miss} > 220$ GeV	$p_T^{jet_1} > 350$ GeV $E_T^{miss} > 350$ GeV	$p_T^{jet_1} > 500$ GeV $E_T^{miss} > 500$ GeV

Table 20: Definition of the four W($\mu\nu$) exclusive control regions (CR).

Backgrounds to this region consist of the electroweak and QCD multi-jet events. The electroweak background is estimated using simulation, and includes (in percentage of simulated W($\mu\nu$) events in CR1): W($\tau\nu$) (4.7%), $t\bar{t}$ + single top (3.2%), Z($\mu\mu$) (2.4%), di-bosons (1.0%), and Z($\tau\tau$) (0.2%) events.

The contribution of the QCD has been estimated with the matrix method following the study performed in the ATLAS Rjets analysis [7]. As its contamination is less than 0.2%, it is considered to be negligible.

In CR1, CR2, CR3 and CR4, a total of 40356, 3581, 363, and 49 W($\mu\nu$) candidate events are selected in Data, respectively. The background contamination is stable at nearly 10%.

614   In addition, comparisons between Data and simulation have been made for the essential kinematic
615 variables, as provided in Figure 15. As for the Z control region, these plots (in CR1) only show shape
616 comparisons, with W and Z simulated events scaled by 0.94. Good agreements between Data and simu-
617 lation are observed.

6.4.1   Correction factors to get the full lepton phase space

619   The same way as in the preceding section, the electroweak background to the control region is removed
620 by multiplying (bin by bin) $N^{Data}_{W(\to\mu\nu)+jets}$ by $(1 - f_{EW})$, where f_{EW} is defined as:

$$f_{EW} = \frac{N^{CR}(\text{All EW channels except W}(\mu\nu))}{N^{CR}(\text{Total EW})} \tag{19}$$

621   with N is the number of simulated events. contamination of the order of 10% is found. Table 21 lists
622 the values of $(1-f_{EW})$ in each W$(\mu\nu)$ control region.

Control regions	$(1-f_{EW})$ (%)
CR 1	89.7 ± 0.1
CR 2	91.0 ± 0.2
CR 3	90.6 ± 0.6
CR 4	91.6 ± 1.6

Table 21: $(1-f_{EW})$ in each W$(\mu\nu)$ control region, with f_{EW} calculated as ratio of integrals (uncertainties are statistical).

623   The correction factors required to recover the full lepton phase space are the muon acceptance (in p_T
624 and η), the muon reconstruction efficiency, and the transverse mass and E_T^{miss} cut efficiency.
625   The acceptance of the muon is defined in each bin of E_T^{miss} by the fration of W$(\mu\nu)$ events that in-
626 cludes one reconstructed muon within p_T and η acceptance. The m_T and E_T^{miss} cuts efficiency (ϵ_W in
627 Equations 16, 18, and 17) is defined by the ratio of simulated events passing the m_T and E_T^{miss} (corrected
628 for the selected muon) cuts given the event has a good muon. Figures 16 and 17 show the muon accep-
629 tance and ϵ_W in the first control region, respectively. Tables 22 and 23 list the average acceptances and
630 ϵ_W efficiencies in each of the W control regions.

631

Control regions	Acceptance (%)
CR 1	78.31 ± 0.10
CR 2	86.51 ± 0.23
CR 3	91.57 ± 0.55
CR 4	94.69 ± 1.22

Table 22: Average values of the muon acceptance corrections in each W$(\mu\nu)$ control region (uncertainties are statistical).

Control regions	ϵ_W (%)
CR 1	63.89 ± 0.12
CR 2	64.36 ± 0.33
CR 3	66.90 ± 0.94
CR 4	73.21 ± 2.37

Table 23: Average values of ϵ_W in each of the W$(\mu\nu)$ control regions (uncertainties are statistical). ϵ_W is the efficiency of the control region cut on m_T and E_T^{miss} (corrected for the selected muon).
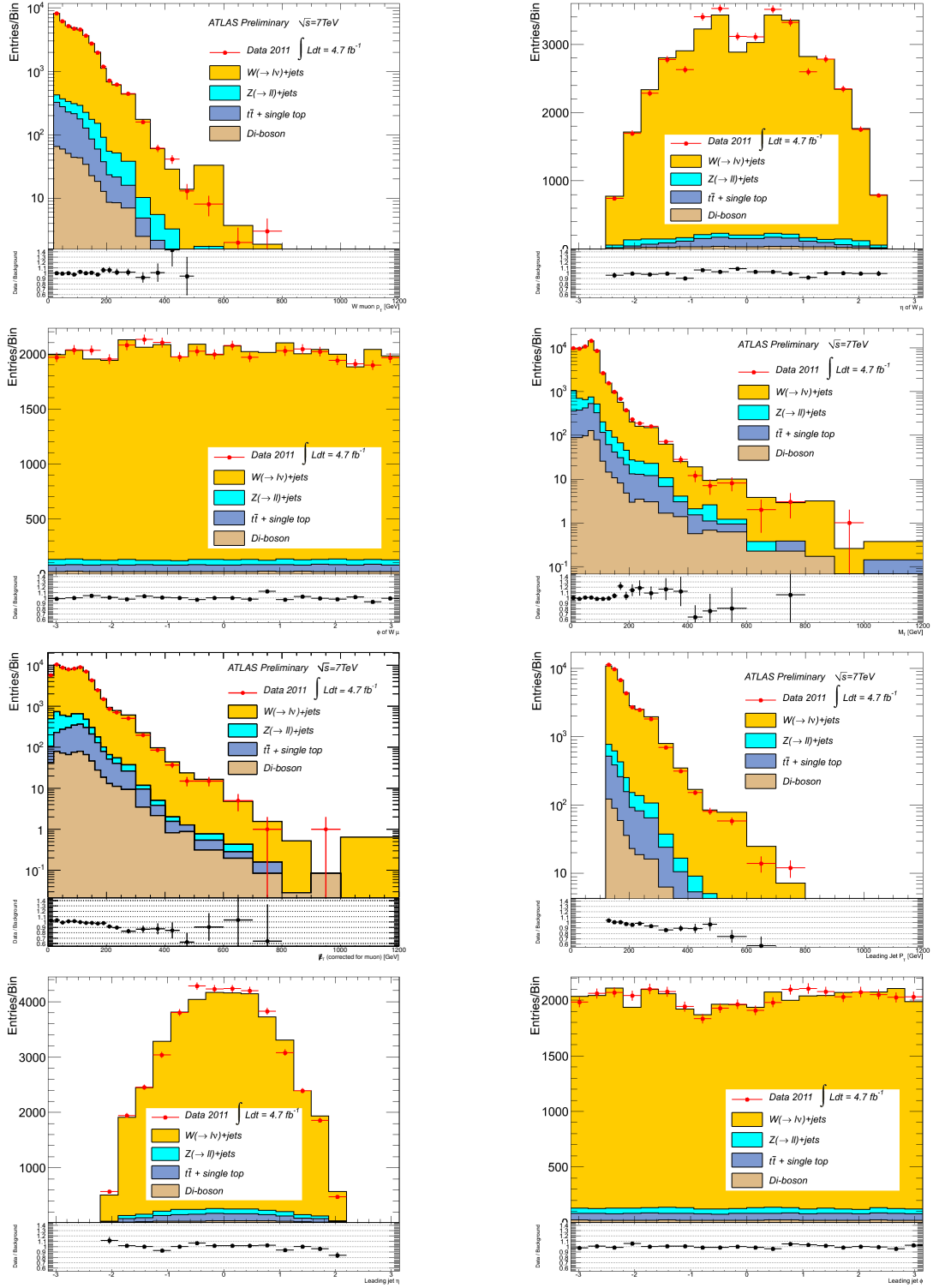
Figure 15: (top left to bottom right) leading muon p_{T}, η, and ϕ, m_T, $E_{\mathrm{T}}^{\mathrm{miss}}$ corrected for the selected muon, leading jet p_{T}, η, and ϕ.
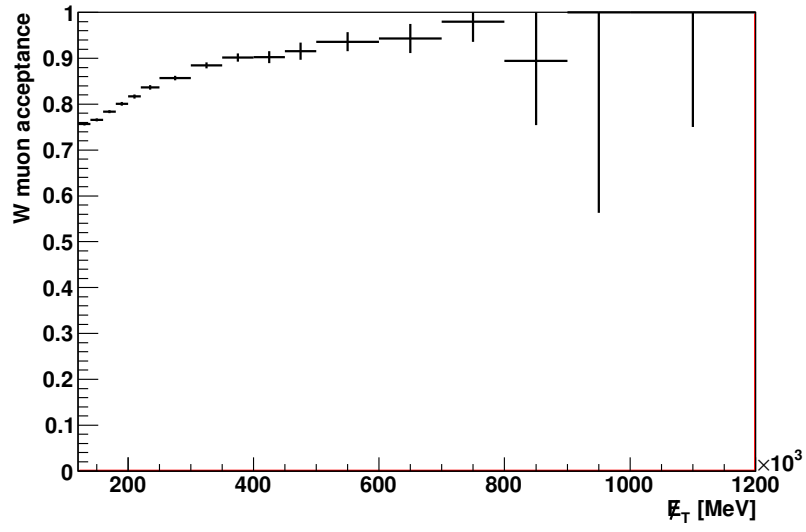
Figure 16: Muon acceptance in W($\mu\nu$) events as function of E_T^{miss}, in W($\mu\nu$) CR1.
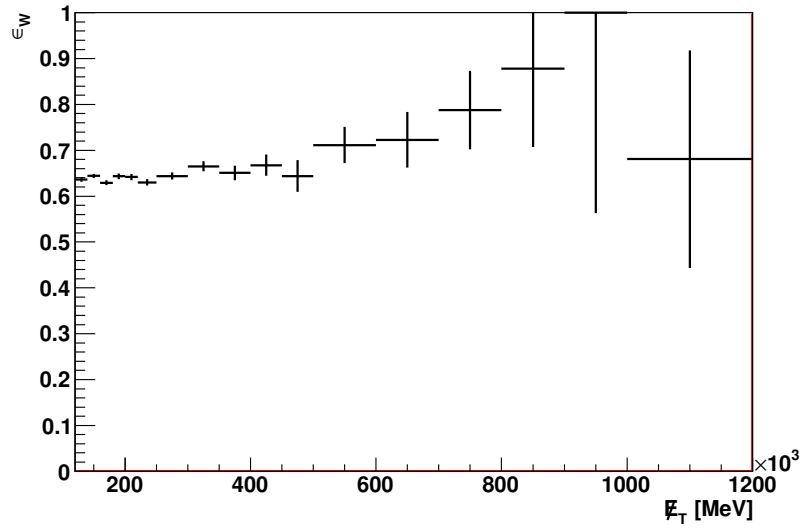
Figure 17: ϵ_W in W($\mu\nu$) CR1 (uncertainties are statistical). ϵ_W is the efficiency of the control region cut on m_T and E_T^{miss} (corrected for the selected muon).

6.4.2 Z($\nu\nu$) correction factors

The contribution of Z($\nu\nu$) events to the mono-jet signal region is determined by applying the following factor to the full lepton phase space of W($\mu\nu$):

$$\frac{N_{Z(\rightarrow\nu\nu)+jets}^{SR}}{N_{W(\rightarrow\mu\nu)+jets}} \tag{20}$$

635   This factor is represented in Figure 18 for the first W($\mu\nu$) control region, and Table 24 details its
636 values as ratios of integrals for all the control regions.
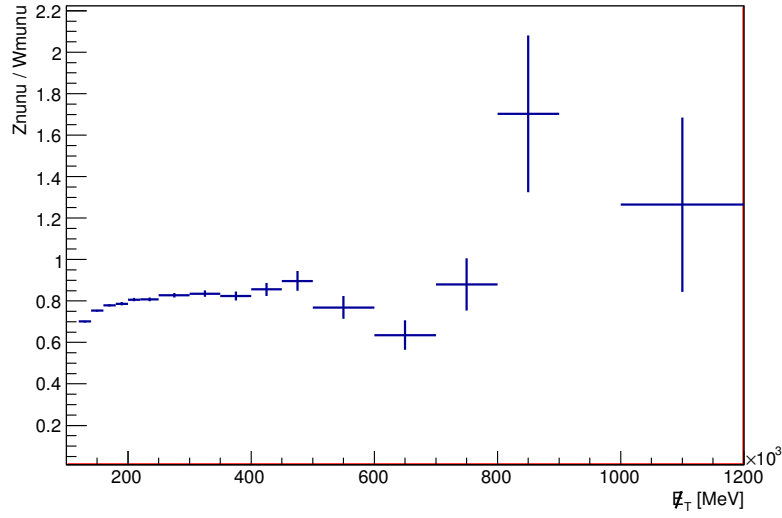
Figure 18: Ratio of Z($\nu\nu$) over W($\mu\nu$) events from simulated event in the first W($\mu\nu$) control region.

Control regions	$\frac{N^{SR}_{Z(\rightarrow\nu\nu)+jets}}{N_{W(\rightarrow\mu\nu)+jets}}$
CR 1	0.795 ± 0.002
CR 2	0.839 ± 0.007
CR 3	0.842 ± 0.018
CR 4	0.795 ± 0.054

Table 24: $\frac{N^{SR}_{Z(\rightarrow\nu\nu)+jets}}{N_{W(\rightarrow\mu\nu)+jets}}$ (ratio of integrals) in each W($\mu\nu$) control region (uncertainties are statistical).

637   This additional factor includes the branching ratio of Z($\nu\nu$) to Z($\mu\mu$), the ratio of the cross-sections
638 of Z($\mu\mu$) to W($\mu\nu$) after mono-jet cuts, and a factor to correct for the differences in the event topologies.

6.4.3   W($\tau\nu$) correction factors

640 The contribution of W($\tau\nu$) events to the mono-jet signal region is determined by applying bin-by-bin the
641 following factor to the full lepton phase space of W($\mu\nu$):

$$T(\not{E}) = \frac{N^{SR}_{W(\rightarrow\tau\nu)+jets}}{N_{W(\rightarrow\mu\nu)+jets}} \qquad (21)$$

642     $T(\not{E})$ is binned as function of E^{miss}_{T}. It corrects for the differences in both the rate and the event
643 topology between W($\mu\nu$) and W($\tau\nu$) events, and is shown in Figure 19 for the low energy W($\mu\nu$) control
644 region. For a given SR, it is the ratio of W($\tau\nu$) events that survive all the SR cuts over the number of
645 W($\mu\nu$) events in the corresponding CR corrected to the full lepton phase space. Table 25 provides the
646 values of $T(\not{E})$ as a ratio of integrals, for each control region.
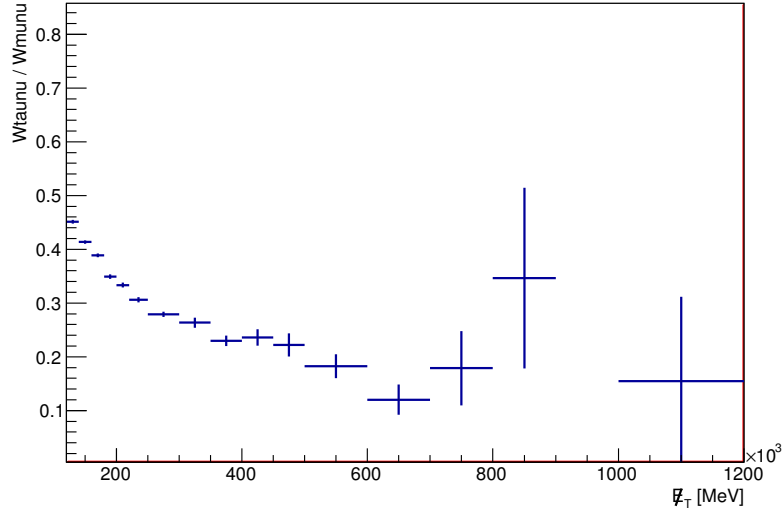
Figure 19: Ratio of W($\tau\nu$) over W($\mu\nu$) events from simulated event in the first W($\mu\nu$) control region.

Control regions	$\dfrac{N^{SR}_{W(\to\tau\nu)+jets}}{N_{W(\to\mu\nu)+jets}}$
CR 1	0.394 ± 0.002
CR 2	0.287 ± 0.004
CR 3	0.222 ± 0.008
CR 4	0.177 ± 0.021

Table 25: $\dfrac{N^{SR}_{W(\to\tau\nu)+jets}}{N_{W(\to\mu\nu)+jets}}$ (ratio of integrals) in each W($\mu\nu$) control region (uncertainties are statistical).

6.4.4 W($\mu\nu$) correction factors

The W($\mu\nu$) background in the signal region is determined from the full lepton phase space of W($\mu\nu$) after applying the correction factor $T(\mu)$ which is the ratio of W($\mu\nu$) events with a muon surviving the muon veto over W($\mu\nu$) events with the full muon phase space:

$$T(\mu) = \frac{N^{SR}_{W(\to\mu\nu)+jets}}{N_{W(\to\mu\nu)+jets}} \tag{22}$$

Since the E_T^{miss} is not exactly the same in events with forward muons compared to those with no requirement on the muon's rapidity, the E_T^{miss} selection can also vary between the numerator and denominator of $T(\mu)$. Most of the contribution comes from out-of-acceptance muons and is due to soft muons. $T(\mu)$ is calculated in bins of E_T^{miss} and can be decomposed as follows:

$$T(\mu) = T(1 - A^{veto}) + T(A^{veto} \times (1 - \epsilon^{veto}_{reco})) \tag{23}$$

where $T(1 - A^{veto})$ is the ratio of W($\mu\nu$) events with a muon out of the veto acceptance, while $T(A^{veto} \times (1 - \epsilon^{veto}_{Reco}))$ is the ratio of W($\mu\nu$) events with a muon within the veto acceptance but not reconstructed (according to the loose muon quality in the lepton veto definition).

A^{veto} is obtained from simulation in bins of E_T^{miss}, and ϵ^{veto}_{reco} is known in Data as function of the muon η, ϕ and p_T, as shown in Section 6.2. To derive $T(1 - A^{veto})$ and $T(A^{veto} \times (1 - \epsilon^{veto}_{reco}))$, W($\mu\nu$) simulated

660 events are first mapped to $1 - A^{veto}$ and $A^{veto} \times (1 - \epsilon_{reco}^{veto})$, respectively. Both factors are then divided
661 by simulated $W(\mu\nu)$ events with the full muon phase space. As described in Section 3, muons with a
662 p_T from as low as 7 GeV are considered for the lepton veto. The η distribution of low-p_T muons is not
663 necessarily the same as that of muons with a p_T above 20 GeV, which affects the E_T^{miss}. Hence $T(1 - A^{veto})$
664 and $T(A^{veto} \times (1 - \epsilon_{reco}^{veto}))$ are scaled to $W(\mu\nu)$ events with the full muon phase space, and not directly to
665 the Data events in CR, since the latter only include good muons with a p_T exceeding 20 GeV.

666   Figure 20 provides the muon acceptance in $W(\mu\nu)$ events for muons fulfilling the quality required for
667 the muon veto. Figure 21 shows $T(\mu)$ in bins of E_T^{miss} in CR1, while Table 26 lists its values as ratios of
668 integrals in the different $W(\mu\nu)$ control regions.
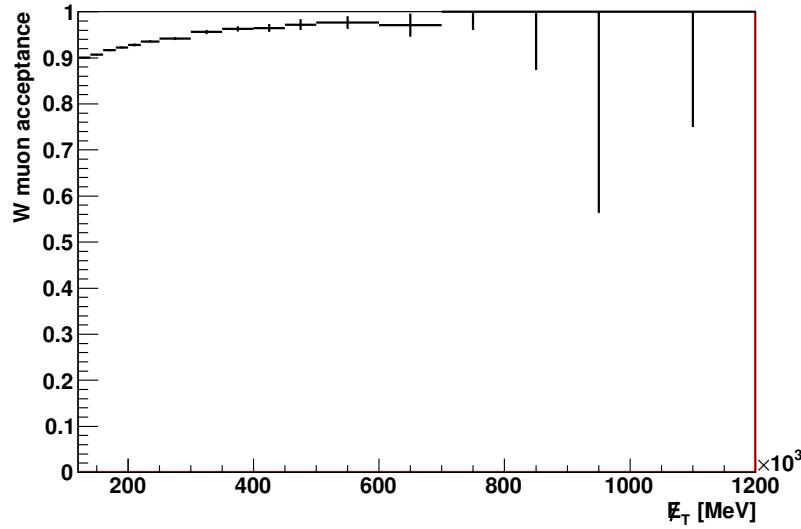
Figure 20: Muon acceptance in $W(\mu\nu)$ events as function of E_T^{miss}, in $W(\mu\nu)$ CR1, and for muons fulfilling the quality required for the muon veto.
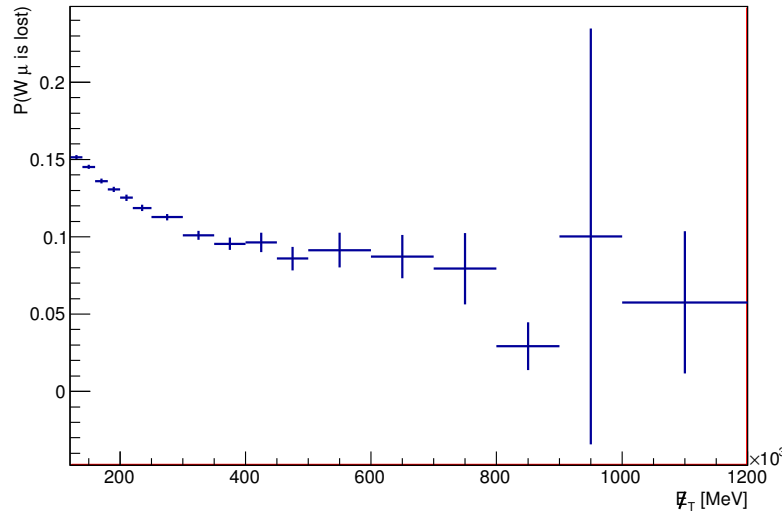
Figure 21: $T(\mu)$ in bins of E_T^{miss}, using $W(\mu\nu)$ events in the full muon phase space.

Control regions	$T(\mu)$
CR 1	0.139 ± 0.001
CR 2	0.109 ± 0.001
CR 3	0.092 ± 0.003
CR 4	0.089 ± 0.011

Table 26: $T(\mu)$ (ratio of integrals) in each W($\mu\nu$) control region (uncertainties are statistical).

6.4.5 Closure Tests

To validate the performance of each of the factors explained in the previous sections, a set of closure tests are performed on simulated samples. In the following only the first signal and control regions are considered.

For the acceptance and efficiency factors, the W($\mu\nu$) MC in the control region after being corrected to the full lepton phase space is compared to W($\mu\nu$) in the full lepton phase space (Fig 22). The Z($\nu\nu$) closure test compares the Z($\nu\nu$) distribution in the signal region (obtained from Z($\nu\nu$) MC samples) to the one obtained from Equation 16 (Fig 23). The closure test for W($\mu\nu$) background compares the W($\mu\nu$) distribution in the signal region to the one obtained from Equation 18 (Fig 24). In Figure 25, W($\tau\nu$) events in the signal region are compared to W($\mu\nu$) events in the full lepton phase space after correcting them using Equation 21.
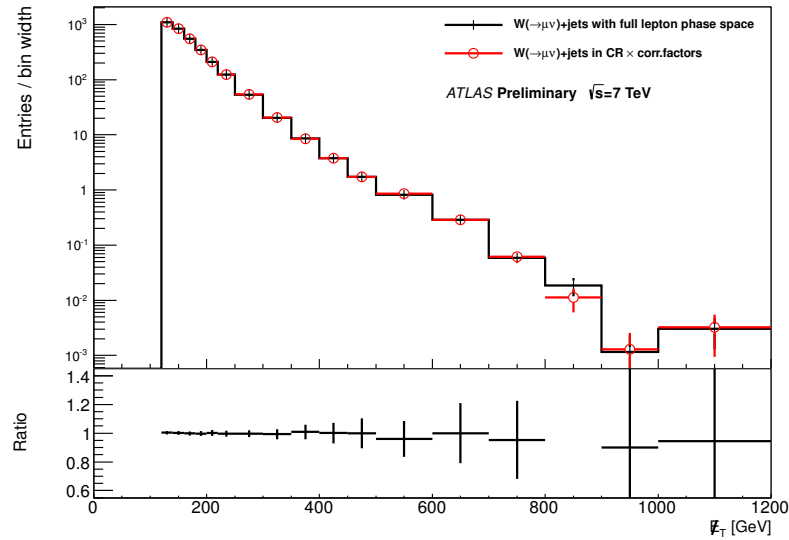
Figure 22: Closure test for W($\mu\nu$)+jets full phase space correction factors.
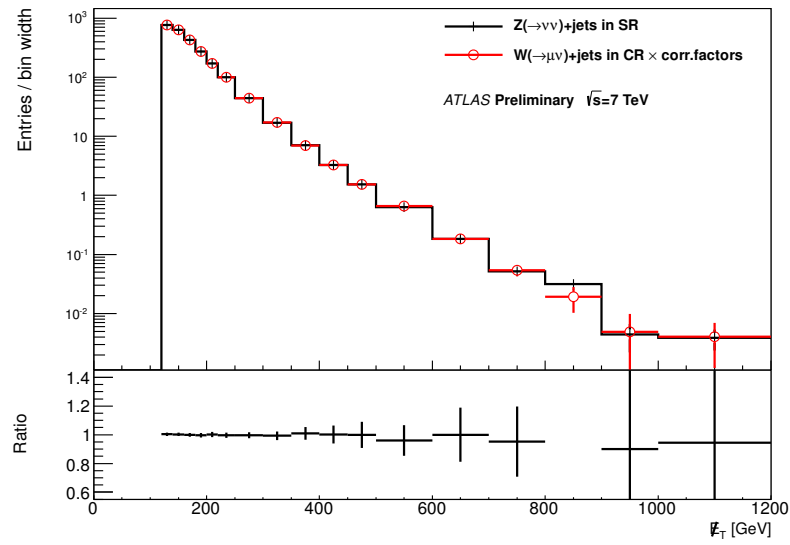
Figure 23: Closure test for Z(νν)+jets determination in the signal region from W(μν) control region.

Figure 24: Closure test for W(μν)+jets determination in the signal region from W(μν) control region.

Figure 25: Closure test for W($\tau\nu$)+jets determination in the signal region from W($\mu\nu$) control region.

6.5 Systematic uncertainties

Various sources of systematic uncertainties include the uncertainties on the jet energy scale and resolution (JES/JER), $E_\mathrm{T}^\mathrm{miss}$ (due to the topo-cluster energy uncertainty), muon energy scale and resolution, data-driven efficiency scale factors, and different parton showering and underlying event modelings in simulated samples used to derive some of the correction factors.

JES, JER, and $E_\mathrm{T}^\mathrm{miss}$ uncertainties   This uncertainty is calculated by varying the p_T of *all* the jets above 20 GeV in the event up/down, and propagating the vector sum of this change[6] to $E_\mathrm{T}^\mathrm{miss}$. This will change both the value and direction of $E_\mathrm{T}^\mathrm{miss}$. The mono-jet kinematic cuts (and the transverse mass cut in case of the W control region) are applied to the new jets and $E_\mathrm{T}^\mathrm{miss}$. In the case of asymmetric errors, the maximum deviation is considered.

Lepton energy scale and resolution uncertainties   The uncertainty on the muon p_T resolution is estimated using the official muon smearing class, while the uncertainty on the muon energy scale is calculated by turning on/off the re-scaling of the muon 4-momentum, as recommended by the MCP group.

No uncertainty due to muon energy scale and resolution is assumed for ϵ_μ derived from simulated samples, as the data-driven SFs are applied to this map.

Uncertainty on the data-driven SFs   The total uncertainty on the data-driven muon reconstructon efficiency scale factors includes both the statistical and the systematic uncertainties on the factors, provided by the MCP group. This uncertainty affects the muon reconstruction efficiency map.

Various MC models   The uncertainty due to various parton showering models (represented by "MC modeling" in the tables below) should in principle be estimated by applying the SHERPA-based correction factors to the W or Z data control regions, and comparing the predictions for each background channel to those predicted by applying ALPGEN-based correction factors to the same data control regions. In order to investigate the significance of such comparisons, the Monte Carlo statistical fluctuations on the difference between the two predictions are estimated; in some regions these statistical fluctuations are large compared to the central value of the difference, showing that this difference is not a good representative of such uncertainty in these kinematic regions (these large statistical fluctuations are mainly due to limited statistics in the SHERPA simulated samples). In general, the actual systematic uncertainty might depend on the kinematic region, and one cannot assign the uncertainy from a lower kinematic region to the higher kinematic regions.

To avoid having such large fluctuations due to the limited statistics in the SHERPA samples, ALPGEN samples are re-weighted with event weights based on the difference in the W p_T distributions between SHERPA and ALPGEN [8]. These weights are then applied to all the correction factors by which the data in the control region is corrected to obtain predictions in different background channels. A conservative uncertainty of 3% is assigend to the prediction of each background channel due to this source of uncertainty.

MC statistical uncertainty   The statistical uncertainty due to the limited statistics of various MC-based correction factors is taken from ALPGEN simulated samples. To get the statistical uncertainty of the correction factors on the prediction of each background channel, the overal statistical fluctuation

---

[6]The effect of estimating the uncertainty on the jets and $E_\mathrm{T}^\mathrm{miss}$ *separately*, due to their different calibrations, has been studied and found to result in larger uncertainty compared to the method explained here. However, for the sake of comparison with the alternative method of background estimation, the method explained in the text has been used for the final results.

718 is considered. As an example, the statistical error of the factor $\frac{N^{SR}_{Z(\to \nu\nu)+jets}}{N^{CR}_{Z(\to \mu\mu)+jets}}$ is taken as the MC statistical
719 uncertainty on the Z($\to \nu\nu$) + *jets* prediction from the Z($\to \mu\mu$) + *jets* control region.

Trigger efficiency 720 No systematic uncertainty is assumed for the trigger efficiency on the background
721 predictions that are based on the muon control region, as the same trigger is used for selecting events in
722 both signal and muon control regions (this will not be the case for the electron control regions).

Uncertainty on f_{EW} 723 Based on the studies done in the RJet analysis [7], a maximum of 1% total uncer-
724 tainty is considered on (1-f_{EW}) in the muon channel.
725

726 Table 27 summarises the systematic uncertainties in the first signal region on each of the correction
727 factors explained in the previous sections. These uncertainties are quoted on correction factors calculated
728 as ratio of integrals, and are not used to get the final uncertainties, except for signal region 4, where there
729 is not enough statistics to apply the bin-by-bin correction factors.
730 To get the total uncertainty on the final background predictions due to a source, all the correction
731 factors affected by that source of uncertainty are varied, and then applied simultaneously to the data
732 control region to study the affect on the final number of predicted events in each background channel.
733 In other words, the contribution of each background channel is re-determined by applying all the *var-
734 ied* correction factors to the data control regions. In the case of the JES-$E_{\mathrm{T}}^{\mathrm{miss}}$ uncertainty, the overal
735 correction factor [7] is varied and applied to the data control regions. Tables 28, 29, 30, 31, 33, and 32
736 summarise the total relative uncertainty from each source for different background channels in each of
737 the 4 signal regions. In case of asymmetric errors, the largest error is considered. The total uncertainty in
738 each background channel is the quadrature some of all the different uncertainties, including the 1% total
739 uncertainty on f_{EW}.
740 To get the total systematic uncertainty on the total number of events in each signal region, correlations
741 between different background channels have been taken into account. Tables 34 and 35 summarise the
742 systematic uncertainties on the total number of events for each signal region due to each source of sys-
743 tematic uncertainty (the two tables correspond to when W or the Z control regions are used respectively,
744 to determine the Z($\nu\nu$) contribution in the signal regions).

---

[7]The overal correction factor is based on the full lepton phase space of the control regions.

factor	JES-$E_{\mathrm{T}}^{\mathrm{miss}}$	MC stat uncertainty (from ALPGEN)	SF	lepton energy scale and resolution
$A_\mu(W)$	0.55	0.23	-	-
ϵ_W	0.67	0.39	-	0.12
$A_\mu(Z)$	1.25	0.57	-	-
ϵ_μ	-	0.01	0.25	-
ϵ_μ^{Veto}	-	0.11	0.29	-
$\dfrac{N^{SR}_{Z(\to \nu\nu)+jets}}{N_{Z(\to \mu\mu)+jets}}$	1.03	1.10	-	-
$\dfrac{N^{SR}_{Z(\to \mu\mu)+jets}}{N_{Z(\to \mu\mu)+jets}}$	0.66	0.32	-	-
f_{EW}	0.89	0.12	-	0.22

Table 27: Relative systematic uncertainties on different correction factors (in %) due to various sources of uncertainty, in the first signal region.

source of systematic	Region1	Region2	Region3	Region4
JES-$E_{\mathrm{T}}^{\mathrm{miss}}$	0.73	2.68	5.58	7.28
lepton energy scale and resolution	0.04	0.02	0.13	0.84
SF	0.31	0.33	0.36	0.37
MC modeling	3	3	3	3
MC stat uncertainty (from ALPGEN)	0.55	1.36	3.77	10.93
Total	3.31	4.38	7.45	13.54

Table 28: Relative systematic uncertainty (in %) on the Z($\nu\nu$) estimation derived from the W control region, in the 4 signal regions.

source of systematic	Region1	Region2	Region3	Region4
JES-$E_{\mathrm{T}}^{\mathrm{miss}}$	0.98	4.28	8.51	6.58
SF	0.80	2.97	0.36	0.75
MC modeling	3	3	3	3
MC stat uncertainty (from ALPGEN)	0.86	2.48	7.12	21.62
Total	3.51	6.58	11.54	22.83

Table 29: Relative systematic uncertainty (in %) on the Z($\nu\nu$) estimation derived from the Z control region, in the 4 signal regions.

source of systematic	Region1	Region2	Region3	Region4
JES-$E_{\mathrm{T}}^{\mathrm{miss}}$	1.08	1.82	3.97	8.40
lepton energy scale and resolution	0.04	0.002	0.12	-
SF	0.30	0.33	0.35	0.35
MC modeling	3	3	3	3
MC stat uncertainty (from ALPGEN)	0.62	1.81	5.06	15.11
Total	3.41	4.09	7.18	17.58

Table 30: Relative systematic uncertainty (in %) on the W($\tau\nu$) estimation in the 4 signal regions.

source of systematic	Region1	Region2	Region3	Region4
JES-$E_{\mathrm{T}}^{\mathrm{miss}}$	3.53	6.78	6.29	11.76
lepton energy scale and resolution	0.04	0.04	0.08	4.14
SF	2.10	3.08	3.37	3.79
MC modeling	3	3	3	3
MC stat uncertainty (from ALPGEN)	0.73	2.17	6.31	19.17
Total	5.24	8.38	10.04	23.39

Table 31: Relative systematic uncertainty (in %) on the W($\mu\nu$) estimation in the 4 signal regions.

source of systematic	Region1	Region2	Region3	Region4
JES-$E_{\mathrm{T}}^{\mathrm{miss}}$	4.37	6.19	46.52	-
SF	0.59	3.19	42.75	0.74
MC modeling	3	3	3	3
MC stat uncertainty (from ALPGEN)	2.25	10.80	37.76	-
Total	5.87	13.23	73.67	-

Table 32: Relative systematic uncertainty (in %) on the Z($\tau\tau$) estimation in the 4 signal regions.

source of systematic	Region1	Region2	Region3	Region4
JES-$E_{\mathrm{T}}^{\mathrm{miss}}$	5.18	16.17	-	-
SF	0.60	0.65	-	-
MC modeling	3	3	3	3
MC stat uncertainty (from ALPGEN)	5.09	24.40	-	-
Total	7.94	29.45	-	-

Table 33: Relative systematic uncertainty (in %) on the Z($\mu\mu$) estimation in the 4 signal regions.

source of systematic	Region1	Region2	Region3	Region4
JES-E_T^{miss}	1.10	2.83	5.05	6.22
lepton energy scale and resolution	0.15	0.02	0.12	0.96
SF	0.45	0.53	0.57	0.61
MC modeling	3	3	3	3
Total	3.38	4.28	5.99	7.07

Table 34: Relative systematic uncertainty (in %) on the total estimation of the electroweak backgrounds (except Wev) in the 4 signal regions, with Z($\nu\nu$) determination from the W control region.

source of systematic	Region1	Region2	Region3	Region4
JES-E_T^{miss}	0.89	3.01	6.38	5.26
lepton energy scale and resolution	0.15	0.02	0.12	0.96
SF	0.53	2.01	0.44	0.65
MC modeling	3	3	3	3
Total	3.33	4.81	7.14	6.25

Table 35: Relative systematic uncertainty (in %) on the total estimation of the electroweak backgrounds (except Wev) in the 4 signal regions, with Z($\nu\nu$) determination from the Z control region.

7 Data-driven electroweak background determination from an electron control region

7.1 Introduction

The Z invisible background contribution can be estimated from the decay of a W/Z boson to leptons by replacing electrons with neutrinos and applying some correction factors such as efficiency of electrons, acceptance of electrons as shown in the following equations:

$$N_{Z\to\nu\nu}^{DD,SR} = \frac{N_{Zee}^{CR} - N_{QCD}^{CR}}{A_e \times \epsilon_e \times L_e} \cdot (1 - f_{EW}) \cdot \epsilon_{E_T^{miss}}^{trig} \cdot L_{E_T^{miss}} \cdot \frac{N_{Z\to\nu\nu}^{SR}}{N_{Z\to ee}} \tag{24}$$

$$N_{Z\to\nu\nu}^{DD,SR} = \frac{N_{We\nu}^{CR} - N_{QCD}^{CR}}{A_e \times \epsilon_e \times \epsilon_W \times L_e} \cdot (1 - f_{EW}) \cdot \epsilon_{E_T^{miss}}^{trig} \cdot L_{E_T^{miss}} \cdot \frac{N_{Z\to\nu\nu}^{SR}}{N_{W\to e\nu}} \tag{25}$$

where $N_{Z\to\nu\nu}^{DD,SR}$ is the data-driven number of events of Z invisible background in SR, N_{Zee}^{CR} is the number of data candidates of Z boson to electrons in CR, $N_{We\nu}^{CR}$ is the number of data candidates of W boson to a electron and a neutrino in CR, N_{QCD}^{CR} is the number of QCD events in CR, A_e is the acceptance of electrons, f_{EW} is the fraction of electroweak background to the CR, ϵ_e is the identification efficiency of electrons, ϵ_W is the simulated efficiency for the W boson specific selection cuts, L_e is the luminosity in the CR, $\epsilon_{E_T^{miss}}^{trig}$ is the efficiency of E_T^{miss} trigger, $L_{E_T^{miss}}$ is the luminosity in SR. $\frac{N_{Z\to\nu\nu}^{SR}}{N_{Z\to ee}}$ is the ratio of simulated $Z \to \nu\nu$ events in SR over simulated $Z \to ee$ events with the full electron phase space. It includes the ratio of branching fraction $\frac{Br(Z\to\nu\nu)}{Br(Z\to ee)}$ and the difference of phase space between $Z \to \nu\nu$ and $Z \to ee$ events. $\frac{N_{Z\to\nu\nu}^{SR}}{N_{W\to e\nu}}$ is the ratio of simulated $Z \to \nu\nu$ events in SR over simulated $W \to e\nu$ events with the full electron phase space. It includes $R_{jets}^{-1} = \frac{\sigma(Z\to\nu\nu)}{\sigma(W\to e\nu)}$ and the difference of phase space between $Z \to \nu\nu$ and $W \to e\nu$ events.

In the following sections, we will first describe how to estimate these correction factors and then we will show results of closure test and the results of the estimation.

7.2 Object definition and pre-selection in CR

Object definition in CR is defined by as follows. The main differences from definitions in SR are that overlap removal between jets and electrons are applied in CR.

- Object definition of an electron in CR:

    - el_mediumPP == true
    - Author = 1 or 3
    - el_OQ & egammaPID::BADCLUSELECTRON = 0
    - p_T >20GeV, $|\eta_{cluster}| < 2.47$
    - dR(e,jet)>0.4

Following is the definition of pre-selection in CR. Almost same definitions as in Standard Model W/Z group are used. But same cleaning as in SR is applied because of the consistency between CR and SR.

- Pre-selections in Zee CR:

778   – Trigger: EF_e20_medium, EF_e22_medium, (EF_e22vh_medium1||EF_e45_medium1)

779   – Cleaning: same cleaning as in SR is applied after overlap removal

780   – Exact 2 mediumPP electrons

781   – leading electron p_T >25GeV

782   – 66GeV<M_{ll} <116GeV

783   • Pre-selections in Weν CR:

784   – Trigger: EF_e20_medium, EF_e22_medium, (EF_e22vh_medium1||EF_e45_medium1)

785   – Cleaning: same cleaning as in SR is applied after overlap removal

786   – 1 tightPP electrons and no other mediumPP electrons

787   – leading electron p_T >25GeV

788   – $p_T$cone20/p_T <0.1

789   – 40GeV< M_T <100GeV

790   – E_T^{miss} >25GeV

791   After these pre-selections, we require same kinematic conditions as in the SR. But in the calculation
792   of E_T^{miss} , electrons are treated as neutrinos.

7.3   The efficiency of an electron

794   The efficiency of an electron in data is obtained by multiplying the efficiency of an electron in monte
795   carlo by scale factors provided by egamma group. In this analysis, alpgen Weν samples are used to
796   estimate the efficiency of an electron in monte carlo. And the efficiency of mc is calculated by matching
797   true electrons with reconstructed electrons. In short, the efficiency of an electron is defined by

$$\epsilon(DATA) = \frac{N_{Rec}^{MC}}{N_{Truth}^{MC}} \cdot \frac{N_{Id}^{MC}}{N_{Rec}^{MC}} \cdot SF \tag{26}$$

798   where $\epsilon(DATA)$ is the efficiency of an electron in data, N_{Rec}^{MC} is the number of reconstructed electrons,
799   N_{Truth}^{MC} is the number of true electrons, N_{Id}^{MC} is the number of identified electrons, SF is the scale factor
800   of an efficiency provided by egamma group.
801   And the definition of true electrons, reconstructed electrons and identified electrons are as follows.

802   • True electrons

803   – PdgId of mother particle = 24

804   – Status of mother particle = 155

805   – |mc_eta| < 2.47

806   • Reconstructed electrons

807   – Author = 1 or 3

808   – el_OQ & egammaPID::BADCLUSELECTRON = 0

809   – |el_cl_eta| < 2.47

810   • Identified electrons
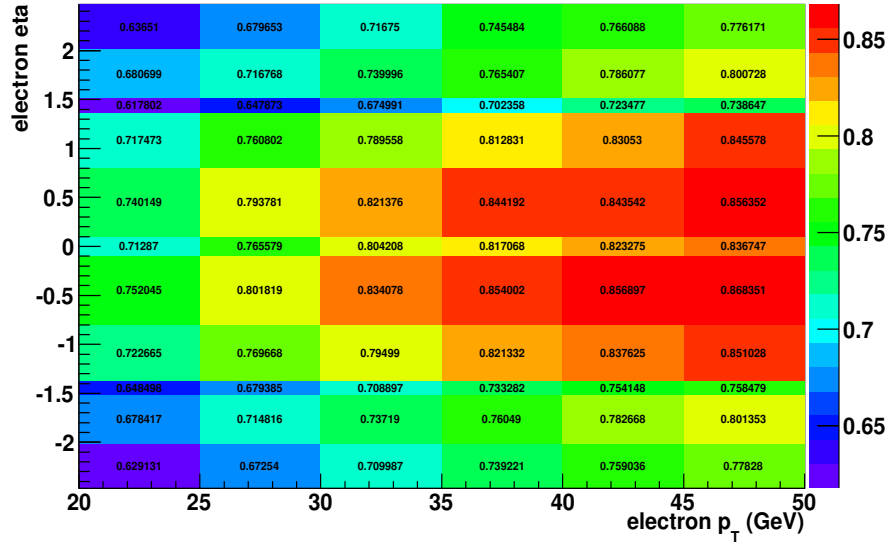
Figure 26: The efficiency of mediumPP estimated by Alpgen Weν sample. This efficiency include the matching efficiency between true electrons and reconstructed electrons.

- Reconstructed electrons

- el_mediumPP == true (Zee control region)

- el_TightPP == true & $p_T cone20/p_T < 0.1$ (Weν control region)

If the dR between true electrons and reconstructed electrons is smaller than 0.2, they are regarded as matched.

Figure 26 and Figure 27 show the result of this estimation. The average efficiency of mediumPP is estimated to be about 0.8 and the average efficiency of tightPP is estimated to be about 0.7.

7.4 Acceptance of electrons

In this analysis, the kinematic acceptance (in p_T amd η) of an electron is calculated as a function of the leading jet p_T. The higher the leading jet p_T is, the more electrons satisfy the acceptance cut criteria, as shown in Figure 28 and 29. The blue line shows the leading jet p_T distribution in each control region after all kinematic selections except the requirement of the identifed elecrons. The red line shows the leading jet p_T distribution after additionally requiring that truth electrons to be inside the electron acceptance.

7.5 The efficiency of transverse mass cut and E_T^{miss} cuts in the Weν control region

In the Weν control region, we require 40GeV$< M_T <$100GeV and $E_T^{miss} >$25GeV in order to enhance the Weν events. This efficiency is referred to as ϵ_W in Equation 25, and is calculated as a function of leading jet p_T. As shown in Figure 30, the efficiency has no dependence on the leading jet p$_T$, and is estimated to be 0.518 ± 0.003 (stat.)
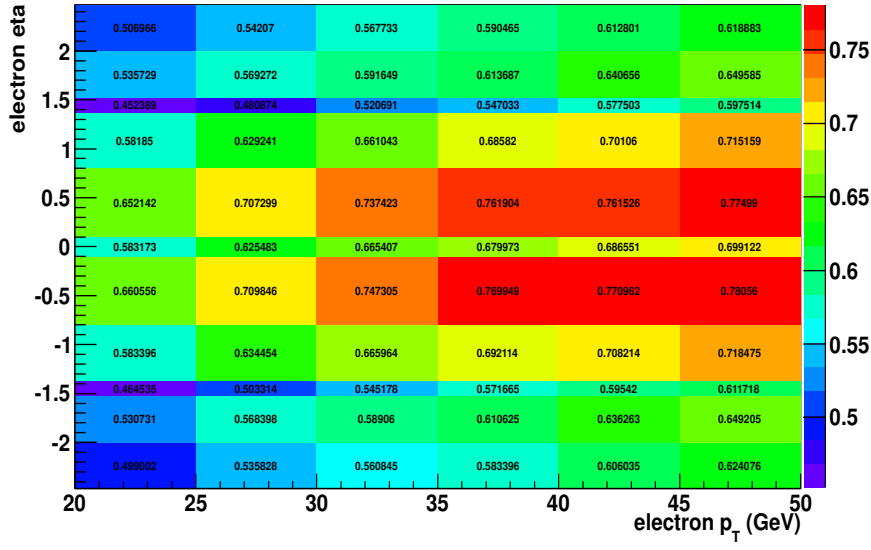
Figure 27: The efficiency of tightPP and $p_T$cone20/p_T <0.1 estimated by Alpgen Weν sample.This efficiency include the matching efficiency between true electrons and reconstructed electrons.
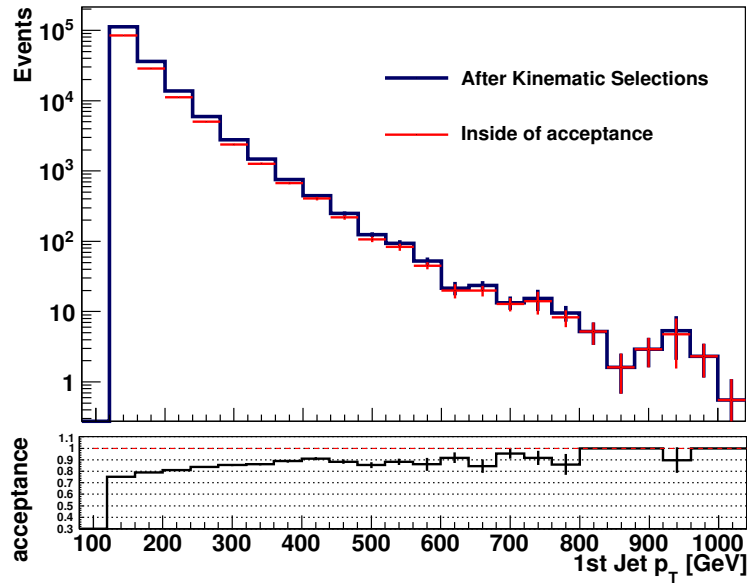
Figure 28: Acceptance of an electron in Weν CR.Top graph shows the 1st jet p_T. The blue line shows the one after Weν control region selections except for the requirement of an electron. The red line shows the one after the requirement of a true electron in addition to the control region selections. The bottom graph shows the acceptance of an electron. This is calculated by dividing the red line by the blue line in the top graph.
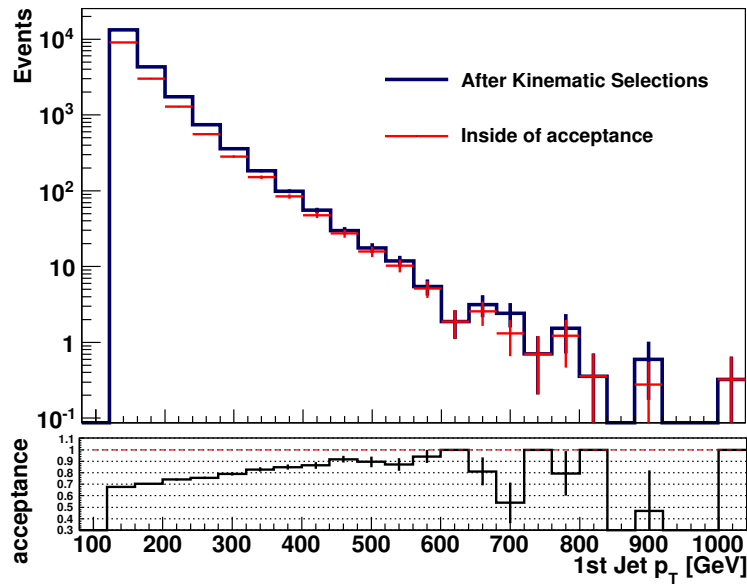
Figure 29: Acceptance of an electron in Zee CR. The top graph shows the 1st jet p_T. Blue line shows the one after Zee control region selections except for the requirement of electrons. The red line shows the one after the requirement of true electrons in addition to the control region selections. The bottom graph shows the acceptance of 2 electrons. This is calculated by dividing the red line by the blue line in the top graph.
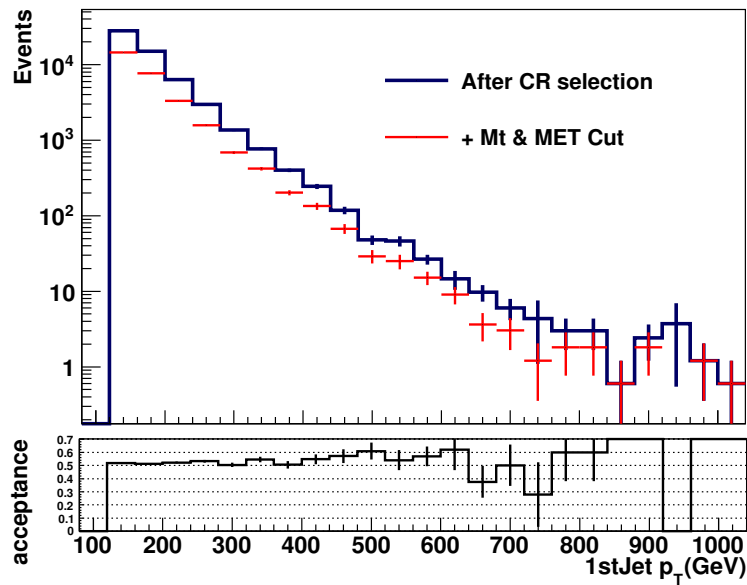
Figure 30: The efficiency of transverse mass cut and E_T^{miss} cut as a function of leading jet p_T. This figure shows that these cuts have no dependence on the leading jet p_T.

7.6 QCD background estimation in the Weν control region

QCD background in the *Weν* control region is estimated in a data-driven way using matrix method. Details are shown in 7.11.1 and following table shows the result of the estimation.

CR1	1660 ± 42(stat.)±1059(sys.)
CR2	79 ± 10(stat.)±65(sys.)
CR3	8.0 ± 3.0(stat.)±6.1(sys.)
CR4	2.0 ± 1.3(stat.)±1.3(sys.)

Table 36: The amount of QCD di-jet background estimated in four signal regions.

7.7 Electroweak background to the CR

The fractions (1-f_{EW}) of Weν and Zee events with respect to all electroweak backgrouds in each CR are estimated from simulation. Because they have no strong dependence on the kinematic selections within statistical errors, values which are estimated in the CR1 are also used for CR2,CR3,CR4.

The background to Weν CR1 includes (in percentage of simulated Weν events): W$\tau\nu$ (4.2%), $t\bar{t}$ (2.0%), single top (1.0%), di-bosons (0.8%), and Zee (0.9%) events. The background to Zee CR1 is composed of (in percentage of simulated Zee events): $t\bar{t}$ (0.3%), di-bosons (1.1%), and single top (0.1%) events.

Table 37 shows (1-f_{EW}) along with systematic uncertainties due to JES, and uncertainties on the cross section of background events.

	1-f_{EW}	stat	JES	xsec
Weν	0.911	1.1%	0.3%	1.0%
Zee	0.985	1.1%	0.1%	0.2%

Table 37: Fraction of Weν and Zee events (1-f_{EW}) wrt to all backgrouds in each CR and their relative systematic uncertainties.

7.8 Transfer factors to Z$\nu\nu$ events

Transfer factors $\frac{N^{SR}_{Z(\to\nu\nu)+jets}}{N_{Z(\to ee)+jets}}$ and $\frac{N^{SR}_{Z(\to\nu\nu)+jets}}{N_{W(\to e\nu)+jets}}$ are estimated as a function of leading jet p_T using alpgen samples. For Z$\to \nu\nu$, selections in low p$_T$ signal regions are applied. And, for Z$\to$ee or Weν events, selections in low p$_T$ control regions are applied.

Figure 31 shows that in low p$_T$ regions, $\frac{N^{SR}_{Z(\to\nu\nu)+jets}}{N_{Z(\to ee)+jets}}$ is slighly higher than 5.99 (the result of LEP experiment for $\frac{Br(Z\to\nu\nu)}{Br(Z\to ee)}$), but in high p$_T$ regions, the result is consistent with that of LEP and has no dependence on the leading jet p$_T$.

The differences with LEP are explained by the fact that we consider $\frac{N^{SR}_{Z(\to\nu\nu)+jets}}{N_{Z(\to ee)+jets}}$ and not $\frac{Br(Z\to\nu\nu)}{Br(Z\to ee)}$. The veto on the third jet creates a difference in the phase space between the two processes, killing some extra Z($\to \ell\ell$) + *jets* events with respect to Z($\to \nu\nu$) + *jets* events (large angle, high p$_T$ photon), hence a correction higher than 5.99. When the jet p$_T$ increases, the effect gets reduced, as we can see.

Table 38 lists the average values of this factor in all control regions. Systematic uncertainties mainly come from the JES uncertainties.

Control regions	$\frac{N^{SR}_{Z(\to \nu\nu)+jets}}{N_{Z(\to ee)+jets}}$
CR 1	$6.60 \pm 0.06(\text{stat.}) \pm 0.21(\text{sys.})$
CR 2,3,4	$6.17 \pm 0.14(\text{stat.}) \pm 0.39(\text{sys.})$

Table 38: Average values of $\frac{N^{SR}_{Z(\to \nu\nu)+jets}}{N_{Z(\to ee)+jets}}$ in each Z(ee) control regions.
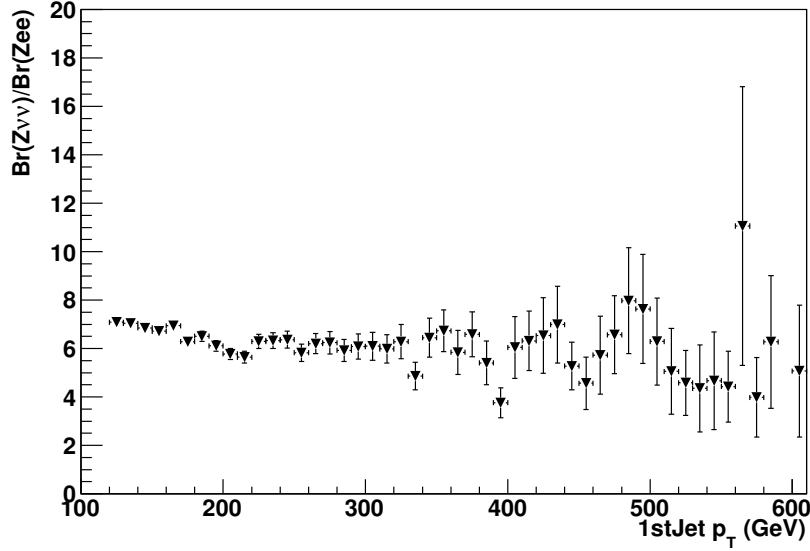
Figure 31: $\frac{N^{SR}_{Z(\to \nu\nu)+jets}}{N_{Z(\to ee)+jets}}$ (including $\frac{Br(Z\to\nu\nu)}{Br(Z\to ee)}$) as a function of leading jet p_T. In the low p_T regions, the ratio is bit more higher than 5.99 which is the result of LEP experiment. But in high p_T regions, the result is closer with the result of LEP experiment.

Figure 32 shows that the distribution of $\frac{N^{SR}_{Z(\to \nu\nu)+jets}}{N_{W(\to e\nu)+jets}}$ has no dependence on the leading jet p_T and it is estimated to be 0.764 ± 0.007 (stat.) ± 0.024 (sys.).

7.9 Closure test

In order to validate the performance of the correction factors explained above to get the estimation of $Z \to \nu\nu$ from $W \to e\nu$ or $Z \to ee$ control regions, closure tests are done using Monte Carlo samples. Figure 33 to Figure 36 present these tests with reasonable agreements.
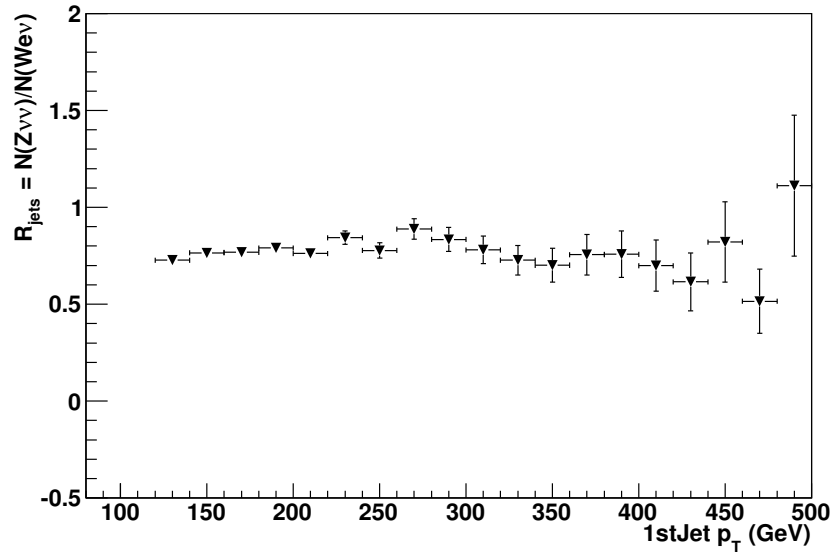
Figure 32: $\frac{N^{SR}_{Z(\to \nu\nu)+jets}}{N_{W(\to e\nu)+jets}}$ as a function of leading jet p$_T$. This figure shows no dependence on the leading jet p$_T$.
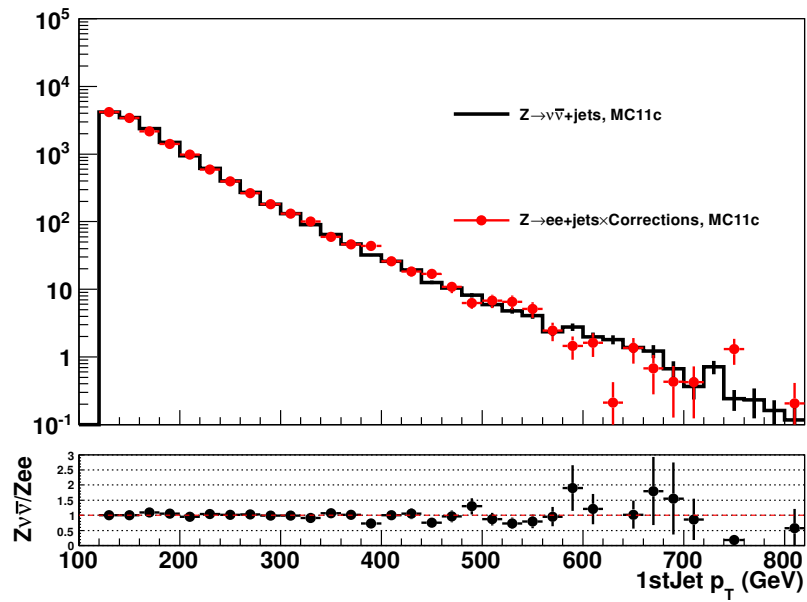
Figure 33: Leading jet p$_T$ distribution. The black line corresponds to the $Z \to \nu\nu$ and red line correspond to the Z→ee multiplied by all correction factors. Good agreement between them is observed.
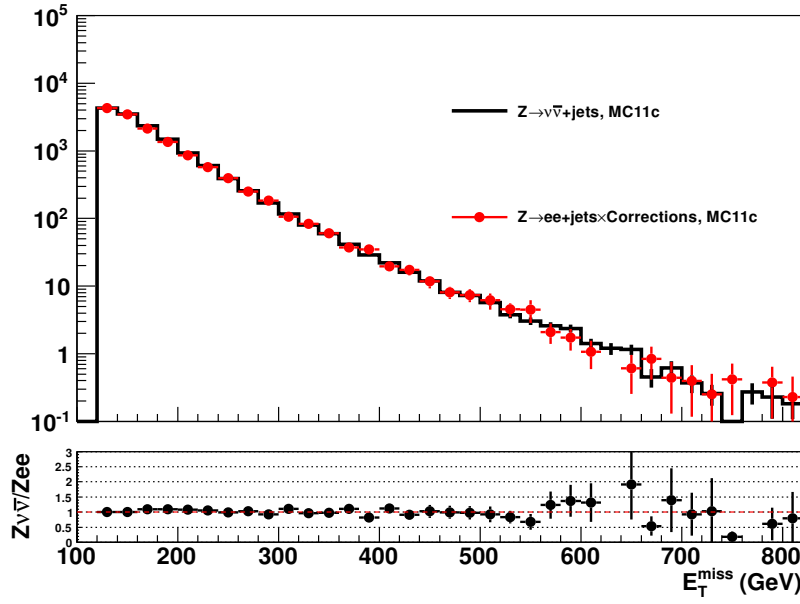
Figure 34: E_T^{miss} distribution. The black line corresponds to the $Z \to \nu\nu$ and red line correspond to the Z→ee multiplied by all correction factors. Good agreement between them is observed.
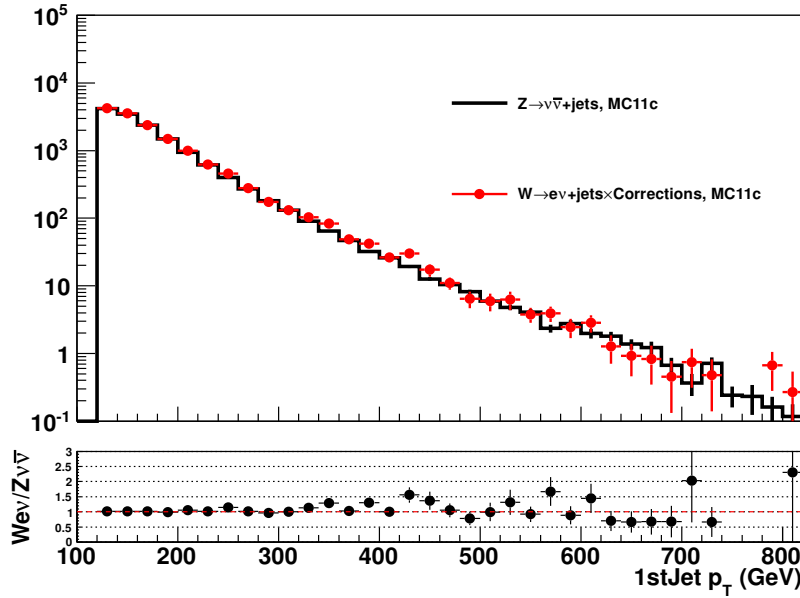
Figure 35: Leading jet p_T distribution. The black line corresponds to the $Z \to \nu\nu$ and red line correspond to the W→eν multiplied by all correction factors. Good agreement between them is observed.

Figure 36: E_T^{miss} distribution. Black line correspond to the $Z \rightarrow \nu\nu$ and red line correspond to the W$\rightarrow e\nu$ multiplied by all correction factors. There is a good agreement between them.

7.10 Estimation from electron control region

Figure 37 to Figure 49 the kinematic distributions in electron control region. All distributions show that data and the expectation from the Standard Model have a good agreement within statistical errors. The following table shows the expected numbers of $Z \rightarrow \nu\nu$ in SR estimated from W$\rightarrow e\nu$ and Z$\rightarrow ee$ control regions, with reasonable agreement. Systematic uncertainties are summarized in tables 40 - 45. The differnce in JES uncertainties between electron and muon control regions is mainly due to the different selection cuts applied in the two control regions.

Jet,E_T^{miss} cut	expectation from Weν CR	expectation from Zee CR
> 120GeV	62331 ± 386(stat.) ± 3802(sys.)	63220 ± 899(stat.) ± 3413(sys.)
> 220GeV	5299 ± 105(stat.) ± 323(sys.)	5312 ± 232(stat.) ± 419(sys.)
> 350GeV	508 ± 31(stat.) ± 30(sys.)	453 ± 64(stat.) ± 36(sys.)
> 500GeV	52.9 ± 10.3(stat.) ± 3.6(sys.)	71.8 ± 25.6(stat.) ± 6.3(sys.)

Table 39: Expected numbers of $Z \rightarrow \nu\nu$ estimated by Weν and Zee control regions.

	SR1	SR2	SR3	SR4
MC stat	0.18	0.40	0.82	2.0
JES Up	-0.35	-0.09	0.49	1.5
JES Down	0.10	0.16	0.43	1.1

Table 40: Systematic uncertainties of acceptance in each signal regions for Weν(in %).

	SR1	SR2	SR3	SR4
MC stat	0.35	0.80	1.7	3.9
JES Up	-0.43	-0.12	-0.54	-0.75
JES Down	0.41	0.43	0.21	0.72

Table 41: Systematic uncertainties of acceptance in each signal regions for Zee(in %).

	Systematic uncertainties(in %)
MC stat	0.58
JES Up	3.2
JES Down	-3.5

Table 42: Systematic uncertainties of efficiency of transverse mass cut and $E_{\text{T}}^{\text{miss}}$ cut in the Weν control region(in %).

	SR1	SR2	SR3	SR4
Weν	1.3	1.4	1.4	1.3
Zee	2.7	2.6	2.6	2.7

Table 43: Systematic uncertainties derived from scale factor of electrons in each signal regions for Zee and Weν (in %).

source of systematic	CR1	CR2	CR3	CR4
JES	4.7	4.7	4.7	4.9
SF	1.3	1.4	1.4	1.3
QCD	1.7	1.2	1.2	2.5
MC modeling	3.0	3.0	3.0	3.0
MC stat uncertainty (from ALPGEN)	1.5	1.6	1.7	2.5
Total	6.1	6.1	6.1	6.8

Table 44: Relative systematic uncertainty (in %) on the Z($\nu\nu$) estimation derived from the Weν control region, in the 4 signal regions.

source of systematic	CR1	CR2	CR3	CR4
JES	3.2	6.3	6.3	6.3
SF	2.7	2.6	2.6	2.7
MC modeling	3.0	3.0	3.0	3.0
MC stat uncertainty (from ALPGEN)	1.5	2.7	3.1	4.7
Total	5.4	7.9	8.1	8.8

Table 45: Relative systematic uncertainty (in %) on the Z($\nu\nu$) estimation derived from the Zee control region, in the 4 signal regions.
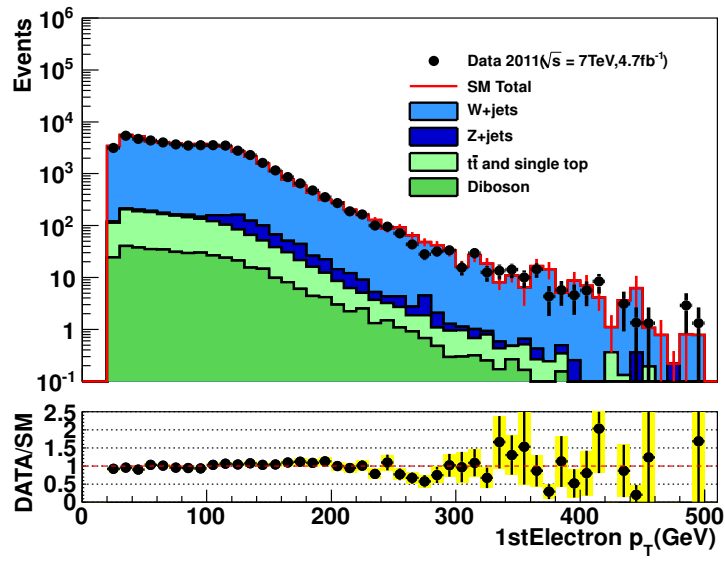
Figure 37: Leading electron p_T distribution in low p_T $We\nu$ control regions.
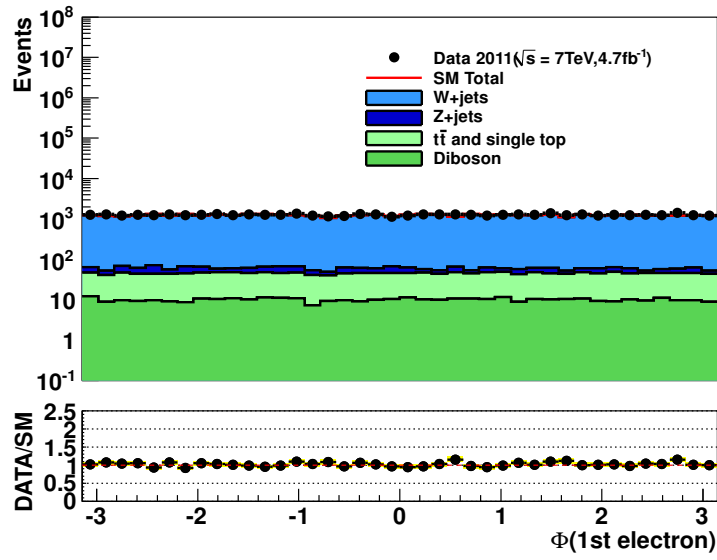
Figure 38: Leading electron phi distribution in low p$_T$ Weν control regions.
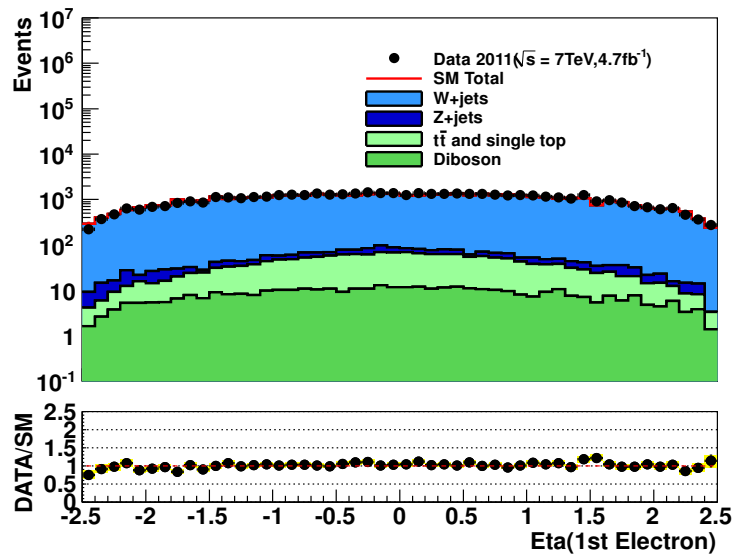
Figure 39: Leading electron eta distribution in low p$_T$ Weν control regions.
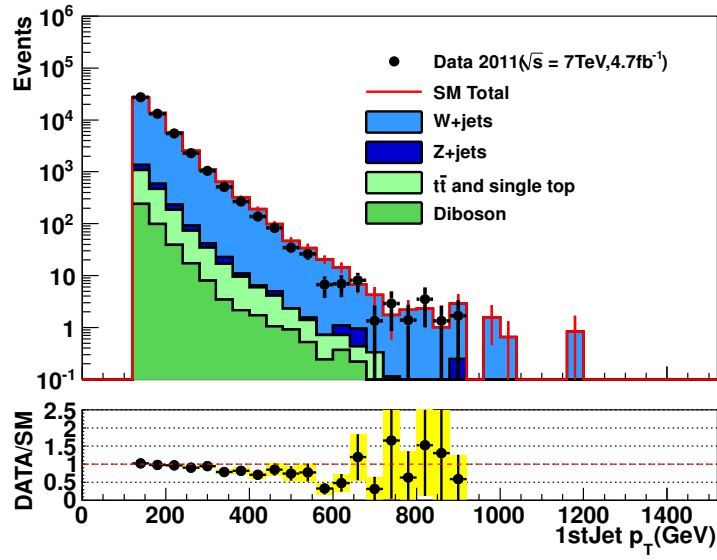
Figure 40: Leading jet p$_T$ distribution in low p$_T$ W$e\nu$ control regions.
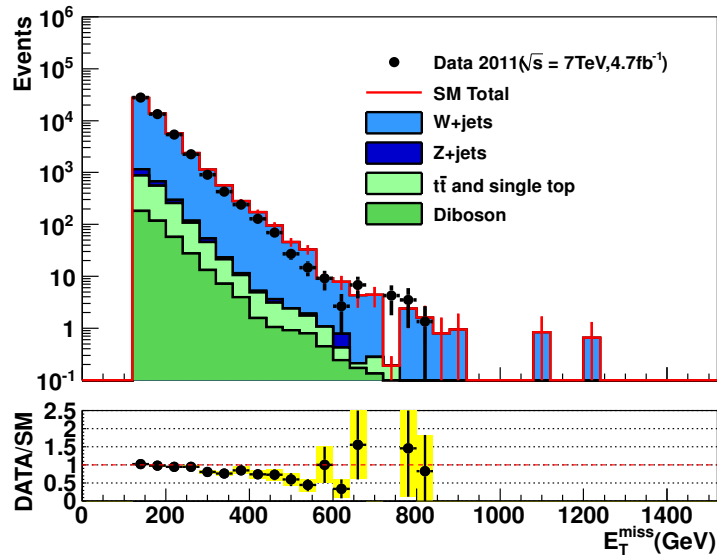
Figure 41: Corrected E_T^{miss} distribution in low p$_T$ W$e\nu$ control regions.
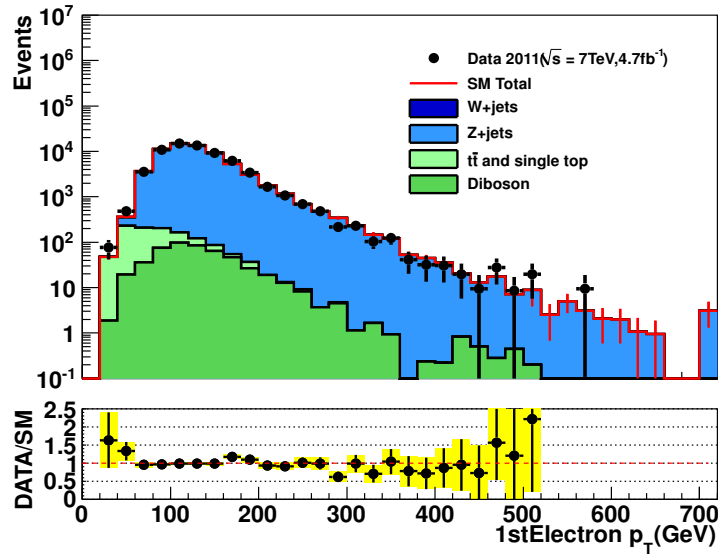
Figure 42: Leading electron p$_T$ distribution in low p$_T$ Zee control regions.
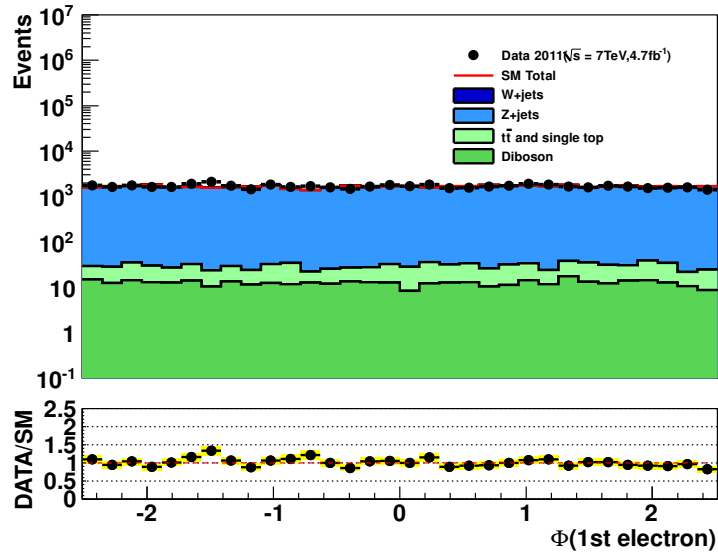
Figure 43: Leading electron phi distribution in low p$_T$ Zee control regions.
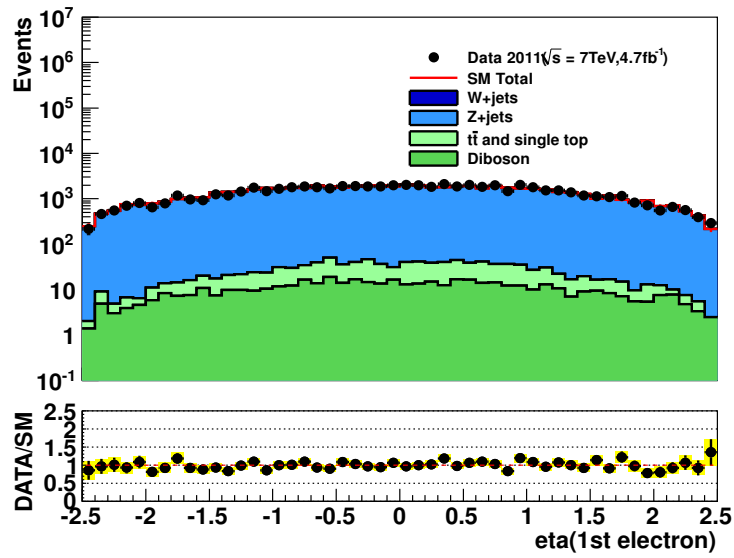
Figure 44: Leading electron eta distribution in low p$_T$ Zee control regions.
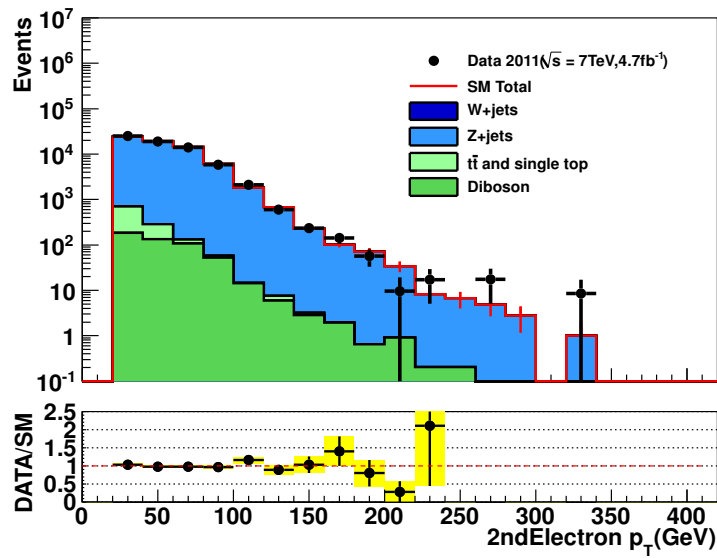
Figure 45: 2nd leading electron p$_T$ distribution in low p$_T$ Zee control regions.
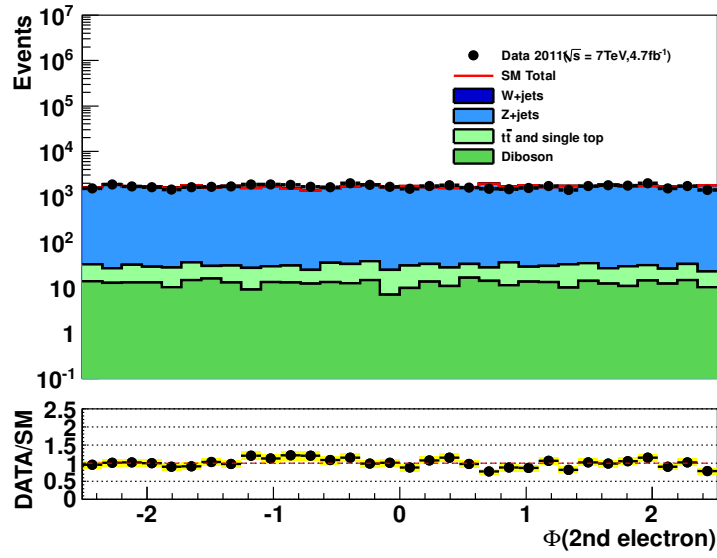
Figure 46: 2nd leading electron phi distribution in low p$_T$ Zee control regions.
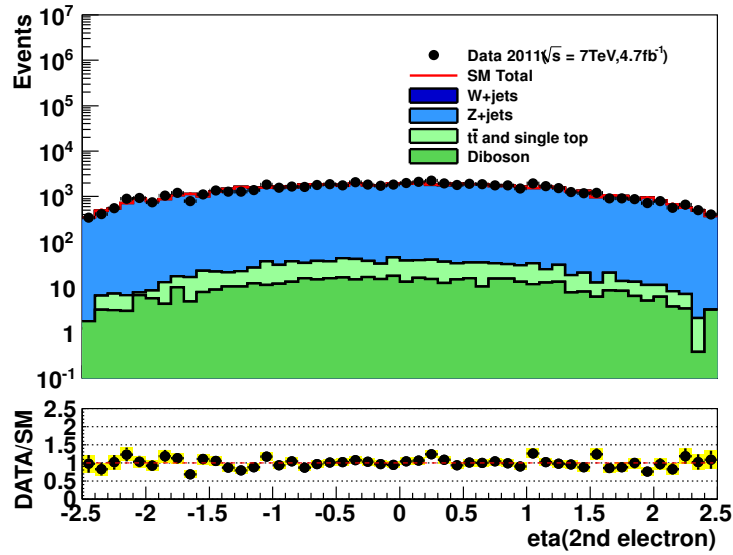
Figure 47: 2nd leading electron eta distribution in low p$_T$ Zee control regions.
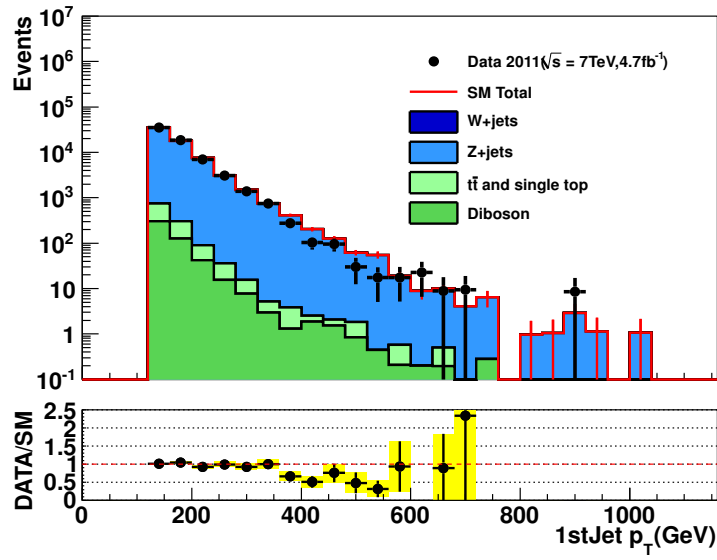
Figure 48: Leading jet p$_T$ distribution in low p$_T$ Zee control regions.
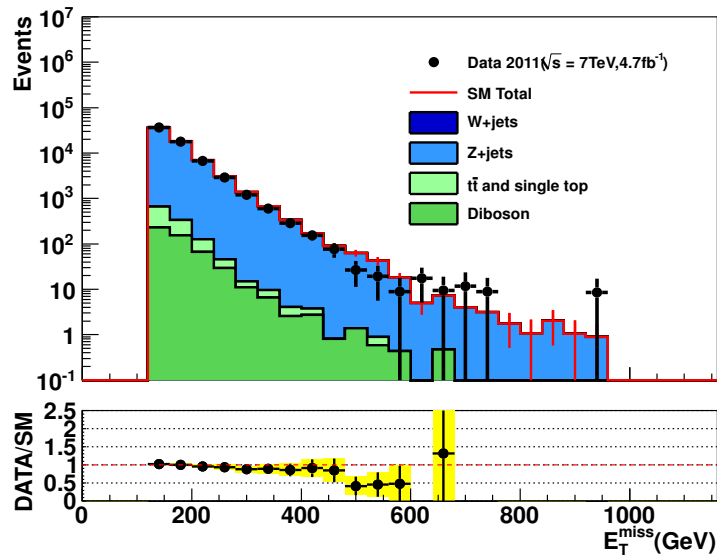
Figure 49: Corrected E_T^{miss} distribution in low p$_T$ Zee control regions.

7.11 Residual $W \to e\nu$ background estimation

Residual $W \to e\nu$ events are not negligible and expected to be 10-15 % with respect to the total SM background in the current mono-jet selection. This background is estimated in a semi data-driven way, such that $W \to e\nu$ is normalized in a control region as a function of E_T^{miss}, i.e. the distributions are also corrected. The current analysis is based on a "cut and counting" way and does not use shape information, however the shape comparison between data and background prediction provides an additional validity check of our background estimation. The observables depending on p_T of a vector boson, especially E_T^{miss} and the leading jet p_T, are strongly affected by a choice of the renormalization scale (Alpgen used in this analysis) and such poor MC description potentially makes us misunderstand the result.

The method of estimating the residual $W \to e\nu$ background is different from the other electroweak background estimation as the situation is slightly complicated. A mis-identified electron mimics a jet if it is not identified while there is no need to consider the effect of mis-identified leptons in muon channel or $Z \to \nu\nu$ estimation from $W \to e\nu$. The correction function is decomposed where it is possible, but the estimation is simplified so that the electron identification part (i.e. fake jet probability) is not fully decomposed. The residual $W \to e\nu$ background is estimated as following.

$$N_{W \to e\nu}^{DD,SR} = (N_{W \to e\nu}^{CR} - N_{QCD}^{CR}) \times (1 - f_{EW}) \times \frac{1}{\epsilon_e \times A_e} \times \frac{\epsilon^{SR}}{\epsilon^{CR*}} \tag{27}$$

$$= N_{W \to e\nu}^{DD,CR*} \times \frac{N_{W \to e\nu}^{SR}}{N_{W \to e\nu}^{CR*}} \tag{28}$$

The amount of QCD background in control region (N_{QCD}^{CR}) is estimated in a data-driven way and subtracted from $W \to e\nu$ control sample ($N_{W \to e\nu}^{CR}$). The other electroweak background ($t\bar{t}$, single-top, di-bosons and other W/Z + jets) is estimated using the MC simulation and these contaminations are removed by considering the fraction (f_{EW}). In this way, the detector related systematic uncertainties (JES, luminosity, lepton identification efficiency) and theory uncertainties are partially canceled out. After subtracting all the background, the lepton acceptance correction (A_e) and the electron identification efficiency (ϵ_e) are applied inversely to recover $W \to e\nu$ events in the full lepton phase space. Finally, residual $W \to e\nu$ events are obtained by applying the ratio of selection efficiencies of signal selection including lepton veto (ϵ^{SR}) and control sample selection without lepton selection (ϵ^{CR*}).

The $W \to e\nu$ control sample is collected as following:

- Egamma stream with the GRL

- Single electron trigger depending on the period, EF_e20_medium (period B-J), EF_e22_medium (period K) and EF_e22vh_medium1 (period L-M).

- Medium cleaning (same as signal region)

- At least one good isolated electron : Tight++, ptcone20/E_T< 0.1 with $p_T > 25$ GeV and $|\eta| < 2.47$, not including the crack region ($1.37 < |\eta| < 1.52$).

- No second electron with Medium++ and $p_T > 20$ GeV nor isolated muon with $p_T > 7$ GeV and ptcone20 < 1.8 GeV (same as signal region)

- Transverse momentum with 40 GeV < m_T < 100 GeV

- At least one jet with $p_T > 120$ GeV and no third jet with $p_T > 30$ GeV and $|\eta| < 4.5$

- $E_T^{\mathrm{miss}} > 120$ GeV and $\Delta\phi(jet2, E_T^{\mathrm{miss}}) > 0.5$

7.11.1 QCD background estimation

QCD background is estimated in a data-driven way using matrix method. The matrix method estimates the fractional events with a fake electron by using QCD (fake lepton) enriched sample by loosing electron identification criteria. Two inputs, real efficiency ϵ_{real} and fake efficiency ϵ_{fake} are obtained using appropriate control samples [9].

$$\begin{pmatrix} n_{loose} \\ n_{tight} \end{pmatrix} = \begin{pmatrix} 1/\epsilon_{fake} & 1/\epsilon_{real} \\ 1 & 1 \end{pmatrix} \begin{pmatrix} n_{fake} \\ n_{real} \end{pmatrix} \tag{29}$$

where $n_{loose}(n_{loose})$ is the number of events passing loose (tight) electron identification criteria. The tight criteria is same as what is used in $W \to e\nu$ control sample selection and loose criteria is Medium++ without isolation. The numbers of events with a fake and real electron are n_{fake} and n_{real}, respectively.

Figure 50 shows E_T^{miss} distribution of estimated QCD background with the loosen control selection; only require $p_T^{1jet} > 120$ GeV and $n_{jet} \le 2$. It is not possible to take QCD enrich regions in higher missing transverse momentum region by loosing electron identification regions. The number of QCD fake events is estimated as 219 ± 81 and all the electroweak background of 261 ± 5 in CR1 and QCD contamination is zero consistent within the error. The main electroweak background comes from $W \to e\nu$. The $W \to e\nu$ Alpgen MC predicts harder E_T^{miss} shape and it gives overestimation in higher E_T^{miss} region and it results in the negative central values in all the control regions. The major uncertainty comes from the systematic uncertainty due to a choice of control samples while data statistical uncertainty becomes larger in higher kinematic regions and no event is left in CR4. In this analysis, the QCD contamination is neglected.

	CR1	CR2	CR3	CR4
Data	7597	609	54	8
QCD CR	$219 \pm 8 \pm 81$	$18 \pm 2 \pm 7$	$0.96 \pm 0.56 \pm 0.38$	0
EW contamination	261 ± 5	23 ± 21	2.0 ± 0.4	0.4 ± 0.2
QCD	$-43 \pm 9 \pm 82$	$-5 \pm 3 \pm 7$	$-1.1 \pm 0.7 \pm 0.4$	$-0.5 \pm 0.2 \pm 0$
Fraction	0.5 ± 1.1 %	-0.8 ± 1.2 %	-2.0 ± 1.4 %	-11 ± 4 %

Table 46: The amount of QCD di-jet background, its absolute statistical (the first error) and systematic uncertainty (the second error) estimated in four kinematic regions.

Figure 50: Missing transverse momentum of QCD background estimated by the matrix-method (black filled circles) and MC electroweak background (red open histogram) in the loose control region with $p_T^{1stjet} > 120$ GeV and $n_{jet} = 2$.

7.11.2 The fraction of the other electroweak background

Figure 51 shows various distributions in the $W \to e\nu$ control region. All SM processes are predicted by the MC simulation. The $W \to e\nu$ Alpgen MC predicts harder missing transverse momentum spectrum than data, which is observed in the various ATLAS analyses. As mentioned above, this difference is corrected after subtracting non $W \to e\nu$ background. Table 47 summarizes the number of events and other electroweak background in each kinematic region. The purity of $W \to e\nu$ is 87 - 94 % in all control regions and the main background is $t\bar{t}$ and di-bosons.

929 The fraction f_{EW} = 0.065 is obtained in CR1 and applied for the other kinematic regions as $E_\mathrm{T}^\mathrm{miss}$
930 dependency is rather flat. It is also because of difficulty to see the tendency due to poor MC statistics
931 and poor agreement between MC and data in W/Z + jet processes. Model systematic uncertainty of
932 11.4 % [7] is considered for all the regions in this analysis. The JES uncertainty is obtained using the
933 JESUncertaintyProvider tool. The energy scale uncertainty of $E_\mathrm{T}^\mathrm{miss}$ is obtained by considering JES
934 uncertainty for LCW jets, where it is assumed that LC calibration is fully correlated to EMJES and
935 energy scale uncertainty due to clusters not belong to any jet is negligible [10]. The largest systematic
936 uncertainty is JES and its relative uncertainty is around 5%. This uncertainty is partially canceled out in
937 $\epsilon^{SR}/\epsilon^{CR*}$, but not fully due to the presence of m_T cut in the CR selection. The f_{EW} and its uncertainty in
938 each kinematic region are summarized in Table 48.

	CR1	CR2	CR3	CR4
$W \rightarrow e\nu$	7445 ± 45	720 ± 13	77 ± 4	9.1 ± 4.1
$t\bar{t}$	196 ± 3	15.0 ± 0.8	0.9 ± 0.2	0.04 ± 0.06
single-top	101 ± 2	9.0 ± 0.6	0.62 ± 0.18	0.08 ± 0.06
di-bosons	175 ± 14	32.7 ± 6.0	4.5 ± 2.2	1.1 ± 1.1
Z+jets	9.6 ± 1.5	1.1 ± 0.5	0.27 ± 0.27	—
Other W+jets	32.3 ± 5.3	2.3 ± 0.5	0.31 ± 0.18	0.11 ± 0.11
f_{ew}	6.46 ± 0.19 %	7.7 ± 0.8 %	7.9 ± 2.7 %	13 ± 10 %

Table 47: Event yield of $W \rightarrow e\nu$ and other electroweak background in each control region. The error includes MC statistical uncertainty only.

	CR1	CR2	CR3	CR4
f_{ew}		6.46 %		
Model		0.72 %		
JES		0.35 %		
JER		0.04 %		
ID efficiency		0.01 %		

Table 48: The fraction of other electroweak background and its absolute uncertainties in each kinematic region.

7.11.3 Correction functions

940 The electron reconstruction efficiency is obtained using MC simulation as shown in Figure 27, but cor-
941 rected by the measurement using $Z \rightarrow ee$ events. The electron acceptance is also computed using
942 four-vector of truth electrons in Alpgen $W \rightarrow e\nu$ MC events. Figure 52(a) shows correction factor for
943 electron identification efficiency $1/\epsilon_e$ and electron acceptance $1/A_e$ as a function of $E_\mathrm{T}^\mathrm{miss}$. The relative
944 efficiencies of mono-jet signal selection with respect to the control sample selection $\epsilon^{SR}/\epsilon^{CR*}$ are shown
945 in Figure 52 (b). The $E_\mathrm{T}^\mathrm{miss}$ dependency of correction $\epsilon^{SR}/\epsilon^{CR*}$ is explained by two effects, the presence
946 of mis-ientified electron in SR and the fact that ϵ^{CR*} is the efficiency after the electron acceptance cor-
947 rection. The CR has $W \rightarrow e\nu$ events with an electron identified while the SR does not, which results
948 in a mis-identified electron mimicking a jet and the event veto rate due to jet veto is higher in the sig-
949 nal region. Table 49 shows the averaged correction factor and the systematic uncertainties. The largest

systematic uncertainty is model uncertainty (3 %) in CR1 while MC statistical and JES uncertainties
dominate in higher kinematic regions.

	CR1	CR2	CR3	CR4
< C >	2.06	1.19	0.800	0.63
JES	0.02	0.03	0.05	0.03
JER	0.02	0.01	0.02	0.08
ID efficiency	0.003	0.002	0.002	0.003
Model	0.06	0.04	0.02	0.02
MC statistics	0.02	0.03	0.06	0.16

Table 49: The averaged correction factor and its absolute uncertainties in each kinematic region.

7.11.4 Result

The residual $W \to e\nu$ background is estimated by applying the set of correction functions based on Eq.
27. Missing transverse distributions of estimated $W \to e\nu$ background in four signal regions are shown
in Figure 53 together with distributions obtained by $W \to e\nu$ MC samples. Table 50 summarizes the
number of estimated residual $W \to e\nu$ background and uncertainties in each signal region.

	CR1	CR2	CR3	CR4
CR data	7597 ± 87	609 ± 25	54 ± 7	8 ± 2.8
$f_{e\nu}$	6.46 ± 0.19 ± 0.81 %	6.46 ± 0.19 ± 0.81 %	6.46 ± 0.19 ± 0.81	6.46 ± 0.19 ± 0.81
Correction	2.06 ± 0.02 ± 0.07 %	1.19 ± 0.03 ± 0.04	0.800 ± 0.06 ± 0.05	0.63 ± 0.16 ± 0.08
Result	14611 ± 168 ± 494	679 ± 28 ± 32	40 ± 5.5 ± 4.3	4.7 ± 1.7 ± 1.3

Table 50: The residual $W \to e\nu$ background and its uncertainties estimated in this analysis.
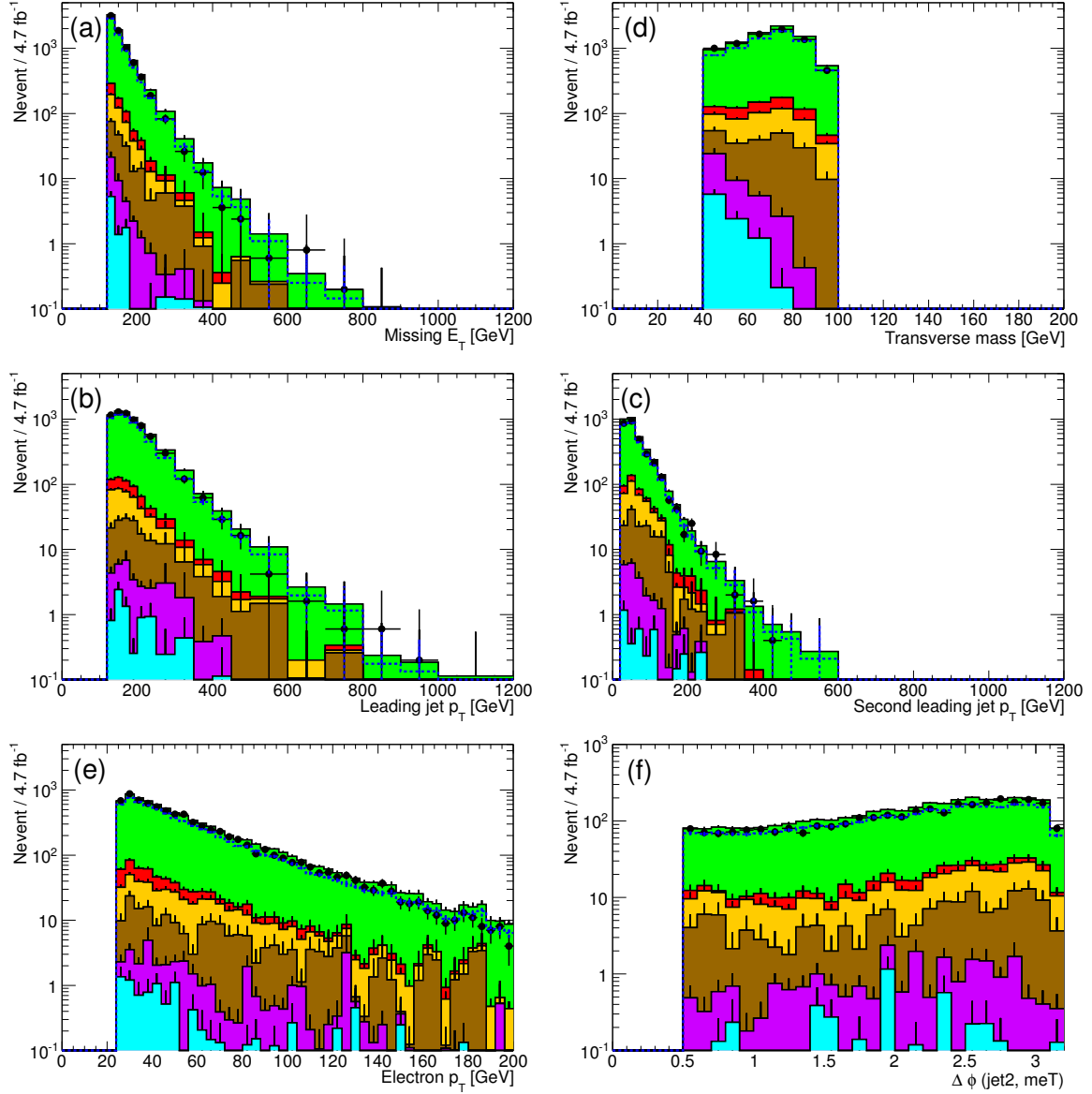
Figure 51: Distributions of the main variables determines the control region: (a) missing transverse momentum, (b) transverse mass, (c) leading jet p_T, (d) second leading jet p_T, (e) leading electron p_T, (f) $\Delta\phi(jet2, E_T^{miss})$. The blue open histogram shows the MC estimation using $W \rightarrow e\nu$ Alpgen sample with Sherpa $W - p_T$ weight.
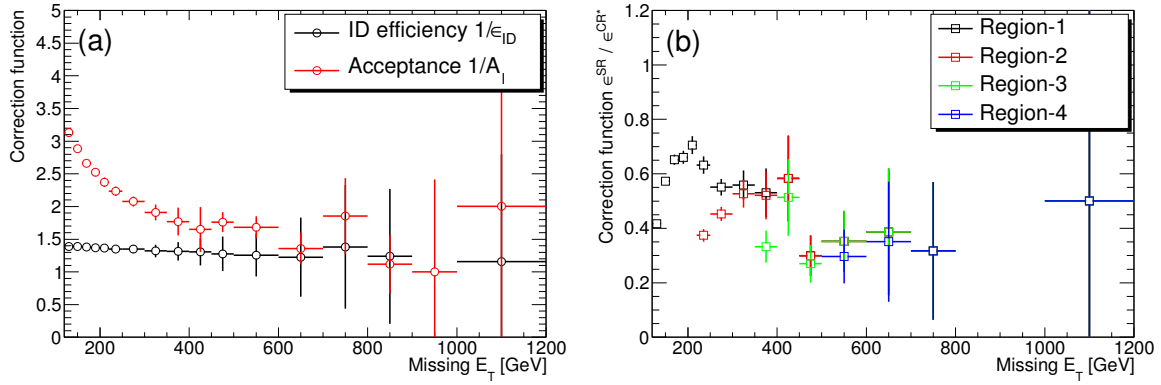
Figure 52: (a) Correction factors as a function of missing transverse energy; identification efficiency (black circle) and acceptance (red circle). (b) Four relative efficiencies of signal selections with respect to the control sample selection as a function of missing transverse energy.
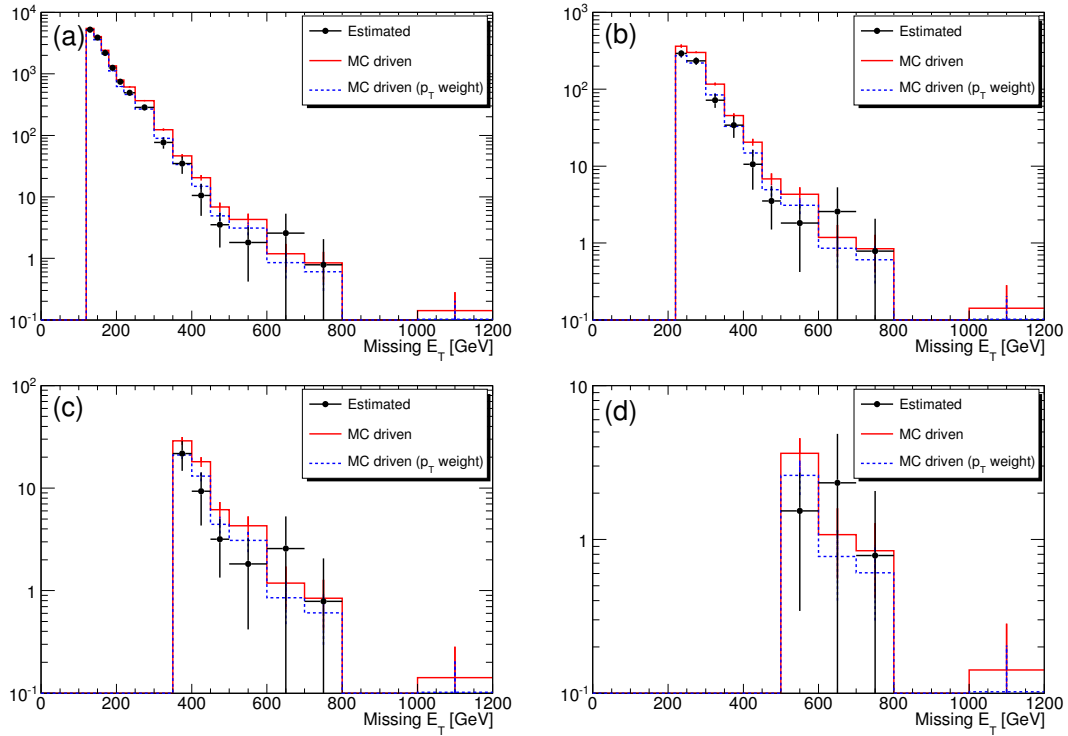
Figure 53: Missing transverse momentum distributions estimated by this analysis (black filled circle), MC driven way (red histogram) and MC driven with Sherpa $W - p_T$ weight (blue histogram).

8 Data-driven electroweak background determination using transfer factors

8.1 Introduction

The production of a vector boson (W or Z) in association with jets constitutes the main background of this analysis. Controlling the total number of events and also the shape of these backgrounds is crucial for reaching a good sensitivity for mono-jet signals coming from new physics.

The MC predictions a priori suffer from large theoretical uncertainties originating for example from the choice of the PDFs and the scales, as well as from experimental uncertainties related to the determination of the absolute JES and luminosity, among others. These sytematic uncertainties affect the absolute normalization and the shape of the predicted distributions. Nevertheless, ATLAS results on boson+jet(s) production [11], [12] demonstrate that the nominal MC predictions describe the data reasonably well and that the data has the potential to constrain the size of the systematic uncertainties of the MC.

This section describes a data-driven method developed in order to estimate the contribution of these processes to the signal region. The method is an improved version of the method that was used for the analysis of the 35 pb^{-1} of 2010 data (published as Physics Lettes B 705 (2011) 294-312), and for the first fb^{-1} of 2011 data (see ATLAS-CONF-2011-096). The method described below is very similar to that used in many other ATLAS Exotic analyses for searching for new physics, and in the SUSY 0-lepton analysis (see ATLAS-CONF-2012-033), for which transfer factors from MC are employed to bring the background contributions, as determined and constrained using data in control regions (CRs), to the signal regions (SRs) for the different measured distributions.

In this analysis, different control regions are considered: inclusive control regions with at least one muon or one electron identified in the final state; and exclusive control regions with an identified W or an idenfied Z boson in the final state. This section mainly focuses on the electroweak background estimation based on the exclusive Ws and Zs samples (and their combination).

8.2 Main method

In this section we will present all the steps needed to estimate the background contributions from the electroweak processes. The dominant contribution comes from the irreducible component of the $Z + jets$ in which $Z\nu\nu$ decays generate large $E_{\mathrm{T}}^{\mathrm{miss}}$. The $W + jets$ background is composed by $W\tau\nu$, $W\mu\nu$ and $We\nu$ events in which no electron or muon is identified. The estimation of each of these contributions is done separately and in a similar way, with a data-driven technique that can be splitted in four steps and which is repeated for each of the observables.

- Select a given control region (CR) (either exclusive $W \rightarrow \mu\nu$, or exclusive $Z \rightarrow \mu\mu$, or inclusive electrons/muons).

- For a given observable, measure the data distribution in the CR.

- For a given observable and using MC, build the transfer factors (see below), that enable observations in the CR to be converted into background estimates in the SR.

- Apply the transfer factors on the measured distribution in data in the CR to get the data-driven estimation of a process in the SR.

The inclusive electron or muon control regions are defined by inverting the electron (or muon) veto of the SR and applying all the other selection cuts. The exclusive W control region in the muon sample is defined selecting events with only one muon and applying an extra selection cut on the transverse mass

to be $40 < m_T < 100$ GeV. Similarly, the Z control region is defined selecting events with two muons with an invariant mass within $76 < m_{\mu\mu} < 116$ GeV.

As an example, in the case of the $Z(\rightarrow \nu\nu) + jets$ process, its constribution to the signal region in a given bin of a given distribution $N(Z(\rightarrow \nu\nu) + jets)_{signal}$ would be determined using the exclusive W or Z control samples according to

$$N(Z(\rightarrow \nu\nu) + jets)_{signal} = (N^{data}_{W\rightarrow\mu\nu,control} - N^{background}_{W,control}) \times \frac{N^{MC}(Z(\rightarrow \nu\nu) + jets)_{signal}}{N^{MC}_{W\rightarrow\mu\nu,control}} \qquad (30)$$

or

$$N(Z(\rightarrow \nu\nu) + jets)_{signal} = (N^{data}_{Z\rightarrow\mu\mu,control} - N^{background}_{Z,control}) \times \frac{N^{MC}(Z(\rightarrow \nu\nu) + jets)_{signal}}{N^{MC}_{Z\rightarrow\mu\mu,control}}, \qquad (31)$$

respectively, where $N^{data}_{W\rightarrow\mu\nu,control}$ ($N^{data}_{Z\rightarrow\mu\mu,control}$) and $N^{MC}_{W\rightarrow\mu\nu,control}$ ($N^{MC}_{Z\rightarrow\mu\mu,control}$) denote the number of $W \rightarrow \mu\nu$ ($Z \rightarrow \mu\mu$) candidates in data and MC in the control region. Similarly, the same background could be determined from the inclusive muon control regions using the same formula.

$$N(Z(\rightarrow \nu\nu) + jets)_{signal} = (N^{data}_{\mu,control} - N^{background}_{\mu,control}) \times \frac{N^{MC}(Z(\rightarrow \nu\nu) + jets)_{signal}}{N^{MC}_{\mu,control}} \qquad (32)$$

where $N^{data}_{\mu,control}$ now denotes the observed events in data in the control region, $N^{background}_{\mu,control}$ is the non-EWK background, $N^{MC}(Z(\rightarrow \nu\nu) + jets)_{signal}$ is the number of $Z(\rightarrow \nu\nu) + jets$ simulated events as determined by the simulation in the signal region, and $N^{MC}_{\mu,control}$ is the predicted MC events in the muon inclusive sample formed by a mixture of W+jets and Z+jets dominated by the W+jets contribution.

Therefore, in each control sample, the transfer factors for each process are simply defined as the ratio of simulated events for the process in the signal region over the total number of simulated events in the control region. In this way the transfer factors include in a single step all effects related to lepton acceptance and efficiency and take as input the predicted branching ratios for the W and Z decays into leptons. MC events are corrected to have the same lepton reconstruction efficiency as in data, following the recommendations of the egamma and the muon performance groups [8].

The EWK processes $Z \rightarrow \nu\nu$+jets, $W \rightarrow \tau\nu$+jets, $W \rightarrow \mu\nu$+jets, and $Z \rightarrow \mu\mu$+jets are estimated using the exclusive $W \rightarrow \mu\nu$+jets or $Z \rightarrow \mu\mu$+jets control samples. The $W \rightarrow e\nu$+jets, $Z \rightarrow \tau\tau$+jets, and $Z \rightarrow ee$ background contributions are extracted using an inclusive electron control samples. In the case of the important $W \rightarrow \tau\nu$+jets contribution, the estimation was carried out using both $W \rightarrow \mu\nu$ and inclusive electron control samples and the results were consistent to each other within uncertainties. For the final results, the estimation based on the $W \rightarrow \mu\nu$ control sample was adopted, although the use of the inclusive electron sample would be justified since the τ in the $W \rightarrow \tau\nu$ background decays dominantly into a narrow jet of hadron or into an electron.

Figures 54 and 55 show the main kinematic distribution of the reconstructed leptons for region SR1 (E_T^{miss}, jet1 $p_T > 120\,GeV$). The distributions of M_T and $M_{\mu\mu}$ before these cuts are shown in Fig. 56 for the inclusive muon control region. In the appendix A we present a further study that show that the muon control region at low M_T ($< 40 GeV$) is very similar to the one corresponding to $40 < m_T < 100$ GeV.

Figures 57 and 58 present the measured E_T^{miss} and jet distributions in the inclusive electron and inclusive muon CRs, respectively, compared to the MC predictions. Similarly, Figs. 59 and 60 show the E_T^{miss} and jet distributions as measured in the exclusive $W \rightarrow \mu\nu$ and $Z \rightarrow \mu\mu$ control regions. In all these plots, an only for illustration to put emphasis on the shape, the MC include a global normalization factor that brings the MC predictions closer to the data. The global normalization factors for the inclusive control regions are collected in Table 51.

---

[8]The recostruction efficiency corrections as well as the p_T smearing procedure for both electrons and muons are described in *https://twiki.cern.ch/twiki/bin/viewauth/AtlasProtected/SusyObjectDefinitionsr17*

	Region A	Region B	Region C	Region D
Muon control region	0.968±0.005	0.87±0.01	0.81±0.04	0.65±0.09
Electron control region	0.926±0.009	0.80±0.03	0.80±0.08	1.0 ±0.3

Table 51: Summary of the scale factors with their corresponding statistical uncertainties.

The bin-by-bin transfer factors are constructed for each of the distributions in the different control regions as explained above. Figures 61 to 65 present the tranfer factors in the E_T^{miss} distribution for some of the most important backgrounds as taken from the inclusive muon and electron control regions. Similar results are obtained for the exclusive regions. Figures 66 to 69 present, for the most relevant background processes, the tranfer factors applied to the E_T^{miss} distribution as determined in the exclusive control regions.

The results from the different methods are then compared for the different background estimations. As an example, Figure 70 presents the comparison of the results for the dominant $Z \rightarrow \nu\nu$+jets background contribution as determined from the different control samples in the different signal regions. The comparison demonstrates the consistency across different control regions. As expected, the results from the inclusive control region are very close to those from the W control region or those from the exclusive W and Z control regions combined. The comparison also illustrates how a data-driven procedure based on the Z sample alone would suffer from large statistical uncertainties.

8.3 Systematic uncertainties

Different sources of uncertainty are considered in the electroweak background determination. Some of them are related to pure experimental aspects as the total integrated luminosity and the determination of the absolute jet energy scale/resolution, and other are related to MC modeling and simulation uncertainties including lepton reconstruction efficiencies, PDFs, parton showers, and the absolute normalization of the background processes.

The data-driven method adopted - with very similarly defined control and signal regions (modulo de presence of the lepton in the final state and minimum cuts to select Ws and Zs) and based on ratio of events in control and signal regions - will allow to cancel the leading contribution of the different sources of uncertainty. The effect on the different sources of systematic uncertainty on the final background estimation is studied in terms on the effect on the computed transfer factors in the MC. This is done separately for each of the analysis using either inclusive or exclusive control regions.

Below we present the list of the systematic uncertainties considered:

- Absolute luminosity[9].

- Jet energy (JES) scale and (JR).

- Lepton identification efficiencies.

- Background subtraction in control regions.

- Initial state and final state radiation (ISR/FSR).

- Factorization and renormalization scales.

---

[9]This uncertainty, which is about 3.4%, is totally absorbed by the data-driven method of the electroweak background estimation because it affect the signal region and the control regio in exactly the same way. Therefore it cancels out completely.
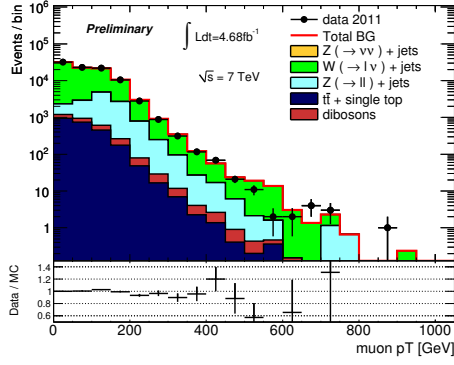
(a)
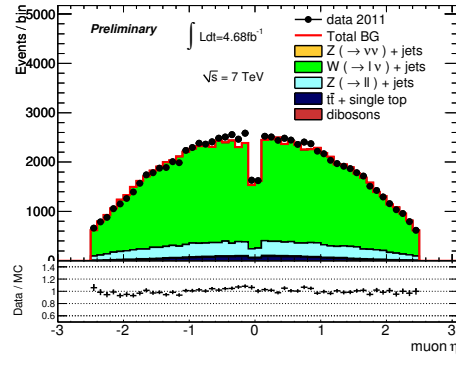
(b)
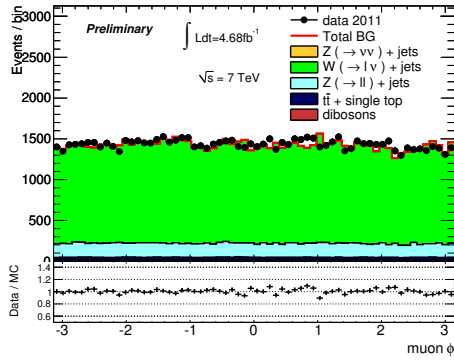
(c)
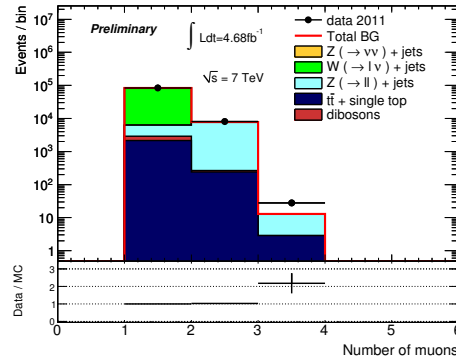
(d)

Figure 54: Kinematic distributions of the identified muons in the inclusive muon control region for the selection cuts of region A (E_T^{miss}, jet1 $p_T > 120$ GeV).

(a)

(b)

(c)

(d)
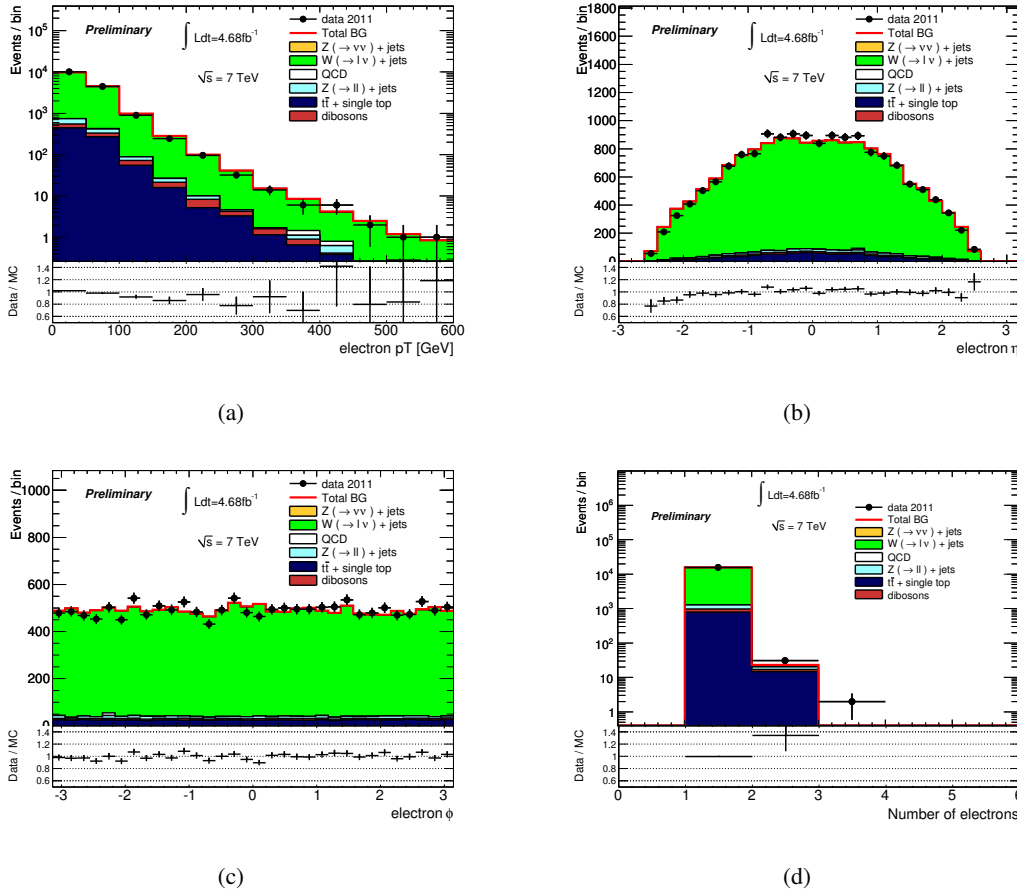
Figure 55: Kinematic distributions of the identified electrons in the inclusive electron control region for the selection cuts of region A ($E_\mathrm{T}^\mathrm{miss}$, jet1 $p_\mathrm{T} > 120\,GeV$).

(a)

(b)
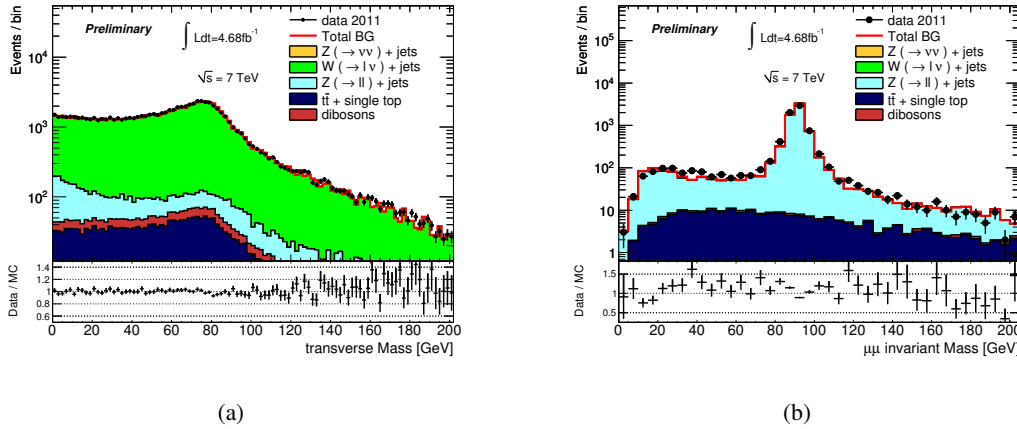
Figure 56: The distributions of M_T and $M_{\mu\mu}$. The exclusive $W \rightarrow \mu\nu$ control region is obtained requiring $M_T > 40 GeV$. Instead the $Z \rightarrow \mu\mu$ exclusive control region is obtained requiring $76 GeV < M_{\mu\mu} < 116 GeV$.
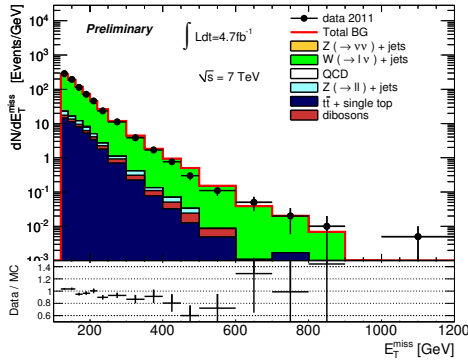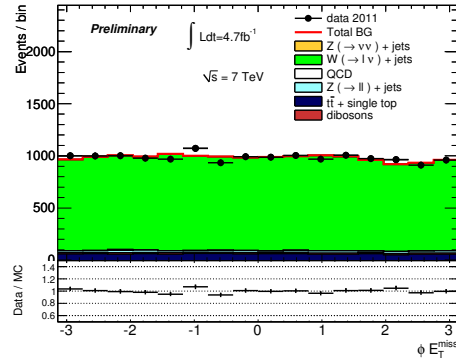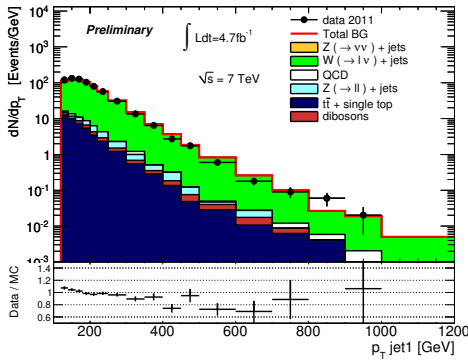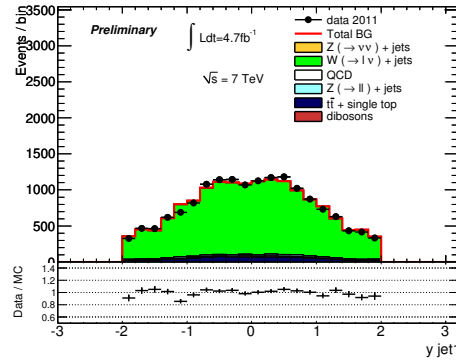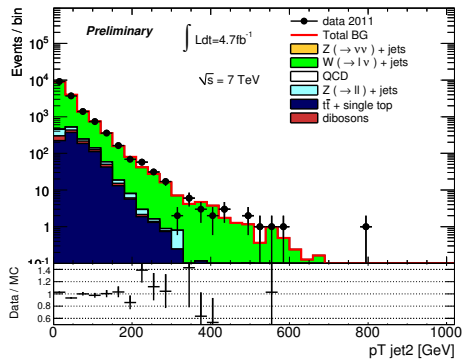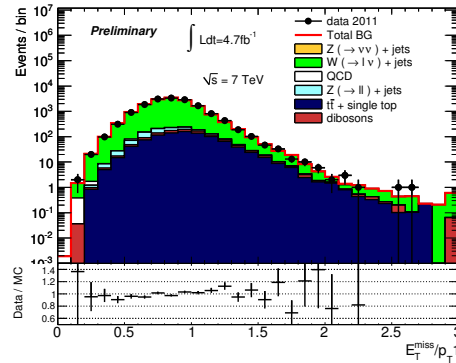
Figure 57: Kinematic distributions of the events in the inclusive electron control region for the selection cuts of region A (E_T^{miss}, jet1 $p_T > 120\,GeV$). These plots make use of Alpgen W+jets and Z+jets samples.
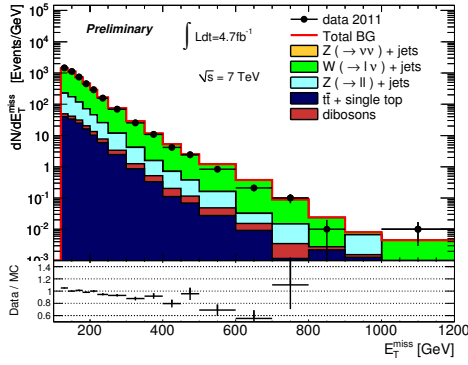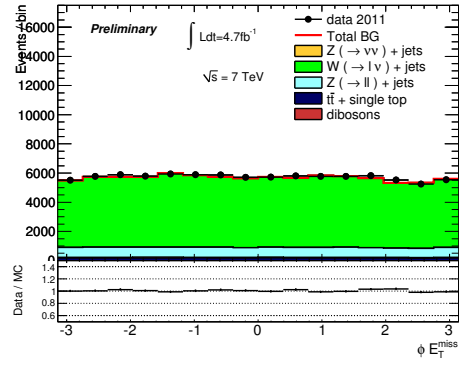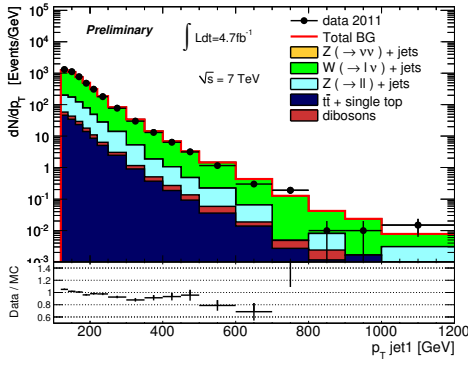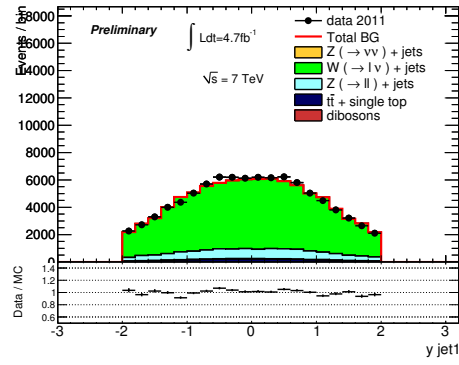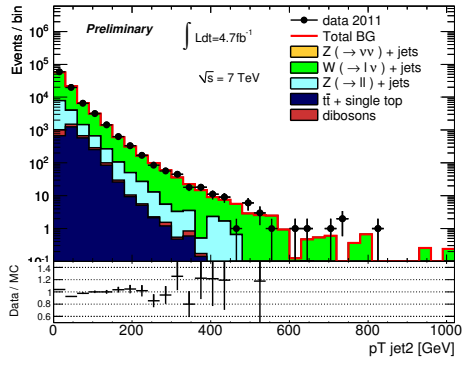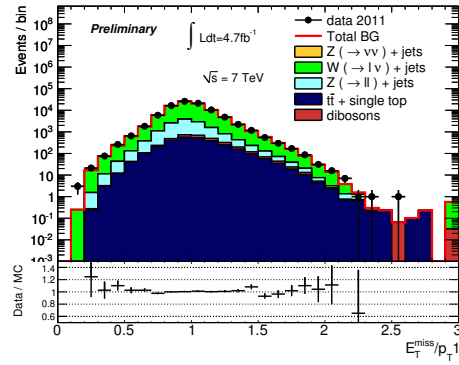
Figure 58: Kinematic distributions of the events in the inclusive muon control region for the selection cuts of region A (E_T^{miss}, jet1 $p_T > 120\,GeV$). These plots make use of Alpgen W+jets and Z+jets samples.
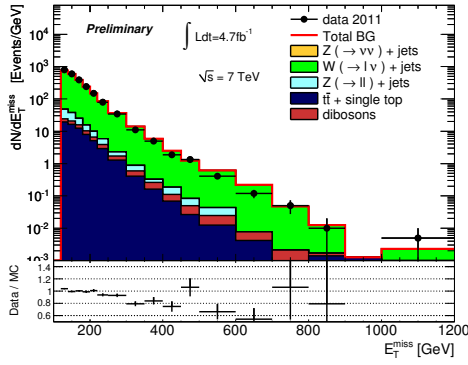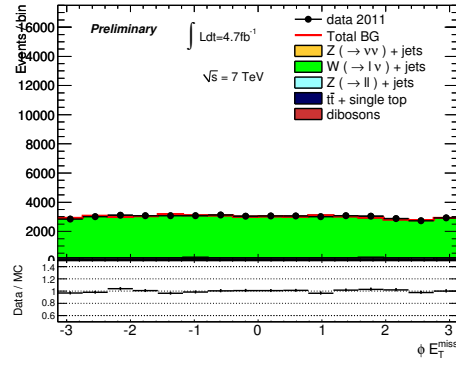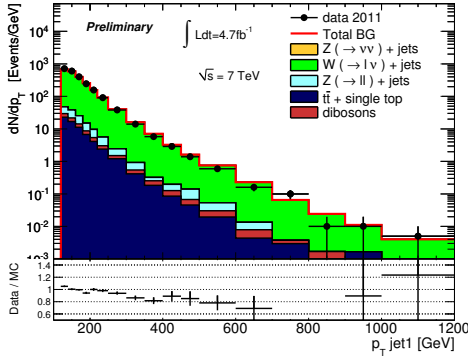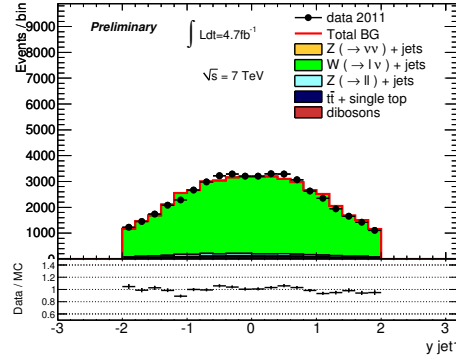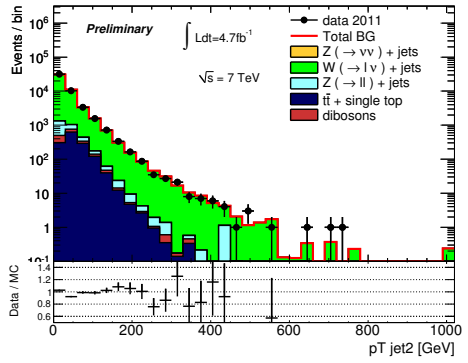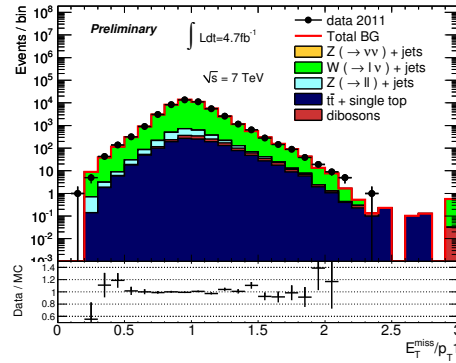
Figure 59: Kinematic distributions of the events in the exclusive $W \rightarrow \mu\nu$+jets control region for the selection cuts of region A (E_T^{miss}, jet1 p_T > 120 GeV). These plots make use of Alpgen W+jets and Z+jets samples.
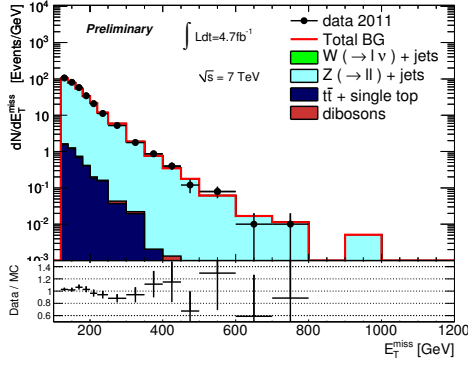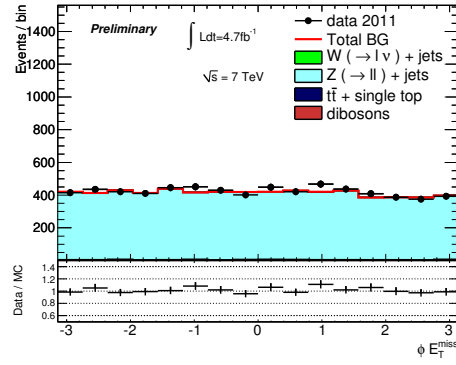
(a)   (b)
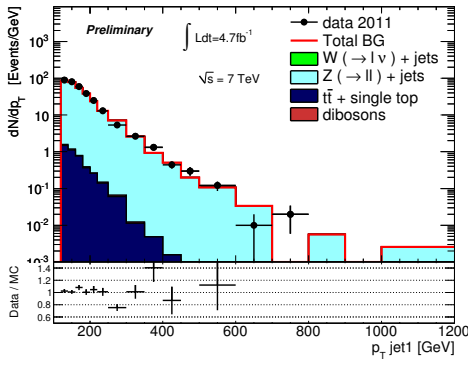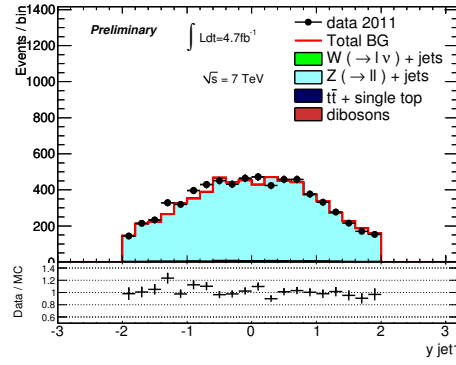
(c)   (d)
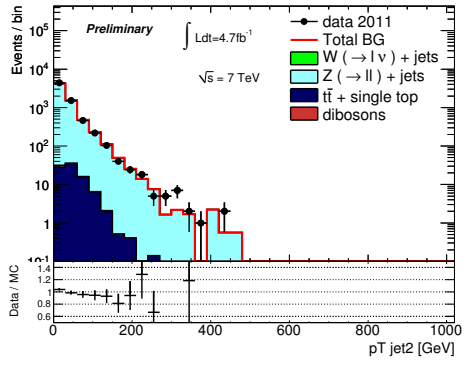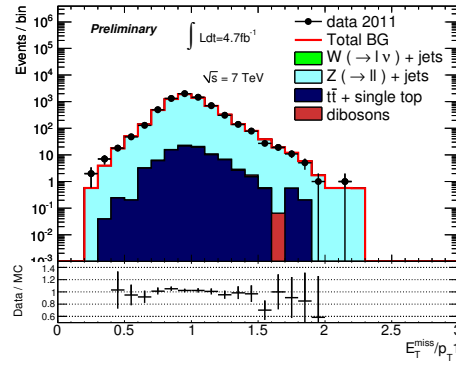
(e)   (f)

Figure 60: Kinematic distributions of the events in the exclusive $Z \to \mu\mu$ control region for the selection cuts of region A (E_T^{miss}, jet1 $p_T > 120\,GeV$). These plots make use of Alpgen W+jets and Z+jets samples.
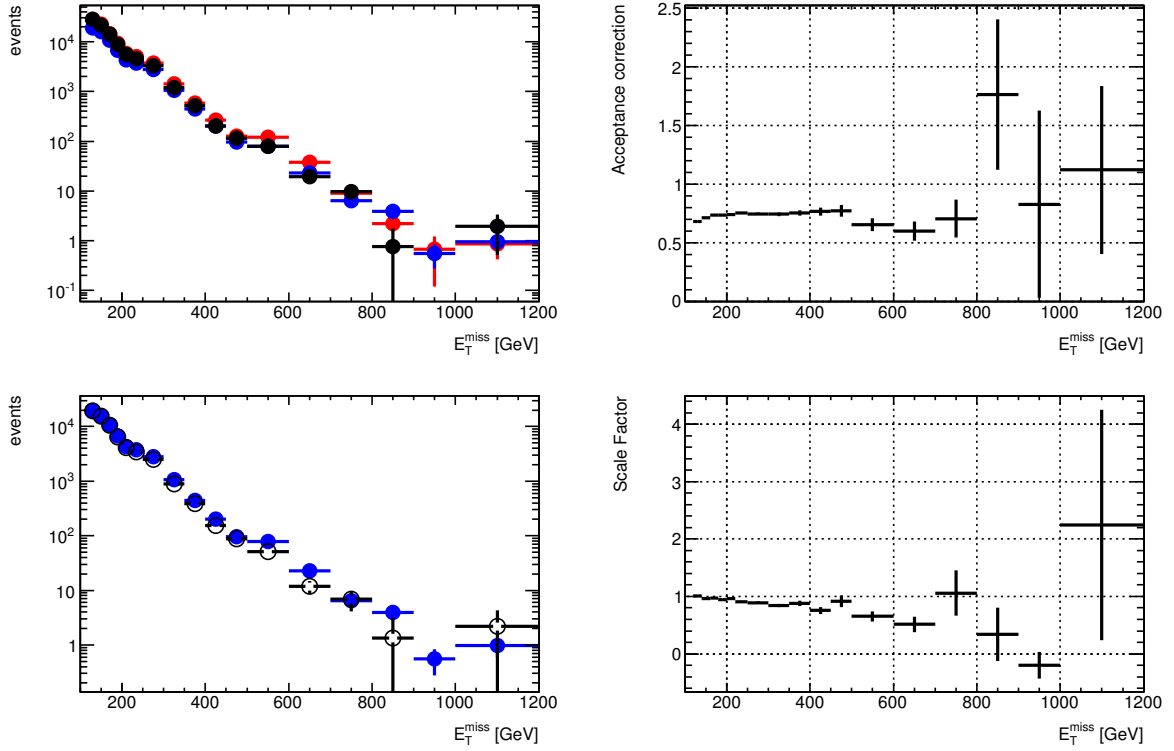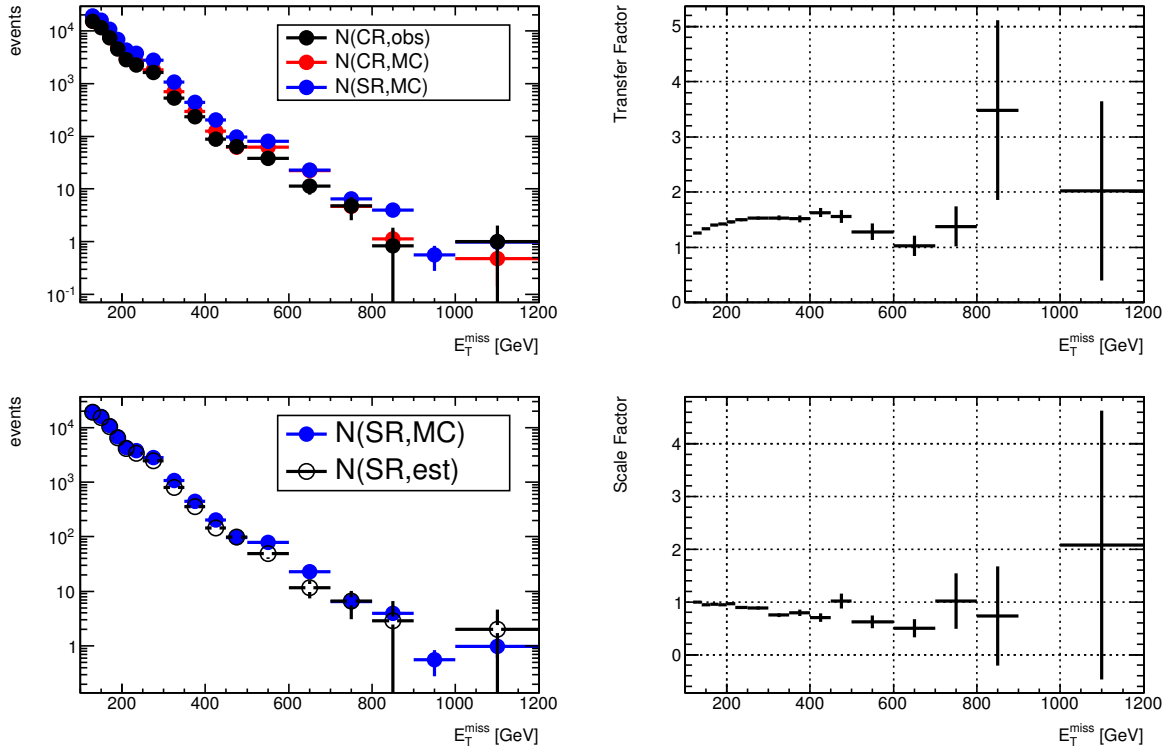
Figure 61: Top left plot shows the distribution of E_T^{miss} for the data (black) and the MC (red) in the muon control region and the $Z\nu\nu$ MC in the signal region (blue). The Top righ plot shows the acceptance corection from control region to signal region as described in the text. The bottom left plot shows the data driven $Z\nu\nu$ E_T^{miss} distribution (open circle) compared to the MC only prediction (blue). The bottom right plot shows the scale factors defined by data over MC in the control region as a function of E_T^{miss} (*these plots will be updated to include the legend*)
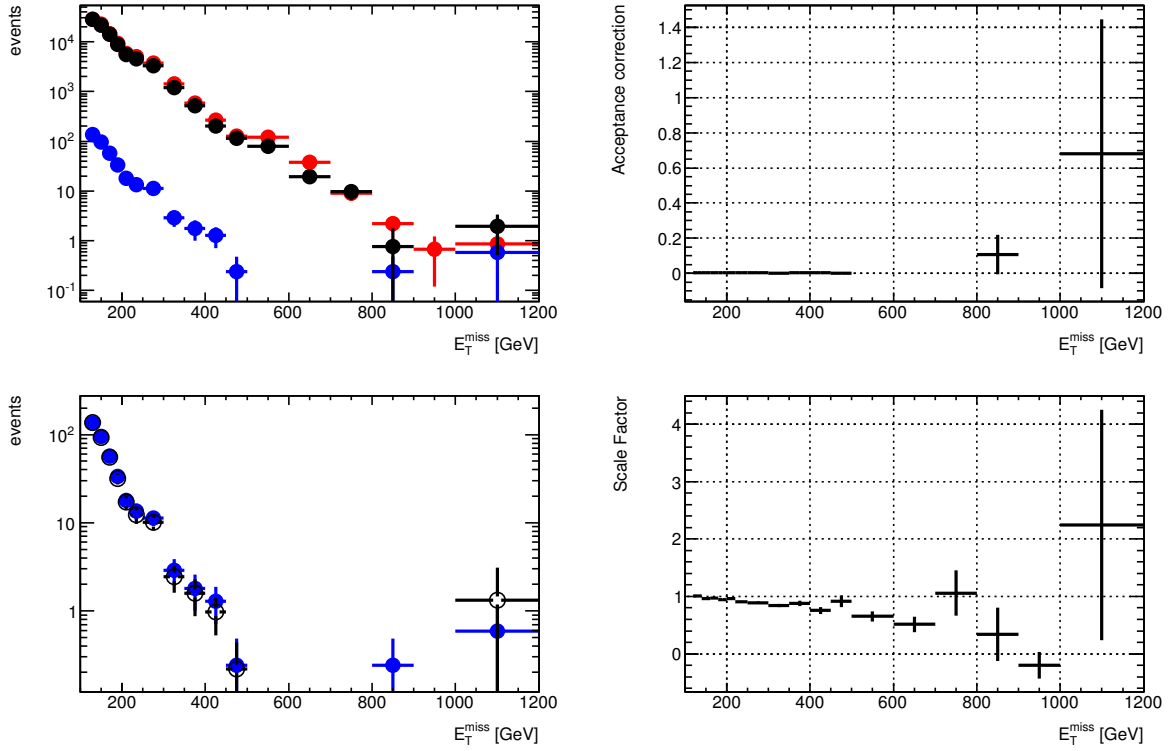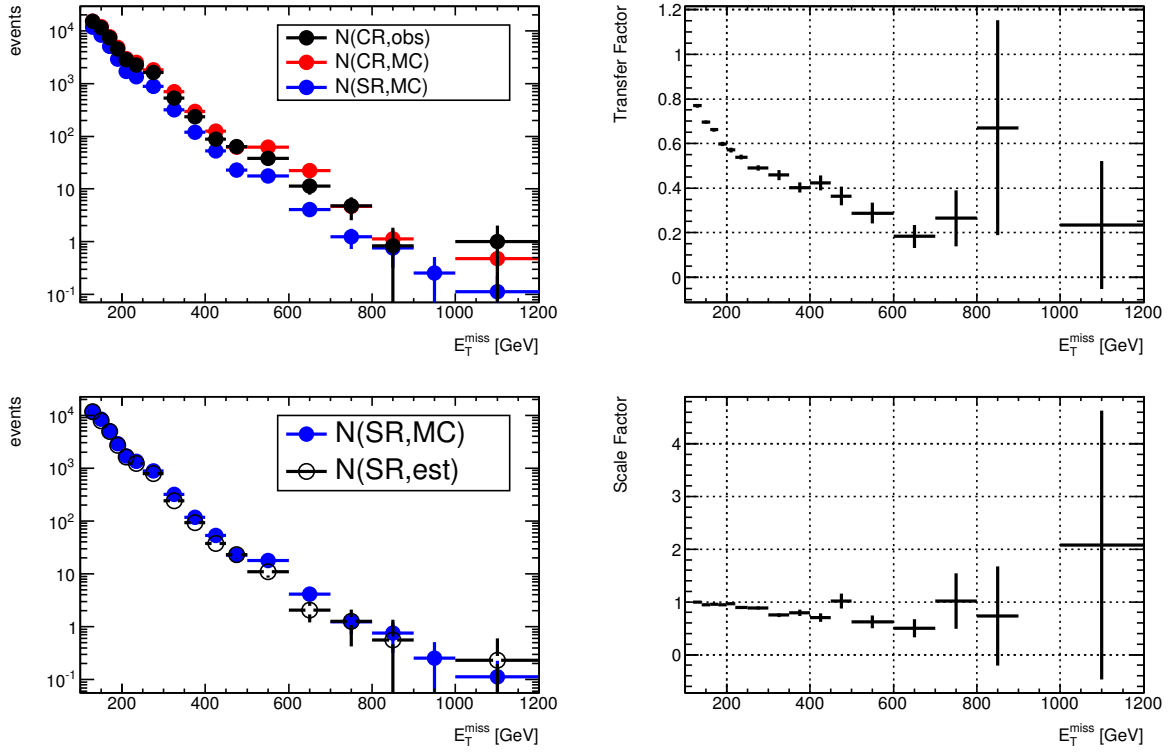
Figure 62: Top left plot shows the distribution of E_T^{miss} for the data (black) and the MC (red) in the muon control region and the $Z\mu\mu$ MC in the signal region (blue). The Top righ plot shows the acceptance corection from control region to signal region as described in the text. The bottom left plot shows the data driven $Z\mu\mu$ E_T^{miss} distribution (open circle) compared to the MC only prediction (blue). The bottom right plot shows the scale factors defined by data over MC in the control region as a function of E_T^{miss} (*these plots will be updated to include the legend*)
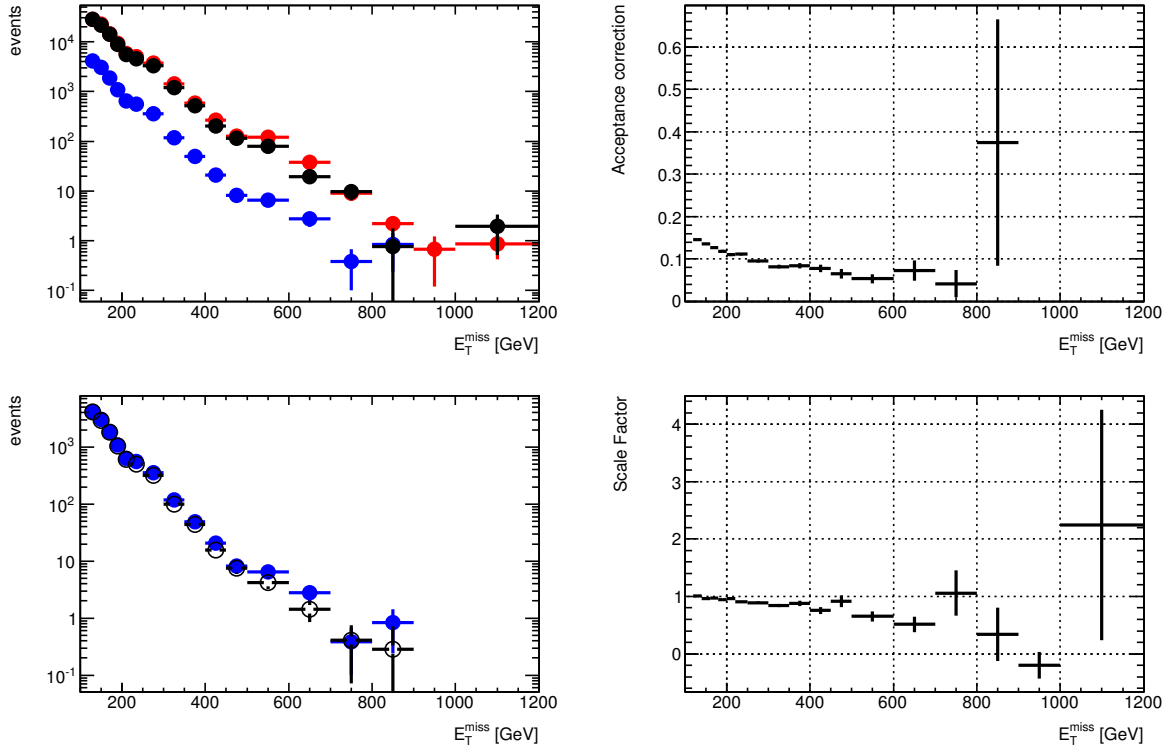
Figure 63: Top left plot shows the distribution of E_T^{miss} for the data (black) and the MC (red) in the muon control region and the $W\mu\nu$ MC in the signal region (blue). The Top righ plot shows the acceptance corection from control region to signal region as described in the text. The bottom left plot shows the data driven $W\mu\nu$ E_T^{miss} distribution (open circle) compared to the MC only prediction (blue). The bottom right plot shows the scale factors defined by data over MC in the control region as a function of E_T^{miss} (*these plots will be updated to include the legend*)
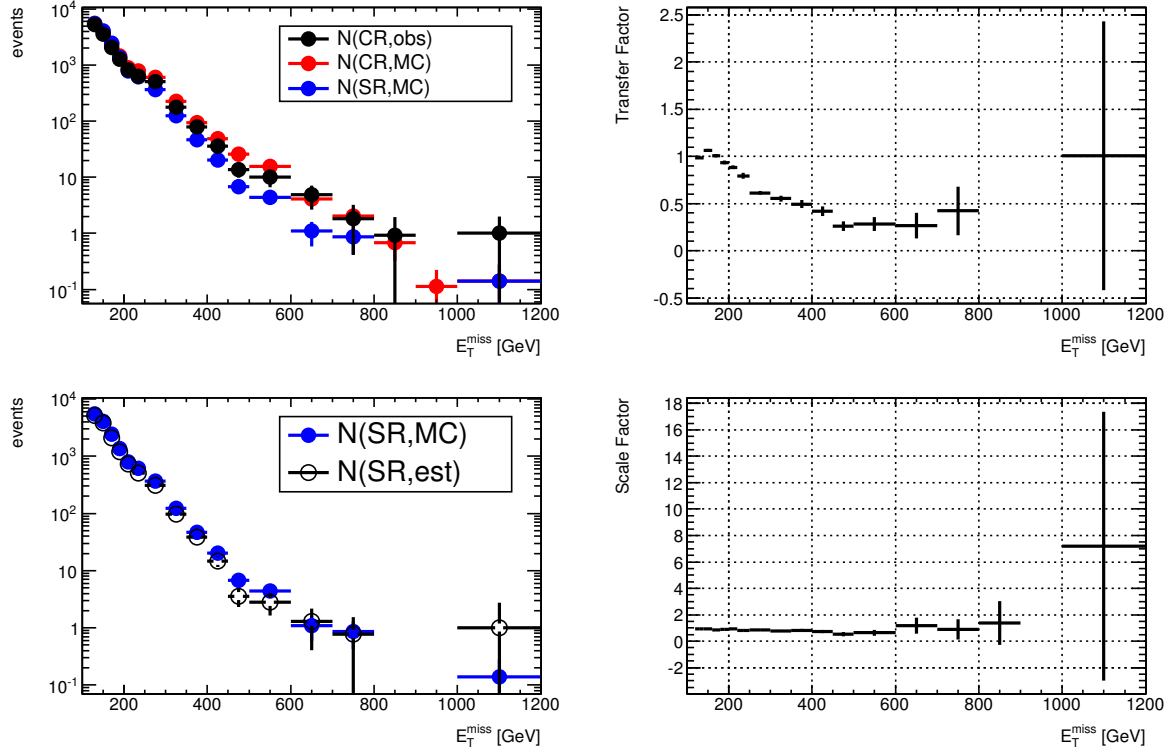
Figure 64: Top left plot shows the distribution of E_T^{miss} for the data (black) and the MC (red) in the electron control region and the *Wev* MC in the signal region (blue). The Top righ plot shows the acceptance corection from control region to signal region as described in the text. The bottom left plot shows the data driven *Wev* E_T^{miss} distribution (open circle) compared to the MC only prediction (blue). The bottom right plot shows the scale factors defined by data over MC in the control region as a function of E_T^{miss} (*these plots will be updated to include the legend*)
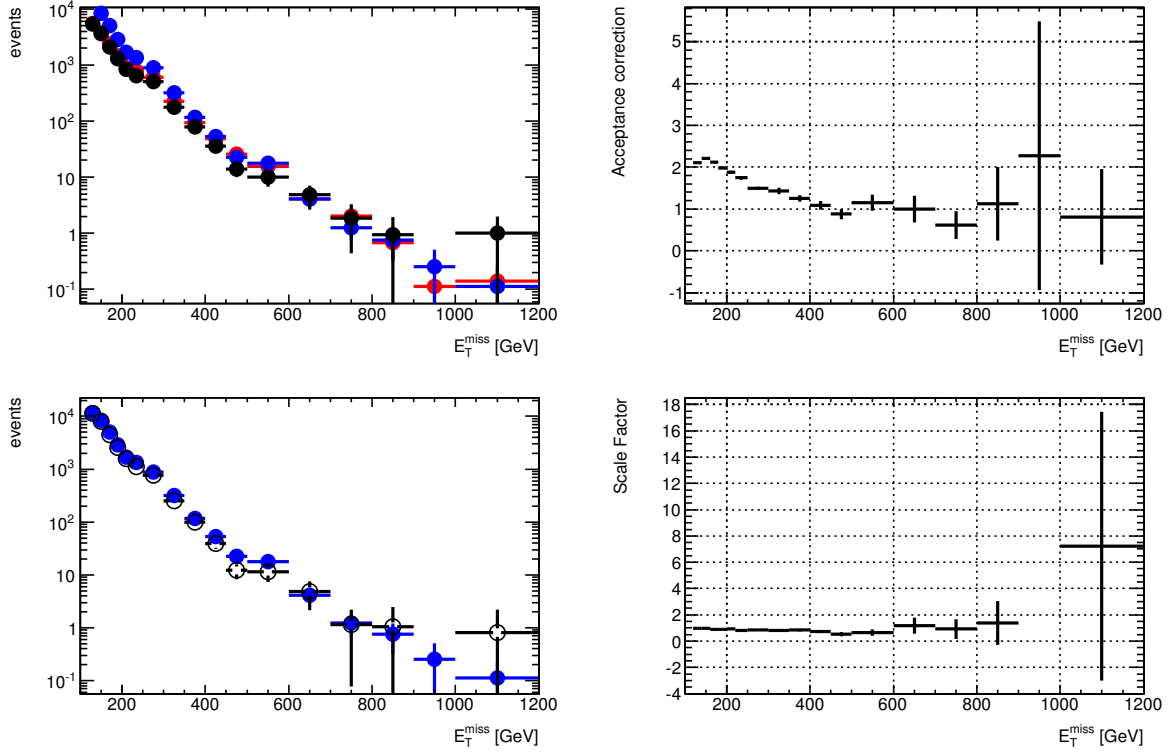
Figure 65: Top left plot shows the distribution of E_T^{miss} for the data (black) and the MC (red) in the electron control region and the $W\tau\nu$ MC in the signal region (blue). The Top righ plot shows the acceptance corection from control region to signal region as described in the text. The bottom left plot shows the data driven $W\tau\nu$ E_T^{miss} distribution (open circle) compared to the MC only prediction (blue). The bottom right plot shows the scale factors defined by data over MC in the control region as a function of E_T^{miss} (*these plots will be updated to include the legend*)
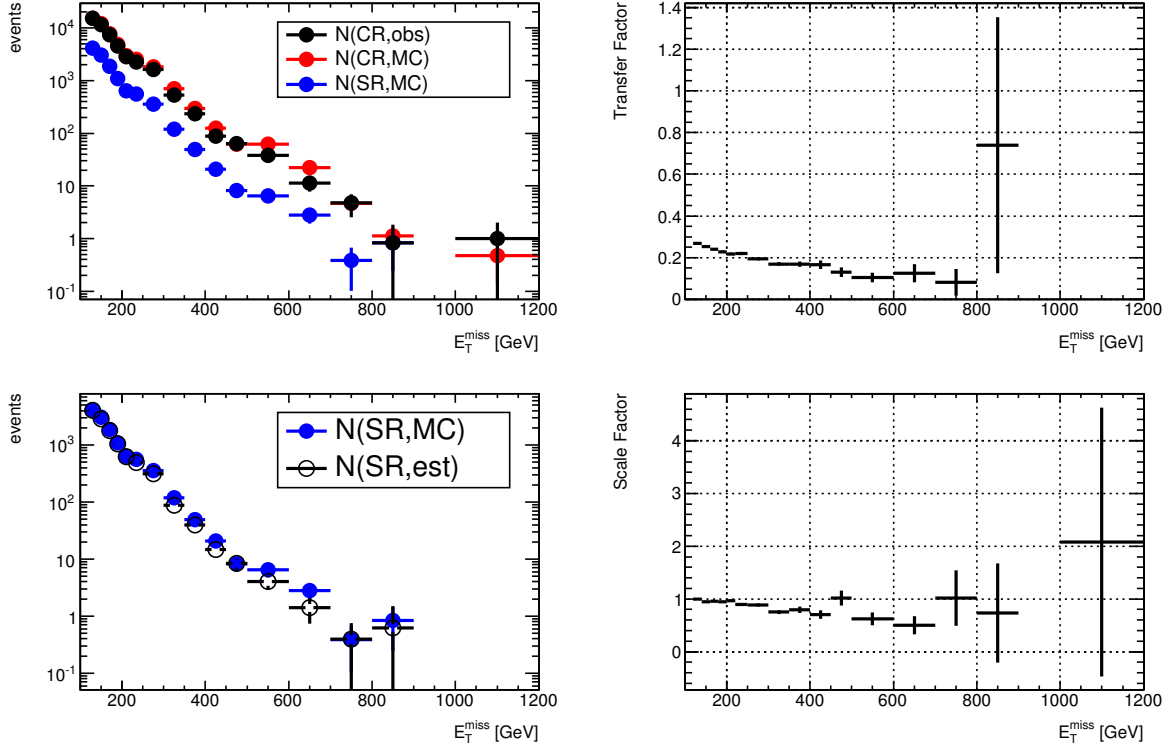
Figure 66: Top left plot shows the distribution of E_T^{miss} for the data (black) and the MC (red) in the W control region and the $W\mu\nu$ MC in the signal region (blue). The Top righ plot shows the acceptance corection from control region to signal region as described in the text. The bottom left plot shows the data driven $W\mu\nu$ E_T^{miss} distribution (open circle) compared to the MC only prediction (blue). The bottom right plot shows the scale factors defined by data over MC in the control region as a function of E_T^{miss}
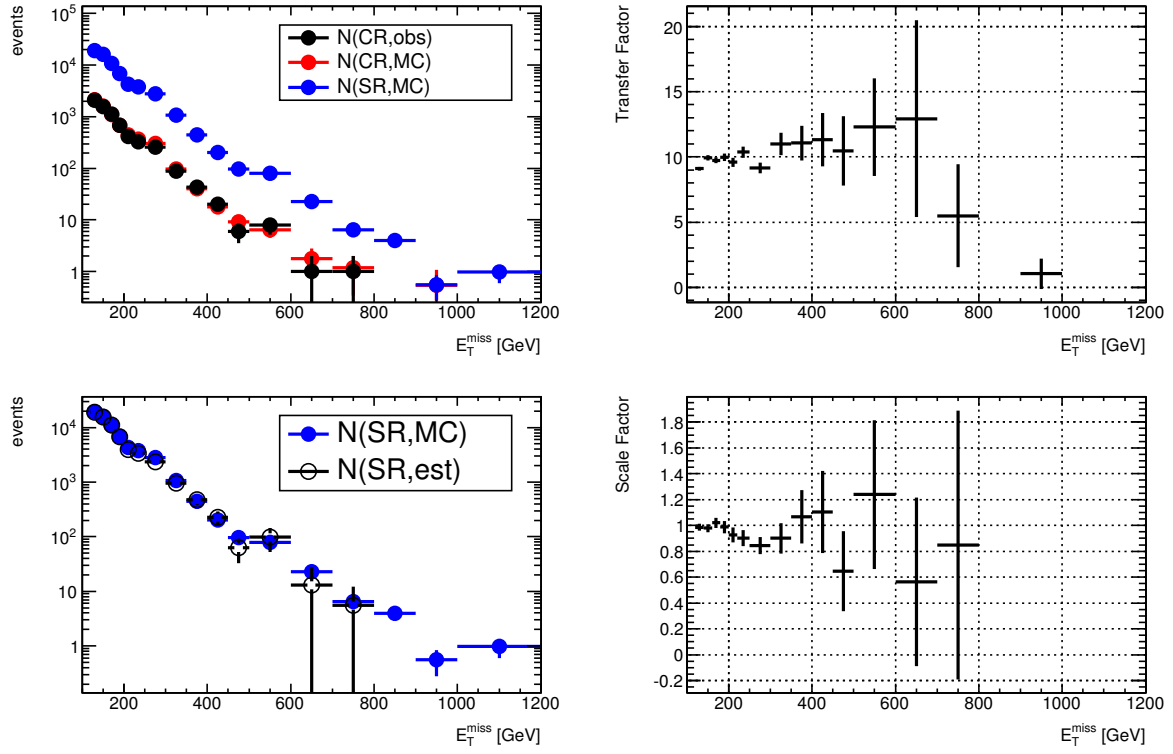
Figure 67: Top left plot shows the distribution of E_T^{miss} for the data (black) and the MC (red) in the Z control region and the $Z\nu\nu$ MC in the signal region (blue). The Top righ plot shows the acceptance corection from control region to signal region as described in the text. The bottom left plot shows the data driven $Z\nu\nu$ E_T^{miss} distribution (open circle) compared to the MC only prediction (blue). The bottom right plot shows the scale factors defined by data over MC in the control region as a function of E_T^{miss}

Figure 68: Top left plot shows the distribution of E_T^{miss} for the data (black) and the MC (red) in the *W* control region and the *Zνν* MC in the signal region (blue). The Top righ plot shows the acceptance corection from control region to signal region as described in the text. The bottom left plot shows the data driven *Zνν* E_T^{miss} distribution (open circle) compared to the MC only prediction (blue). The bottom right plot shows the scale factors defined by data over MC in the control region as a function of E_T^{miss}

Figure 69: Top left plot shows the distribution of E_T^{miss} for the data (black) and the MC (red) in the W control region and the $W\tau\nu$ MC in the signal region (blue). The Top righ plot shows the acceptance corection from control region to signal region as described in the text. The bottom left plot shows the data driven $W\tau\nu$ E_T^{miss} distribution (open circle) compared to the MC only prediction (blue). The bottom right plot shows the scale factors defined by data over MC in the control region as a function of E_T^{miss}
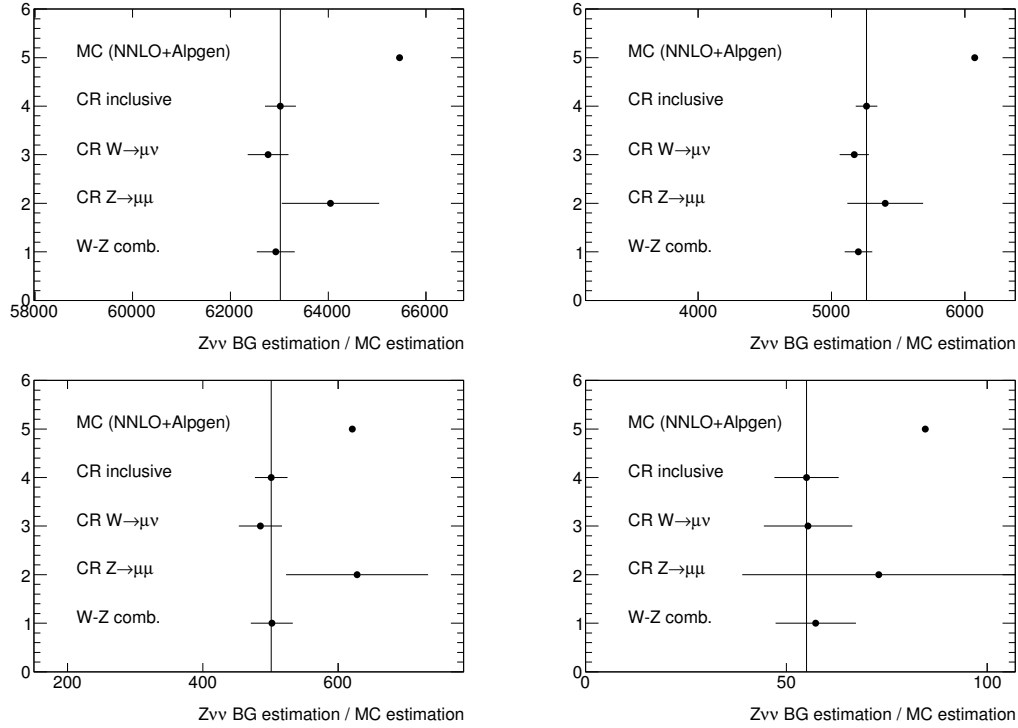
Figure 70: Comparison of *Zνν* estimations using different methods for the four signal regions. The E_T^{miss} and jet p_T increase from top to bottom and left to right.

These uncertainty are discussed in details in the next sections where the impact is discussed in terms of the analysis using the inclusive control regions. The table 52 below summarizes the systematic uncertainties on the electroweak background estimation for each of the analyses using either inclusive or exclusive control regions. In the case of the exclusive control regions, we present the results based on the $W \rightarrow \mu\nu$ control region and the combination with the $Z \rightarrow \mu\mu$ control region.

8.3.1 Uncertainties from jet energy (JES) scale and (JR)

We evaluate the impact due to the JES uncertainty by moving it up and down within the uncertainties provided by the `JESUncertaintyProvider` [13]. The MET_LocHadTopo is also varied according to the relative variation of an estimator of E_T^{miss} that is computed from the leading and next to leading jets, taking into account the $\Delta\phi(\text{jet1}, \text{jet2})$. As MET_LocHadTopo is computed using all topo-clusters up to $|\eta| < 4.5$, and not only the ones associated with the jets, the uncertainty from the unassociated topo-clusters with jets has to be evaluated. This is done by changing the topo-cluster energy scale according to the recommended method described in the supporting document of the W cross-section measurement [14]. The effect of this component on the transfer factors is negligible.

The total uncertainty due to JES on the final number of background events in the signal region is about 2% at low and moderate p_T. It is worth mentioning that the Monte Carlo predictions in the signal region and the control region both move by $O(20\%)$. Thus the 2% is the residual uncertainty after taking the ratio of the two MC numbers. At very large p_T the uncertainty increases up to 4% but reflected the limited MC statistics. The impact due to the JER uncertainty has been evaluated by smearing the jet p_T. The effect on the TF is negligible.

8.3.2 Uncertainties from lepton identification efficiencies

The systematic uncertainties from applying a veto on electrons and muons in the final state come from the difference of lepton identification efficiencies between data and MC. This systematic uncertainty is not absorved/reduced by the data-driven method because the variation of the identification efficiency implies a migration of events between the control region and the signal region. Therefore the ratio between the number of events in the two regions will either increase or decrease. The MC is corrected for difference between data and MC lepton efficiencies using lepton ID scale factor as dictated by ATLAS and the remaining uncertainties are propagated to the final result. This translates into a 0.8% to 3% uncertainty in the total background as the jet p_T and missing transverse energy increase in the case of the muon control region. Similarly, the uncertainty on the electron ID scale factors introduces an uncertainty on the total background that varies between 0.4% and 0.3%. The finaly systematic uncertainty on the TF due to the lepton ID uncertainy is taken as the quadratic sum of the two (muon and electron) components. It is about 1%, 1.5%, 2% and 3% for the four selection regions from the lowest to the the highest.

8.3.3 Uncertainties from background subtraction in control regions

In the lepton control regions there is a small contribution from the $t\bar{t}$, single top and di-bosons. These processes are subtraction from the control regions using Monte Carlo. The uncertainty on the subtraction propagates as an uncertainty on the number of data events in the control region, which leads to an uncertainty on the electroweak background determination in the signal region. A 20% fully correlated uncertainty is considered on the number of $t\bar{t}$, single top and di-bonsons. The full correlation is justified by the fact that the JES uncertainty (about 16%) is the dominant uncertainty on these backgrounds. This subtraction uncertainty results in about 1% uncertainty on the electroweak background in the signal regions.

8.3.4 Uncertainties on the parton shower modeling

An improvement of the analysis with respect to "EPS" is the release of the veto on the second jet. Thus the current analysis is expected to be much less sensitive to initial-state and final-state radiations because it will only play a role on the third jet, which is vetoed in this analysis.

In order to estimate the uncertainty on the final background due to the MC model used for multi-parton emissions, we repeated the whole analysis using Sherpa instead of Alpgen MC samples (see appendix C). This is motivated by the first comparisons between data, Alpgen and Sherpa predictions for the inclusive Z+jet production using 5 fb-1 of data, indicating large differences between Algen and Shepa at very large jet p_T[10]. We therefore consider this a conservative approach. The comparison between the resuls using Alpgen and Sherpa translates into a 1.6% ± 1% uncertainty on the total background estimation for the first signal region. Due to the severe lack of statistics in the Sherpa samples the comparison suffers from large uncertainties as one increases the E_T^{miss} and jet p_T thresholds. We carried out a second comparison where now the p_T distribution of the W/Z bosons in ALPGEN is reweighted to come closer to that in Sherpa. The comparison between the original ALPGEN predictions and the predictions from the modified ALPGEN is about 3% in the low p_T region. Unfortunately, the weights, as determined by the SUSY group, are rather flat in the W/Z p_T which invalidates the test for larger E_T^{miss} and jet p_T since the weight is taken the same for Ws and Zs and is eaten in the data-driven procedure. Therefore, we conservatively assumed a 3% uncertainty independent of E_T^{miss} and p_T for the different signal regions (see Figure 71.

Alternatively we explored the impact on the variations of renormalization/factorization scale Q and the jet-parton matching parameter kt_{fac} in modified ALPGEN Z/W+jets samples. The results are broadly

---

[10]as presented by Jean-Baptiste Sauvan at the SM Plenary Meeting on 08/03/12

compatible with those obtained using Sherpa but, unfortunately, the rather limited statistics in the modified Alpgen samples did not allow a meaninful result beyond the observation of large statistical fluctuations.

Inclusive control regions				
Systematics	Region A	Region B	Region C	Region D
JES and E_T^{miss}	1.5%	2.7%	3.7%	4.0%
Lepton identification efficiency	1%	1.5%	2%	3%
Background subtraction	1.0%	0.8%	0.8%	1.1%
Comparison with SHERPA	3.0%	3.0%	3.0%	3.0%
Exclusive Ws				
Systematics	Region A	Region B	Region C	Region D
JES and E_T^{miss}	2.2%	3.4%	3.8%	2.6%
Lepton identification efficiency	0.7%	1.1%	1.4%	2.4%
Background subtraction	1.1%	0.9%	1.0%	1.2%
Comparison with SHERPA	3.0%	3.0%	3.0%	3.0%
Combined Exclusive Ws and Zs				
Systematics	Region A	Region B	Region C	Region D
JES and E_T^{miss}	2.1 %	2.9%	3.9%	2.1%
Lepton identification efficiency	0.7 %	1.1%	1.4%	2.4%
Background subtraction	1.1 %	0.9%	0.9%	1.1%
Comparison with SHERPA	3.0 %	3.0%	3.0%	3.0%

Table 52: Summary of the systematic uncertainties on the electroweak background
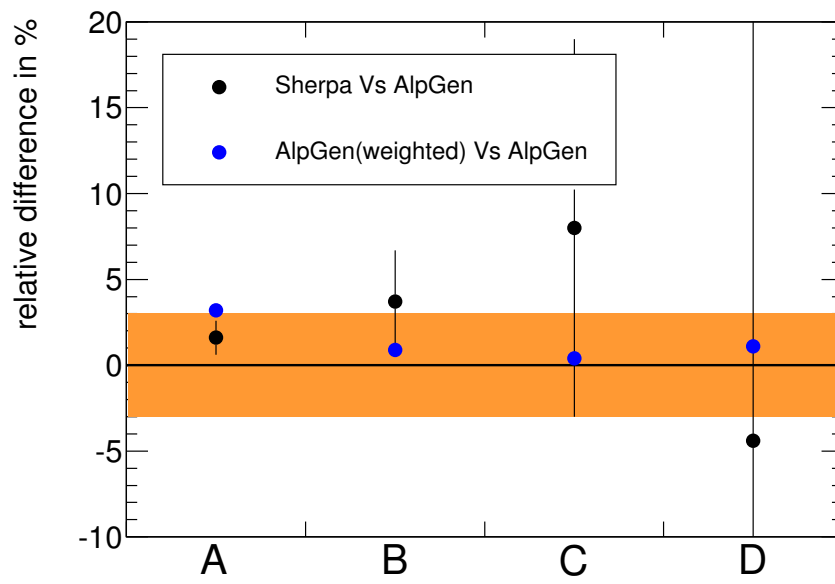
Figure 71: Detail of the estimation of the shower model dependence using Sherpa vs Alpgen comparison.

9   Data-driven QCD multi-jet background determination

The QCD background for our mono-jet event selection is expected to be relatively small compared to the electroweak backgrounds. Therefore its precise determination is not crucial and reaching an uncertainty $O(100\%)$ is sufficient to make sure that its effect on the total background determination is small.

QCD events enter the signal region when one or more jets are mis-measured or completely lost in dead regions of the detector. As represented in figure 72 there are two dominant configurations of QCD multijet events passing the selection cuts: di-jet and tri-jet. In both cases the E_T^{miss} points to the ϕ direction of the mis-measured jet. It is much more probable to mis-measure or loose only one jet than two or more jets in the same event. Therefore we neglect the QCD background contamination of loosing more then one jet.
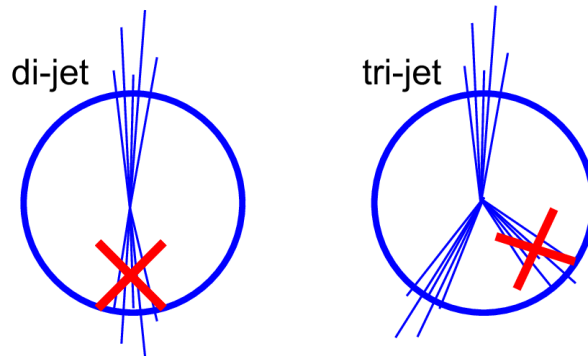
Figure 72: There are two dominant configurations for the QCD events entering in the signal region: di-jet events (left) and tri-jet events (right). In both cases the E_T^{miss} points to the direction of the mis-reconstructed jet. Configurations with more then one mis-measured jet in the same event are neglected.

The QCD background is estimated in a data-driven way by looking at the p_T spectrum of the mis-measured jet and extrapolating it below the 30 GeV threshold, hence in the signal region. For this estimation we first create two control regions dedicated to the estimation of the di-jet and tri-jet components separetely.

9.1   Di-jet control region

The di-jet control region is obtained applying the signal region selection but requiring a second jet with $p_T > 30$ GeV and $\Delta\phi(\text{jet2}, E_T^{miss}) \leq 0.5$. The distribution of $\Delta\phi(\text{jet2}, E_T^{miss})$ before the cut is shown in figure 73 (a). This region is ortogonal to the signal region and is dominated by QCD di-jet events, in which the mis-measurement of the second jet leads to a high E_T^{miss} ($E_T^{miss} > 120$ GeV).

Figures 74 and 75 show the distributions of the relevant quantities for the leading jet, second leading jet and the E_T^{miss} in the A selection (leading jet, $E_T^{miss} > 120$ GeV). For the comparison with data, the QCD Monte Carlo samples are initialy normalized to the PYTHIA LO cross section. A scale factor is retrieved, normalizing the QCD samples to the data after subtracting the non-QCD backgrounds. This leads to a normalization factor for the QCD Monte Carlo of 0.76.

Figure 76 shows the p_T of the second jet for data and for PYTHIA MC for A and B regions. For the A region a linear fit is used, while for the region B a fit to a constant was performed as it gives a conservative estimation. For regions C and D this background is considered negligible. The systematic

(a)

(b)
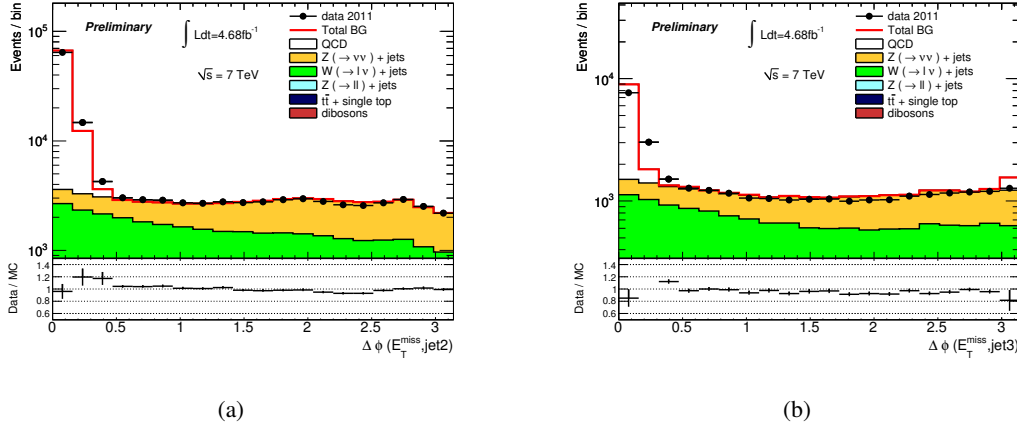
Figure 73: Figure (a) shows the distribution of $\Delta\phi(\text{jet2}, E_{\text{T}}^{\text{miss}})$ in a di-jet configuration. The events with $\Delta\phi \leq 0.5$ are used for the di-jet control region. Figure (b) shows $\Delta\phi(\text{jet3}, E_{\text{T}}^{\text{miss}})$ in events with a tri-jet configuration, and the events with $\Delta\phi \leq 0.5$ are used for the tri-jet control region.

uncertainty is obtained by varying the range of the fit and by changing the EW scaling factors with a 10% uncertainty. Results are shown in table 53.

	A	B	C	D
di-jet background	$757 \pm 28 \pm 643$	$64 \pm 8 \pm 64$	$8 \pm 3 \pm 8$	-
tri-jet background	$350 \pm 18 \pm 296$	-	-	-
total multi-jet	$1107 \pm 33 \pm 940$	$64 \pm 8 \pm 64$	$8 \pm 3 \pm 8$	-

Table 53: Results of the QCD background estimation.

9.2 Tri-jet control region

The tri-jet control region is obtained applying the signal region selection but requiring a third jet with $p_{\text{T}} > 30 \, \text{GeV}$, $\Delta\phi(\text{jet3}, E_{\text{T}}^{\text{miss}}) \leq 0.5$ and no fourth jets with $p_{\text{T}} > 30 \, \text{GeV}$. The distribution of $\Delta\phi(\text{jet3}, E_{\text{T}}^{\text{miss}})$ before the cut is shown in figure 73 (b). This region is ortogonal to the signal region and to the di-jet region previously defined. It's dominated by QCD tri-jet events, in which the mis-measurement of the third jet leads to a high $E_{\text{T}}^{\text{miss}}$ ($E_{\text{T}}^{\text{miss}} > 120 GeV$).

Figures 77 and 78 show the distributions of the relevant quantities for the first 3 leading jets and the $E_{\text{T}}^{\text{miss}}$ in the A selection (leading jet, $E_{\text{T}}^{\text{miss}} > 120 \, \text{GeV}$). As for the di-jet region plots, QCD Monte Carlo samples are normalized to the data. This leads to a normalization factor for the QCD Monte Carlo of 0.78.

Figure 79 shows the p_{T} of the third jet for data and for PYTHIA MC for A and B regions. For the A region is used a fit with a second degree polinome. For the regions B, C and D a fit to a constant was performed and the result are compatible with zero. Therefore this background for those regions is considered negligible. The systematic uncertainty is obtained in the same way as for the di-jet estimation. Results are shown in table 53.
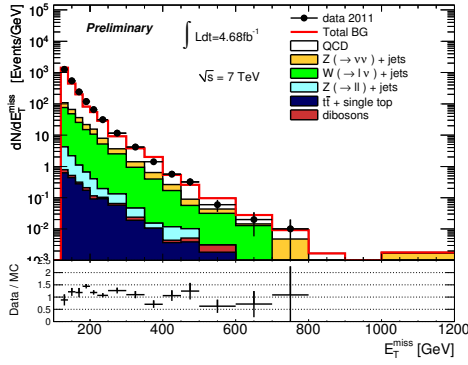
(a)
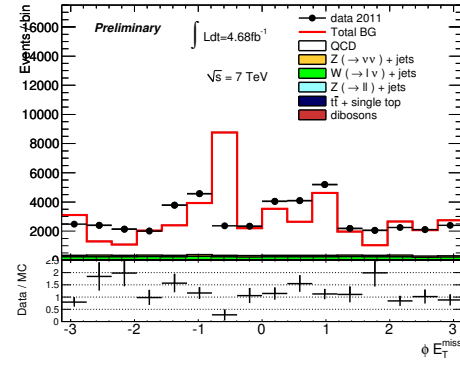
(b)
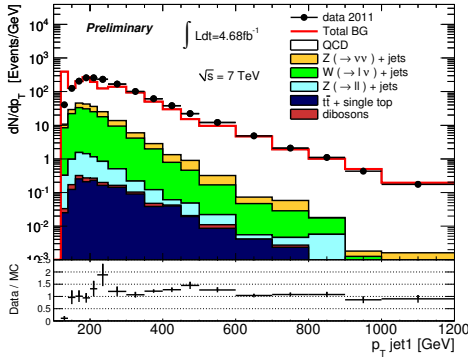
(c)
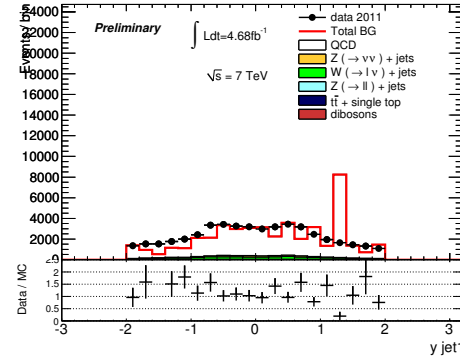
(d)

Figure 74: Distribution of E_T^{miss} (a), E_T^{miss} ϕ (b), leading jet p_T and rapidity (c)(d), in the di-jet QCD control region for the A selection (leading jet p_T, $E_T^{miss} > 120$ GeV).

(a)

(b)

(c)

(d)
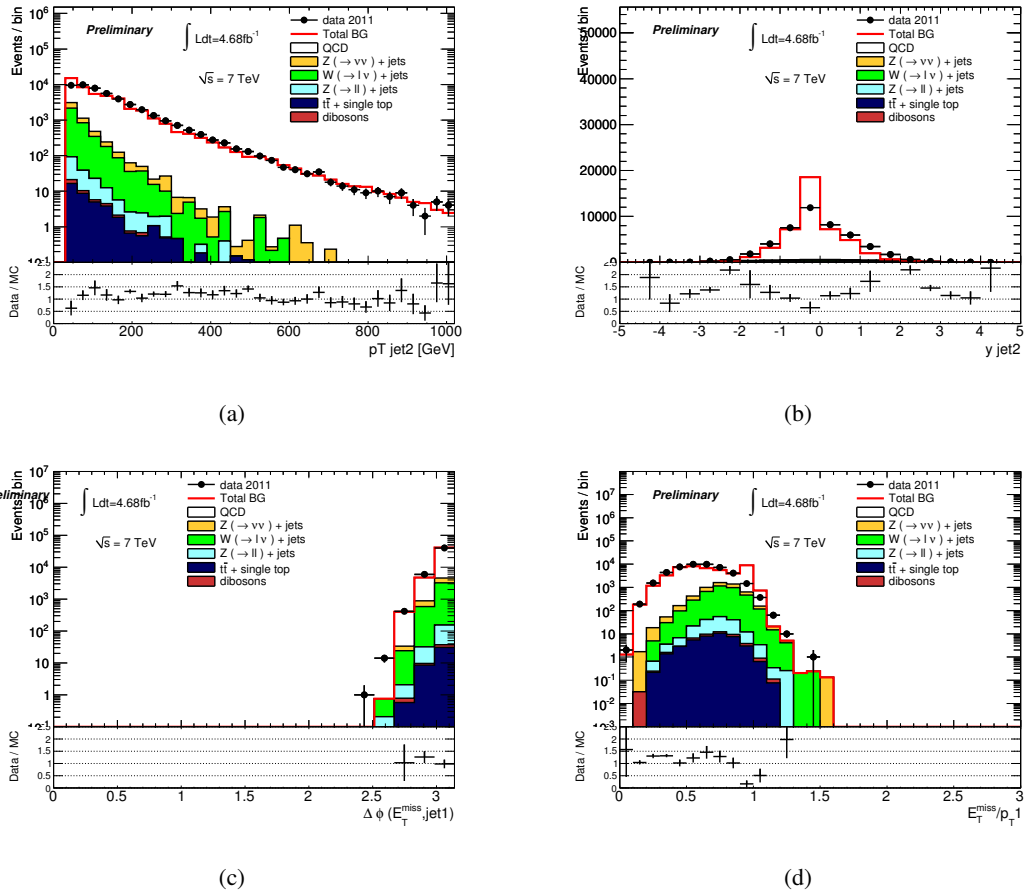
Figure 75: Distribution of second leading jet p_T and rapidity (a)(b), azimuthal direction difference between leading jet and E_T^{miss} (c), ratio between E_T^{miss} and leading jet p_T, in the di-jet QCD control region for the A selection (leading jet p_T, $E_T^{miss} > 120$ GeV).
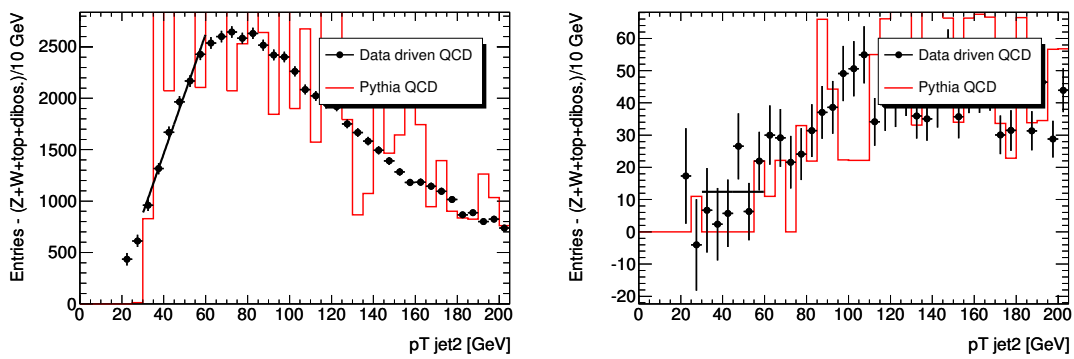
Figure 76: Transverse momentum of the second jet in the dijet events with the extrapolation to the signal region using linear fit for the region A (a), and a fit to a constant in region B (b). Z/W+jets,top and dibosons background are subtracted from the data, and data points can therefore be below zero. Note that the relevant part of the distribution is the region below 100 GeV.
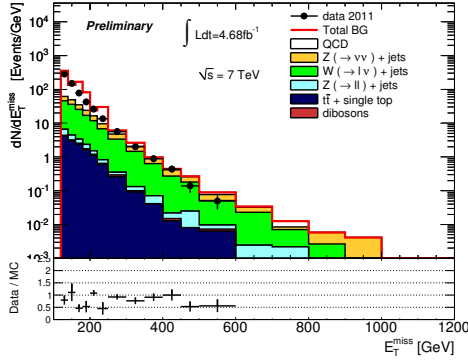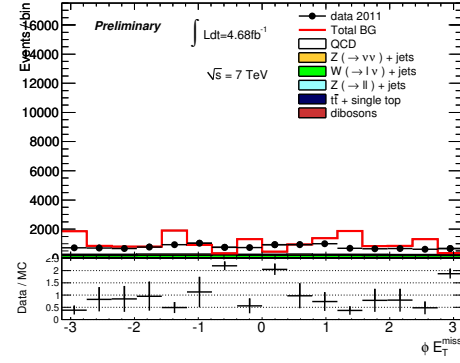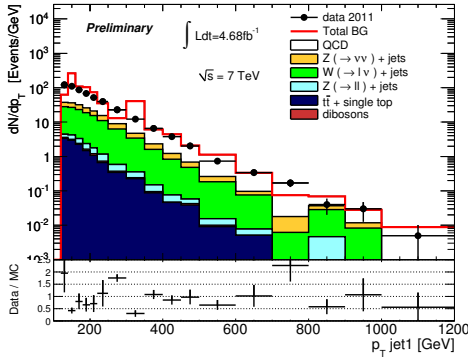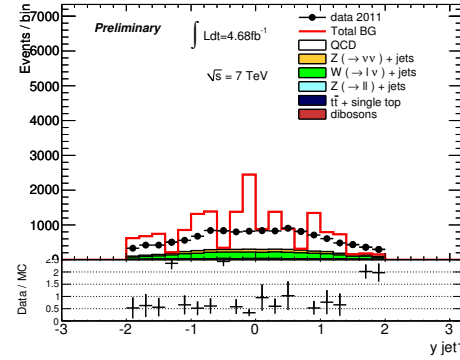
Figure 77: Distribution of E_T^{miss} (a), E_T^{miss} ϕ (b), leading jet p_T and rapidity (c)(d), in the tri-jet QCD control region for the A selection (leading jet p_T, $E_T^{miss} > 120$ GeV).

(a)

(b)

(c)

(d)
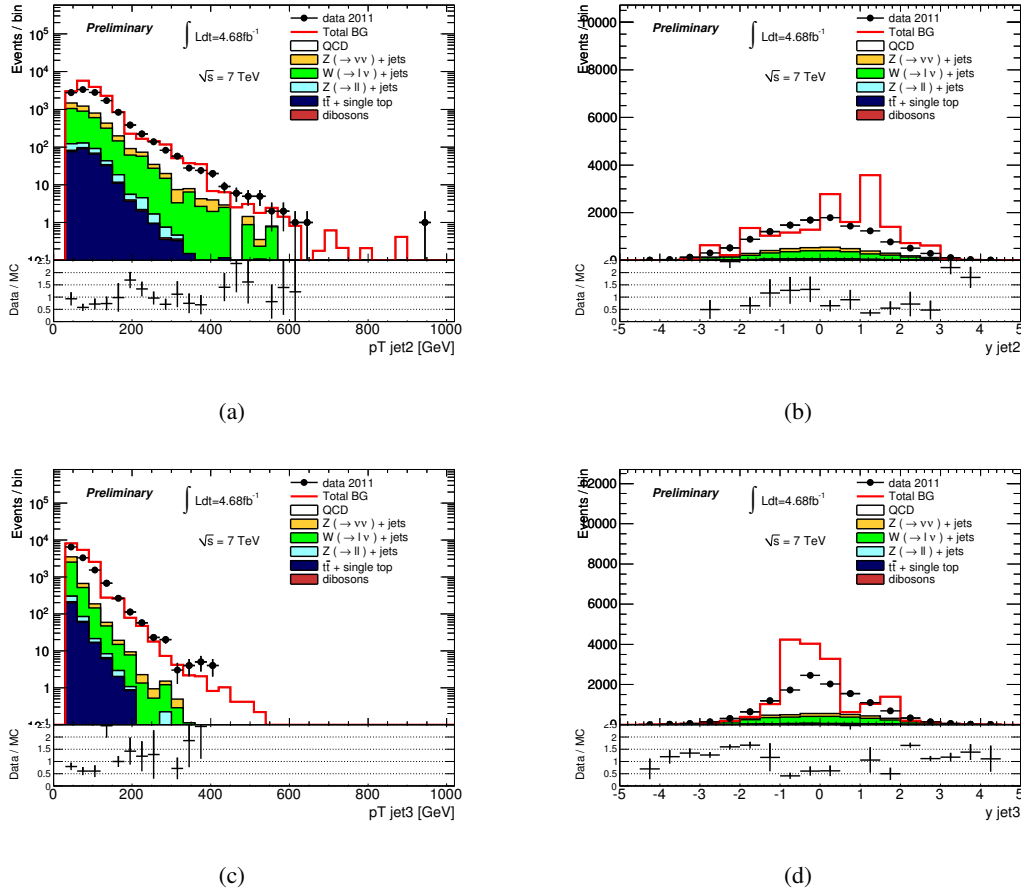
Figure 78: Distribution of second leading jet p_T and rapidity (a)(b), third leading jet p_T and rapidity (c)(d), in the tri-jet QCD control region for the A selection (leading jet p_T, E_T^{miss} > 120 GeV).
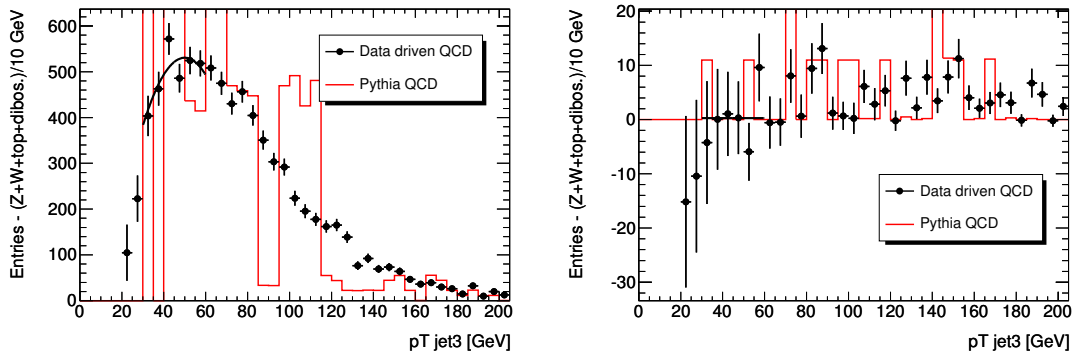
Figure 79: Transverse momentum of the third jet in the tri-jet events with the extrapolation to the signal region using linear fit for the region A (a), and a fit to a constant in region B (b). For region B the result of the extrapolation is compatible with zero. Therefore this contribution is considered negligible. Z/W+jets,top and dibosons background are subtracted from the data, and data points can therefore be below zero. Note that the relevant part of the distribution is the region below 100 GeV.

10 Data-driven non-collision background determination

The non-collision background in the monojet analysis is calculated using the Beam Background Identification Method [15]. It consists of various approaches to the beam halo identification in the unpaired bunch crossings as well as in the paired bunches where a beam halo muon can appear on top of a collision. The Beam Background Identification Method combines the information from the calorimeters (LAr, Tile) and muon detector (CSC, inner MDT end-caps) in order to identify a beam halo muon traversing the detector along the beam pipe.

The note [15] describe in detail all ways of detecting beam halo muons implemented in the Beam Background Identification Method. It is shown that the *two-sided method* has constant beam halo tagging efficiency as a function of jet p_T, η, ϕ and time, and therefore is the most suitable one for use in physics analyses. It has a tagging efficiency of $\epsilon = 16\%$ and a mis-identification probability of 10^{-5}. The non-collision background estimate in the signal region can then simply be obtained as $N_{\text{ncb}} = N_{\text{tagged}}^{\text{two-sided}}/\epsilon$.

As a cross-check, the *one-sided tight* method has been used. This method has slightly larger tagging efficiency of 25% and is the purest one among all the methods with a mis-identification probability $< 10^{-5}$. However, this method is only efficient in the central η region. It is shown that the charge fraction cut does not have constant fake jet rejection power in the whole η range [15]. Due to this fact an additional correction factor needs to be applied for the monojet analysis in order to obtain the non-collision background estimate. The final equation in this case is $N_{\text{ncb}} = N_{\text{tagged}}^{\text{one-sided tight}}/\epsilon \cdot 1.25$.

The note [15] describes in addition other approaches for the non-collision background estimates using the Beam Background Identification Method. The difference between these estimates is $\sim 5\%$. The measurement of beam halo rate described in the note shows a 10% difference between the beam halo rate in two samples from unpaired bunch crossigs, which can be taken as a systematic uncertainty. One sample is selected by unpaired isolated trigger, the other one by unpaired non-isolated trigger. Given that there are qualitative differences between the two samples (not only could there be a bunch-by-bunch effect of background levels, but the amount of spurious collisions in both samples may also vary and hence introduce a bias), 10% systematic uncertainty is to be considered conservative.

We assume furthermore that this estimate covers background from cosmic-ray muons, too. The rate of cosmic events in the paired bunch crossings is the same as in the unpaired bunch crossings, which are used to evaluate the efficiency of the beam halo tagging methods. Therefore, the efficiency already accounts for the cosmic background as well. No detailed study of this is available at the time of writing this note, hence we keep the conservative 10% systematic uncertainty.

Table 54 shows the final non-collision background estimates in the signal regions provided by the two-sided method. It also gives the number of tagged events in data and Monte Carlo. Beam halo muons are not simulated in Monte Carlo, therefore the number of tagged events there relates to the mis-identification probability of this method in Monte Carlo. Table 54 gives the results from the one-sided tight method. The numbers in both tables are compatible. The final non-collision background estimate is $575 \pm 60 \pm 57$, $25 \pm 13 \pm 3$, 0 and 0 in signal regions 1, 2, 3 and 4, respectively.

SR	$N_{\text{tagged}}^{\text{data}}$	$N_{\text{tagged}}^{\text{MC}}$	$N_{\text{ncb}} \pm \text{stat} \pm \text{sys}$
1	92	0.2	$575 \pm 60 \pm 57$
2	4	0	$25 \pm 13 \pm 3$
3	0	0	-
4	0	0	-

Table 54: Number of non-collision background events in the signal regions as estimated by the two-sided method which is used for the final non-collision background estimate. Number of identified events in data and Monte Carlo is also shown.

SR	$N_{\text{tagged}}^{\text{data}}$	$N_{\text{tagged}}^{\text{MC}}$	$N_{\text{ncb}} \pm \text{stat} \pm \text{sys}$
1	121	0	$605 \pm 55 \pm 60$
2	5	0	$25 \pm 11 \pm 3$
3	0	0	-
4	0	0	-

Table 55: Number of non-collision background events in the signal regions as estimated by the one-sided tight method. This method is used just for cross-checking the results provided by the two-sided method. Number of identified events in data and Monte Carlo is also shown.

11 Experimental results

11.1 Final results using the exclusive control regions

Table 56 summarises the total number of events for each background channel in the 4 signal regions, with its corresponding statistical (from data and MC) and total systematic uncertainties. The total systematic uncertainty on the total number of events in each regin is calculated after taking into account the correlations between different background channels. Presented are also the three predictions for $Z(\to \nu\nu)$ from the combination of the results of the 4 electron and muon channels.

Tables 57 - 60 list the contribution of individual sources of systematic uncertainty to the total number of background events in each signal region, corresponding to Bgd (1) - Bgd (4) presented in Table 56.

Figure 80 provides the comparisons between the selected Data and all the background, as function of $E_{\mathrm{T}}^{\mathrm{miss}}$, in the signal regions 1, 2, 3 and 4. In these plots, $Z(\to \nu\nu) + jets$ is determined using $W(\to \mu\nu) + jets$ events. ADD and WIMPs signal samples are shown in SR1 with given parameters, together with Data and background estimates. Figure 81 and 82 include similar comparisons between Data and background, as function of the leading and trailing jet p_{T}, respectively.

Combination of Z($\nu\nu$) predictions Four predictions for the contribution of the $Z\nu\nu$ background to the signal regions are available; two from the muon (W$\mu\nu$, Z$\mu\mu$) and two from the electron (W$e\nu$, Zee) control regions. In order to benefit from the higher statistics in some of these control regions, or the lower systematic uncertainties in some others, we investigate the gain of combining the 4 measurements. The combination is done using the Best Linear Unbiased Estimator (BLUE) method, as explained in Reference [16]. The uncertainties related to JES/$E_{\mathrm{T}}^{\mathrm{miss}}$, MC modeling, and f_{EW} are considered fully correlated among the four predictions, while the uncertainties due to SFs, and lepton energy scale and resolution are assumed to be fully correlated between the 2 predictions from Z($\mu\mu$) and W($\mu\nu$) , or from Z(ee) and W($e\nu$), and fully uncorrelated among the predictions from the electron and muon channels. The data statistical uncertainties are assumed to be uncorrelated among all the four predictions. When treating correlations among the MC statistical uncertainties, these uncertainties are further decomposed to the uncertaities on the numerators and denminators of various MC-based correction factors, due to the fact that the correlations among different channels are sometimes only on the denominator of the correction factor (e.g. correlations between W($\tau\nu$) and Z($\nu\nu$) background predictions from the W($\mu\nu$) control region), and sometimes only on the numerator of the factor (e.g. correlations between the two Z($\nu\nu$) predictions from the W and Z control regions).

	Background Predictions ± (data stat.) ± (MC stat.) ± (syst.)			
	Region 1	Region 2	Region 3	Region 4
$Z\nu\nu$ (W$\mu\nu$)	63166 ± 351 ± 347 ± 2059	5405 ± 99 ± 74 ± 225	505 ± 30 ± 19 ± 32	59 ± 9 ± 6 ± 5
$Z\nu\nu$ (Z$\mu\mu$)	63055 ± 931 ± 542 ± 2150	5137 ± 248 ± 127 ± 313	544 ± 83 ± 39 ± 49	75 ± 32 ± 16 ± 6
$Z\nu\nu$ (Comb W$\mu\nu$, Z$\mu\mu$)	63158 ± 332 ± 329 ± 2064	5399 ± 97 ± 72 ± 226	508 ± 28 ± 18 ± 34	60 ± 9 ± 6 ± 5
$Z\nu\nu$ (W$e\nu$)	62331 ± 386 ± 505 ± 3989	5299 ± 119 ± 85 ± 311	508 ± 31 ± 34 ± 30	53 ± 10 ± 8 ± 4
$Z\nu\nu$ (Zee)	63220 ± 899 ± 518 ± 3256	5312 ± 232 ± 118 ± 396	453 ± 64 ± 28 ± 34	72 ± 26 ± 10 ± 5
$Z\nu\nu$ (Comb W$e\nu$, Zee)	63049 ± 729 ± 434 ± 3287	5299 ± 103 ± 117 ± 313	493 ± 29 ± 26 ± 31	56 ± 10 ± 7 ± 4
$Z\nu\nu$ (Comb All)	63247 ± 348 ± 336 ± 2050	5400 ± 101 ± 74 ± 220	500 ± 20 ± 17 ± 31	58 ± 7 ± 5 ± 4
W$\tau\nu$	31442 ± 177 ± 195 ± 1006	1853 ± 35 ± 34 ± 65	133 ± 8 ± 7 ± 7	13 ± 2 ± 2 ± 1
W$\mu\nu$	11071 ± 62 ± 81 ± 563	704 ± 13 ± 15 ± 57	55 ± 3 ± 3 ± 4	6 ± 1 ± 1 ± -
Z$\tau\tau$	421 ± 7 ± 9 ± 22	15 ± 1 ± 2 ± 1	2 ± - ± 1 ± 1	-
Z$\mu\mu$	204 ± 3 ± 10 ± 16	8 ± - ± 2 ± 3	-	-
W$e\nu$	14611 ± 168 ± 121 ± 479	679 ± 28 ± 20 ± 25	40 ± 6 ± 4 ± 3	5 ± 2 ± 1 ± 1
Multi-jets	1100 ± 33 ± - ± 940	64 ± 8 ± - ± 64	8 ± 3 ± - ± 8	-
$t\bar{t}$+single t	1237 ± - ± 11 ± 247	57 ± - ± 3 ± 12	4 ± - ± 1 ± 1	-
Di-bosons	302 ± - ± 5 ± 61	29 ± - ± 1 ± 5	5 ± - ± 1 ± 1	1 ± - ± - ± -
NCB	575 ± 60 ± - ± 57	25 ± 13 ± - ± 3	-	-
Data	124703	8631	785	77
Bgd (1)	124129 ± 617 ± 633 ± 4184	8839 ± 150 ± 118 ± 372	752 ± 41 ± 28 ± 45	84 ± 12 ± 9 ± 6
Bgd (2)	124018 ± 987 ± 576 ± 4126	8571 ± 255 ± 133 ± 399	791 ± 85 ± 40 ± 56	100 ± 33 ± 16 ± 6
Bgd (3)	124121 ± 598 ± 612 ± 4185	8833 ± 148 ± 116 ± 373	755 ± 39 ± 27 ± 46	85 ± 12 ± 9 ± 6
Bgd (4)	124210 ± 618 ± 626 ± 4152	8834 ± 153 ± 120 ± 367	747 ± 32 ± 25 ± 44	83 ± 10 ± 7 ± 6

Table 56: [**For Approval**] Background contributions in the 4 signal regions, compared to Data. Background (1) - (4) refer to the total amount of background in the case where $Z\nu\nu$ is determined using W$\mu\nu$ events, Z$\mu\mu$ events, the combination of the two, and the combination of the 4 available predictions (from W$\mu\nu$, Z$\mu\mu$, W$e\nu$, and Zee events), respectively. The first, second, and third uncertainties correspond to the data statistical , MC statistical, and systematic uncertainties, respectively. The determination of the SM background referred to as Bgd (4) (full combination of all the EW channels) will be used for the calculation of the limits.

Systematic	Region 1	Region 2	Region 3	Region 4
JES-$E_{\mathrm{T}}^{\mathrm{miss}}$	1.07%	2.71%	4.99%	6.52%
μ energy scale and resolution	0.13%	0.02%	0.11%	0.90%
SF	0.39%	0.48%	0.53%	0.57%
MC modeling	2.92%	2.94%	2.94%	2.99%
f_{EW}	0.95%	0.96%	0.97%	0.99%
non-EW systematics	0.79%	0.74%	1.08%	0.24%
MC stat uncertainty	0.51%	1.33%	3.71%	10.88%
Total systematic uncertainty	3.41%	4.42%	7.05%	13.12%
data stat uncertainty	0.50%	1.70%	5.45%	14.78%

Table 57: Relative contribution of different sources of uncertainties to BG (1).

Systematic	Region 1	Region 2	Region 3	Region 4
JES-$E_\mathrm{T}^\mathrm{miss}$	0.89%	2.87%	6.23%	5.56%
μ energy scale and resolution	0.13%	0.02%	0.11%	0.91%
SF	0.45%	0.18%	0.41%	0.62%
MC modeling	2.92%	2.94%	2.94%	2.99%
f_{EW}	0.95%	0.96%	0.97%	0.99%
non-EW systematics	0.79%	0.76%	1.02%	0.20%
MC stat uncertainty	0.46%	1.56%	5.01%	16.50%
Total systematic uncertainty	3.36%	4.91%	8.64%	17.73%
data stat uncertainty	0.80%	2.98%	10.69%	32.68%

Table 58: Relative contribution of different sources of uncertainties to BG (2).

Systematic	Region 1	Region 2	Region 3	Region 4
JES-$E_\mathrm{T}^\mathrm{miss}$	1.08%	2.74%	5.14%	6.49%
μ energy scale and resolution	0.03%	0.02%	0.11%	0.85%
SF	0.38%	0.49%	0.49%	0.57%
MC modeling	2.92%	2.94%	2.94%	3.04%
f_{EW}	0.95%	0.96%	0.97%	0.99%
non-EW systematics	0.79%	0.74%	1.07%	0.24%
MC stat uncertainty	0.49%	1.32%	3.58%	10.24%
Total systematic uncertainty	3.41%	4.43%	7.08%	12.58%
data stat uncertainty	0.48%	1.68%	5.23	14.12%

Table 59: Relative contribution of different sources of uncertainties to BG (3).

Systematic	Region 1	Region 2	Region 3	Region 4
JES-$E_\mathrm{T}^\mathrm{miss}$	0.97%	2.64%	4.88%	5.81%
μ energy scale and resolution	0.03%	0.02%	0.08%	0.61%
SF	0.39%	0.46%	0.65%	0.68%
MC modeling	2.92%	2.94%	2.94%	3.03%
f_{EW}	0.96%	0.95%	0.66%	0.67%
non-EW systematics	0.79%	0.74%	1.08%	0.25%
MC stat uncertainty	0.50%	1.36%	3.37%	8.90%
Total systematic uncertainty	3.38%	4.38%	6.77%	11.12%
data stat uncertainty	0.50%	1.74%	4.28%	11.80%

Table 60: [**For Approval**] Relative contribution of different sources of uncertainties to BG (4).
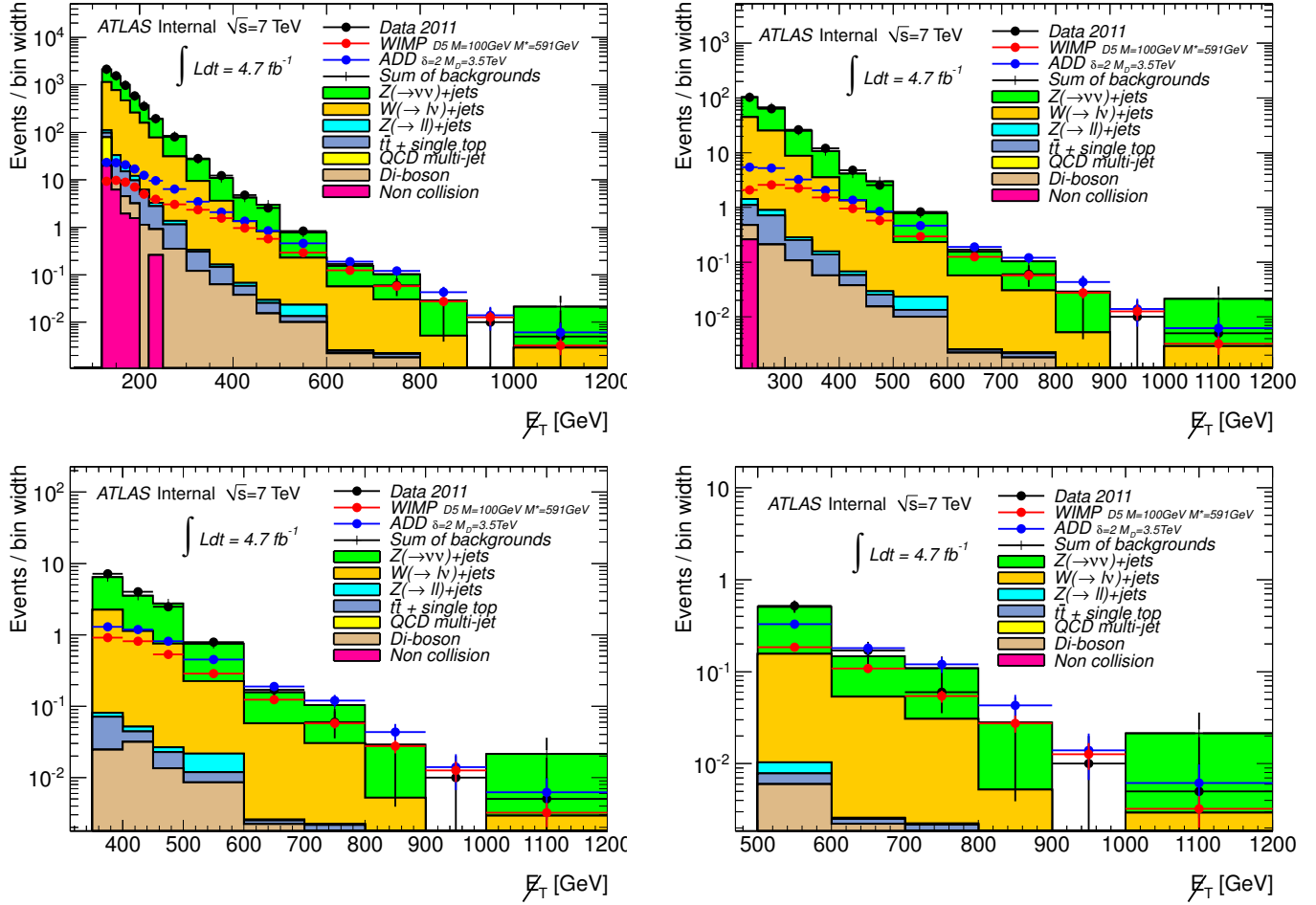
Figure 80: [**For Approval**] Comparisons between the selected Data and all the background, as function of the leading jet E_T^{miss}, in the signal regions 1 (upper left), 2 (upper right), 3 (lower left) and 4 (lower right). ADD and WIMPs signal samples are shown in region 1, with given parameters.
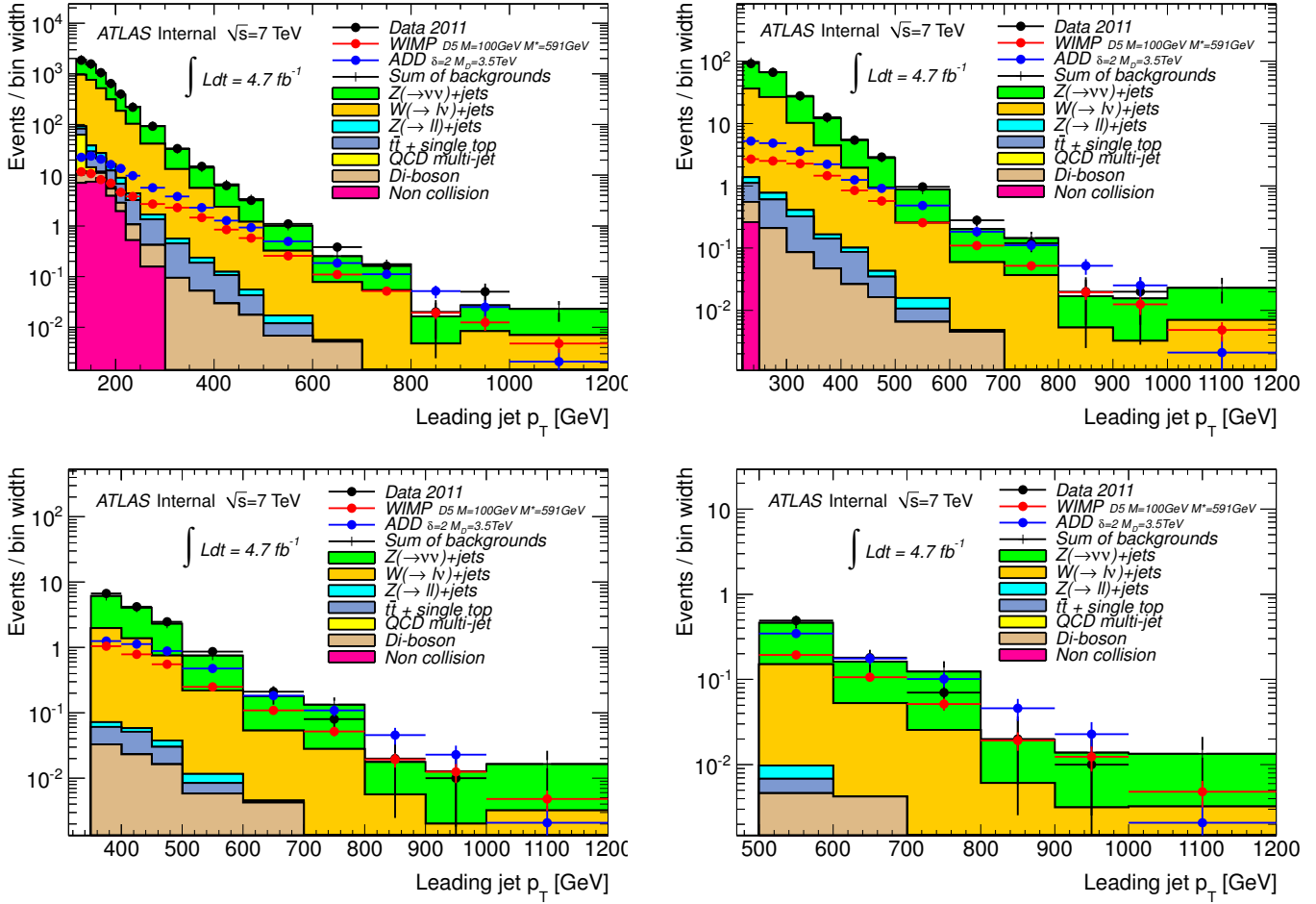
Figure 81: [**For Approval**] Comparisons between the selected Data and all the background, as function of the leading jet p_T, in the signal regions 1 (upper left), 2 (upper right), 3 (lower left) and 4 (lower right).
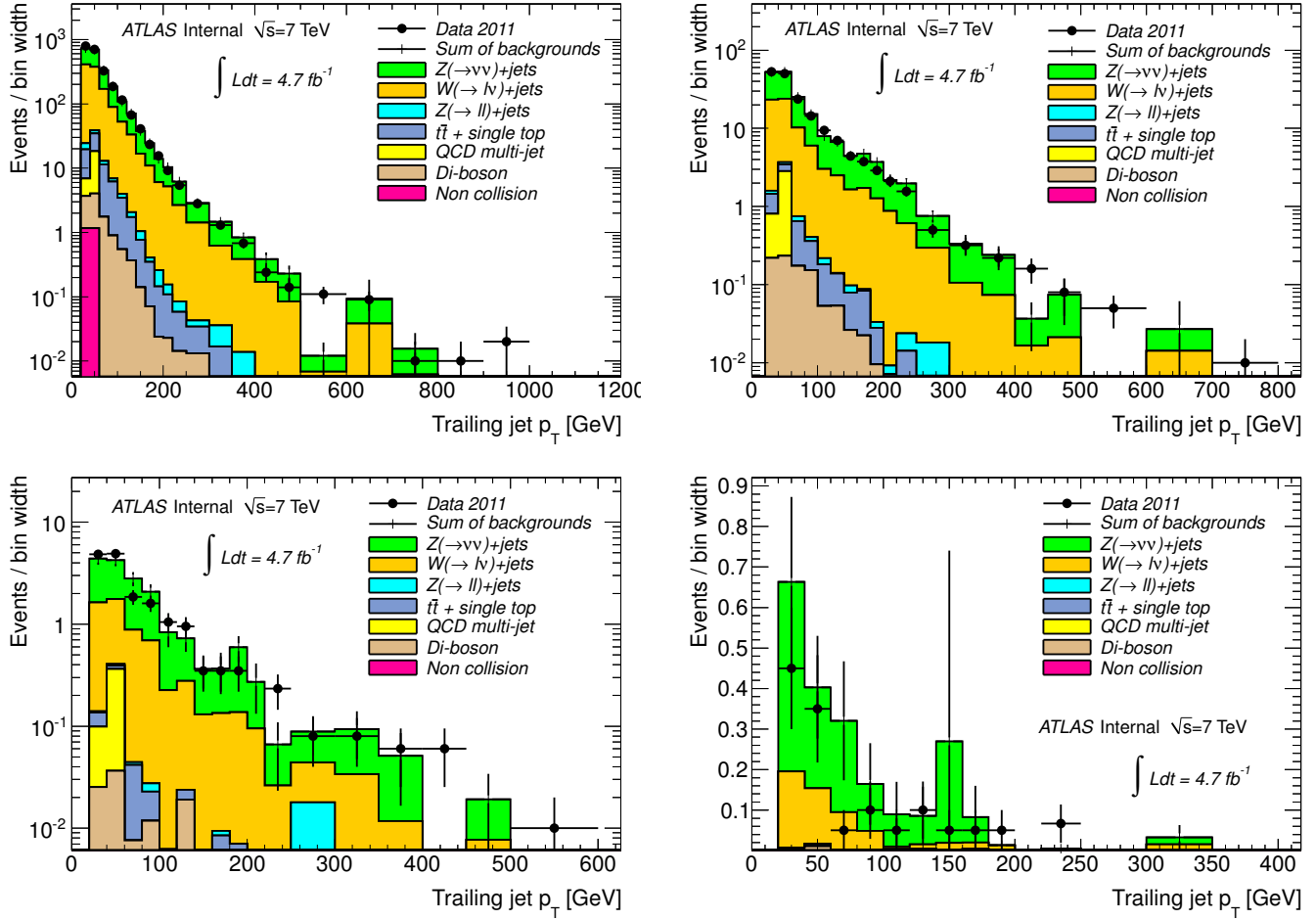
Figure 82: [**For Approval**] Comparisons between the selected Data and all the background, as function of the trailing jet p_T, in the signal regions 1 (upper left), 2 (upper right), 3 (lower left) and 4 (lower right).

11.2 Final results using Transfer Factors

Table 61 lists the expected number of background events and their statistical and systematic uncertainties for the four selection regions, as well as the total observed number of events in 4.7 fb^{-1} of data.

The determination of the electroweak processes and their systematic uncertainties have been discussed in details in the previous sections. Here we briefly remind that the final results were obtained with a data-driven method by measuring the electroweak distributions in $W \rightarrow \mu\nu$ and $Z \rightarrow \mu\mu$ exclusive control regions for which the results are then combined. The background contributions from $W \rightarrow e\nu$+jets, $Z \rightarrow \tau\tau$+jets, and $Z \rightarrow ee$+jets processes are determined using an electron inclusive control region. ALPGEN is used to provide the corrections from the control regions to the signal regions. The di-bosons contributions are estimated using Monte Carlo predictions from Sherpa and Herwig normalized to NLO calculation. The $t\bar{t}$ and single top are estimated using MC@NLO normalized to NLO/NNLL cross-section calculated for $m_t = 172.5$ GeV. The systematic uncertainties on the top and di-bosons are estimated taking the quadratic sum of the JES uncertainty (using the `JESUncertaintyProvider` [13]) and the luminosity uncertainty of 3.4% and a 10% uncertainty on the absolute cross-section. The QCD background and the non-collision background are estimated using data driven methods, which are explained in details in the following sections (Section 9 and Section 10).

The observed number of events in the four regions are compatible within the errors with the total expected number of background events. This agreement is remarkable giving the small uncertainties on the expected number of background events which are at the level of 4.0%, 4.8%, 7.7% and 17% for the four selection regions respectively.

These results constitute a precicion test for the Standard Model predictions since no significant excess above the expectation is observed.

Not reviewed, for internal circulation only

| | Background Predictions ± (stat.data)± (stat.MC) ± (syst.) | | | |
	Region A	Region B	Region C	Region D
$Z \to \nu\nu$+jets(from $W \to \mu\nu$ CR)	62770 ± 298 ± 290 ± 2988	5171 ± 89 ± 64 ± 253	485 ± 27 ± 17 ± 26	55 ± 9 ± 6 ± 2
$Z \to \nu\nu$+jets(from $Z \to \mu\mu$ CR)	64045 ± 792 ± 605 ± 2417	5403 ± 230 ± 166 ± 168	628 ± 83 ± 64 ± 40	73 ± 28 ± 20 ± 5
$Z \to \nu\nu$+jets (W-Z comb.)	62928 ± 279 ± 270 ± 2914	5202 ± 83 ± 61 ± 231	502 ± 26 ± 17 ± 27	57 ± 8 ± 6 ± 2
$W \to \tau\nu$+jets	31194 ± 138 ± 159 ± 1325	1779 ± 28 ± 30 ± 89	133 ± 7 ± 6 ± 5	13 ± 2 ± 2 ± 2
$W \to e\nu$+jets	13945 ± 121 ± 89 ± 557	687 ± 20 ± 19 ± 30	47 ± 4 ± 3 ± 3	5.4 ± 1.4 ± 1.2 ± 0.5
$W \to \mu\nu$+jets	11382 ± 50 ± 101 ± 520	692 ± 11 ± 18 ± 47	53 ± 3 ± 4 ± 6	6 ± 1 ± 1 ± 1
$Z \to \tau\tau$+jets	480 ± 4 ± 10 ± 17	20 ± 1 ± 2 ± 2	2.4 ± 0.2 ± 0.7 ± 0.5	0.7 ± 0.2 ± 0.6 ± 0.3
$Z \to \mu\mu$+jets	357 ± 2 ± 15 ± 13	22 ± 0 ± 3 ± 2	2.1 ± 0.1 ± 0.8 ± 0.1	0.6 ± 0.1 ± 0.4 ± 0.1
$Z \to ee$+jets	0.5 ± 0.5 ± 0.1	–	–	–
Multi-jets	1107 ± 33 ± 940	64 ± 8 ± 64	8 ± 3 ± 8	–
$t\bar{t}$ + single t	1257 ± 11 ± 251	59 ± 2 ± 12	6 ± 1 ± 1	1.3 ± 0.3 ± 0.3
Di-bosons	289 ± 3 ± 58	27 ± 1 ± 5	4.3 ± 0.4 ± 0.9	0.9 ± 0.2 ± 0.2
Non-collision background	575 ± 60 ± 57	25 ± 13 ± 3	–	–
Total background	123514 ± 491 ± 460 ± 4887	8578 ± 125 ± 92 ± 382	758 ± 36 ± 23 ± 40	84 ± 11 ± 8 ± 4
Data	124724	8632	785	77

Table 61: Summary of background estimations and total number of observed events in 4.7 fb^{-1} of data for the four mono-jet selection regions. The estimation of the EWK background correspond to the combination of the results obtained in the W and Z exclusive control regions. In cases where both data and MCs play a role in the statistical errors, the two contributions are shown separated as second and third uncertainties. The last quoted uncertainty is the systematic uncertainty.
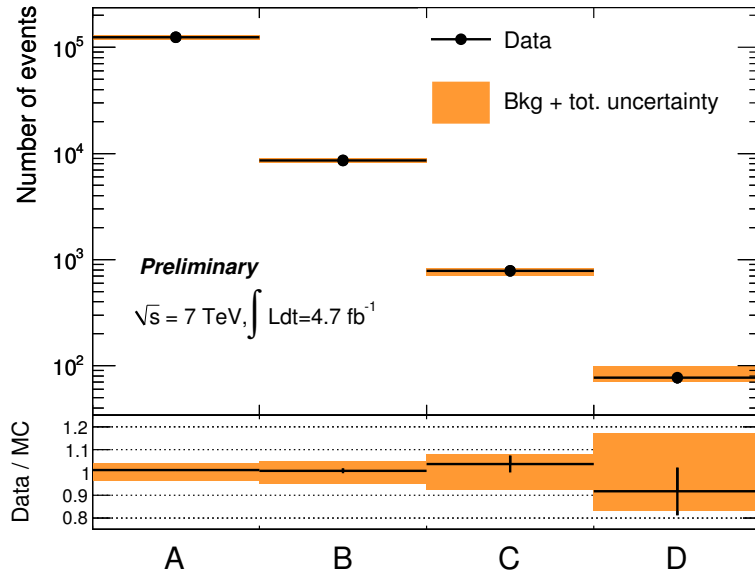
Figure 83: Comparison of the number of observed events in 4.7 fb^{-1} of data to the expected number of background events in the four analysis regions. The total uncertainties on the expected number of background events is also shown.
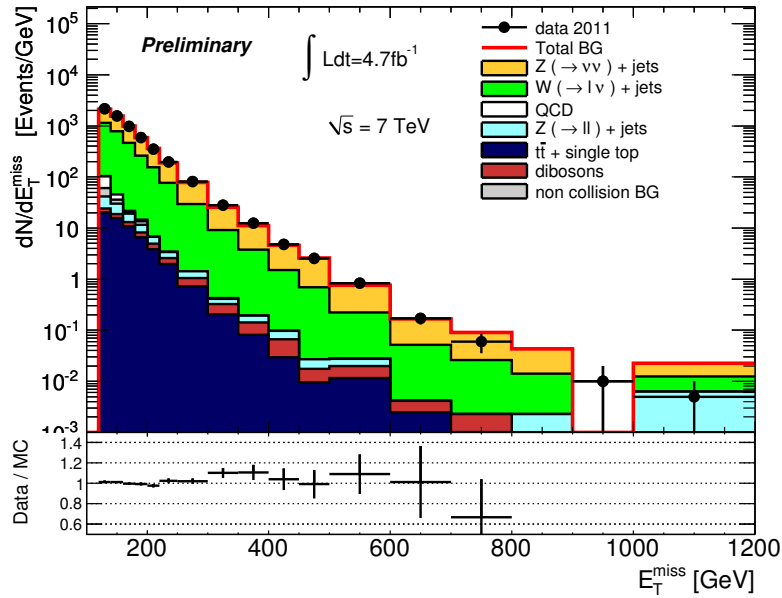
Figure 84: Data and Monte Carlo comparison in Region A.
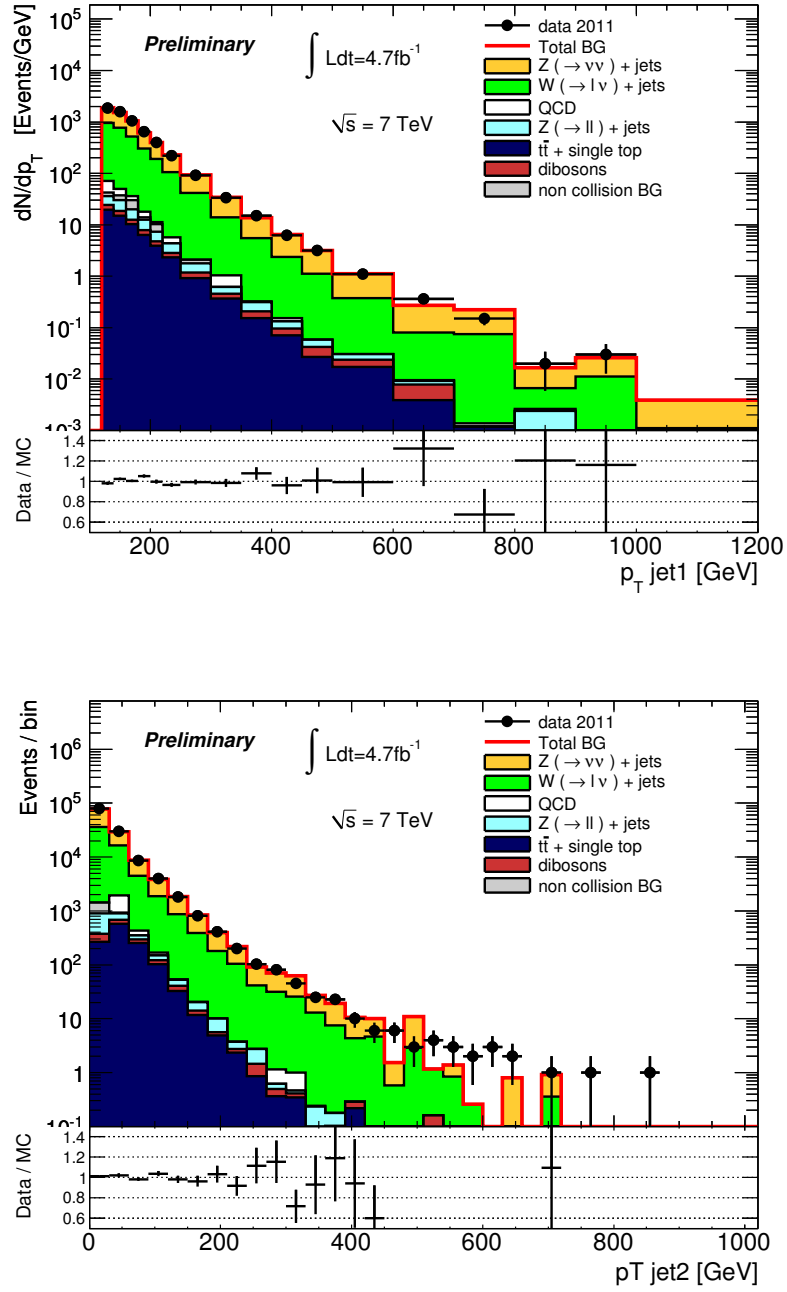
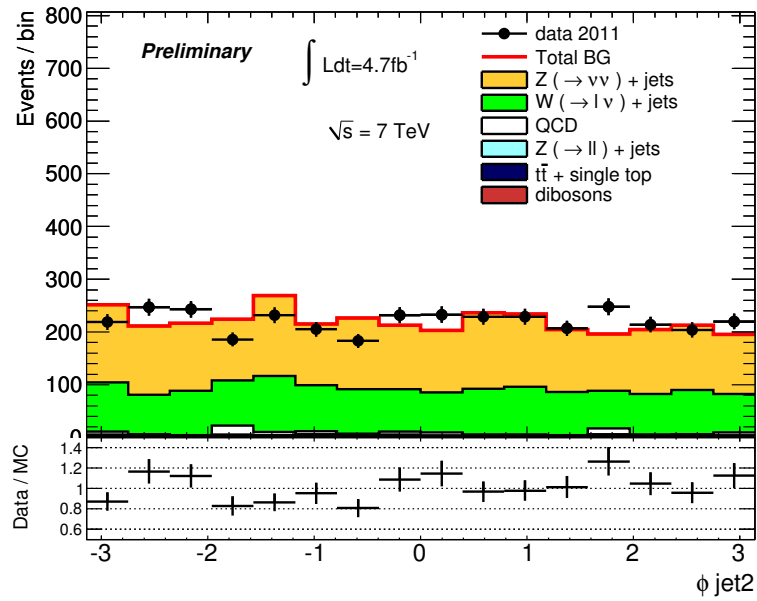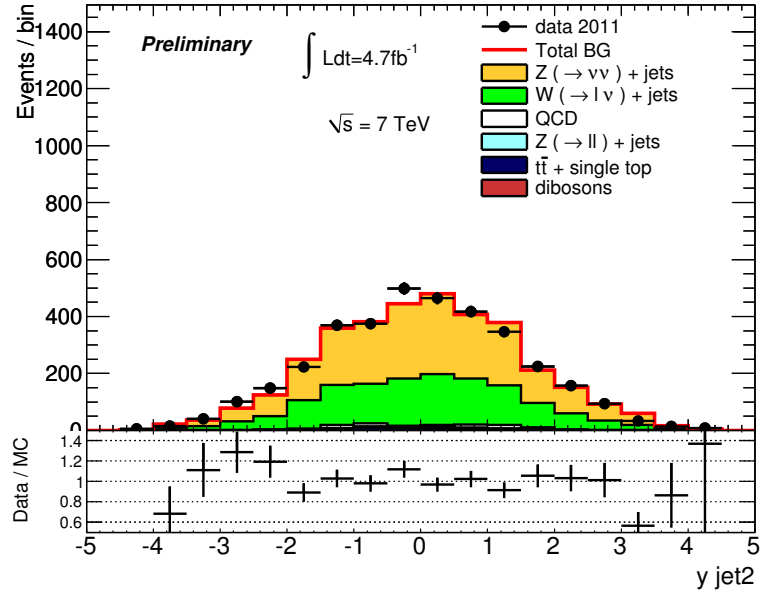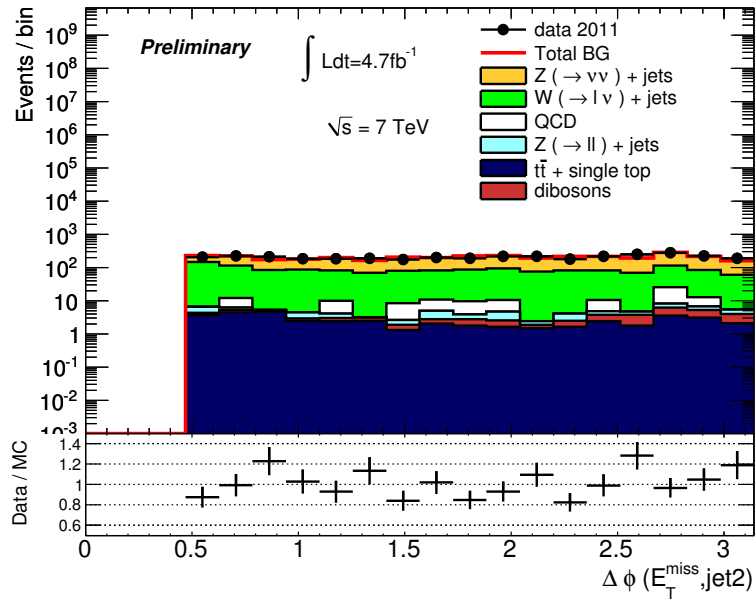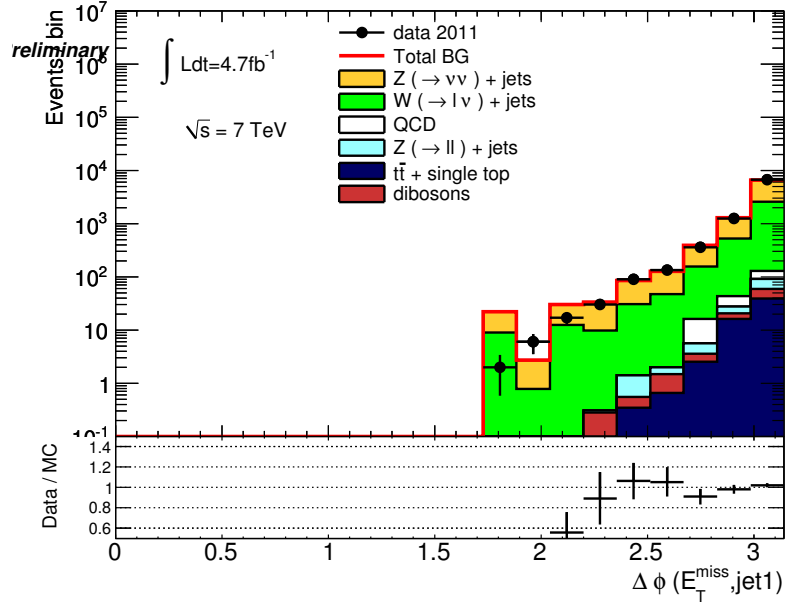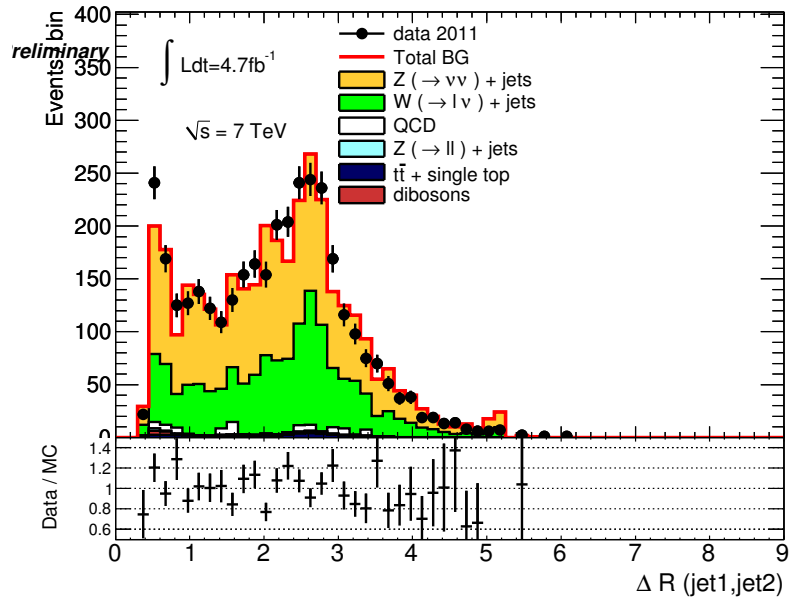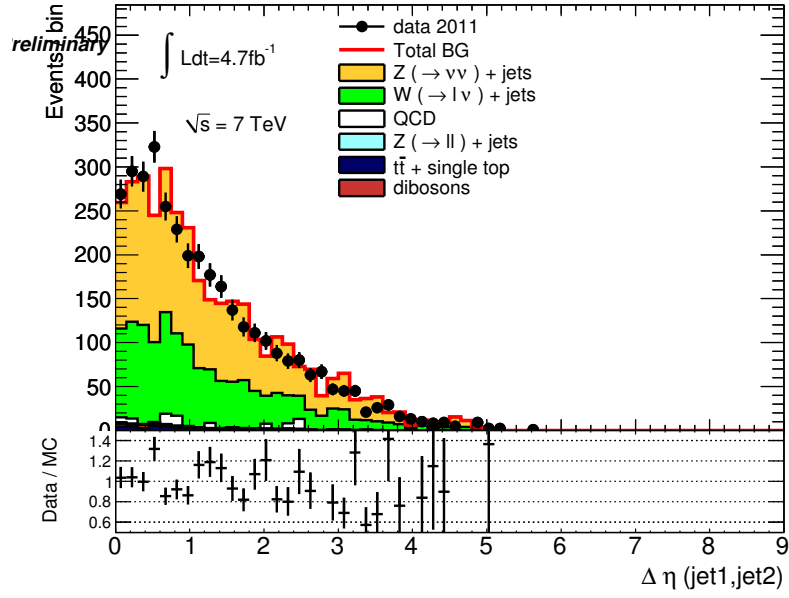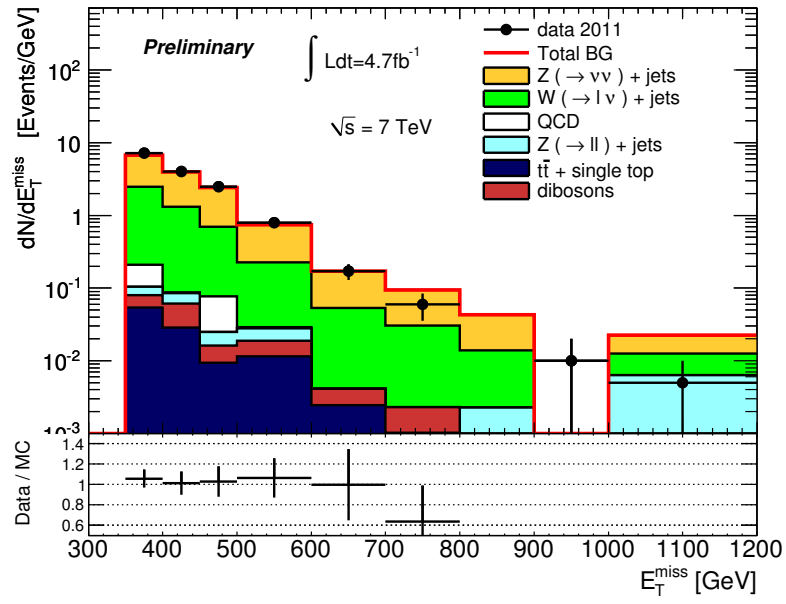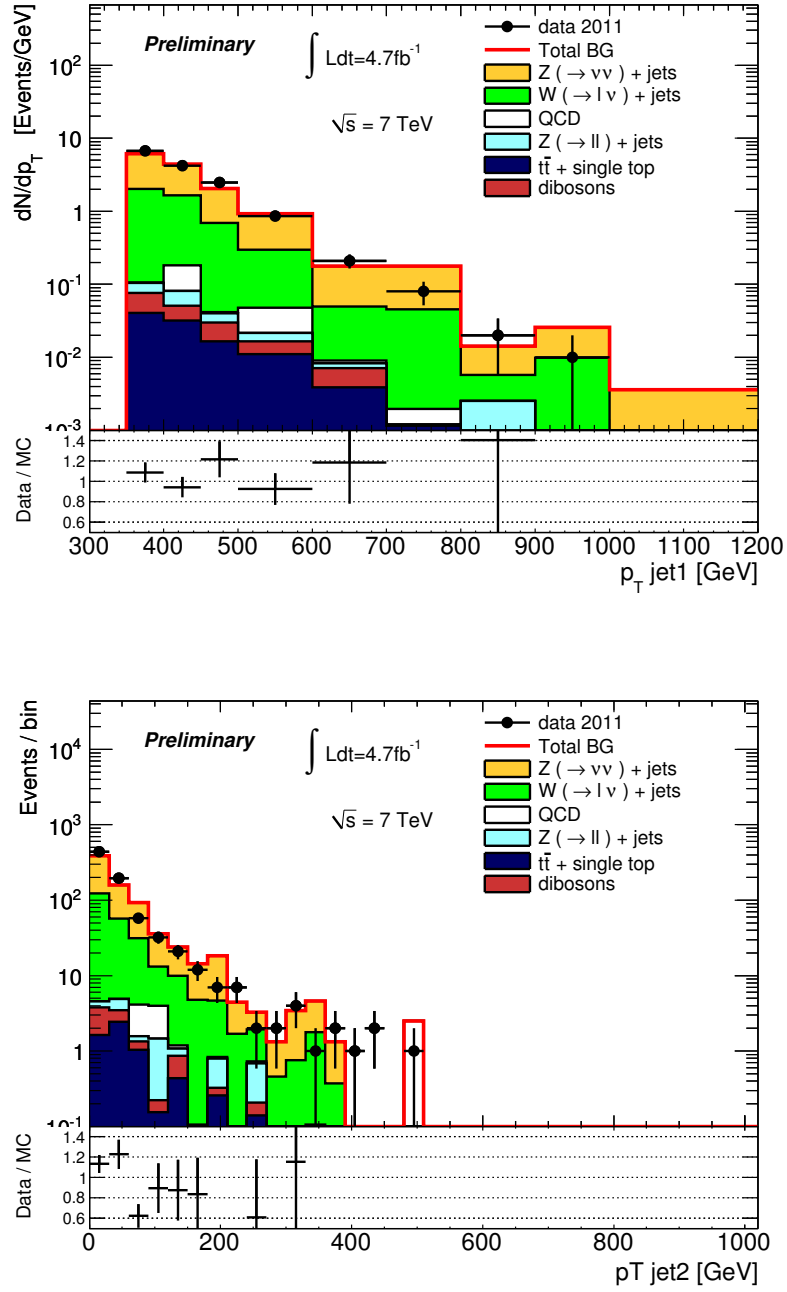Figure 85: Data and Monte Carlo comparison in Region A.
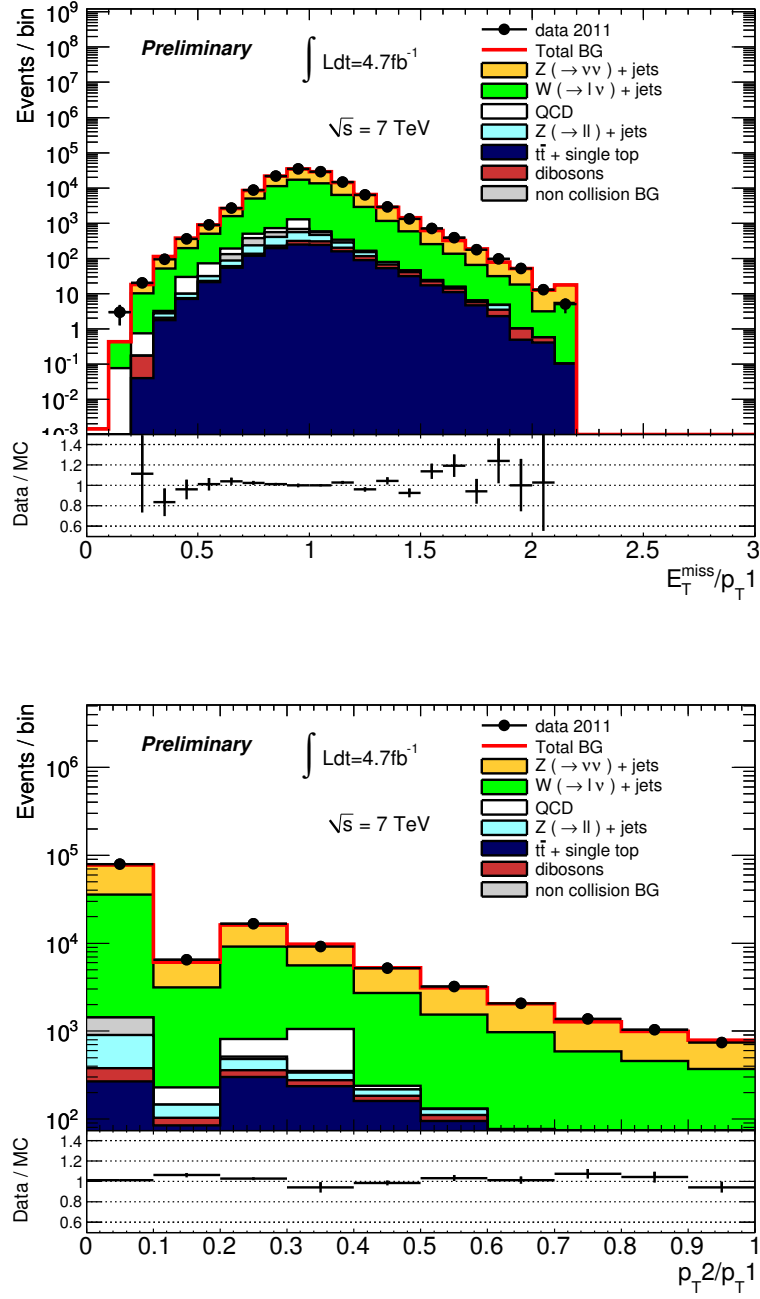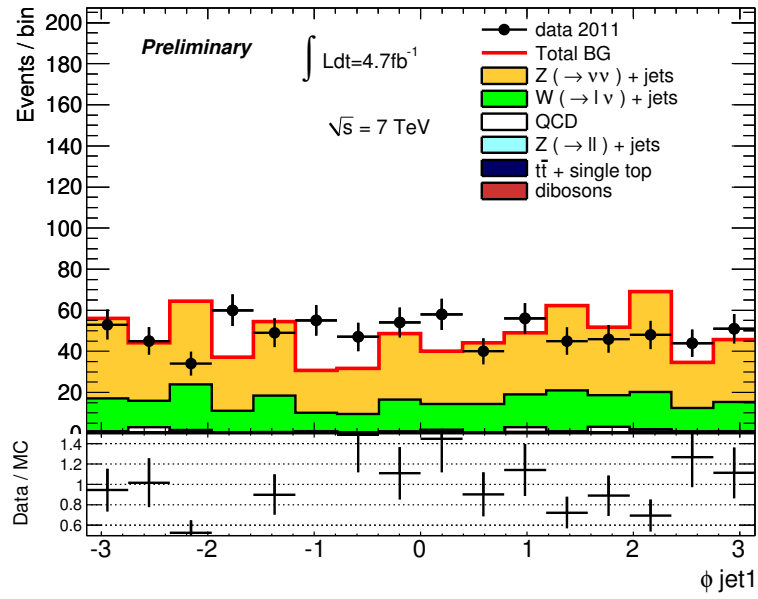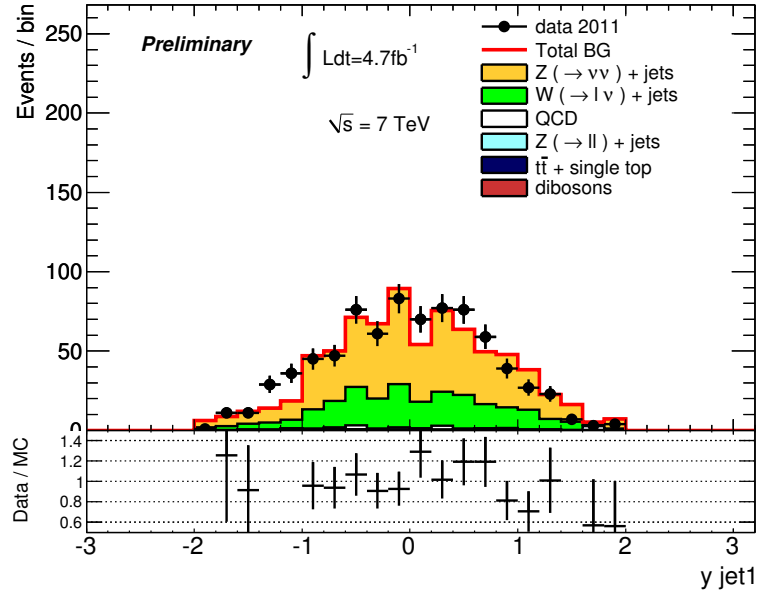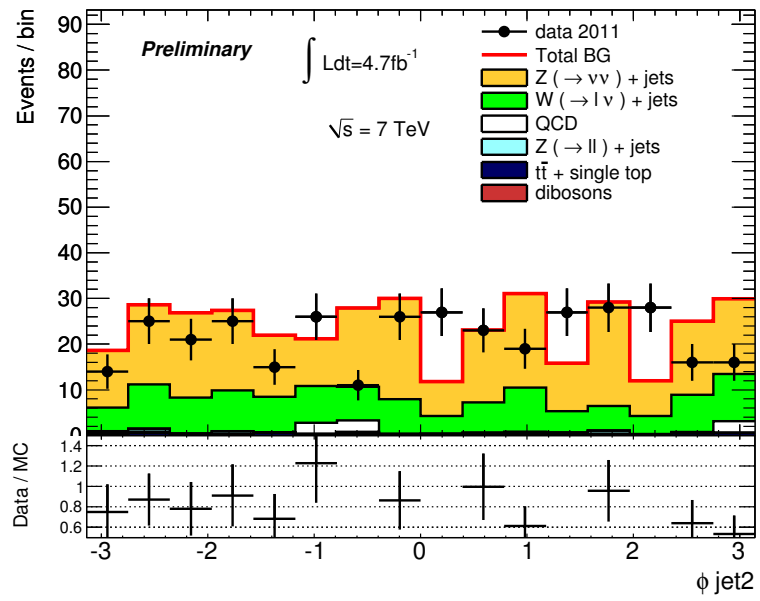
Figure 86: Data and Monte Carlo comparison in Region A.
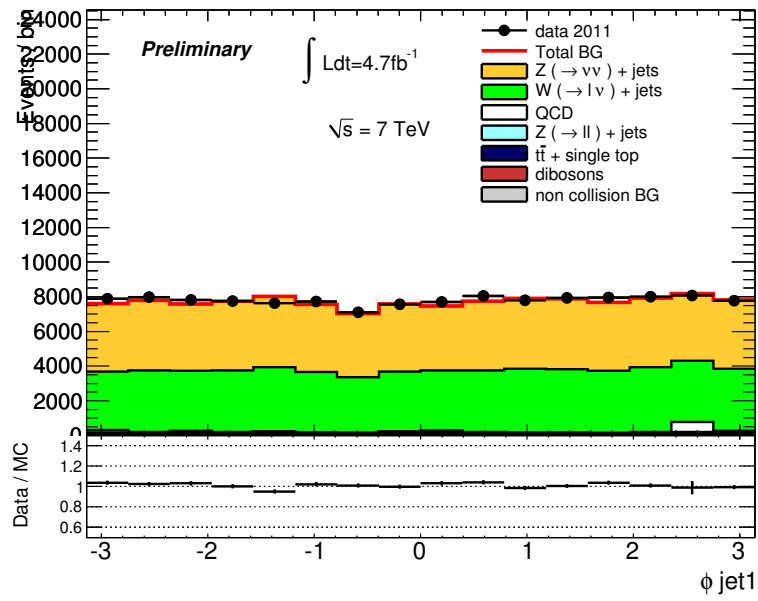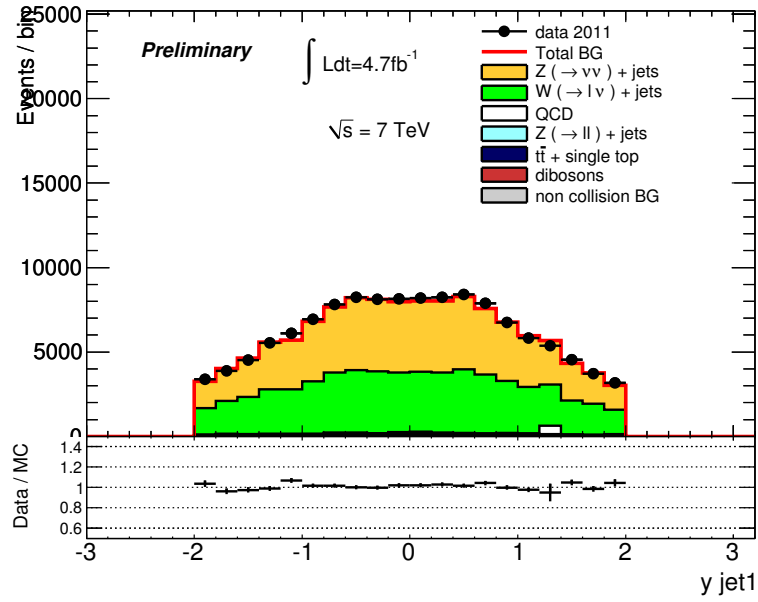
Figure 87: Data and Monte Carlo comparison in Region A.
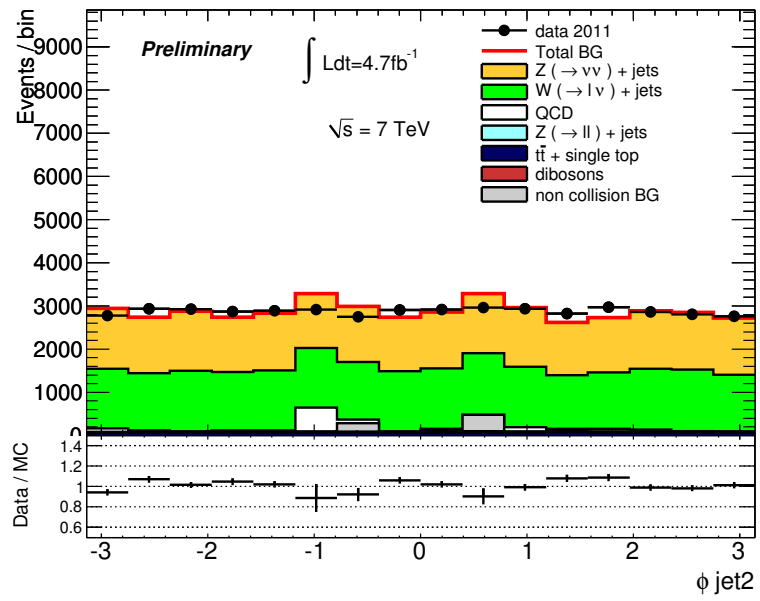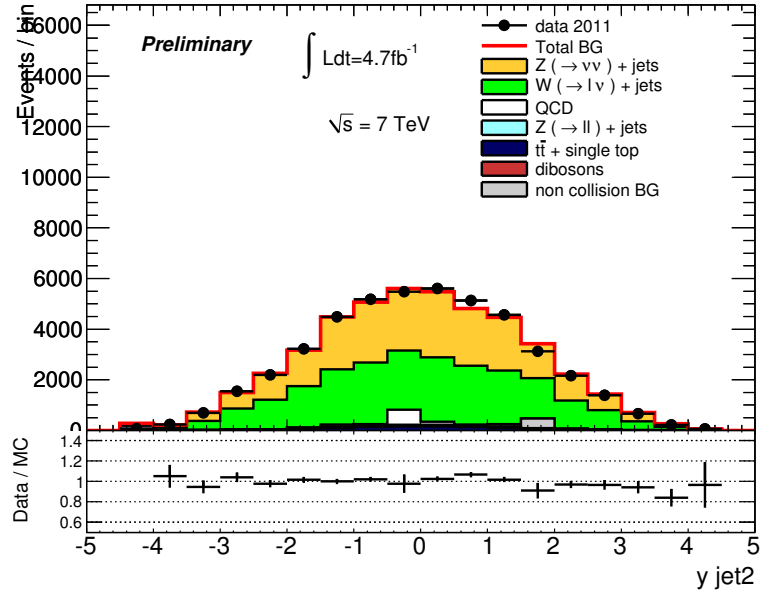
Figure 88: Data and Monte Carlo comparison in Region A.
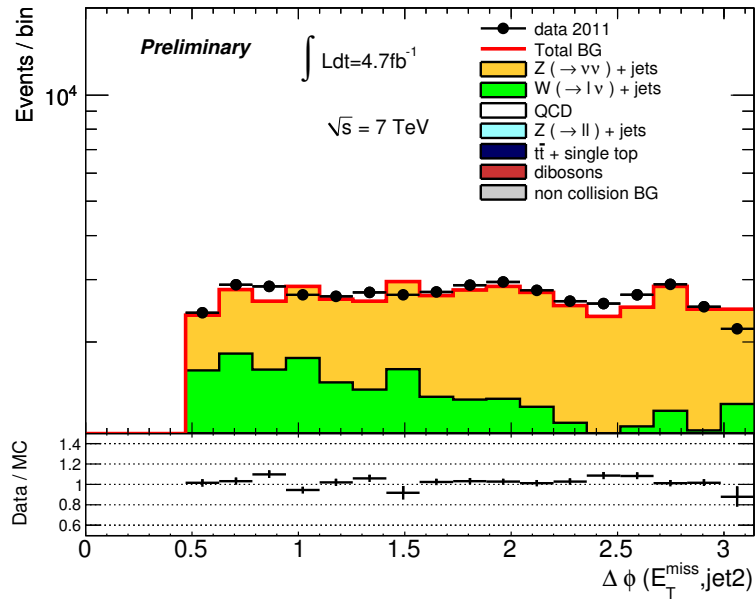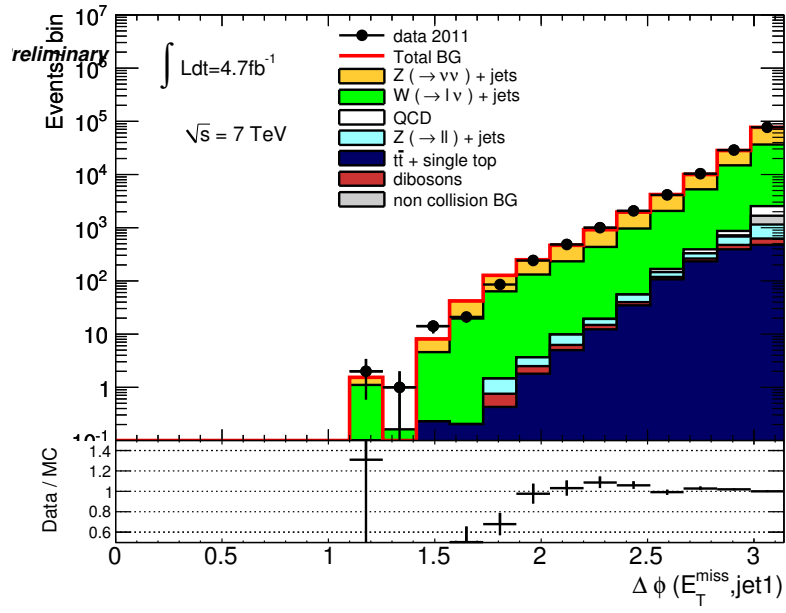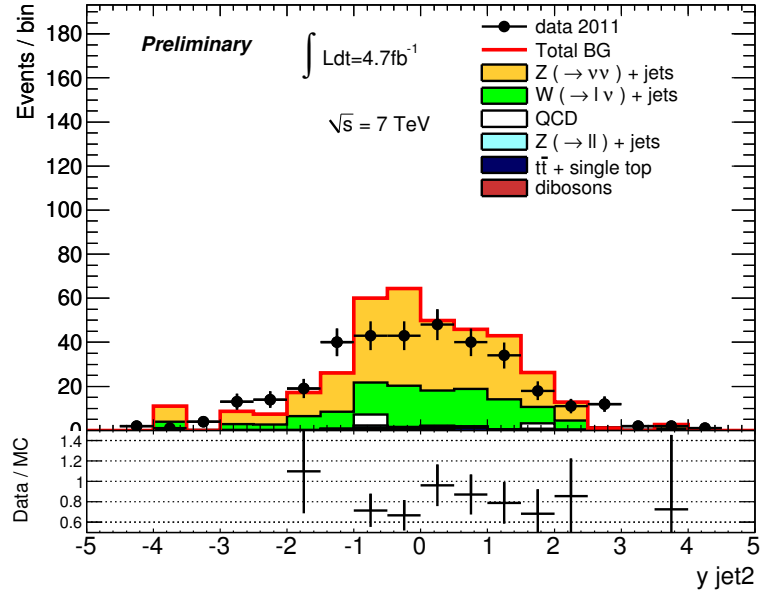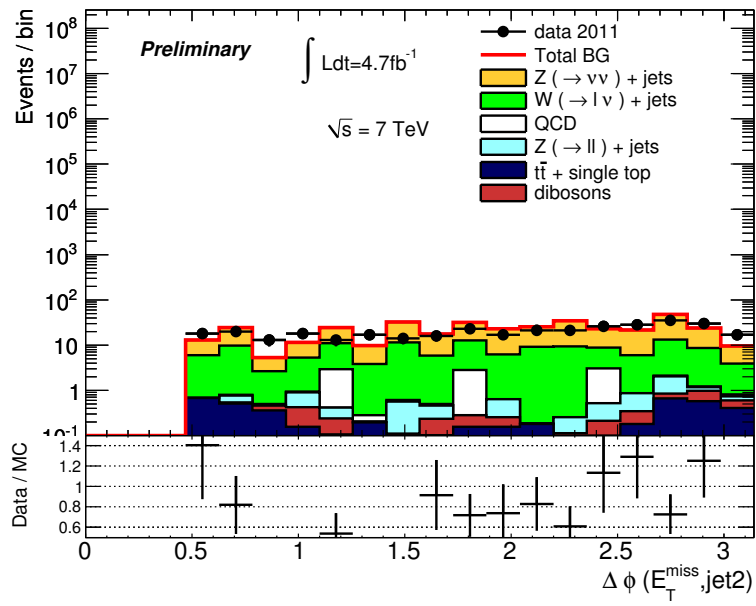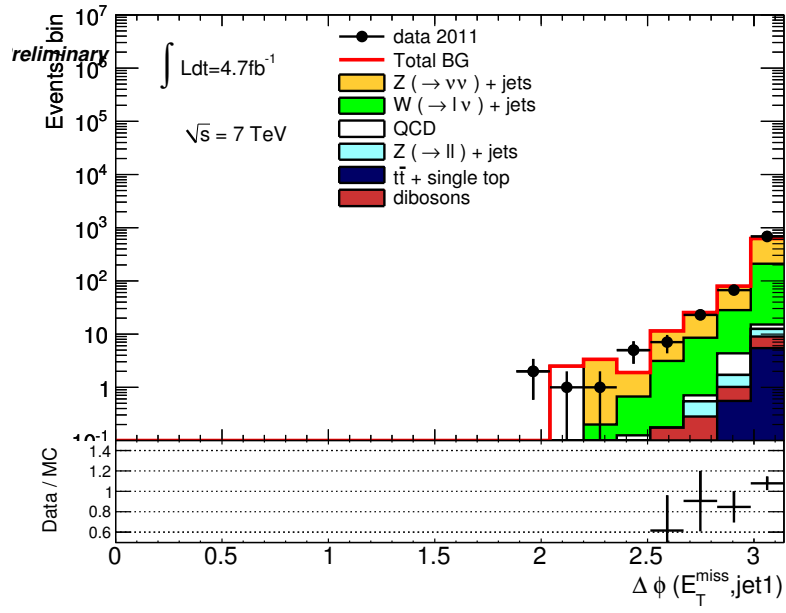
Figure 89: Data and Monte Carlo comparison in Region A.
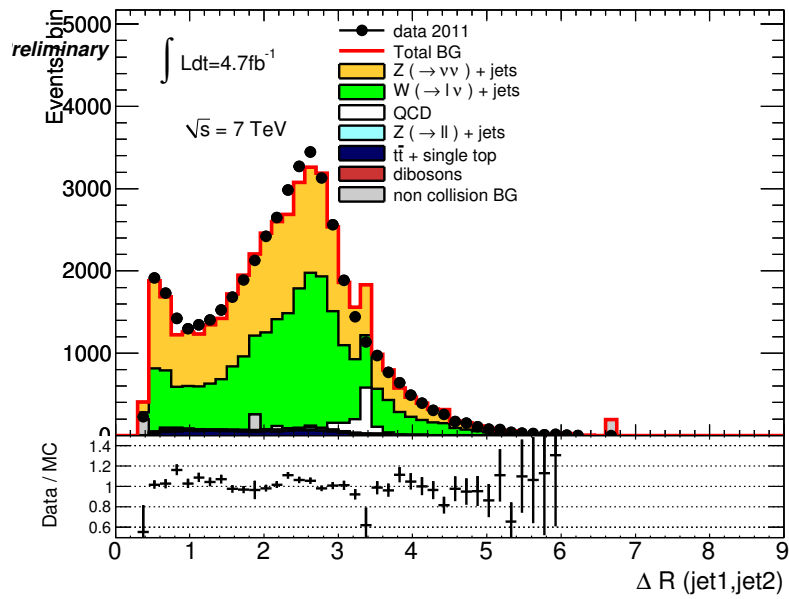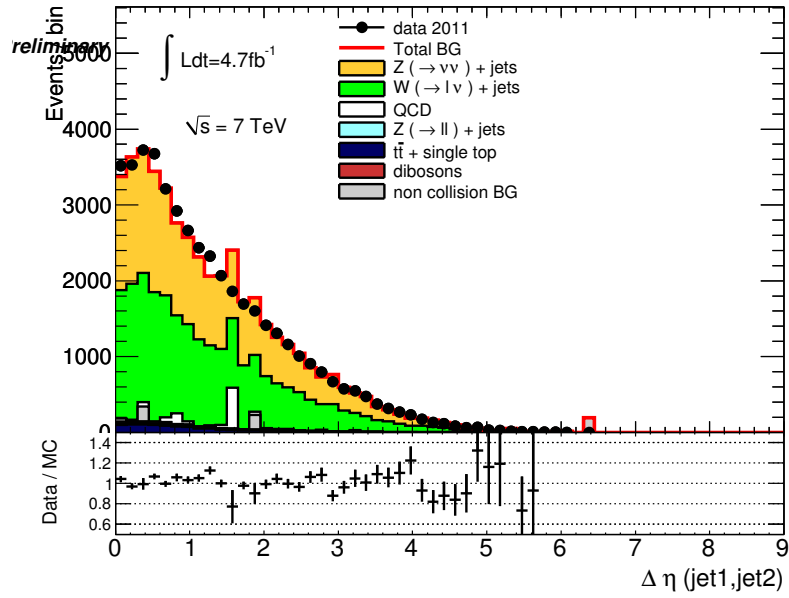
Figure 90: Data and Monte Carlo comparison in Region A.
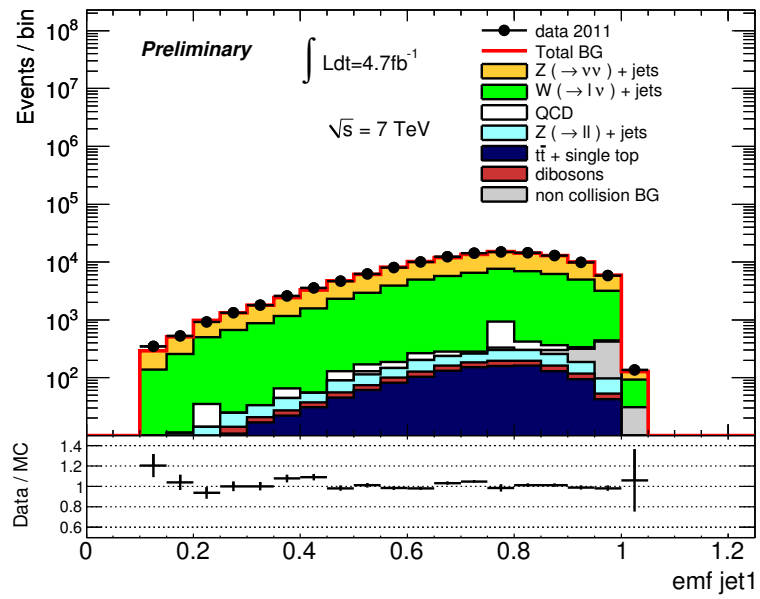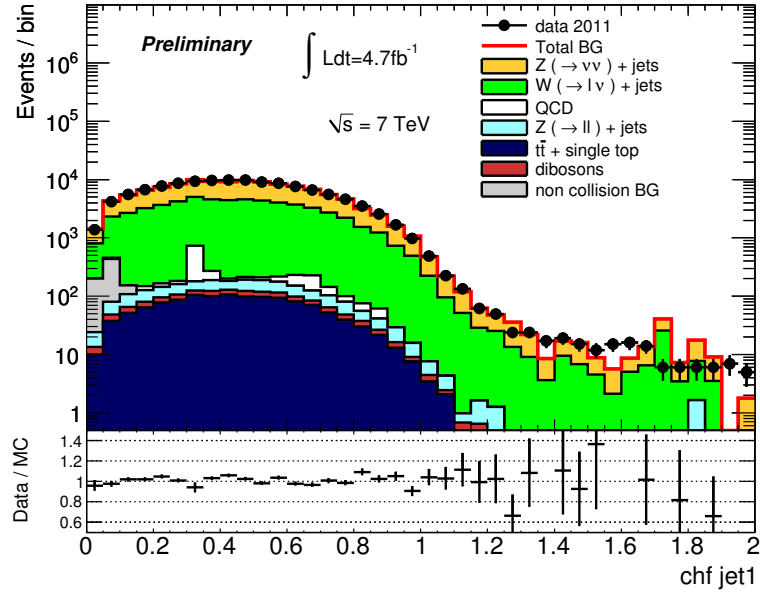
Figure 91: Data and Monte Carlo comparison in Region A.
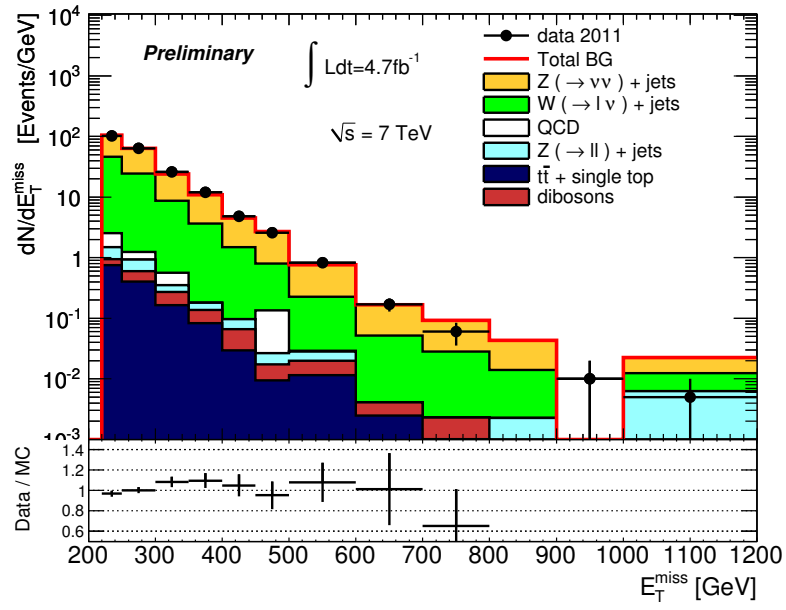
Figure 92: Data and Monte Carlo comparison in Region B.
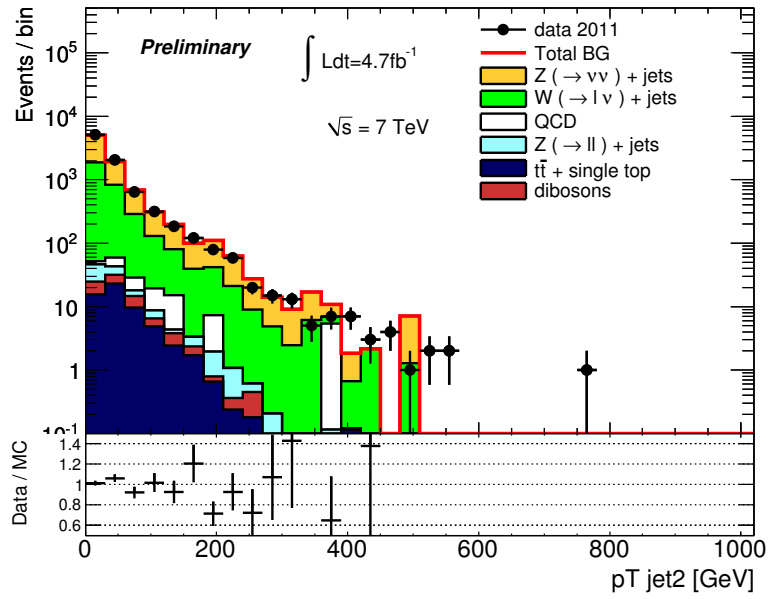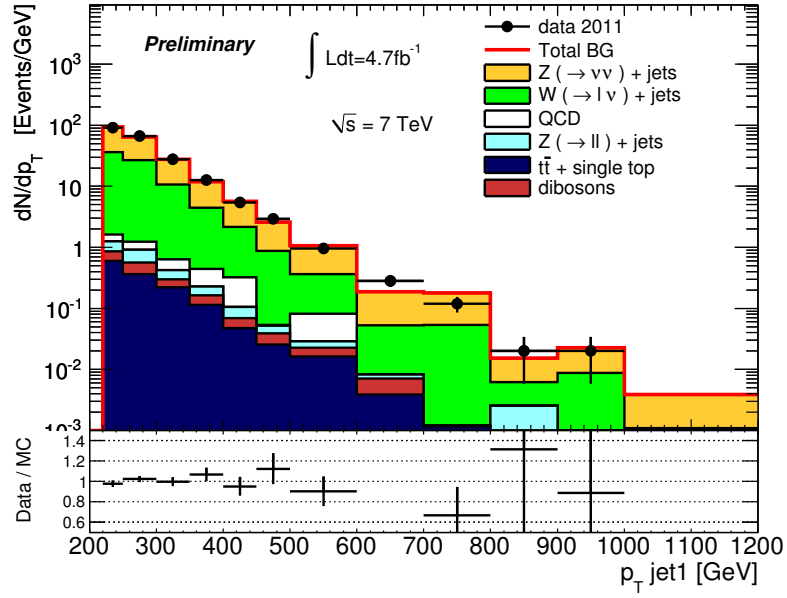
Figure 93: Data and Monte Carlo comparison in Region B.
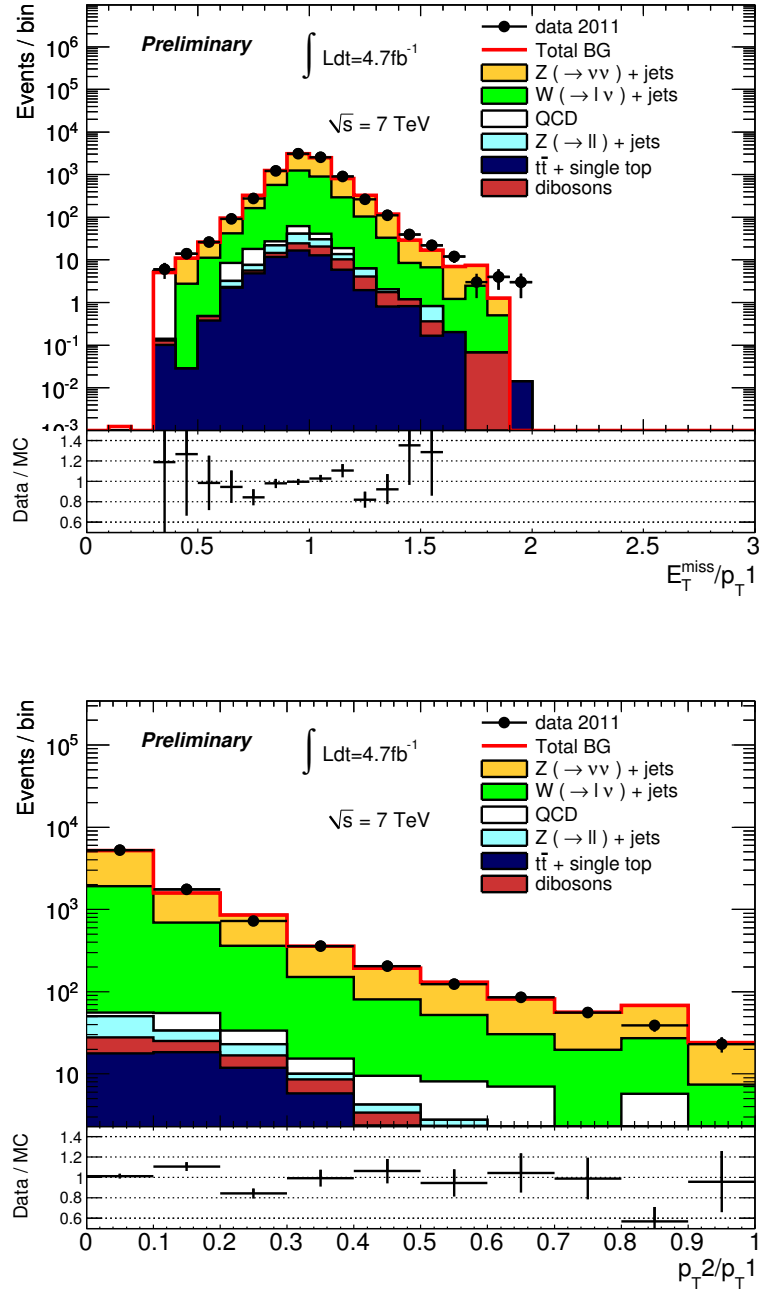
Figure 94: Data and Monte Carlo comparison in Region B.
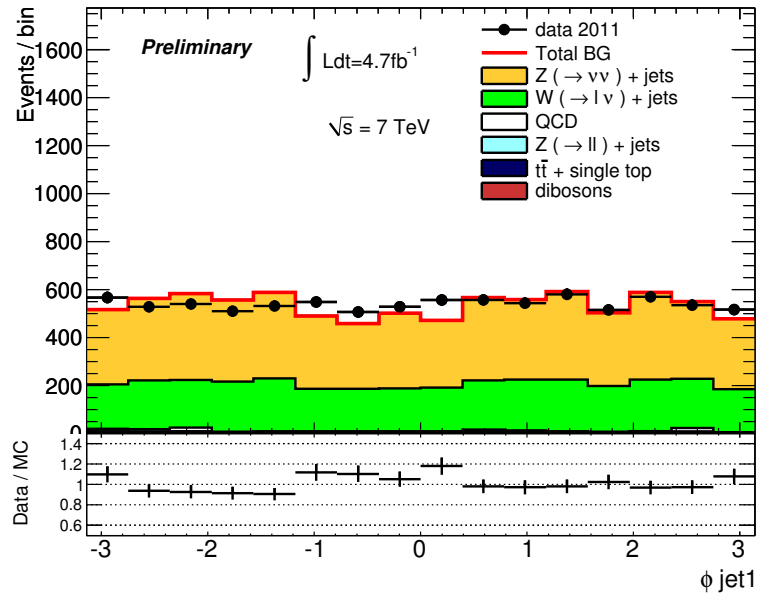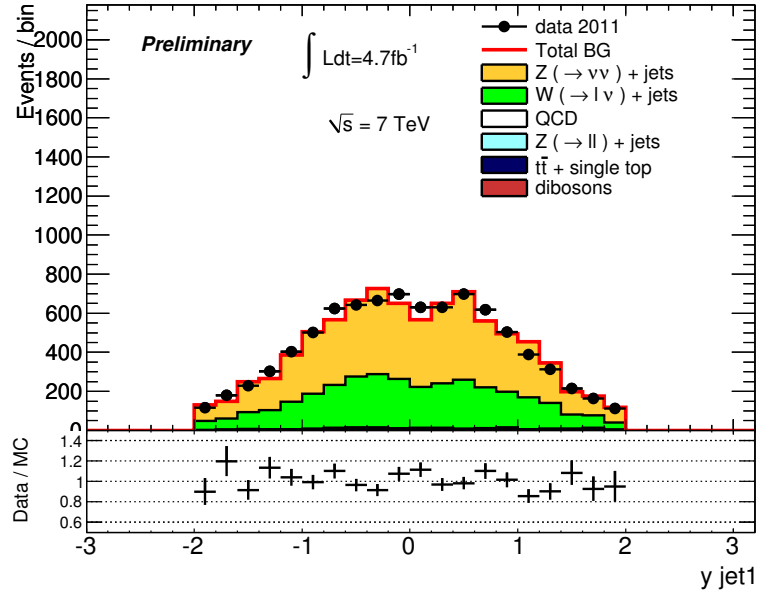
Figure 95: Data and Monte Carlo comparison in Region B.

Figure 96: Data and Monte Carlo comparison in Region B.

Figure 97: Data and Monte Carlo comparison in Region B.

Figure 98: Data and Monte Carlo comparison in Region B.

Figure 99: Data and Monte Carlo comparison in Region C.

Figure 100: Data and Monte Carlo comparison in Region C.

Figure 101: Data and Monte Carlo comparison in Region C.

Figure 102: Data and Monte Carlo comparison in Region C.

Figure 103: Data and Monte Carlo comparison in Region C.
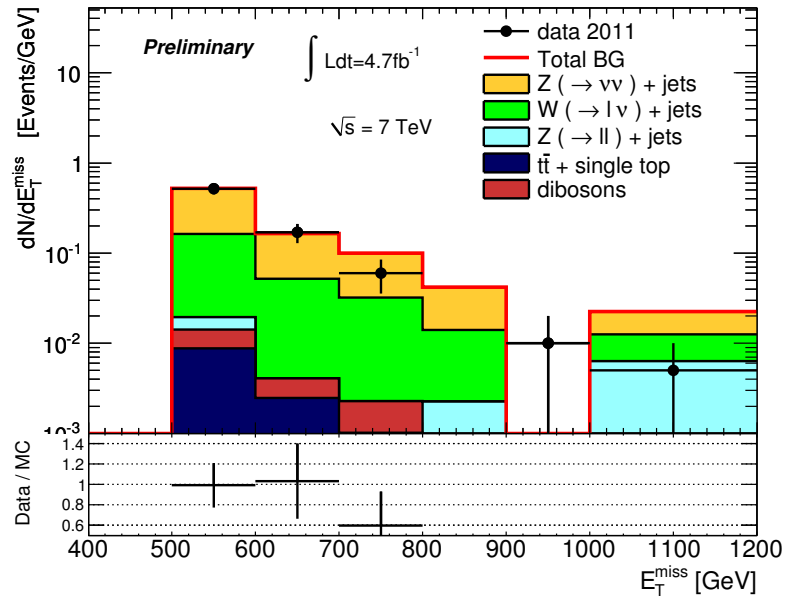
Figure 104: Data and Monte Carlo comparison in Region D.
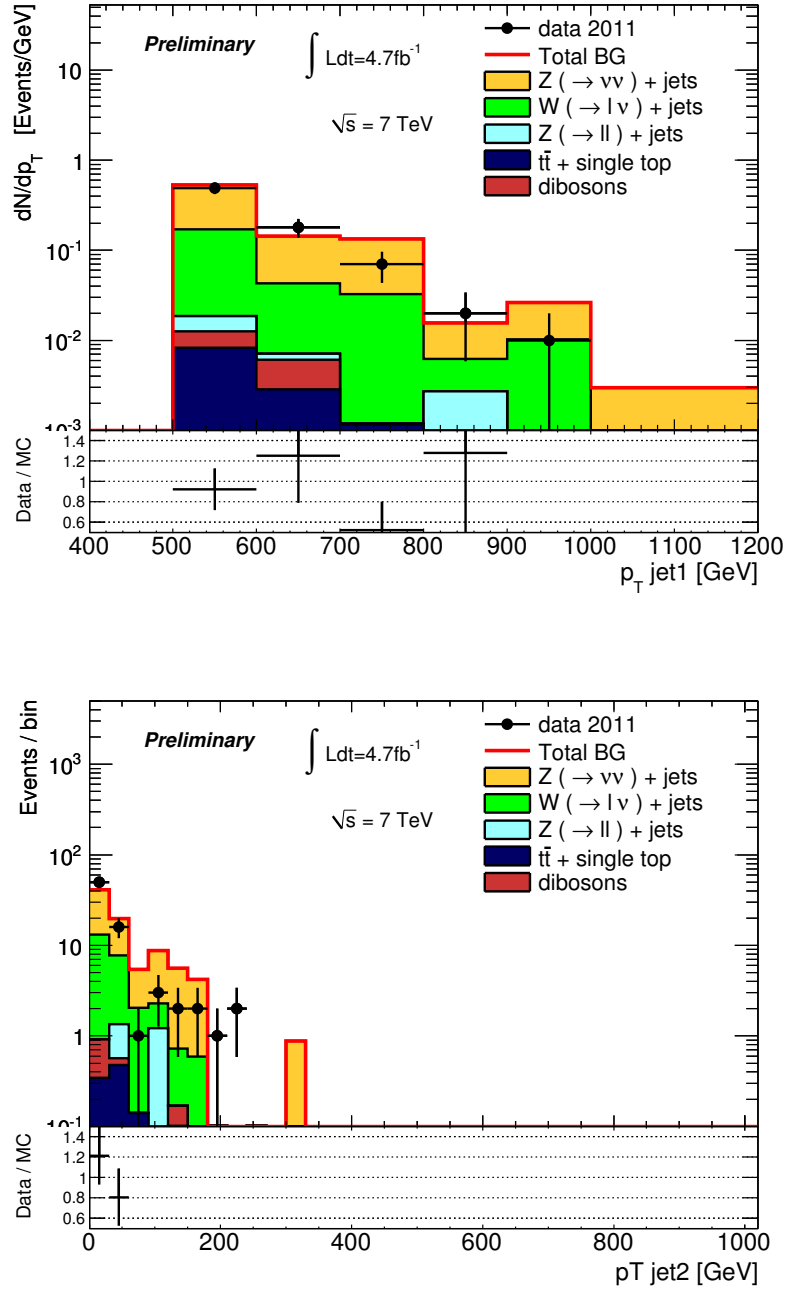
Figure 105: Data and Monte Carlo comparison in Region D.

1265   Although the results based on the combination of *W* and *Z* exclusive regions to determine the EWK
1266 backgrounds are considered the nominal results, Table 62 collects the results where only the *W* sample
1267 is used. Finally, the results obtained using inclusive control regions for both electon and muon samples
1268 are collected in appendix B.

	Background Predictions ± (stat.data) ± (stat.MC) ± (syst.)			
$Z \to \nu\nu$+jets(from $W \to \mu\nu$ CR)	$62770 \pm 298 \pm 290 \pm 2988$	$5171 \pm 89 \pm 64 \pm 253$	$485 \pm 27 \pm 17 \pm 26$	$55 \pm 9 \pm 6 \pm 2$
$Z \to \nu\nu$+jets(from $Z \to \mu\mu$ CR)	$64045 \pm 792 \pm 605 \pm 2417$	$5403 \pm 230 \pm 166 \pm 168$	$628 \pm 83 \pm 64 \pm 40$	$73 \pm 28 \pm 20 \pm 5$
$W \to \tau\nu$+jets	$31116 \pm 148 \pm 168 \pm 1349$	$1769 \pm 30 \pm 30 \pm 97$	$128 \pm 7 \pm 6 \pm 5$	$12 \pm 2 \pm 2 \pm 2$
$W \to e\nu$ +jets	$13945 \pm 121 \pm 89 \pm 557$	$687 \pm 20 \pm 19 \pm 30$	$47 \pm 4 \pm 3 \pm 3$	$5.4 \pm 1.4 \pm 1.2 \pm 0.5$
$W \to \mu\nu$ +jets	$11354 \pm 54 \pm 103 \pm 525$	$688 \pm 12 \pm 18 \pm 48$	$51 \pm 3 \pm 4 \pm 6$	$5 \pm 1 \pm 1 \pm 1$
$Z \to \tau\tau$+jets	$480 \pm 4 \pm 10 \pm 17$	$20 \pm 1 \pm 2 \pm 2$	$2.4 \pm 0.2 \pm 0.7 \pm 0.5$	$0.7 \pm 0.2 \pm 0.6 \pm 0.3$
$Z \to \mu\mu$+jets	$356 \pm 2 \pm 15 \pm 13$	$22 \pm 0 \pm 3 \pm 2$	$2.0 \pm 0.1 \pm 0.7 \pm 0.1$	$0.5 \pm 0.1 \pm 0.4 \pm 0.1$
$Z \to ee$+jets	$0.5 \pm 0.5 \pm 0.1$	–	–	–
Multi-jets	$1107 \pm 33 \pm 940$	$64 \pm 8 \pm 64$	$8 \pm 3 \pm 8$	–
$t\bar{t}$ + single t	$1257 \pm 11 \pm 251$	$59 \pm 2 \pm 12$	$6 \pm 1 \pm 1$	$1.3 \pm 0.3 \pm 0.3$
Di-bosons	$289 \pm 3 \pm 58$	$27 \pm 1 \pm 5$	$4.3 \pm 0.4 \pm 0.9$	$0.9 \pm 0.2 \pm 0.2$
Non-collision background	$575 \pm 60 \pm 57$	$25 \pm 13 \pm 3$	–	–
Total background	$123249 \pm 522 \pm 493 \pm 4980$	$8532 \pm 134 \pm 96 \pm 413$	$734 \pm 38 \pm 23 \pm 38$	$82 \pm 12 \pm 8 \pm 4$
Data	124724	8632	785	77

Table 62: Summary of background estimations and total number of observed events in 4.7 fb^{-1} of data for the four mono-jet selection regions. The estimation of the EWK background correspond to the W exclusive control region alone. In cases where both data and MCs play a role in the statistical errors, the two contributions are shown separated as second and third uncertainties. The last quoted uncertainty is the systematic uncertainty.

12 Interpretations

12.1 Graviton production with ADD Large Extra Dimension model

For the description of the theoretical model, the reader is referred to Reference [10] (Section 11.1).

12.1.1 Signal Acceptance

Signal acceptance (ratio of signal events passing all the mono-jet selection cuts defined in section 3) is shown in Table 63 for various number of extra dimensions. There is a slight dependency of the signal acceptance on M_D, since in the generation of events the maximum mass of the graviton has been set to M_D, the scale of the theory, above which the calculations of the effective field theory are not reliable. This dependency is found to be negligible[11] as shown in Table 63 for two different values of M_D for 2 extra dimensions.

(δ, M_D)	Region1	Region2	Region3	Region4
(2, 3.5)	0.288 ± 0.002	0.084 ± 0.001	0.0236 ± 0.0006	0.0067 ± 0.0003
(2, 4.5)	0.288 ± 0.002	0.085 ± 0.001	0.0242 ± 0.0006	0.0071 ± 0.0003
(3, 2.5)	0.312 ± 0.002	0.109 ± 0.001	0.0362 ± 0.0008	0.0111 ± 0.0004
(4, 2.5)	0.321 ± 0.002	0.127 ± 0.001	0.0456 ± 0.0009	0.0151 ± 0.0005
(5, 2.5)	0.326 ± 0.002	0.134 ± 0.001	0.0502 ± 0.0009	0.0179 ± 0.0005
(6, 2.5)	0.325 ± 0.002	0.137 ± 0.001	0.0544 ± 0.0009	0.0198 ± 0.0005

Table 63: ADD signal acceptance in %, for the four signal regions.

Figure 106 shows the distributions of the leading jet p_T and E_T^{miss} for 2-6 extra dimensions after the selection cuts of the first signal region explained in section 3.

12.1.2 Systematic uncertainties

Various sources of systematic uncertainties are considered, as explained in the following paragraphs. The effect of each source is investigated for different number of extra dimensions.

Parton distribution function The default PDF set used in MC11c simulated signal samples is MRST LO**. To study the PDF uncertainties, CTEQ6.6 and its 44 error sets are used[12]. Tables 64 and 65 list the PDF uncertainties on the ADD signal acceptance and cross-section for various number of extra dimensions. The final uncertainty is estimated using the Hessian method, and is divided by 1.645 to convert to the 68%CL. The maximum of the up and down variations is then quoted for each signal region, as shown in table 64.

Initial and final state radiation To investigate the effect of QCD initial and final state radiation ISR/FSR) on signal acceptance, Monte Carlo samples with more or less ISR/FSR have been generated and used at Truth level. This is done by varying the values of `parp64`, `parp67` (for ISR) and `parp72`, `parj82` (for FSR) in the `ExoGraviton_i` generator through the jobOption file (Table 66). ISR/FSR can affect the acceptance mainly due to the third jet veto. Tables 67 and 68 list the realtive uncertainties on the signal yield due to less and more level of ISR/FSR, respectively. The maximum deviation is considered for the final uncertainty due to ISR/FSR.

---

[11]This will not be the case if one considers *truncated* samples for which the contribution of events with $\hat{s} > M_D^2$ is suppressed.

[12]The PDF re-weighting tool is used to get the signal yields corrresponding to this PDF set and its error eigenvectors. They correspond to `mstp(51) = 10550-10594`.
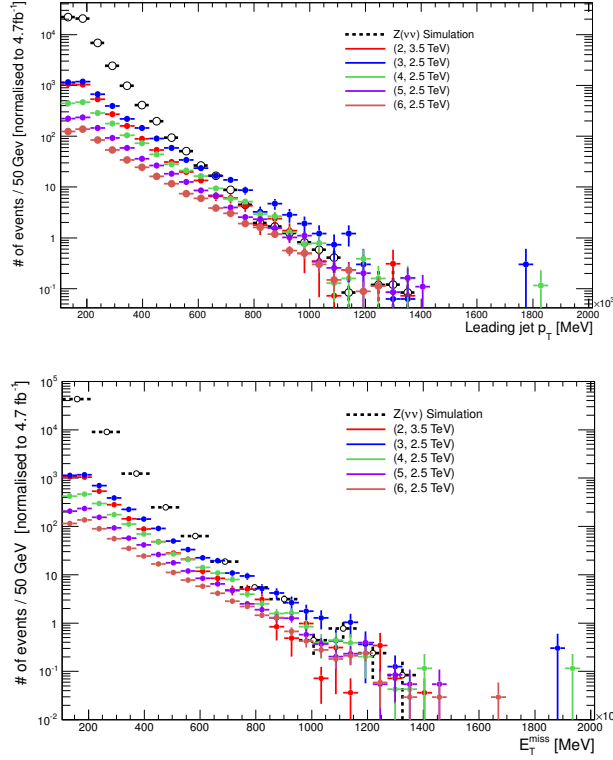
Figure 106: Distributions of the leading jet p_T and E_T^{miss} for various (δ, M_D) phase space points, after the selection cuts of the first signal region, normalised to 4.7 fb^{-1} integrated luminosity.

Renormalisation and factorisation scales The momentum transfer of the process, Q^2, is used in the cross-section calculations, and also in PDF sets[13]. At the leading order, it only enters the cross-section calculations via the running strong coupling constant α_S. The value used in the `ExoGraviton_i` generator is $\frac{1}{2} m_{kk}^2 + p_T^2$, where m_{KK} is the mass of the graviton mode, and p_T is the transverse momentum of the recoiling parton. To investigate the relative uncertainty due to the choice of the scale, the value of Q is changed to half and two times this value, and the resulting signal yield is compared to the central value (at Truth), after being normalised to the new cross-sections (corresponding to the new choice of Q). This will take into account the impact on both the signal acceptance and cross-section. The maximum deviation is considered for the final uncertainty. Table 69 lists the corresponding relative uncertainties on the signal yield.

---

[13] Via `PYPDFU(2212,X1,Q2,XP1)` in the generator.

(δ, M_D)	Region1	Region2	Region3	Region4
(2, 3.5)	0.47	1.52	2.67	3.88
(3, 2.5)	1.29	0.79	1.50	2.58
(4, 2.5)	2.65	1.73	1.33	1.75
(5, 2.5)	4.17	3.22	2.26	1.82
(6, 2.5)	5.42	4.58	3.54	2.75

Table 64: PDF uncertainty on the ADD signal *acceptance*, in %.

(δ, M_D)	up variation	down variation
(2, 3.5)	4.00	3.55
(3, 2.5)	6.71	5.51
(4, 2.5)	9.30	7.26
(5, 2.5)	11.43	8.61
(6, 2.5)	13.17	9.64

Table 65: Asymmetric PDF uncertainties on the ADD signal *cross-section*, in %.

parameter	less ISR/FSR	more ISR/FSR
`parp64`	4.08	1.02
`parp67`	0.75	1.75
`parp72`	0.2635	0.7905
`parj82`	1.66	0.5

Table 66: Values of ISR/FSR parameters used for the uncertainty studies.

Jet energy scale and resolution, and E_T^{miss} The JES-E_T^{miss} uncertainty is calculated by varying the p_T of *all* the jets (above 15 GeV in p_T) in the event up/down, and propagating the vector sum of this change to E_T^{miss}. This will change both the value and direction of E_T^{miss}. The mono-jet kinematic cuts are then applied to the new jets and E_T^{miss}. In the case of asymmetric errors, the maximum deviation is considered. Table 70 shows the resulting relative uncertainties on the ADD signal yield.

Luminosity There is a 3.9% uncertainty on the total integrated luminosity.

Trigger efficiency There is a difference of 0.66% between the trigger efficiencies obtained from data and simulation (Sec.4), which is considered as a source of systematic uncertainty on the signal yield.

PileUp The effect of pile-up is studied by re-weighting the signal samples using the `PileupReweighting` tool. This results in $\sim 0.15\%$ uncertainty on the signal yield, and $\sim 0.12\%$ uncertainty on the signal acceptance. Hence this uncertainty is neglected. Figure 107 shows signal acceptance as a function of the average number of interactions per bunch-crossing, and number of good vertices in the event.

Tables 71-74 list the total uncertainty on the ADD signal yield in the 4 signal regions, due to various sources explained above, as well as the statistical uncertainty due to the limited statistics of the simulated signal samples.

(δ, M_D)	Region1	Region2	Region3	Region4
(2, 3.5)	5.99	2.73	6.70	8.68
(3, 2.5)	7.62	7.89	7.11	11.70
(4, 2.5)	6.87	3.30	2.76	6.00
(5, 2.5)	5.38	4.81	6.19	7.74
(6, 3.5)	4.84	3.20	2.84	6.40

Table 67: Uncertainty due to less ISR/FSR on the ADD signal yield, in %.

(δ, M_D)	Region1	Region2	Region3	Region4
(2, 3.5)	2.95	1.21	3.09	6.52
(3, 2.5)	4.07	0.87	1.09	7.68
(4, 2.5)	3.09	2.97	0.54	3.72
(5, 2.5)	2.52	5.31	4.12	13.78
(6, 3.5)	3.18	3.13	0.44	9.61

Table 68: Uncertainty due to more ISR/FSR on the ADD signal yield, in %.

(δ, M_D)	Region1		Region2		Region3		Region4	
(2, 3.5)	19.06	23.67	15.66	29.65	18.44	30.28	22.51	40.15
(3, 2.5)	19.03	25.25	20.44	25.18	31.36	11.07	31.22	18.18
(4, 2.5)	20.59	25.74	22.50	25.85	23.89	24.08	23.74	68.09
(5, 2.5)	20.44	25.88	19.72	30.23	17.91	36.25	35.52	47.26
(6, 2.5)	20.44	25.13	20.53	26.96	18.90	33.77	8.11	48.97

Table 69: Relative scale uncertainty (in %) on the ADD signal yield in each region, when changing the scale up and down, respectively.

12.1.3 Limits on M_D

Limits based on cross section method To set upper limits on the $\sigma \times A \times \epsilon$, the `HistFitter` package [14] based on RooStats, is used. Table 75 summarises the 95% CL *model-independent*[15] upper limits on $\sigma \times A \times \epsilon$ for each of the 4 signal regions, using the Z($\nu\nu$) prediction from the combination of W($\mu\nu$), Z($\mu\mu$), W($e\nu$), and Z(ee) events (BG4 of Table 56). To get the observed and expected lower limits on the scale of the model, M_D, correlations of the JES/E_T^{miss} uncertainty between signal and background, as well as luminosity, trigger, and MC statistical uncertainties on the signal yield are considered. The resulting upper limit on $\sigma \times A \times \epsilon$ is then used to set the lower limits on M_D. For each value of number of extra dimensions, a central value for the observed lower limit on M_D is computed ignoring signal theoretical uncertainties (PDF, ISR/FSR, Scale Q). As shown in Figure 108, this refers to the intersection of the blue horizontal line [16] with each of the signal theoretical curves. The upper and lower bands on this central value are then computed considering the total signal theoretical uncertainties; these are the intersections of the blue horizontal line with the upper and lower edges of each of the theoretical curves.

---

[14]https://twiki.cern.ch/twiki/bin/viewauth/AtlasProtected/SusyFitter

[15]Luminosity and trigger uncertainties on the signal yield are considered, but no JES correlation between signal and background is assumed, and the MC statistical uncertainty of the signal yield has been set to zero.

[16]The horizontal line representing the 95% CL observed upper limit on $\sigma \times A \times \epsilon$ is obtained after taking into account the JES uncertainty correlation between signal and background, as well as luminosity, trigger, and MC statistical uncertainties on the signal yield.

(δ, M_D)	Region1	Region2	Region3	Region4
(2, 3.5)	4.13	7.42	9.83	12.30
(3, 2.5)	3.11	5.92	8.02	9.43
(4, 2.5)	2.39	4.63	7.68	8.68
(5, 2.5)	4.88	4.49	6.92	10.43
(6, 2.5)	6.65	3.96	5.60	9.45

Table 70: Relative uncertainty in %, due to JES and E_T^{miss} on the ADD signal yield.
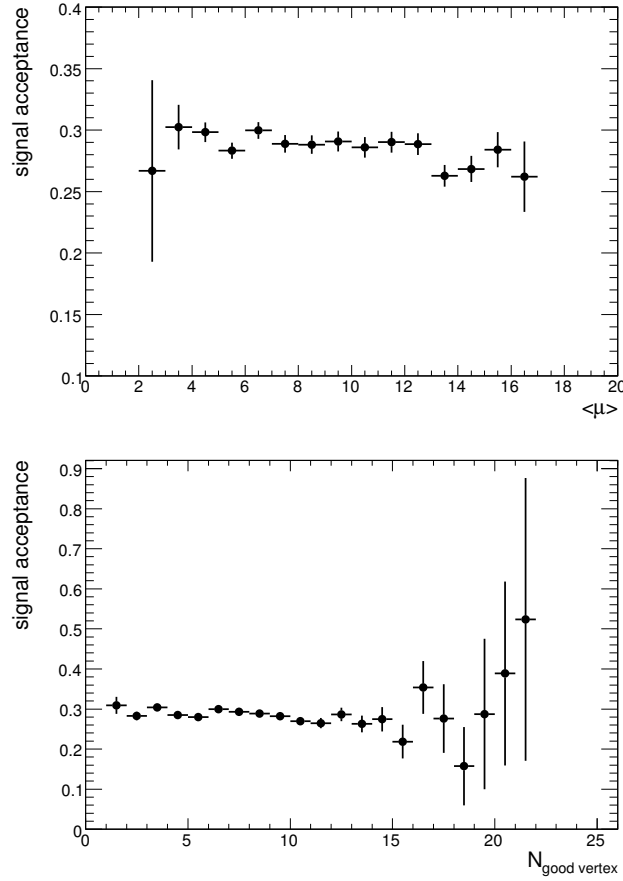
Figure 107: ADD signal acceptance as a function of average number of interactions per bunch-crossing, and also number of good vertices in the event.

The expected lower limits on M_D are calculated without considering any signal theoretical uncertainty (the intersection of the red horizontal line with each of the signal theoretical curves). The error bands on the expected limits are calculated by varying the total background estimation by $\pm 1 - \sigma_{BG}$ and recalculating the limits. The resulting 95% CL expected and observed lower limits on M_D are shown in Figure 109, and the values are quoted in Table 76. The final quoted observed limits on M_D are taken from the lower error band of the observed limit, as listed in Table 77.

Assuming compactification on a torus, one can relate M_D to the size of the extra dimensions[17]:

$$R = \frac{1}{M_D} \cdot [\frac{M_P}{\sqrt{8\pi}M_D}]^{\frac{2}{\delta}} \tag{33}$$

Limits based on TF method The Confidence Levels (CL) are computed using a Likelihood ratios with a semi-Bayesian method by running thousands of Monte Carlo experiments. The limits are based on a cut and count experiment where the numbers of events for signal, background, and data events are given to the program as inputs. The *CLs* approach is used including statistical and systematic uncertainties. The systematic uncertainties on the signal and background are considered as nuisance parameters according

---

[17]For the explanation of the notations, the reader is referred to Reference [10] (Section 11.1)

δ	PDF	ISR/FSR	Scale	JES/E_T^{miss}	Luminosity	Trigger	Total (.syst)	MC statistics
2	4.00	5.99	23.67	4.13	3.9	0.66	25.39	0.79
3	6.71	7.62	25.25	3.11	3.9	0.66	27.68	0.73
4	9.30	6.87	25.74	2.39	3.9	0.66	28.59	0.72
5	11.43	5.38	25.88	4.88	3.9	0.66	29.48	0.71
6	13.17	4.84	25.13	6.65	3.9	0.66	29.80	0.72

Table 71: Relative systematic uncertainties from each source, along with the total relative systematic and statistical uncertainties, (in %), on the ADD signal yield ($\sigma * A$) in the first signal region.

δ	PDF	ISR/FSR	Scale	JES/E_T^{miss}	Luminosity	Trigger	Total (.syst)	MC statistics
2	4.00	2.73	29.65	7.42	3.9	0.66	31.20	1.47
3	6.71	7.89	25.18	5.92	3.9	0.66	28.14	1.25
4	9.30	3.30	25.85	4.63	3.9	0.66	28.33	1.18
5	11.43	5.31	30.23	4.49	3.9	0.66	33.29	1.15
6	13.17	3.20	26.96	3.96	3.9	0.66	30.69	1.13

Table 72: Relative systematic uncertainties from each source, along with the total relative systematic and statistical uncertainties, (in %), on the ADD signal yield ($\sigma * A$) in the second signal region.

to Gaussian distributions. The correlations between the systematics of the background and signal are not trivial since the total background is dominated by electroweak processes that are estimated with a data-driven method. Thus the components that would correlate, e.g. JES, are signifiantly reduced for the background leaving at the end little residuals. However these residuals can be considered fully correlated with the uncertainties on the signal. (*a list with all the uncertainties and their correlation will be provided later*).

Expected and observed limits on M_D are computed for the different analyses regions, and the results are shown in table 78. Observed 95% CL upper limits on the size of the extra dimensions R assuming compactification on a torus are shown in figure 79. The independant limits of $\sigma * A$ are computed setting all the signal uncertainties to zero. Table 80 shows the expected and observed 95% CL lower limits. Figure 110 shows graphically the $\sigma * A$ of the signal as a function of M_D and the observed $\sigma * A$ exclusion limits from regions 2 and 3. The total signal uncertainties are shown as error bands on the central curves. Finally figure 111 shows the new observed limits on M_D with 5 fb^{-1} for the different number of extra dimensions. Are also presented the last latest limits from LEP and CDF and the ATLAS limits from the analysis of 1 fb^{-1}.

δ	PDF	ISR/FSR	Scale	JES/E_T^{miss}	Luminosity	Trigger	Total (.syst)	MC statistics
2	4.00	6.70	30.28	9.83	3.9	0.66	33.02	2.82
3	6.71	7.11	31.36	8.02	3.9	0.66	34.04	2.20
4	9.30	2.76	24.08	7.68	3.9	0.66	27.36	2.03
5	11.43	6.19	36.25	6.92	3.9	0.66	39.33	1.93
6	13.17	2.84	33.77	5.60	3.9	0.66	36.40	1.85

Table 73: Relative systematic uncertainties from each source, along with the total relative systematic and statistical uncertainties, (in %), on the ADD signal yield ($\sigma * A$) in the third signal region.

δ	PDF	ISR/FSR	Scale	JES/E_T^{miss}	Luminosity	Trigger	Total (.syst)	MC statistics
2	4.00	8.68	30.28	12.30	3.9	0.66	34.28	5.24
3	6.71	11.70	31.36	9.43	3.9	0.66	35.64	4.01
4	9.30	6.00	24.08	8.68	3.9	0.66	28.17	3.56
5	11.43	13.78	36.25	10.43	3.9	0.66	41.94	3.27
6	13.17	9.61	33.77	9.45	3.9	0.66	38.87	3.13

Table 74: Relative systematic uncertainties from each source, along with the total relative systematic and statistical uncertainties, (in %), on the ADD signal yield ($\sigma * A$) in the fourth signal region.

	Expected [pb]	Observed [pb]
Region1	1.737	1.805
Region2	0.160	0.136
Region3	0.024	0.030
Region4	0.0078	0.0068

Table 75: [**For Approval**] 95% CL model-independent expected and observed upper limits on $\sigma \times A \times \epsilon$ [pb] in each of the 4 signal regions, using the combination of Z$\nu\nu$ predictions from the four channels: W$\mu\nu$, Z$\mu\mu$, W$e\nu$, and Zee (BG4 in Table 56).

	Region 1		Region 2		Region 3		Region 4	
δ	exp [TeV]	obs [TeV]	exp [TeV]	obs [TeV]	exp [TeV]	obs [TeV]	exp [TeV]	obs [TeV]
2	2.69 +0.23 -0.22	2.66 +0.15 -0.18	3.62 +0.31 -0.28	3.78 +0.25 -0.32	4.15 +0.39 -0.38	3.90 +0.28 -0.34	4.02 +0.40 -0.42	4.17 +0.30 -0.38
3	2.14 +0.14 -0.14	2.12 +0.21 -0.13	2.80 +0.19 -0.17	2.90 +0.14 -0.18	3.26 +0.24 -0.27	3.08 +0.20 -0.24	3.22 +0.26 -0.29	3.32 +0.18 -0.29
4	1.91 +0.11 -0.12	1.88 +0.09 -0.11	2.46 +0.14 -0.13	2.53 +0.11 -0.14	2.81 +0.18 -0.17	2.70 +0.11 -0.14	2.82 +0.19 -0.20	2.90 +0.11 -0.15
5	1.77 +0.09 -0.10	1.76 +0.08 -0.10	2.26 +0.11 -0.12	2.32 +0.10 -0.15	2.56 +0.15 -0.14	2.47 +0.12 -0.18	2.60 +0.16 -0.17	2.66 +0.14 -0.20
6	1.67 +0.09 -0.09	1.66 +0.08 -0.09	2.12 +0.11 -0.09	2.17 +0.09 -0.11	2.42 +0.12 -0.14	2.33 +0.10 -0.15	2.45 +0.13 -0.16	2.51 +0.11 -0.17

Table 76: [**For Approval**] 95% CL expected and observed lower limits on M_D [TeV] for each number of extra dimensions, and in each signal region, using the combination of Z$\nu\nu$ predictions from the four channels: W$\mu\nu$, Z$\mu\mu$, W$e\nu$, and Zee (BG4 in Table 56). The errors on expected and observed limits are also quoted.

δ	Region1	Region2	Region3	Region4
2	2.48	3.46	3.56	3.79
3	1.99	2.72	2.84	3.03
4	1.77	2.39	2.56	2.75
5	1.66	2.17	2.29	2.46
6	1.57	2.06	2.18	2.34

Table 77: [**For Approval**] 95% CL observed lower limits on M_D [TeV] for each number of extra dimensions, and in each signal region, using the combination of Z$\nu\nu$ predictions from the four channels: W$\mu\nu$, Z$\mu\mu$, W$e\nu$, and Zee (BG4 in Table 56). These observed limits are taken from the lower error band on the observed limit central line shown in Fig 109.
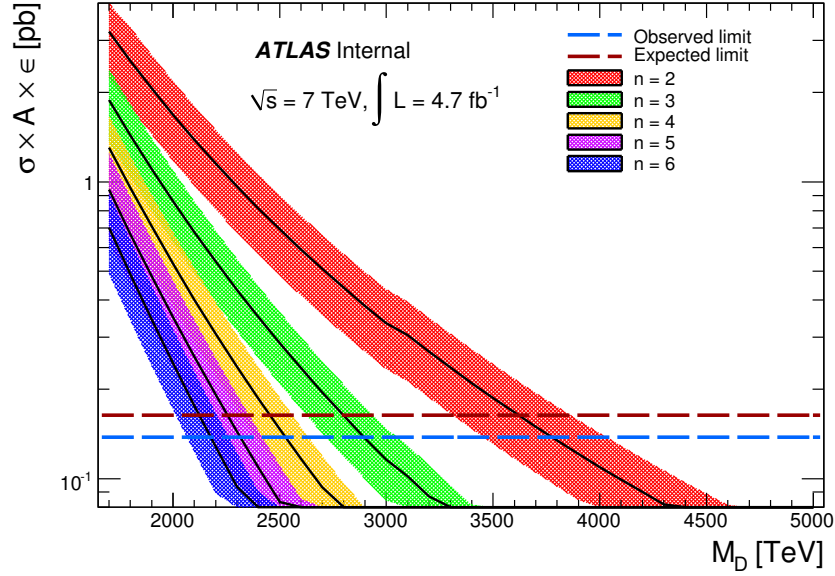
Figure 108: [**For Approval**] 95% CL expected and observed upper limits on $\sigma \times A \times \epsilon$ [pb] (red and blue dashed horizontal lines), along with signal $\sigma \times A \times \epsilon$ for 2-6 extra dimensions, in SR2. The error bands on the theoretical curves are the total theoretical uncertainties (PDF, ISR/FSR, and Scale Q uncertainties). The horizontal lines are obtained after taking into account the JES uncertainty correlation between signal and background, as well as luminosity, trigger, and MC statistical uncertainties on the signal yields.
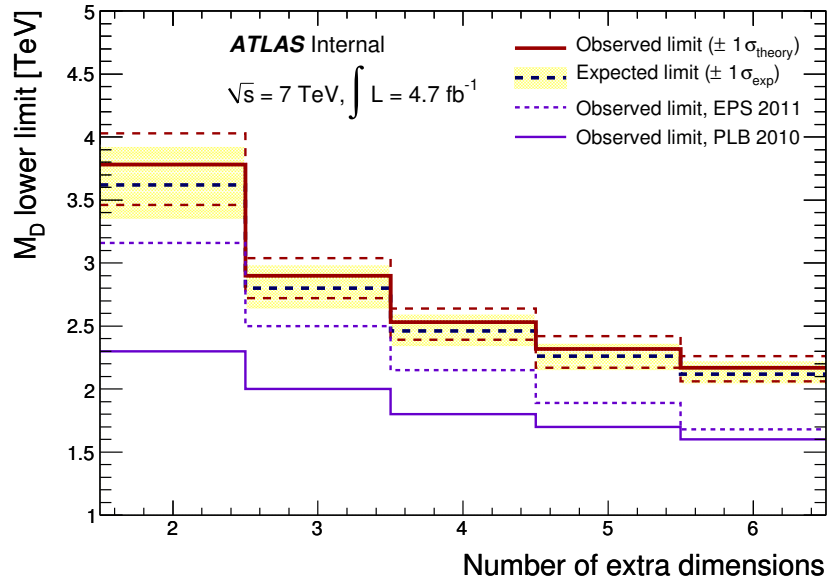
Figure 109: [**For Approval**] 95% CL observed and expected lower limits on M_D [TeV],based on SR2. The red dashed error bands around the observed limit show the impact of the total signal theoretical uncertainties (PDF, ISR/FSR, and Scale Q uncertainties) on the limits, and its lower band is quoted as the final limit (Table 77). The yellow error bands on the expected limits are calculated by varying the total background estimation by $\pm 1 - \sigma_{BG}$.

	Region 1		Region 2		Region 3		Region 4	
δ	exp [TeV]	obs [TeV]	exp [TeV]	obs [TeV]	exp [TeV]	obs [TeV]	exp [TeV]	obs [TeV]
2	3.01	2.92	3.50	3.43	3.80	3.65	3.70	3.83
3	2.37	2.29	2.77	2.73	3.06	2.96	3.09	3.20
4	2.09	2.04	2.44	2.41	2.72	2.64	2.81	2.89
5	1.94	1.91	2.26	2.24	2.53	2.46	2.60	2.67
6	1.85	1.83	2.15	2.13	2.39	2.33	2.47	2.54

95% CL limits on M_D for the ADD model

Table 78: *Produced using the TF method from combined W and Z.* Expected and observed 95% CL lower limits on M_D as a function of the number of extra dimensions in the ADD model for the four selection regions.

δ	Region1	Region2	Region3	Region4
2	5.64 e+01	4.08 e+01	3.61 e+01	3.28 e+01
3	8.98 e-04	6.70 e-04	5.85 e-04	5.14 e-04
4	3.34 e-06	2.60 e-06	2.27 e-06	1.98 e-06
5	1.14 e-07	9.11 e-08	7.99 e-08	7.12 e-08
6	1.19 e-08	9.69 e-09	8.59 e-09	7.66 e-09

Table 79: *Produced using the TF method from combined W and Z.* 95% CL observed upper limits on the size of the extra dimensions, R [μm], for each number of extra dimensions, and in each signal region.

	Expected [pb]	Observed [pb]
Region1	1.03	1.13
Region2	0.14	0.15
Region3	0.026	0.030
Region4	0.007	0.006

Table 80: *Produced using the TF method from combined W and Z.* 95% CL model-independent expected and observed upper limits on $\sigma \times A$ [pb] in each of the 4 signal regions, using the TF method and the combined *W* and *Z* control regions.
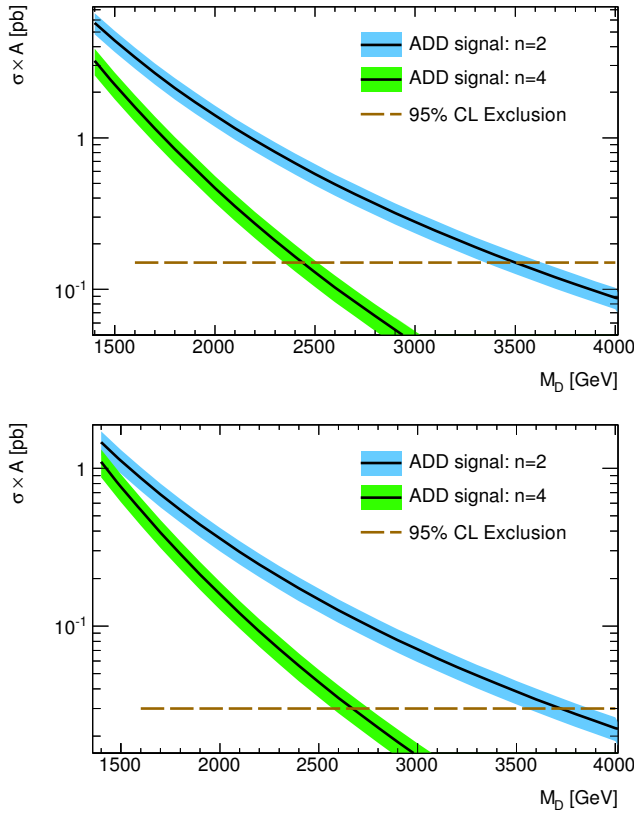
Figure 110: *Produced using the TF method from combined W and Z 95% CL observed upper limit on cross-section times detector acceptance for region 2 (left) and region 3 (right). Are also shown two cross section curves predicted by the effective theory for 2 and 4 extra dimensions.*
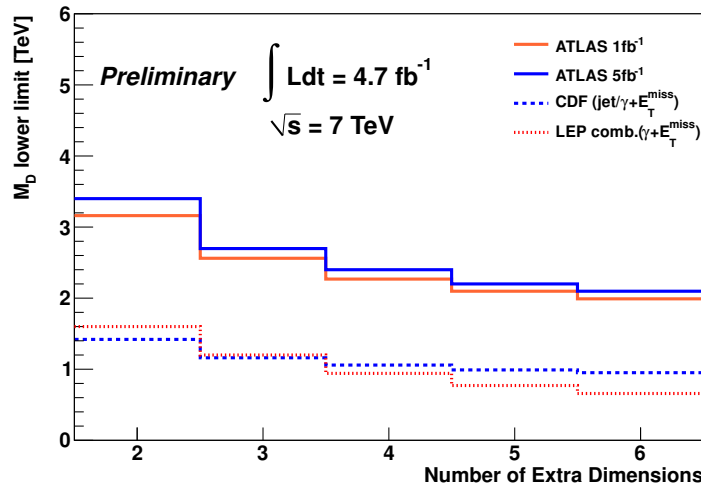
Figure 111: *Produced using the TF method from combined W and Z. 95% CL observed lower limits on M_D for different numbers of extra dimensions. Results are taken from region 2 (although we didn't show the truncated results but we know from EPS results that the truncation effect is reasonnable for region 2.)*

12.2 WIMP Pair Production

12.2.1 Introduction
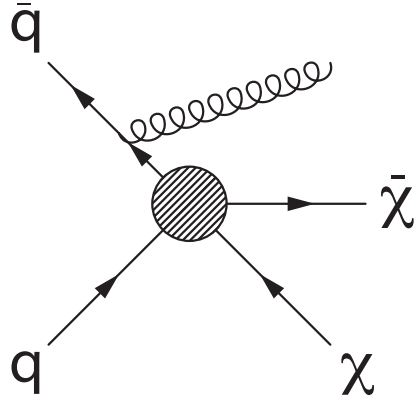
Figure 112: Dark Matter production in association with a single jet at the LHC (sketch from [17]).

A monojet final state can be interpreted as a pair of Weakly Interacting Massive Particles (WIMPs) that is boosted to yield $E_{\mathrm{T}}^{\mathrm{miss}}$ by an initial state radiation jet or photon (cf. for example [18] and [17] and references therein), see the sketch in Figure 112. This process can be described as a contact interaction and is potentially measurable at the LHC under the following assumptions:

- WIMPs can be pair produced at the LHC, that is, their mass is kinematically in reach and they couple to the Standard Model.

- Any new particle mediating the new interaction between WIMPs and the Standard Model (*the mediators*) is at a high scale and too heavy to be produced directly at the LHC. In this case the mediators can be effectively integrated out and the interaction is reduced to a contact interaction.

Name	Operator	Name	Operator
D1	$\frac{m_q}{(M^\star)^3}\bar{\chi}\chi\bar{q}q$	D2	$\frac{m_q}{(M^\star)^3}\bar{\chi}\gamma^5\chi\bar{q}q$
D3	$\frac{m_q}{(M^\star)^3}\bar{\chi}\chi\bar{q}\gamma^5 q$	D4	$\frac{m_q}{(M^\star)^3}\bar{\chi}\gamma^5\chi\bar{q}\gamma^5 q$
D5	$\frac{1}{(M^\star)^2}\bar{\chi}\gamma^\mu\chi\bar{q}\gamma_\mu q$	D6	$\frac{1}{(M^\star)^2}\bar{\chi}\gamma^\mu\gamma^5\chi\bar{q}\gamma_\mu q$
D7	$\frac{1}{(M^\star)^2}\bar{\chi}\gamma^\mu\chi\bar{q}\gamma_\mu\gamma^5 q$	D8	$\frac{1}{(M^\star)^2}\bar{\chi}\gamma^\mu\gamma^5\chi\bar{q}\gamma_\mu\gamma^5 q$
D9	$\frac{1}{(M^\star)^2}\bar{\chi}\sigma^{\mu\nu}\chi\bar{q}\sigma_{\mu\nu}q$	D10	$\frac{1}{(M^\star)^2}\epsilon^{\mu\nu\alpha\beta}\bar{\chi}\sigma^{\mu\nu}\gamma^5\chi\bar{q}\sigma_{\alpha\beta}q$
D11	$\frac{1}{(4M^\star)^3}\bar{\chi}\chi\alpha_s(G_{\mu\nu}^a)^2$	D12	$\frac{1}{(4M^\star)^3}\bar{\chi}\gamma^5\chi\alpha_s(G_{\mu\nu}^a)^2$
D13	$\frac{1}{(4M^\star)^3}\bar{\chi}\chi\alpha_s G_{\mu\nu}^a\tilde{G}^{a,\mu\nu}$	D14	$\frac{1}{(4M^\star)^3}\bar{\chi}\gamma^5\chi\alpha_s G_{\mu\nu}^a\tilde{G}^{a,\mu\nu}$

Table 81: Operators coupling Dirac fermion WIMPs to Standard Model quarks of gluons.

This approach allows to put the LHC monojet search into perspective of a Dark Matter particle search. The contact interaction is parametrised with higher dimensional operators in the Lagrangian as an effec-

1376 tive field theory. The particular implementation used here is described in [18]. It implements the WIMPs
1377 as Dirac fermions. The operators originally considered are given in Table 81. These correspond to
1378 all possible Lorentz-invariant dimension-6 operators describing a contact interaction of Standard Model
1379 quarks or gluons and a pair of WIMPs (cf. [18] for more details).
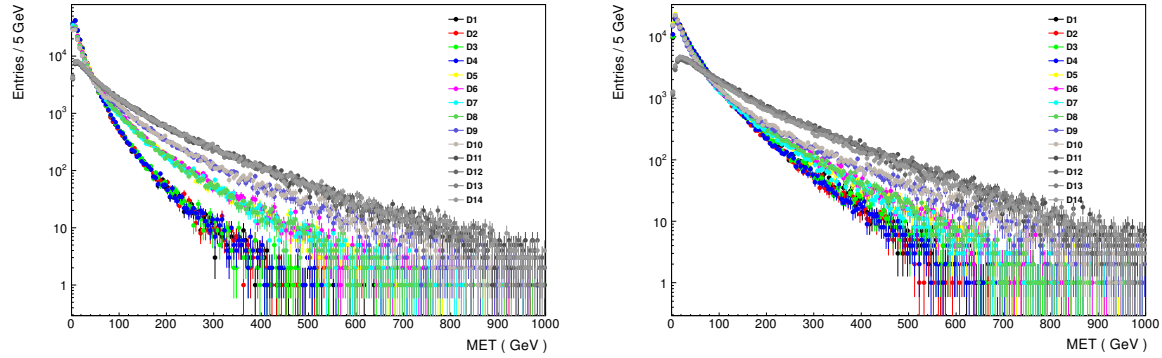
Figure 113: Operator comparisons at truth-level indicating that the acceptances fall into four classes. **Left:** 0 GeV WIMP mass, **right:** 200 GeV WIMP mass.

1380   Truth-level studies shown in Figure 113 revealed that of the 14 operators, there are four classes with
1381 distinct acceptances (that means, E_T^{miss} spectra were found to separate into four classes). Hence one
1382 operator of each class was simulated in the production system, namely *D1, D5, D9, D11*, which describe
1383 a scalar, vector, axial-vector quark-quark to WIMP-WIMP interaction, and a gluon-gluon to WIMP-
1384 WIMP interaction in that order. M^* in Table 81 is the suppression parameter that can be thought of as
1385 mass of the heavy mediator particle divided by coupling constants g, $M^* = \frac{M}{\sqrt{g_{SM}g_{WIMP}}}$ for one possible
1386 UV completion. M^* is set to 1 TeV in all simulated samples. It was verified that the acceptance does not
1387 change with M^*, as shown in Figure 114 (left).
1388   For each operator, four WIMP mass points were simulated, 10, 50, 100, 200 GeV (20k events each
1389 point). The choice of these four mass points was done based on Figure 114 (right), were truth E_T^{miss}
1390 distributions are shown for operator D1 for a number of different WIMP masses. Late during the analysis
1391 review an additional set of four mass points, 400, 700, 1000, 1300 GeV, was requested for simulation.
1392 These additional points will be eventually added, the sample generation is in its final phase.
1393   The contact operator implementation is done in MadGraph5, which is interfaced to Pythia6 (MC11c).
1394 With a lead-parton cut of 80 GeV, WIMP pairs plus one and two jets are simulated with MadGraph, the
1395 Pythia parton shower is added to these events with MLM matching (QCUT 80 GeV). Operators D1 and
1396 D5 have substantially steeper E_T^{miss} spectra than D9 and D11, and it turned out that with 20k events
1397 the high-pt signal regions were not sufficiently populated. A second sample for each mass point was
1398 therefore done, with a lead-parton cut of 300 GeV, again 20k events. E_T^{miss} distributions illustrating the
1399 two samples with different lead parton cuts are shown in Figure 115 for D1 and D5.
1400   Fast-simulation samples (*Atlfast2*) have been requested in all cases (cf. Section 12.1 for a full- versus
1401 fast-simulation comparison), the production cross sections are given in Section 2, Table 7.

12.2.2 Systematic uncertainties

1403 The systematic uncertainties are evaluated like:

1404 • **ISR/FSR:** following the SUSY group recipe (`https://twiki.cern.ch/twiki/bin/viewauth/`
1405 `AtlasProtected/SUSYMadGraph`), the MLM matching scale is varied up and down by a factor
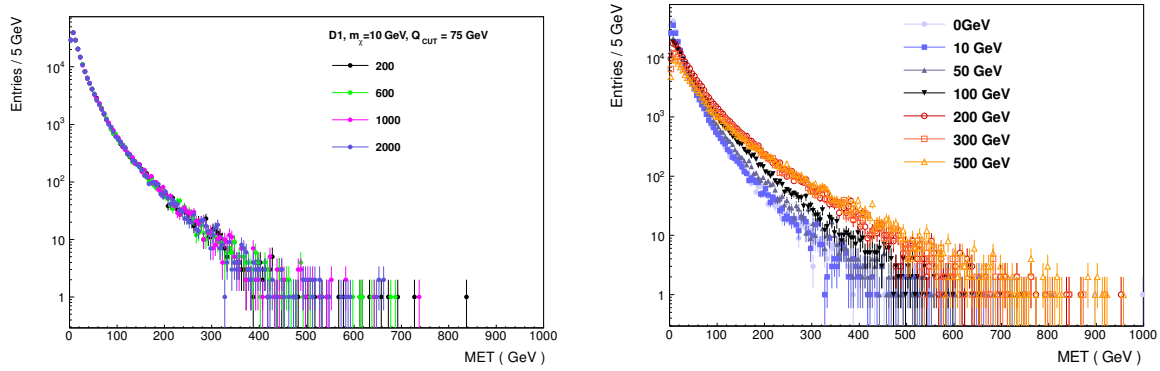
Figure 114: **Left:** E_T^{miss} spectra for a number of values of M^* (200, 600, 1000, 2000 GeV), demonstrating that the acceptance does not change with this suppression scale parameter. **Right:** Truth E_T^{miss} spectra for operator D1 for a range of WIMP masses illustrating modest acceptance changes with increasing WIMP masses.

of two, in addition α_s is varied by using 4th generation Pythia tunes 351 and 352 (equivalent to varying PARP(64).

Truth-samples for all four signal regions have been studied for D5 and D11, at 10 and 200 GeV WIMP mass, respectively. No dependence on operator or WIMP mass was found, hence the uncertainties are averaged over these two operators and WIMP masses, and they amount to 2.8 to 6.3%. Figure 116 middle and bottom show the resulting matching scale and α_s uncertainties for D5 and D11, Table 82 lists the exact values used.

- **Renormalisation and factorisation scale:** varied at the MadGraph level by a factor of two up and down.

  Truth-samples for all four signal regions have been studied for D5 and D11, at 10 and 200 GeV WIMP mass, respectively. A moderate dependence on operator and signal region is found, in all cases uncertainties range from 20 to 30%, see Figure 116 (top) for an overview of the scale uncertainties in all signal regions for operators D5 and D11. Given that MadGraph is a leading order (LO) generator, and event scales are somewhat ill defined in LO calculations, the largest uncertainty found (31.5%) is conservatively used for all operators and signal regions.

- **PDF uncertainties:** instead of the nominal PDF set CTEQ6L1, CTEQ6M is used. The 40 available error sets are combined following the Hessian method to derive the relative variations (accounting for these error sets to be at 90%, not 68%).

  All simulated samples listed in Section 2, Table 7 are used in this case. Acceptance variations were found to be negligible against cross section variations for all operators. They are hence ignored. The systematic uncertainties from cross section variations amount to 29% for D1, 8% for D5, 6% for D9, and 27% for D11. This one number is used per operator for all signal regions.

- **JES, JER, and missing ET:** uncertainties are determined in a combined way using the standard jet/etmiss uncertainty providers.

  All simulated samples listed in Section 2, Table 7 are used here. The uncertainties are found to vary over operators and signal regions, ranging from 1 to 19%.
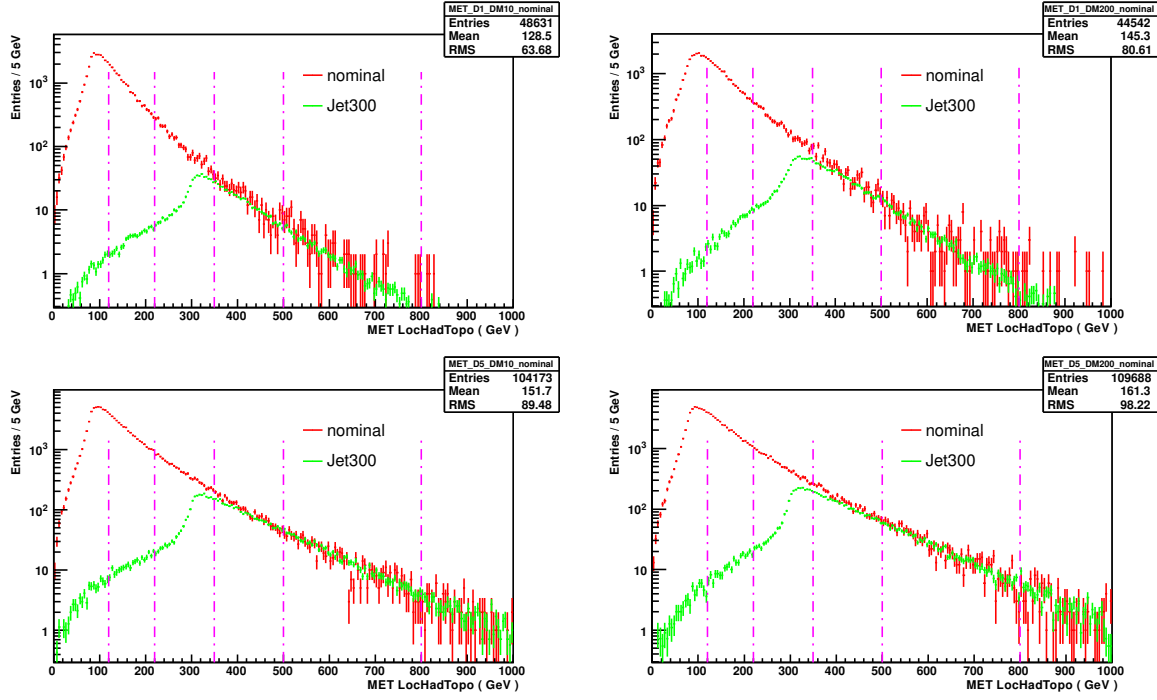
Figure 115: Simulated samples for D1 and D5, 10 and 200 GeV WIMP mass, with lead parton cuts at 80 and 300 GeV, normalised by the respective cross sections.

- The luminosity and trigger efficiency uncertainty amount to 3.9% and 0.66%, respectively (see above), and are summed in quadrature with the values quoted above.

All resulting uncertainties are summarised in Table 82.

Uncertainty	Operator	SR1	SR2	SR3	SR4
JES / JER / $E_{\mathrm{T}}^{\mathrm{miss}}$	D1	6.4	8.8	13.7	18.8
	D5	5.2	7.9	10.3	17.2
	D9	3.3	5.1	6.5	12.2
	D11	0.8	2.3	5.6	10.0
α_s	All	4.4	5.2	6.3	6.3
Matching scale	All	2.8	2.8	2.8	5.1
Event scale Q	All	31.5	31.5	31.5	31.5
PDF	D1	17.6	17.6	17.6	17.6
	D5	4.9	4.9	4.9	4.9
	D9	3.6	3.6	3.6	3.6
	D11	16.4	16.4	16.4	16.4
Luminosity	All	3.9	3.9	3.9	3.9
Trigger	All	0.66	0.66	0.66	0.66

Table 82: Overview of WIMP signal relative uncertainties (percentage).
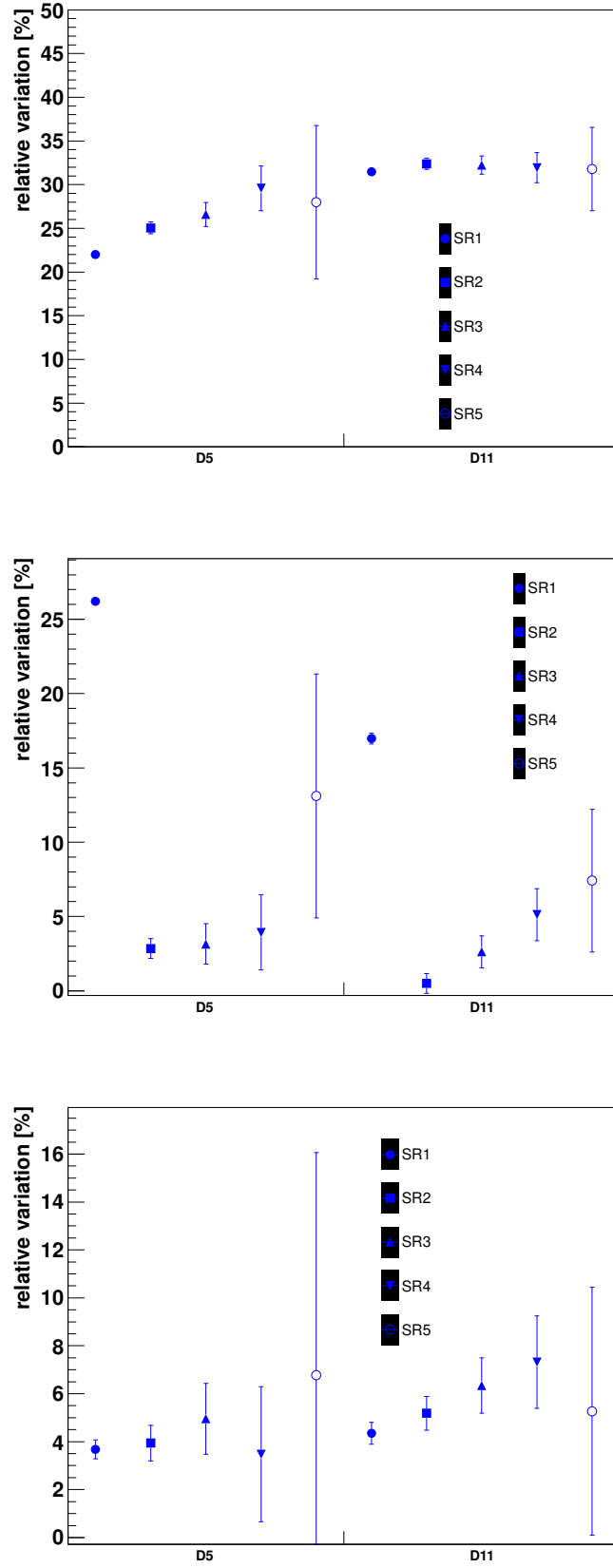
Figure 116: Systematic uncertainties obtained from operators D5 and D11 in the four signal regions, averaged over 10 and 200 GeV WIMP masses. Shown from top to bottom are the renormalisation and factorisation scale uncertainties, the matching scale uncertainties, and the uncertainties from the value of α_s. **Note** that the SR1 point of the middle plot (matching scale) is artificially large and not considered for any uncertainty. When varying the matching scale up by a factor of two to 160 GeV the SR1 E_T^{miss} falls into the turn-on region of the spectrum.

12.2.3 Limits on $M^\star$

As in Section 12.1.3, limits on New-Physics signatures are derived using `HistFitter` [18]. Limits on the visible cross section of any New Physics signature are given in Table 83. These limits do not rely on any particular model. Note that the limits are calculated at 90% **and** 95% confidence level. This is because these limits are needed in the next section for comparisons with other experiments searching for particle Dark Matter, and depending on the field either 90 or 95% are commonly used.

Signal region	Expected σ_{vis} (pb)		Observed σ_{vis} (pb)	
	90% CL	95% CL	90% CL	95% CL
Region1	1.465	1.743	1.536	1.807
Region2	0.135	0.160	0.113	0.136
Region3	0.020	0.024	0.026	0.030
Region4	0.006	0.008	0.006	0.007

Table 83: 90% confidence level upper limits on $\sigma \times A$ (*visible cross section,* σ_{vis}) in the four signal regions.

Figure 117 compares the limits on the visible cross section per signal region (cf. Table 83) to theory curves including systematic uncertainties on the signal. The plots illustrate how signal uncertainties affect the limits on $M^\star$ (in a rather modest way).

Figure 118 shows the final limits on the suppression scale $M^\star$ at 90% CL. The limits are compared for all four signal regions, expected versus observed in all cases. The final limits are based on the signal regions with the best expected limit. They are shown in figures 119 and 120 at 90 and 95% confidence level, respectively. The limit presentation follows the SUSY group recipe detailed at `https://twiki.cern.ch/twiki/bin/viewauth/AtlasProtected/SUSYLimitPlotting`. Thick dashed red lines correspond to the actual observed limits including only experimental uncertainties. Experimental uncertainties for the signal are assumed to be fully correlated with those of the background estimates. Thinner dashed red lines correspond to the $\pm 1\sigma$ theoretical uncertainties on the observed limits. This is to illustrate the impact of PDF, ISR/FSR, and event scale (Q) uncertainties on the limit. Finally the black dashed line surrounded by a gray band is the expected limit without theory uncertainties including its 1σ band. The limits taken as search result are the lower thin red dashed lines, that is, the observed central limit -1σ theory uncertainty.

Figures 119 and 120 feature a green *thermal relic* line. These values are taken from [18]. They correspond, for a given WIMP mass value, to the value of M^* at which WIMPs annihilating exclusively via the given operator to quarks or gluons result exactly in the thermal relic density observed with WMAP [19]. Larger cutoff scales correspond to weaker couplings, hence values of M^* above the green line correspond to overabundant WIMP densities in conflict with WMAP's measurement. Such regions are effectively ruled out.

---

[18]`https://twiki.cern.ch/twiki/bin/viewauth/AtlasProtected/SusyFitter`
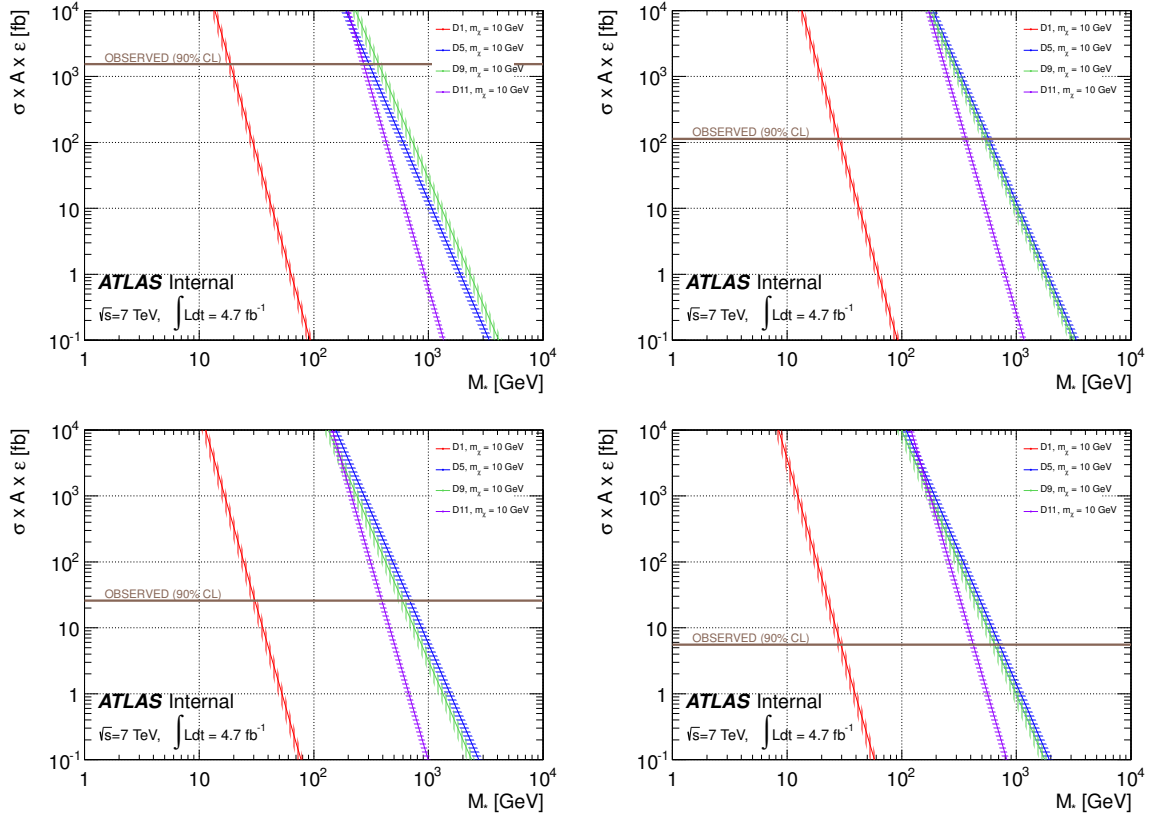
Figure 117: Observed 90% confidence level upper limits on $\sigma \times A \times \epsilon$ (σ_{vis}, solid horizontal line) compared to WIMP model curves as a function of the suppression scale $M^\star$. The error bands correspond to the systematic signal uncertainties given in Table 82. **Top left:** signal region 1, **top right:** signal region 2, **bottom left:** signal region 3, **bottom right:** signal region 4.
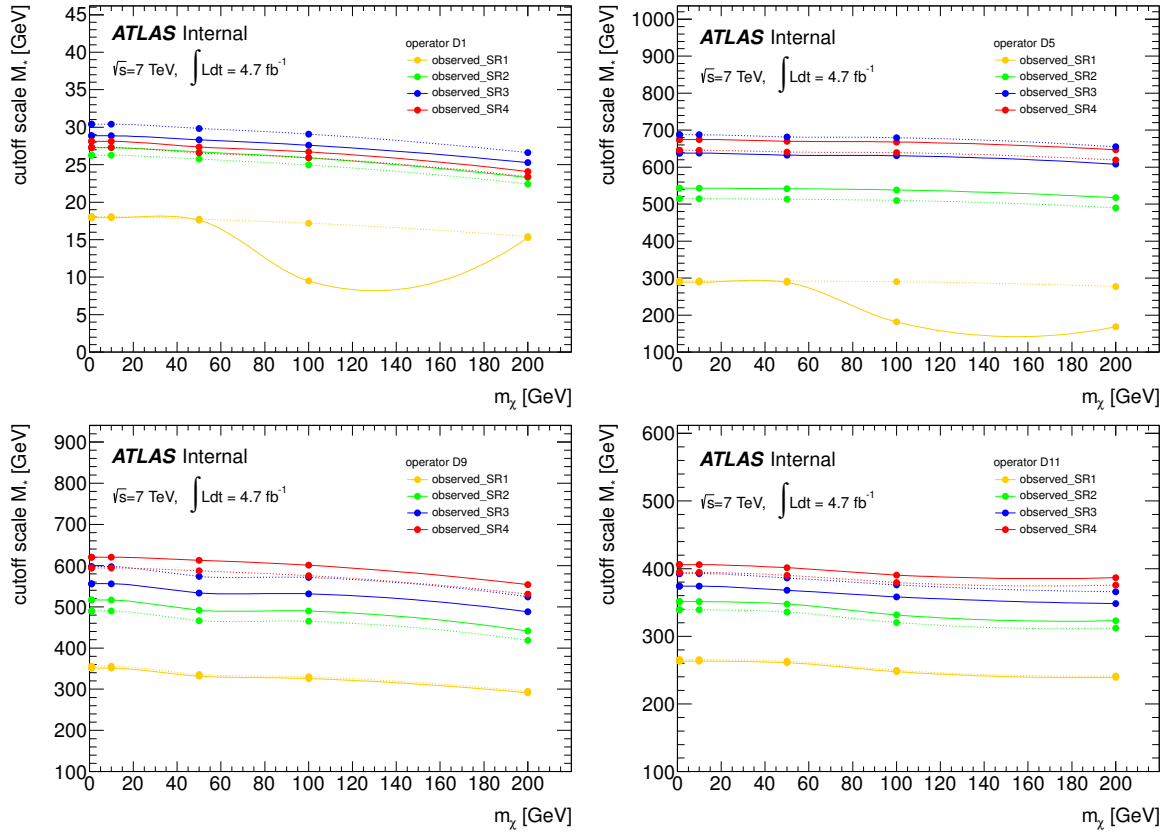
Figure 118: 90% confidence level limits on $M^\star$ versus WIMP mass. All operators are shown here, four signal regions are in each case compared to each other. Observed limits are solid lines, expected ones are dashed. Changes of observed with respect to expected limits in SR1 (100 and 200 GeV for D1 and D5) are considered a technical problem of the limit setting. This problem is ignored since SR3 and SR4 have better sensitivities to all operators tested, and are hence used for final limits.
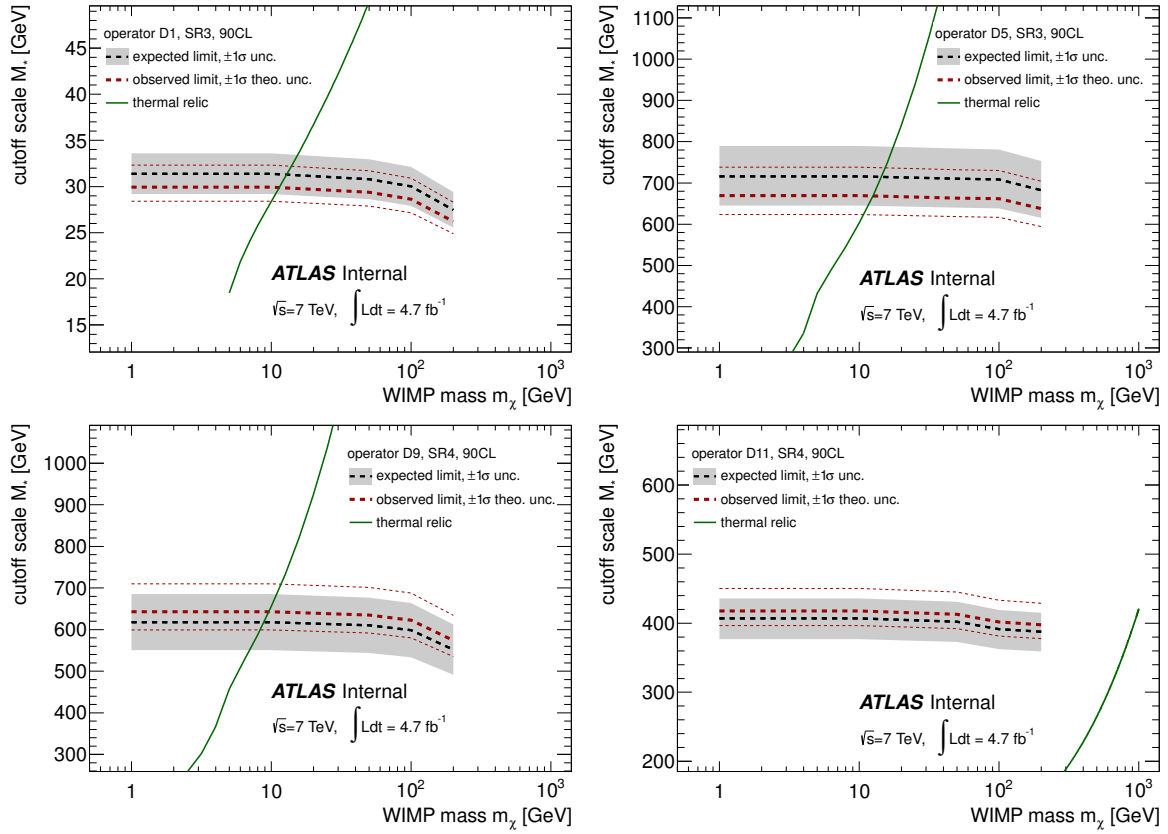
Figure 119: Final limits at 90% CL. Displayed are the final observed and expected limits not including theory uncertainties (PDF, ISR/FSR, scale Q) as dashed thick red and black line, respectively. The gray error band corresponds to the $\pm 1\sigma$ uncertainty on the expected limit. The slightly thinner dashed red lines illustrate the $\pm 1\sigma$ signal theory uncertainties on the observed limit. Quoted as limit on M^* is the lower thin dashed red line.
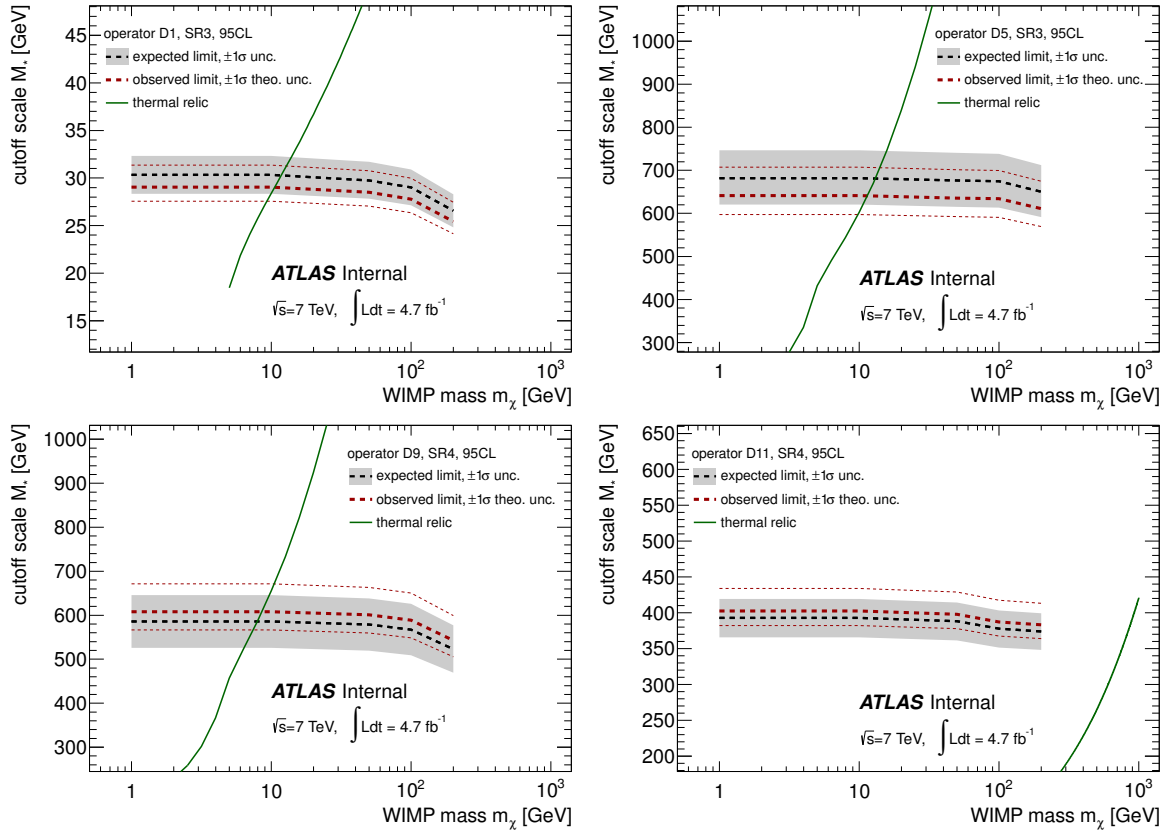
Figure 120: Final limits at 95% CL. Displayed are the final observed and expected limits not including theory uncertainties (PDF, ISR/FSR, scale Q) as dashed thick red and black line, respectively. The gray error band corresponds to the $\pm 1\sigma$ uncertainty on the expected limit. The slightly thinner dashed red lines illustrate the $\pm 1\sigma$ signal theory uncertainties on the observed limit. Quoted as limit on M^* is the lower thin dashed red line.

12.2.4 Valid region of effective field-theory approach

The effective field theory used here to parametrise WIMP pair production may break down at LHC energies. The precise point at which the breakdown occurs depends on the UV physics, that is, the unknown physics at the high scale that is attempted to be captured with the effective field theory at the low scale.

If one imagines the UV completion of the contact interaction to be an interaction mediated by a heavy particle, that is too heavy to be produced at the LHC and integrated out in the effective field theory, the mapping of the suppression scale M^* to the parameters of the UV complete theory, which are the mass of the heavy mediator M and the coupling constants for incoming SM particles and outgoing WIMPs, may be expressed as $M^* = \frac{M}{\sqrt{g_{SM}g_{WIMP}}}$. The effective field theory is valid as long as M is very large. Thus even for moderate values of M^* the mass parameter M can be very large if the theory is strongly coupled, if the coupling constants are large. Since an effective theory requires $M > 2m_{WIMP}$, and a perturbative theory $g_{SM}g_{WIMP} \leq (4\pi)^2$, the strongest coupled UV completion can satisfy $m_{WIMP} = 4\pi M^*$. In other words, for a given WIMP mass, there is a lower bound on M^*: $M^* > m_{WIMP}/(4\pi)$ where the UV completion is as strongly coupled as makes sense. This lower bound is indicated by the filled gray area in the M^* limits in Figure 121. Note that the operator D1 is normalised by the quark mass m_q. This factor is artificially decreasing the suppression scale parameter M^* and is taken out when calculating the lower bounds in the figure.

Similar to the argument made above, the effective field theory is strictly speaking only valid if the mediator mass is larger than the energy transfer in the event. Since the actual break down of the effective field theory depends on the unknown UV completion, no further criteria on the event energy transfer are applied here to avoid invalid regions, not to make further assumptions about the unknown high-scale physics.
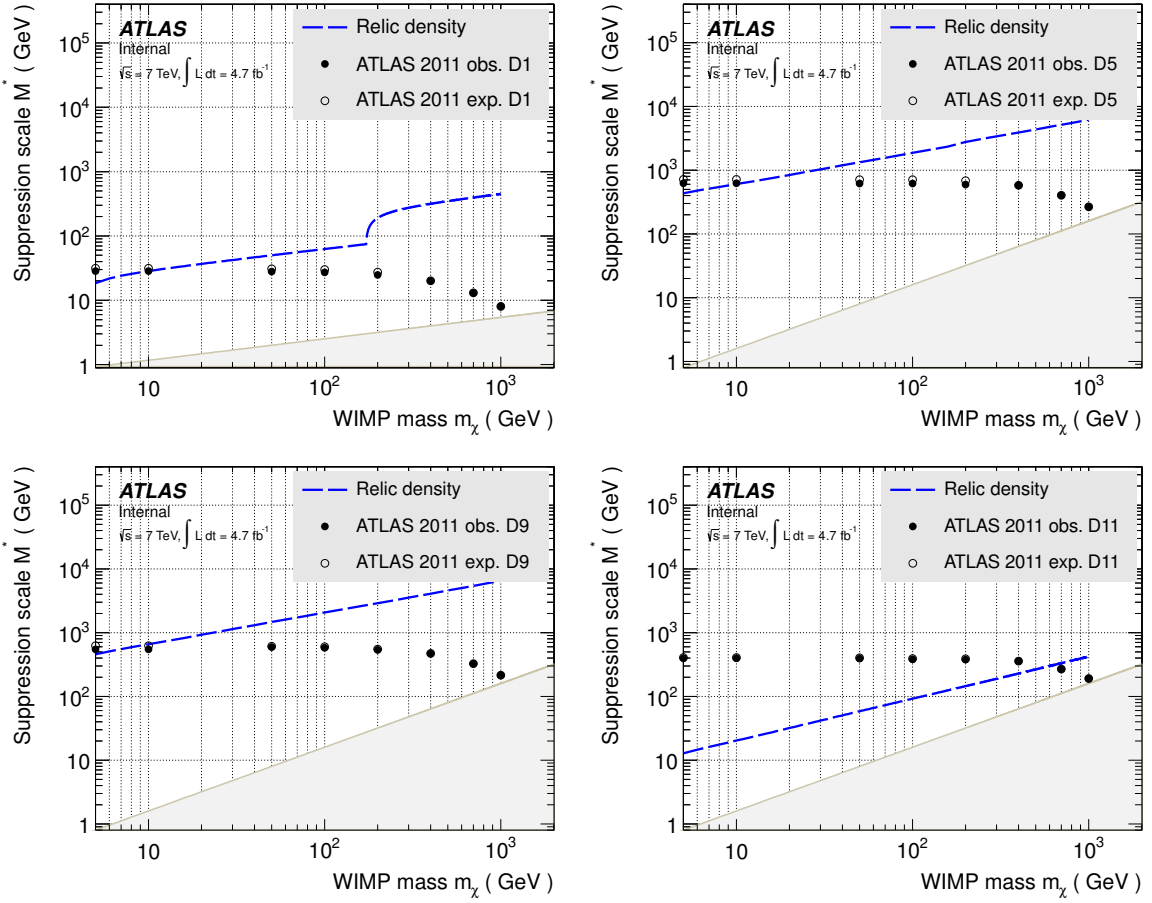
Figure 121: Reproduction of M^* limits shown in Figure 119, indicating for illustration the region where the effective field theory breaks down as filled gray region.

12.2.5 LHC limits in direct and indirect Dark Matter detection plane

The contact operator approach to WIMP pair production at the LHC is useful for comparing limits on particle Dark Matter between different fields. In the following, the ATLAS limits on the suppression scale parameter $M^\star$ are converted and compared to limits on the WIMP-nucleon cross section determined by so called direct detection experiments and to limits on the annihilation cross section of WIMP pairs in the early universe as determined by very-high-energy gamma-ray experiments.

The ATLAS limits on WIMP-nucleon scattering are shown in figures 122 and 123. The conversion of ATLAS M^* limits to scattering cross sections is done as described in [18]. Note that limits for 1 and 5 GeV WIMP mass are produced from the 10 GeV mass point. This is feasible because WIMPs of 1, 5, or 10 GeV mass are produced with identical cross sections and kinematic distributions at the LHC (verified at truth level). Moreover, an additional operator is shown in figure 123, D8, which is an axial-vector interaction that produces spin-dependent WIMP-nucleon scatterings. This limit is derived from D5, the vector operator, which is identical in cross section and kinematics at the LHC.

Figure 124 illustrates the ATLAS limits on vector and axial-vector interactions in the annihilation cross section versus WIMP mass plane. The conversion is done following [17], assuming WIMPs annihilate exclusively to the four light quark flavours (which are the ones that were simulated for the ATLAS limits). Once again the thermal relic cross section value is indicated denoting the lower bound of the annihilation cross section. Values below this line would result in overabundant WIMPs in the early universe.
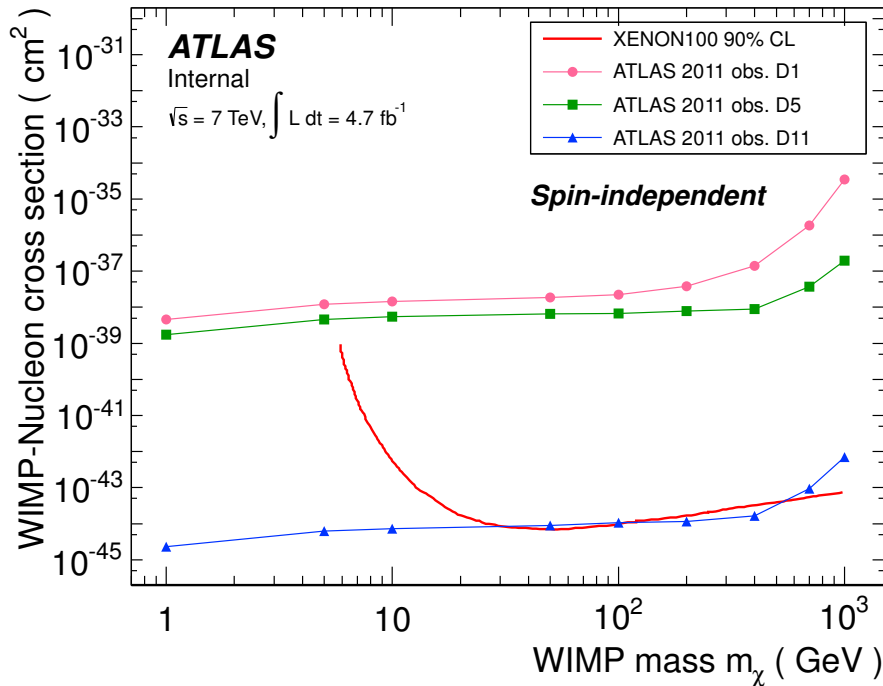
Figure 122: ATLAS 90% CL limits transferred to direct Dark Matter detection plane of **spin-independent** WIMP-nucleon scattering cross sections versus WIMP mass. **Note that WIMP masses up to 1 TeV are shown here. These values are predictions and to be taken as placeholders until new high-mass simulations are done.**
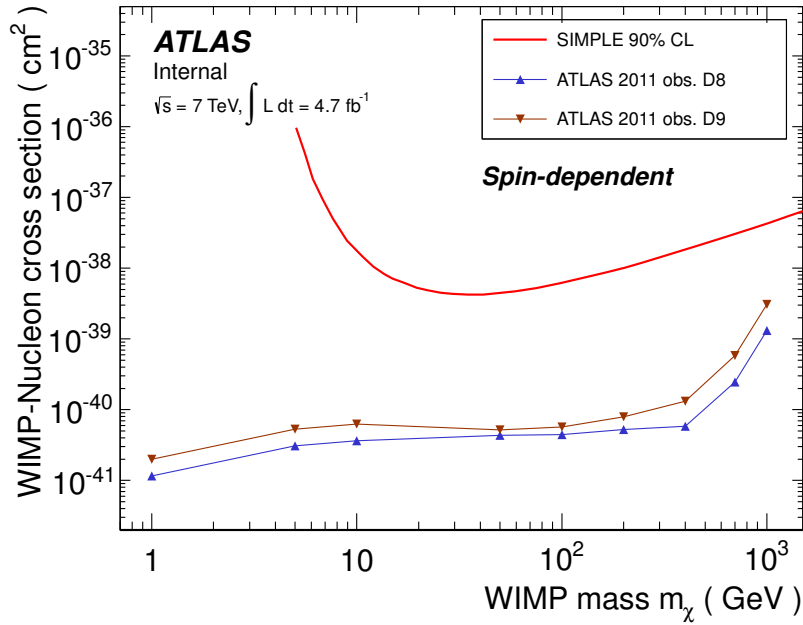
Figure 123: ATLAS 90% CL limits transferred to direct Dark Matter detection plane of **spin-dependent** WIMP-nucleon scattering cross sections versus WIMP mass. **Note that WIMP masses up to 1 TeV are shown here. These values are predictions and to be taken as placeholders until new high-mass simulations are done.**

12.2.6 Validation of MadGraph implementation

To validate the operator implementation, cross sections of the MadGraph5 model were compared to those obtained by another group of theorists with both MadGraph4 and MadGraph5 (for the same operators). Furthermore, a Pythia Z' implementation for a very large mass was used to validate kinematic distributions of the operator describing a vector interaction (D5). The good agreement found is a non-trivial cross check of the operator implementation used.

12.2.7 Issues

There are two issues with the simulated MadGraph samples. Number one appeared when comparing the cross sections output by MadGraph for different MadGraph versions. MadGraph5 in version 1.3.16 was used for the production samples, version 1.3.33 was used as a cross check. The latter version produces larger cross sections, and slightly different kinematic distributions (negligible compared to the systematic signal uncertainties). The problem is related to a bug in the matching code of MadGraph5, that was fixed for version 1.3.33. The problem is accounted for by using the correct cross sections, neglecting the small differences in kinematic distributions.

The second problem was found when comparing limits of the gluon operator D11 to published limits of a gluon contact operator implementation (in the paper using the ATLAS EPS 2011 monojet result to set WIMP pair production limits, [17]). It turned out that the simulated version of the gluon operator was missing a factor of α_s, which resulted in $1/\alpha_s^2$ too large cross sections, and, since MadGraph evaluates α_s per event at the hard scale of the event, the missing factor resulted in modified kinematic distributions, too. None of the kinematic changes introduced significant differences, given the large systematic uncertainties of the WIMP operators. Hence the cross section is corrected, the kinematic distributions are kept
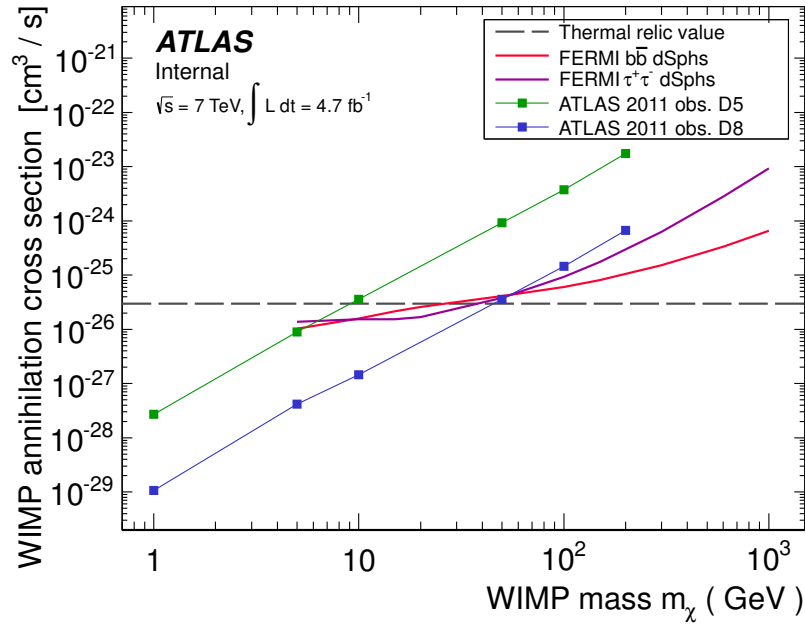
Figure 124: ATLAS 95% CL limits transferred to indirect Dark Matter detection plane of velocity averaged WIMP annihilation cross sections versus WIMP mass. For comparison high-energy gamma-ray limits from the FERMI LAT [20] are shown, too.

1525 unchanged.

13 Conclusion

The search for physics beyond the Standard Model in events with a final state consisting of an energetic jet and large missing transverse energy has been performed using 4.7 fb^{-1} of Data collected by the ATLAS detector. The analysis is improved with respect to the previous ATLAS results and covers four inclusive kinematic signal regions, mainly defined by symmetricly increasing lower thresholds on the missing transverse energy and the leading jet p_{T}, from 120 to 500 GeV. The main background, originating from electroweak processes, has been determined with a data-driven method, using control regions based on W and Z events in the electron and muon channels.

The Data has been compared to the Standard Model background, and a good agreement has been observed. Model-independant 95% CL upper bounds on $\sigma \times A \times \epsilon$ have been set in each of the four signal regions. These limits are 1.81, 0.14, 0.03 and 0.007 pb, respectively. In addition, two theoretical models are tested.

The results are interpreted in the context of the Large Extra Dimensions ADD scenario. An effective field theory, valid below the scale M_D, is used to calculate the ADD graviton production cross-sections. 95% CL lower limits are set on the scale of the theory, M_D, for various number of extra dimensions. Using the CTEQ6.6 PDF set, and the second signal region, the observed 95% CL lower limits on M_D are 3.46, 2.72, 2.39, 2.17, and 2.06 TeV for 2 to 6 extra dimensions, respectively.

In addition, the search is also put into the context of particle Dark Matter by interpreting the final state as WIMP pair production. An effective field theory approach is followed, and limits are set on the suppression scale of the effective theory, M^*, as a function of WIMP mass. The monojet search criteria were not optimised for this particular interpretation, but were verified to achieve reasonable sensitivity.

Depending on the type of interaction assumed for the SM–WIMP contact vertex, 95% CL limits on M^* range from 28 to 600 GeV are set. One of the strengths of the effective field theory approach is that with a few assumptions it allows to transfer LHC WIMP limits determined in a large-momentum transfer environment to low-momentum transfer environments that are usually explored by direct or indirect Dark Matter searches (looking for signs of WIMP-nucleon scatterings or WIMP annihilations). Compared to these experiments, LHC limits can be very competitive at small WIMP masses (10 GeV and below), assuming the chosen interaction type exists and the contact operator approach is valid. This demonstrates a particular strength of particle colliders in searches for Dark Matter, and illustrates the complementarity of the different experimental approaches to search for particle Dark Matter.

A   Studies on the inclusive muon control region

In this appendix we detail two studies that support the possible use of an inclusive muon control region (from now on called IMCR). The IMCR has the same selection cuts as the signal region but requiring at least one muon. For this control region there is no further selection. This has been decided in order to reduce systematic and statistical uncertainties on the EW background prediction. In principle, every selection cut applied in defining the control region that has not a corresponding signal-region cut has the potential to enhance the systematic uncertainties since it will rely on the MC description and will not be cancelled out in the ratios defining transfer factors.

At large transverse momenta, a selection on the transverse mass of the W will not help in reducing QCD background that already has a negligible contribution[19]. In addition, other backgrounds with real Ws decaying with leptons in the final state (ttbar and diboson contributions) are not suppressed.

In the sub-section A.1 we present a study on possible QCD multi-jet background in the IMCR. Instead in sub-section A.2 we show a comparison between events at low transverse mass ($M_T < 40 GeV$) and those at the W peak ($40 GeV < M_T < 100 GeV$).

A.1   QCD multi-jet background in the inclusive muon control region

In this subsection we want to estimate the contamination of the QCD background in the IMCR. This background is expected to be very small because of the high E_T^{miss}, the $\Delta\phi(E_T^{miss}, j2)$ cut and for the presence of at least an isolated muon. Nevertheless we want to estimate the QCD contamination in a data-driven way to make sure that the backgrounds description in the IMCR is under control.

To do this estimation we use a modified version of the method used for the QCD background in the signal region (section 9). First we create a di-jet control region with a muon, requiring:

- at least one reconstructed muon

- a second leading jet with $p_T > 30 GeV$ and $\Delta\phi(E_T^{miss}, j2) < 0.5$ cut

This control region is dominated by W+jets and Z+jets events, but the QCD events are enhanced respect to the IMCR, because we require a second jet aligned with the E_T^{miss}. As it is done in section 9 we want to extrapolate the distribution of the second leading jet p_T below the 30 GeV threshold after a subtraction of the non-QCD processes. The second jet p_T distribution after this sutraction is shown in figure 125. The points near the 30 GeV threshold are below zero because of a non perfect subtraction. Therefore is not possible to do an extrapolation. If we would have get an extrapolated function of 50 events per bin to QCD estimated background would have been 300 events, that is 0.3% of the total number of events in the whole control region. Therefore we conclude the QCD background in the IMCR is indeed negligible.

This QCD estimation is done for region A. For signal regions with higher cuts in E_T^{miss} and leading jet p_T the relative contamination of QCD events is expected to be lower then in region A.

A.2   MC description at low transverse mass

Figures 126, 127 and 128 show a comparison of the distribution of muons, jets and E_T^{miss} between the events at low transverse mass ($M_T < 40 GeV$) and those at the W peak ($40 GeV < M_T < 100 GeV$). The events at $M_T < 40 GeV$ are also well described by AlpGen. This further proves that there is no need for a cut on transverse mass and that one can make full use of the entire kinematic range and MC statistics to define the control regions and the transfer functions and reduce the related systematic uncertainties.

---

[19]In W+jets cross section measurements ATL-COM-PHYS-2011-769 a cut on the transverse mass is applied in order to suppress the QCD background. But due to the high E_T^{miss}, the $\Delta\phi(E_T^{miss}, j2)$ cut and the presence of an isolated muon the contribution of QCD multi-jet events is negligible.
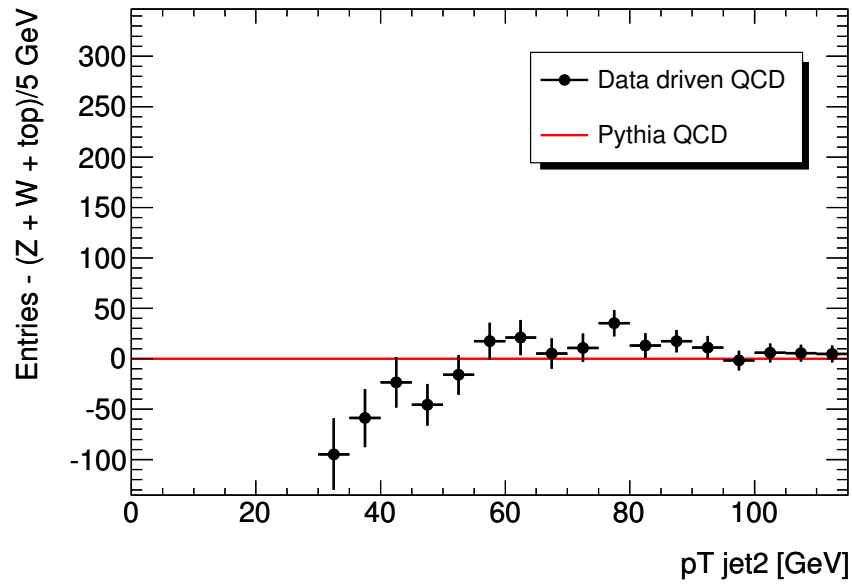
Figure 125: QCD background estimation in the inclusive muon control region. The plot shows the second leading jet p_T extrapolation after the subtraction of non QCD process. Points can go below zero for a non perfect subtraction. The extrapolation of the points below $70 GeV$ gives a negative result and therefore is not taken into account.
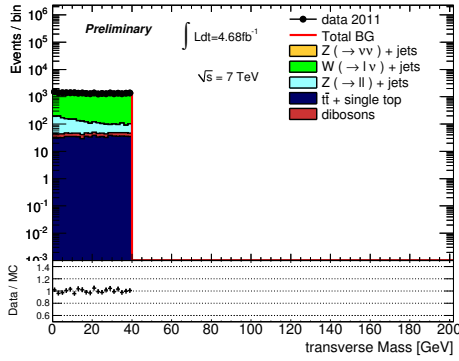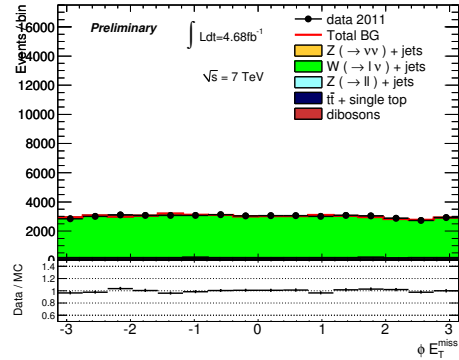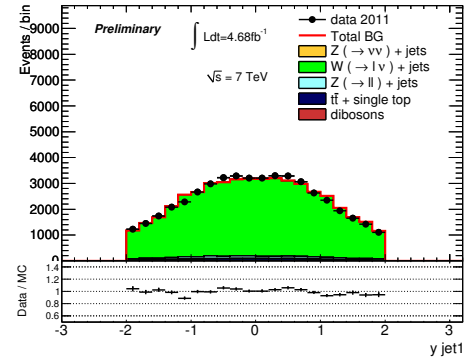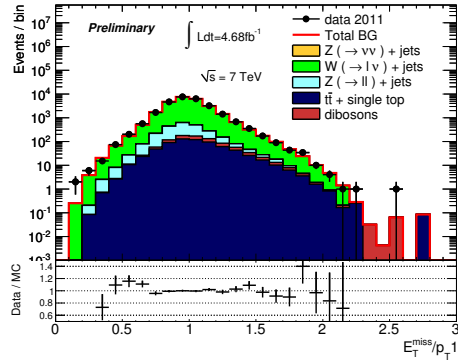
(a)
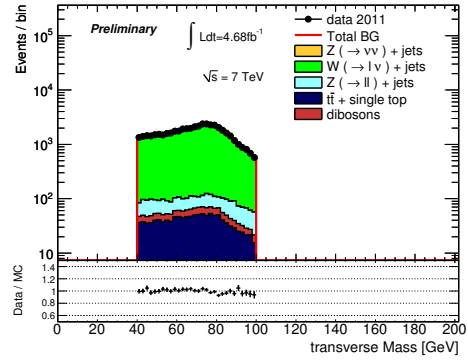
(b)
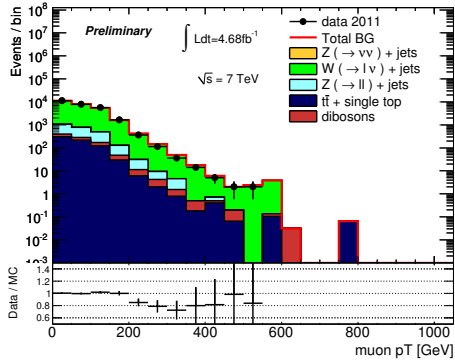
(c)
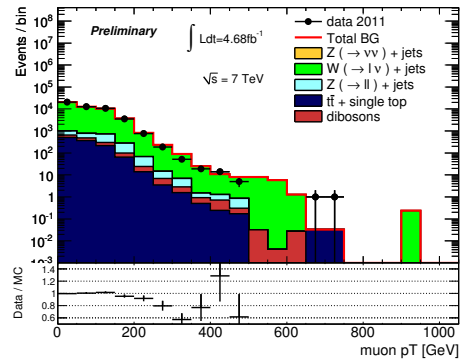
(d)
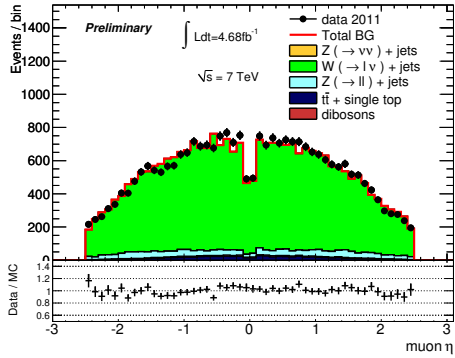
(e)
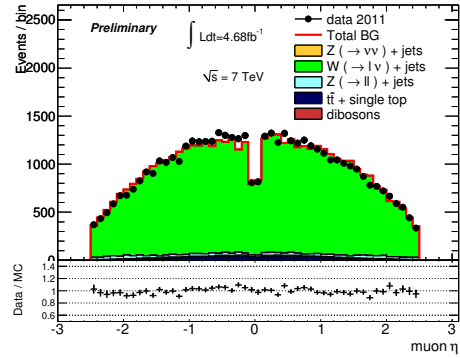
(f)

Figure 126: The plots on the left are from the events with $M_T < 40 GeV$ and the ones on the right are those with $40 GeV < M_T < 100 GeV$. The distributions are the transverse mass itself (figures (a) and (b)), the muon p_T (figures (c) and (d)) and muon pseudorapidity (figures (e) and (f)). These plots make use of AlpGen W+jets and Z+jets samples.
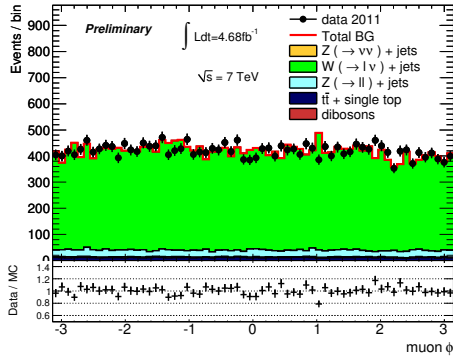
(a)
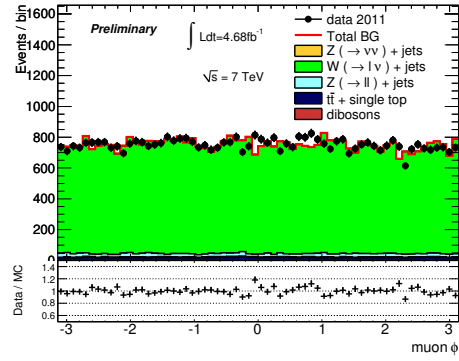
(b)
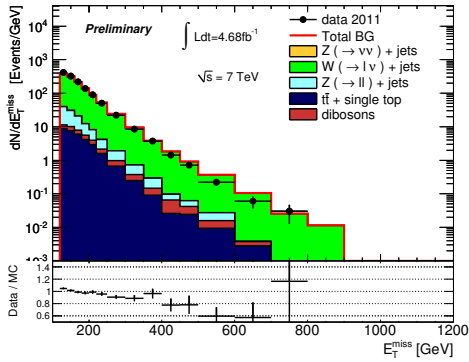
(c)
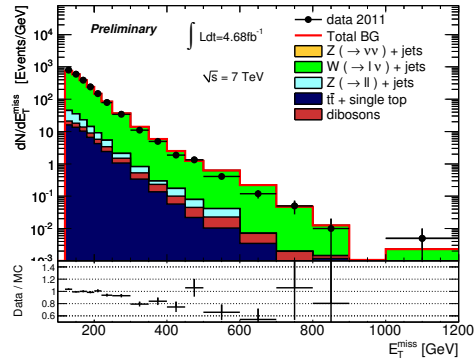
(d)
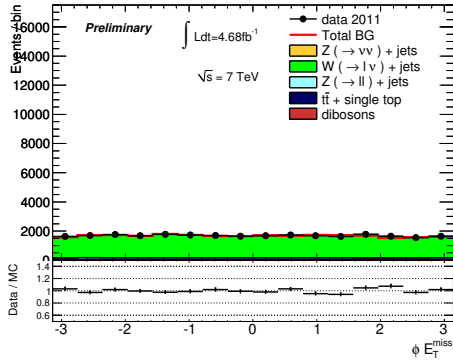
(e)

(f)

Figure 127: The plots on the left are from the events with $M_T < 40 GeV$ and the ones on the right are those with $40 GeV < M_T < 100 GeV$. The distributions are the muon ϕ (figures (a) and (b)), the E_T^{miss} (figures (c) and (d)) and the ϕ of the E_T^{miss} (figures (e) and (f)). These plots make use of AlpGen W+jets and Z+jets samples.
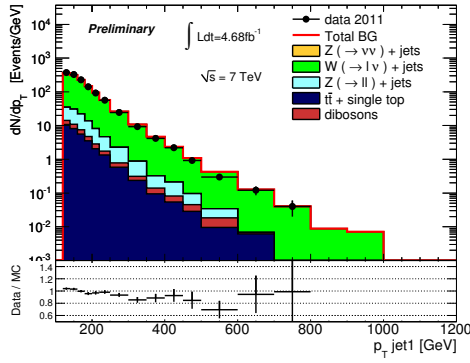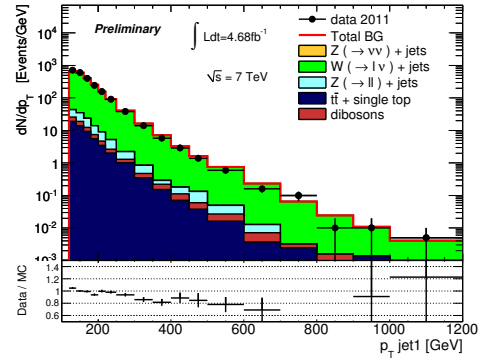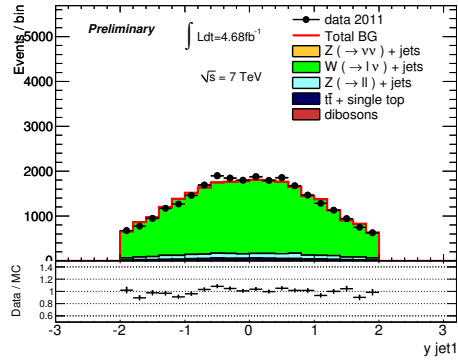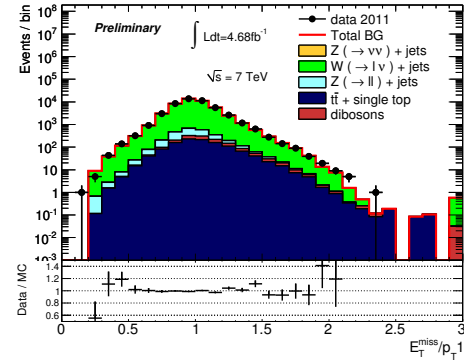
Figure 128: The plots on the left are from the events with $M_T < 40 GeV$ and the ones on the right are those with $40 GeV < M_T < 100 GeV$. The distributions are the leading jet p_T (figures (a) and (b)), the leading jet rapidity (figures (c) and (d)) and the ratio between E_T^{miss} and the leading jet p_T (figures (e) and (f)). These plots make use of AlpGen W+jets and Z+jets samples.

B Results using transfer factors and inclusive control regions

In this appendix, we collect the results based on inclusive electron and muon control regions. In this case, the inclusive muon control region (a mixture of $W \to \mu\nu$ and $Z \to \mu\mu$ contribution dominated by the Ws) is used to extract the transfer factors for $Z \to \nu\nu$+jets, $W \to \mu\nu$+jets, and $Z \to \mu\mu$+jets. The $W \to e\nu$+jets, $W \to e\nu$, $Z \to \tau\tau$+jets, and $Z \to ee$ background contributions are extracted using an inclusive electron control samples.

| | Background Predictions ± (stat.data)± (stat.MC) ± (syst.) | | | |
	Region A	Region B	Region C	Region D
$Z \to \nu\nu$+jets	$63372 \pm 316 \pm 2195$	$5285 \pm 81 \pm 181$	$504 \pm 24 \pm 23$	$55 \pm 8 \pm 4$
$W \to \tau\nu$+jets	$30041 \pm 303 \pm 730$	$1671 \pm 57 \pm 74$	$131 \pm 13 \pm 4$	$18.2 \pm 5.3 \pm 0.4$
$W \to e\nu$ +jets	$14101 \pm 151 \pm 407$	$693 \pm 28 \pm 24$	$47 \pm 5 \pm 3$	$5.5 \pm 1.8 \pm 0.5$
$W \to \mu\nu$ +jets	$11462 \pm 106 \pm 627$	$703 \pm 19 \pm 73$	$53 \pm 4 \pm 10$	$5 \pm 1 \pm 2$
$Z \to \tau\tau$+jets	$485 \pm 11 \pm 11$	$20 \pm 2 \pm 2$	$2.5 \pm 0.8 \pm 0.5$	$0.7 \pm 0.6 \pm 0.3$
$Z \to \mu\mu$+jets	$360 \pm 15 \pm 8$	$22 \pm 3 \pm 2$	$2.1 \pm 0.8 \pm 0.1$	$0.5 \pm 0.4 \pm 0.2$
$Z \to ee$+jets	$0.5 \pm 0.5 \pm 0.1$	-	-	-
Multi-jets	$1100 \pm 33 \pm 940$	$64 \pm 8 \pm 64$	$8 \pm 3 \pm 8$	-
$t\bar{t}$ + single t	$1046 \pm 9 \pm 209$	$49 \pm 2 \pm 10$	$5.1 \pm 0.6 \pm 1.0$	$1.1 \pm 0.3 \pm 0.2$
Di-bosons	$288 \pm 3 \pm 58$	$27 \pm 1 \pm 5$	$4.3 \pm 0.4 \pm 0.9$	$0.9 \pm 0.2 \pm 0.2$
Non-collision background	$430 \pm 69 \pm 400$	-	-	-
Total background	$122685 \pm 699 \pm 3339$	$8534 \pm 106 \pm 312$	$757 \pm 28 \pm 36$	$87 \pm 10 \pm 5$
Data	124724 ± 353	8632 ± 93	785 ± 28	77 ± 9

Table 84: Summary of background estimations and total number of observed events in 4.7 fb^{-1} of data for the four mono-jet selection regions. The estimation of the EWK background correspond to inclusive electron and muon control regions.

C   Studies on EW backgrounds estimate with Sherpa

The baseline EW background estimation makes use of Alpgen as main MC generator for W+jets and Z+jets processes. Sherpa W+jets and Z+jets samples have been also used in order to validate the results by Alpgen and to estimate systematic uncertainties on them. The Sherpa samples are significaly smaller than the ones available for AlpGen and the background estimation using Sherpa suffers from larger statistical uncertainties compared to what is presented in the section 8.

The method to estimate the EW background with Sherpa is the same used for AlpGen and that has been described in section 8 and appendix B. Figures 129 and 130 show the kinematic distributions of the reconstructed muons and electrons in inclusive control regions. Distributions of the $E_\mathrm{T}^\mathrm{miss}$ and first two leading jets for the inclusive muon (and electron) control region are shown in figure 131 (and figure 132). The agreement between data and Sherpa in the inclusive control regions is as good as the one from AlpGen presented in section 8.

Transfer factors are retrieved from Sherpa as the ratio of events in signal and control regions in the same way as it is done for Alpgen. Figure 133 shows the comparison between the transfer factors retrieved by AlpGen and Sherpa. The results after the whole procedure are listed in table 85. In this table the systematic uncertainty are treated in the same way as it was described in section 8. The estimated background distributions for the signal region compared with the data are shown in figures 134 and 135.

The results are in agreement with the data. The statistical uncertainties of the background estimations made with Sherpa are twice as large as the one from AlpGen. Therefore the baseline background estimation is done with AlpGen and the results made with Sherpa are used as a cross-check and to asses systematics.

	Background Predictions ± (stat.) ± (syst.)			
	Region A	Region B	Region C	Region D
$Z \to \nu\nu$+jets	64850 ± 749 ± 1277	5674 ± 221 ± 230	576 ± 70 ± 54	47 ± 14 ± 3
$W \to \tau\nu$+jets	30585 ± 823 ± 830	1661 ± 154 ± 72	145 ± 43 ± 7	26 ± 18 ± 1
$W \to e\nu$ +jets	14399 ± 446 ± 662	729 ± 83 ± 34	45 ± 19 ± 12	9 ± 8 ± 1
$W \to \mu\nu$ +jets	11286 ± 288 ± 1216	608 ± 64 ± 149	35 ± 15 ± 21	-
$Z \to \tau\tau$+jets	403 ± 54 ± 42	24 ± 12 ± 3	-	-
$Z \to \mu\mu$+jets	234 ± 12 ± 9	10.8 ± 2.4 ± 0.4	-	-
$Z \to ee$+jets	-	-	-	-
Multi-jets	1100 ± 33 ± 940	64 ± 8 ± 64	8 ± 3 ± 8	-
$t\bar{t}$ + single t	1046 ± 9 ± 209	49 ± 2 ± 10	5.1 ± 0.6 ± 1.0	1.1 ± 0.3 ± 0.2
Di-bosons	288 ± 3 ± 58	27 ± 1 ± 5	4.3 ± 0.4 ± 0.9	0.9 ± 0.2 ± 0.2
Non-collision	430 ± 69 ± 400	-	-	-
Total background	124621 ± 1336 ± 3267	8847 ± 290 ± 272	818 ± 85 ± 84	83 ± 24 ± 8
Data	124724 ± 353	8632 ± 93	785 ± 28	77 ± 9

Table 85: Summary of background estimations and total number of observed events in 4.68 fb^{-1} of data for the four mono-jet selection regions. The Z+jets and W+jets background estimations make use of Sherpa samples. The statistics in the Sherpa samples is lower then the one available with AlpGen. Therefore this estimation suffer from statistical uncertainty more then the one presented in the section 8 that make use of Alpgen samples. Systematic uncertainty are treated in the same way as it was described in section 8.
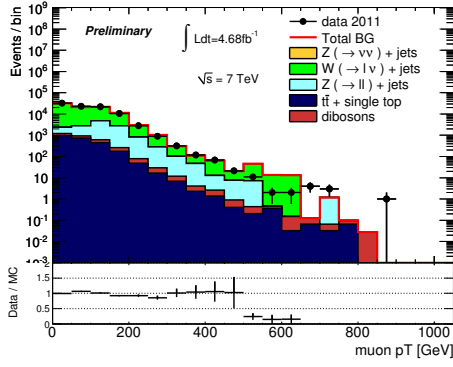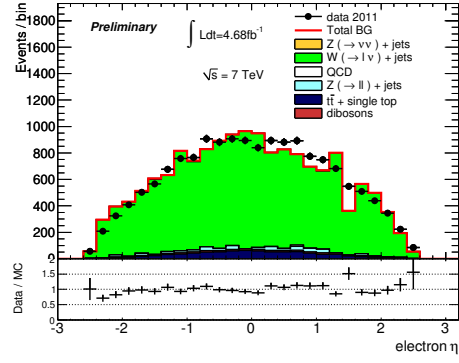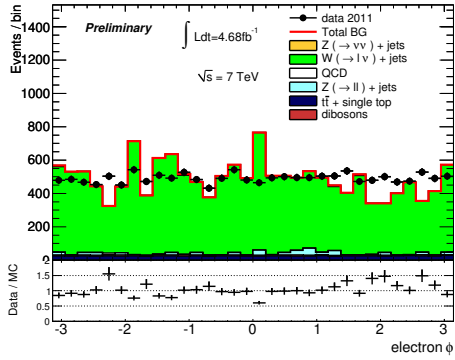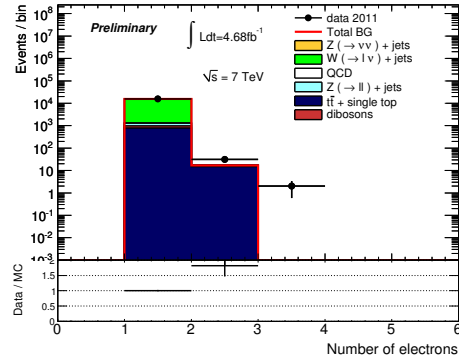
(a)
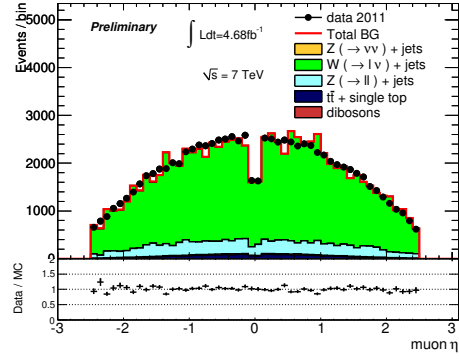
(b)
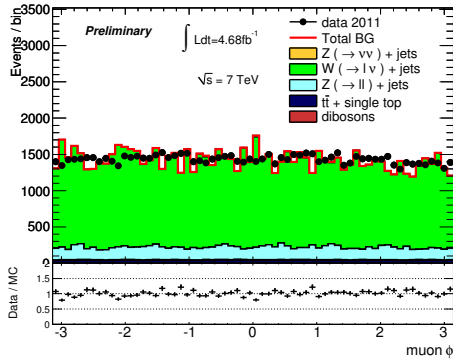
(c)
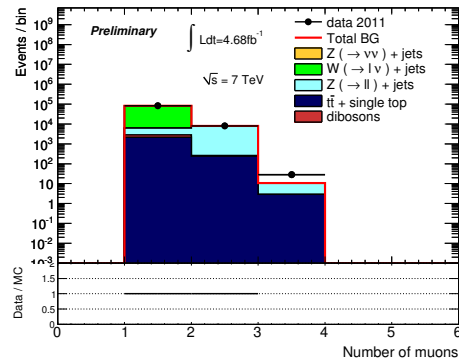
(d)

Figure 129: Kinematic distributions of the identified muons in the inclusive muon control region for the selection cuts of region A ($E_{\mathrm{T}}^{\mathrm{miss}}$, jet1 $p_{\mathrm{T}} > 120\ GeV$). These plots make use of Sherpa W+jets and Z+jets samples.
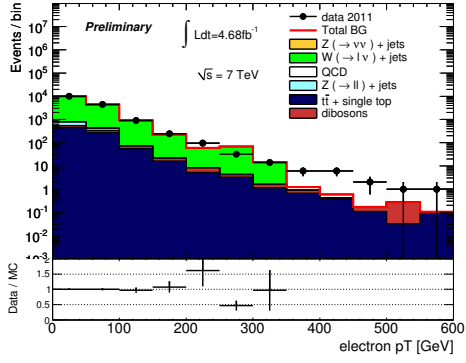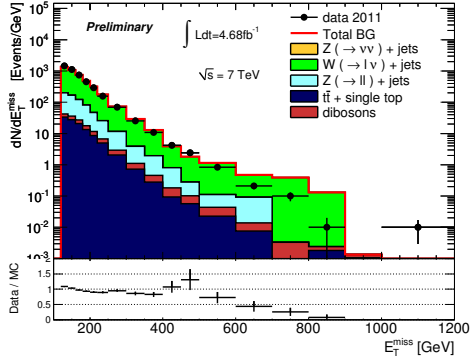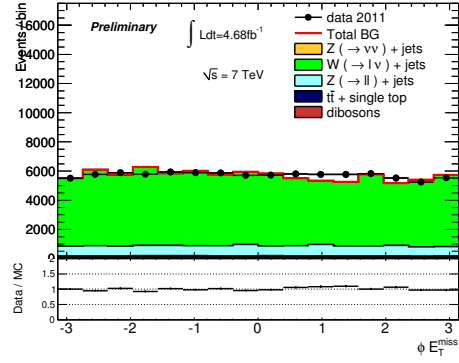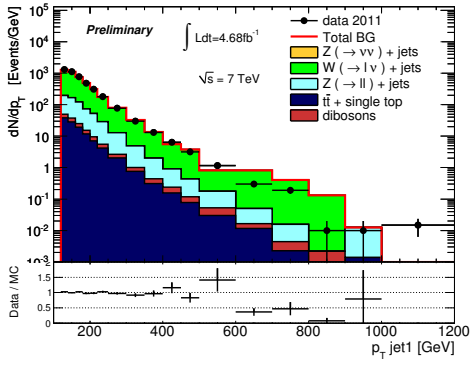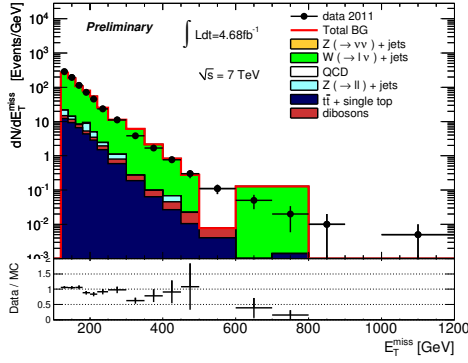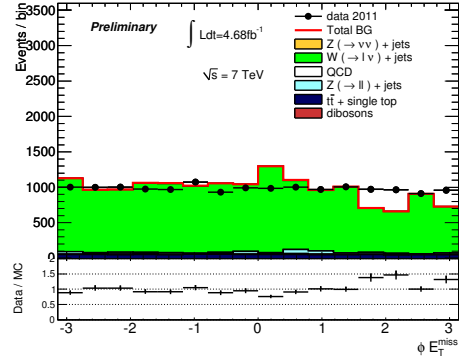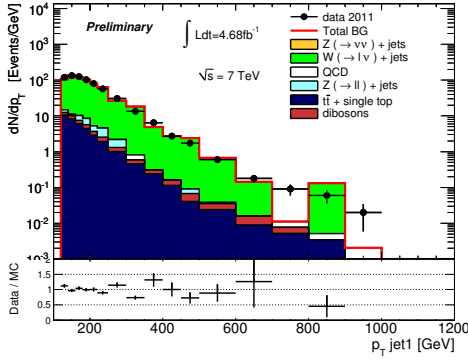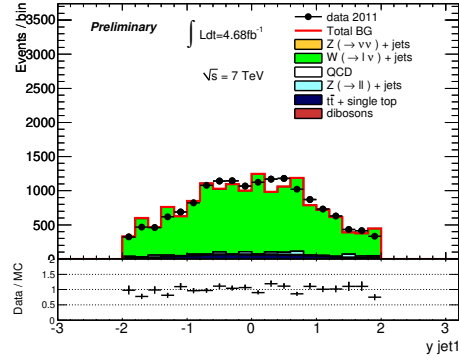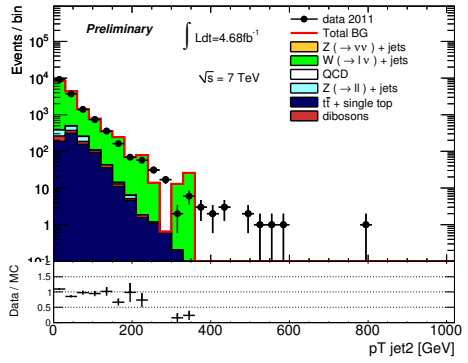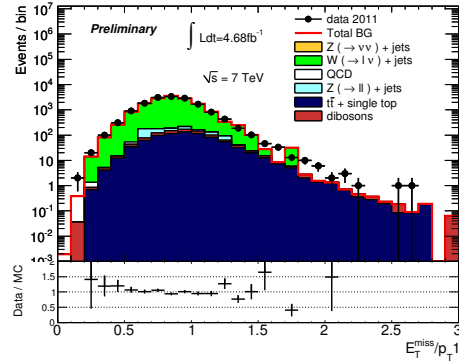
Figure 130: Kinematic distributions of the identified electrons in the inclusive electron control region for the selection cuts of region A (E_T^{miss}, jet1 p_T > 120 GeV). These plots make use of Sherpa W+jets and Z+jets samples.

(a)

(b)

(c)
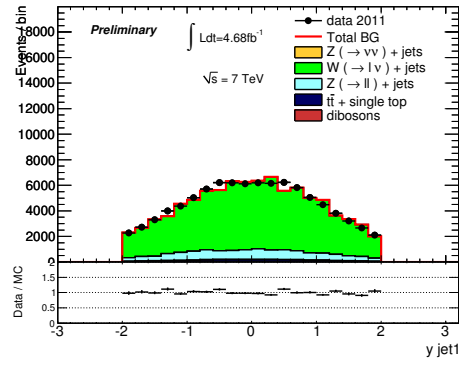
(d)
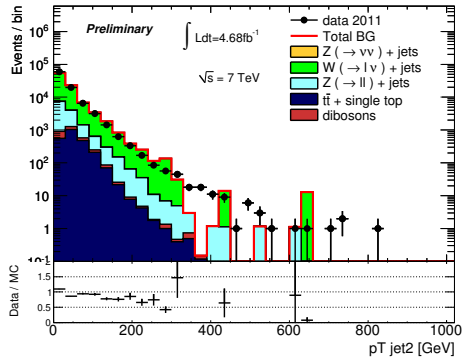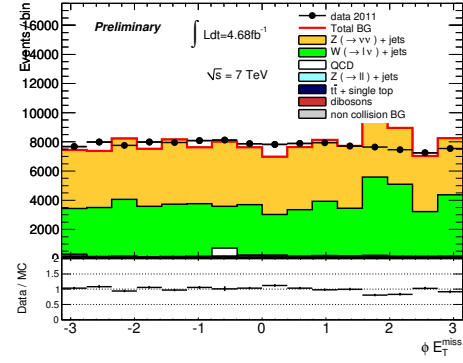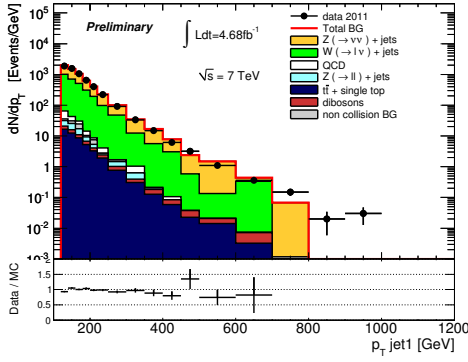
(e)
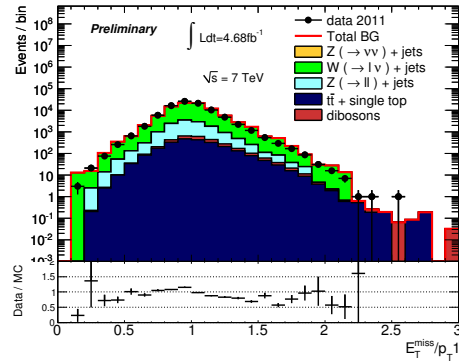
(f)

Figure 131: Kinematic distributions of the events in the inclusive muon control region for the selection cuts of region A (E_T^{miss}, jet1 p_T > 120 GeV). These plots make use of Sherpa W+jets and Z+jets samples.

Not reviewed, for internal circulation only

(a)

(b)

(c)

(d)

(e)

(f)

Figure 132: Kinematic distributions of the events in the inclusive electron control region for the selection cuts of region A (E_T^{miss}, jet1 $p_T > 120\,GeV$). These plots make use of Sherpa W+jets and Z+jets samples.
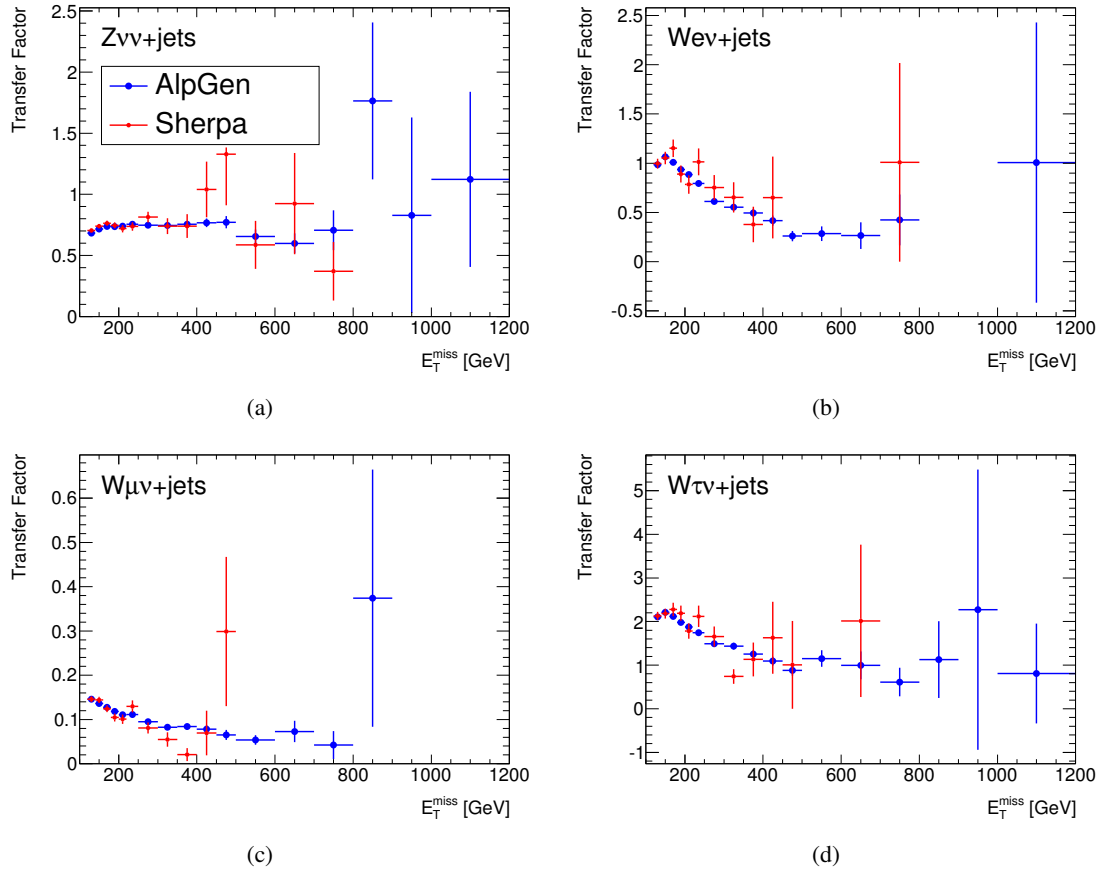
Figure 133: Transfer factor comparison between AlpGen and Sherpa for region A. The errors reported are statistical only.
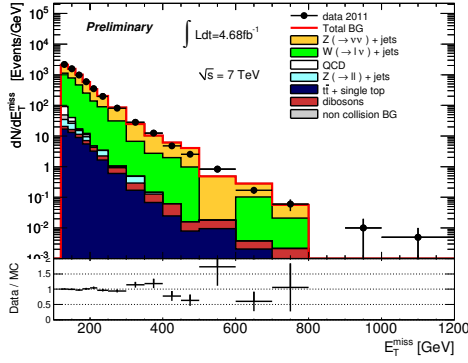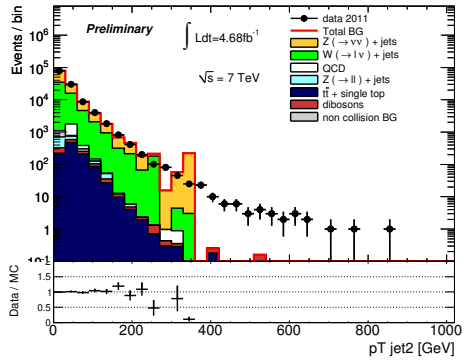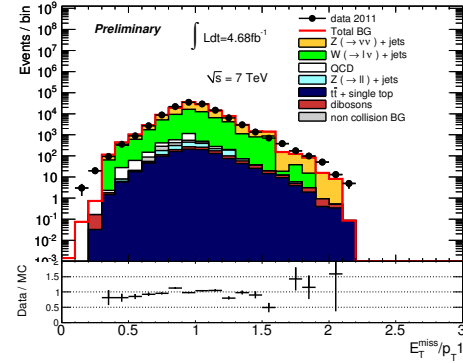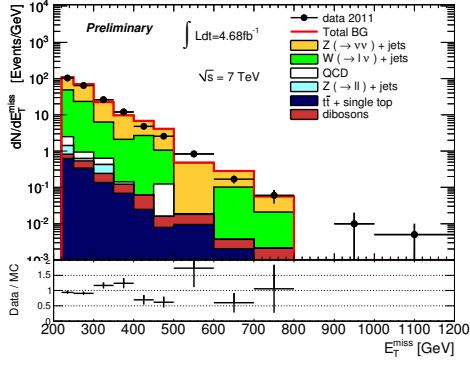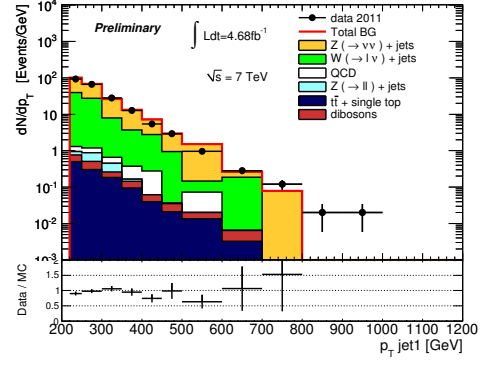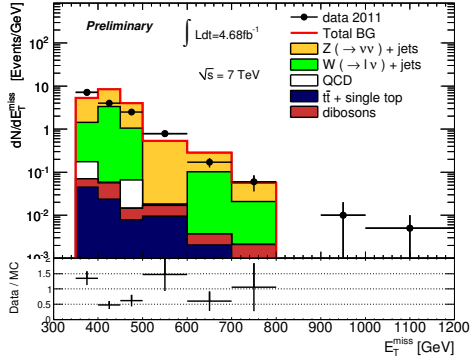
(a)

(b)

(c)
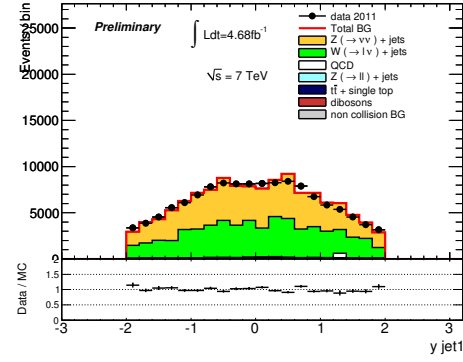
(d)

(e)

(f)

Figure 134: Kinematic distributions of the events in the signal region for the selection cuts of region A (E_T^{miss}, jet1 $p_T > 120 \, GeV$). The estimated Z+jets and W+jets make use of Sherpa samples.
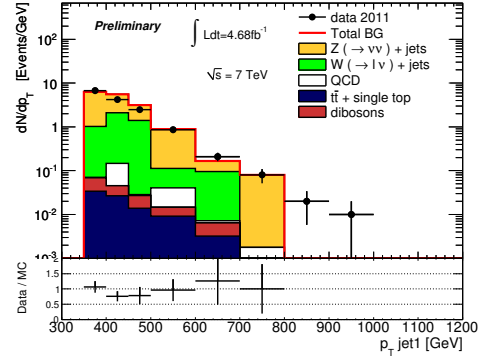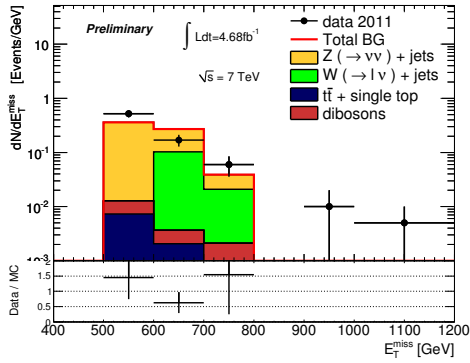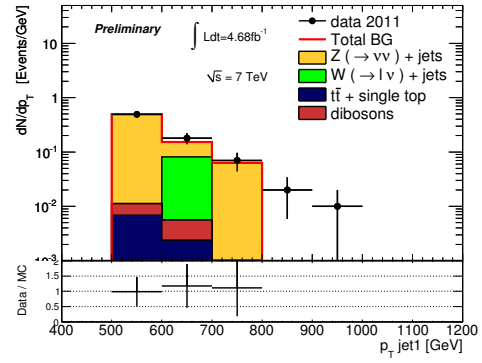
(a)

(b)

(c)

(d)

(e)

(f)

Figure 135: Distributions of E_T^{miss} and leading jet p_T in the signal region for the selection cuts of region B (figures 135(a)) and 135(b)), region C (figures 135(c)) and 135(d)) and region D (figures 135(e)) and 135(f)). The estimated Z+jets and W+jets make use of Sherpa samples.

D Stability of the Data

Some conditions of data-taking are evolving with time, as the pile-up, non collision backgrounds, or dead and problematic regions of the detector. In order to check the stability of the results with time, event yields for the different data periods are compared. The event yields are defined by the ratio of the number of events passing the monojet selection over the integrated luminosity of a data period.

The four left plots in Figure 136 show the event yields of the signal region compared with those of inclusive muon and electron control regions, as defined in Section 8 by inverting the lepton veto. For signal regions 2, 3, and 4, the event yields among the different periods prove to be compatible within the statistical errors. In region 1 the event yields of Data periods L and M are lower than in the other Data periods by a few percents. This is due to a lower trigger efficiency because of the increased pile-up. This behaviour is seen in both signal and control regions, so that it is taken into account by the data-driven background estimations performed in this analysis, and it does not need to be treated as a systematic uncertainty.

The four right plots in Figure 136 show the ratio of the number of events between in the signal regions over that of the control regions. The uncertainties on the ratios are not accounting for the correlation between the numerator and denominator. The covariance terms for a ratio have a negative sign, therefore these statistical errors are overestimated.
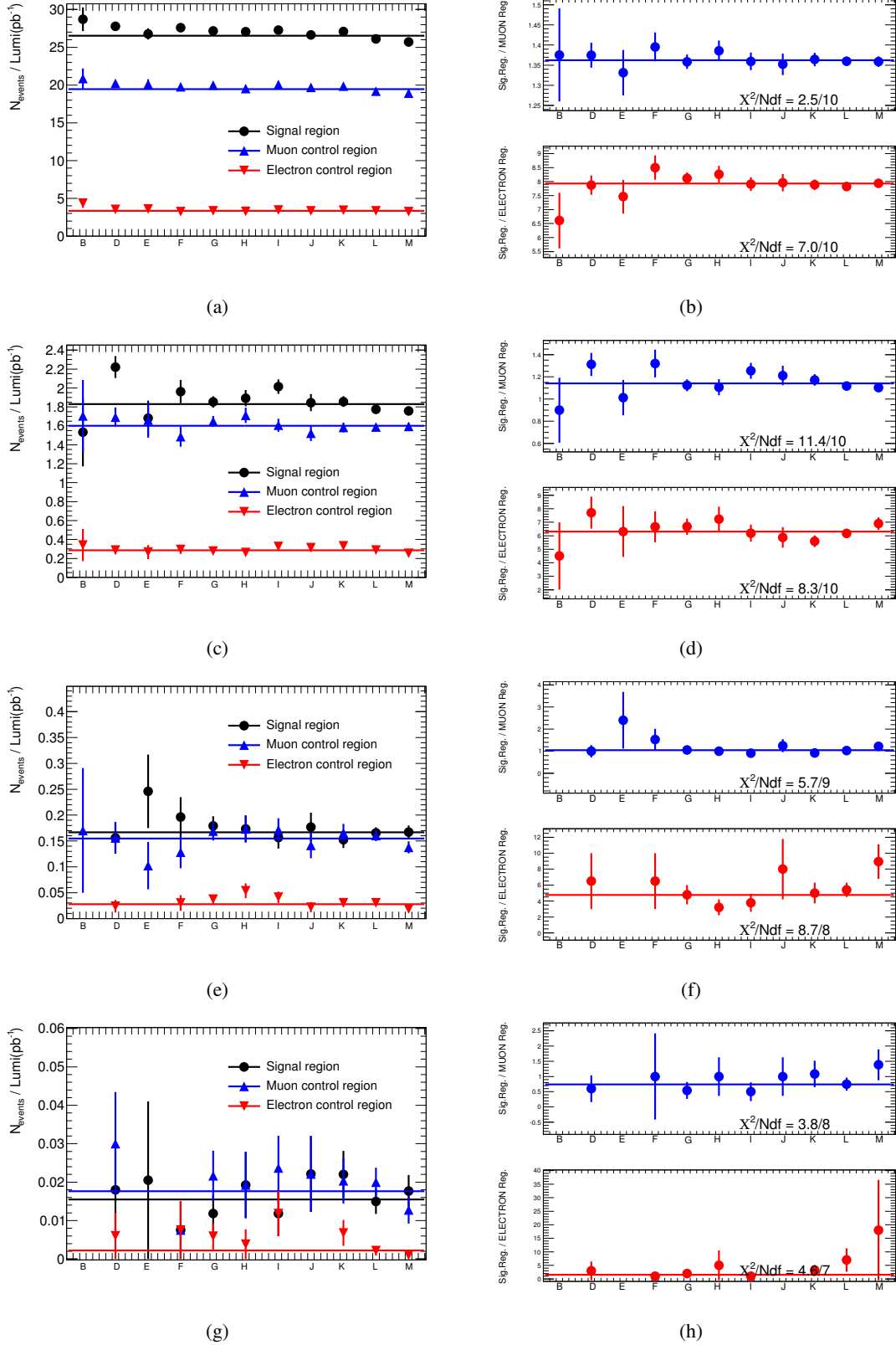
(a)

(b)

(c)

(d)

(e)

(f)

(g)

(h)

Figure 136: Figure *a* (*c*, *e* and *g*) shows the event yields for the signal region 1 (2, 3 and 4) which corresponds to a lower cut on the leading jet p_T and E_T^{miss} of 120 GeV (220, 350 and 500 GeV). The event yields are defined by the ratio of the number of events selected in a data period over the luminosity of that period. A fit to a constant value is performed and the fitted line is plotted on the data points. An electron and a muon control region are considered for each signal region, using the definitions of Section 8. Figure *b* ((*d*, *f* and *h*)) shows the ratios of the event yields in the signal region 1 over that of the associated electron or muon control regions. Correlation between the numerator and denominator are not taken into account, therefore the statistical uncertainties are overestimated.

References

[1] *Search for New Phenomena in Monojet plus Missing Transverse Momentum Final States using 1 fb-1 of pp Collisions at sqrts=7 TeV with the ATLAS Detector*, Tech. Rep. ATLAS-CONF-2011-096, CERN, Geneva, Jul, 2011.

[2] N. Arkani-Hamed, S. Dimopoulos and G.R. Dvali, *The Hierarchy problem and new dimensions at a millimeter*, Phys. Lett. **B429** (1998) 263.

[3] R. Rezvani and H. Beauchemin, *ExoGraviton_i Package; the ADD Graviton Generator in Athena Software*, Tech. Rep. ATL-COM-PHYS-2011-336, CERN, Geneva, Mar, 2011.

[4] Casadei, D . *et al.*, *The implementation of the ATLAS missing Et triggers for the initial LHC operation*, Tech. Rep. ATL-DAQ-PUB-2011-00, CERN, Geneva, 2011.

[5] ATLAS Collaboration, N. Makovec, *Selection of jets produced in proton-proton collisions with the ATLAS detector using 2011 data*, 2012. ATLAS-COM-CONF-2012-019.

[6] T. A. collaboration, *Determination of the muon reconstruction efficiency in ATLAS at the Z resonance in proton-proton collisons at sqrt(s)=7 TeV*, Tech. Rep. ATLAS-CONF-2011-008, CERN, Geneva, Feb, 2011.

[7] T. A. collaboration, *A measurement of the ratio of the W + 1 jet to Z + 1 jet cross sections with ATLAS*, Tech. Rep. ATL-COM-PHYS-2011-457, CERN, Geneva, May, 2011.

[8] A. Collaboration, *Search for Supersymmetry with jets and missing transverse momentum and one or more leptons at sqrt(s) = 7 TeV*, Tech. Rep. ATL-COM-PHYS-2011-1743, CERN, Geneva, Dec, 2011.

[9] T. A. collaboration, *Search for Supersymmetry with jets and missing transverse momentum and one lepton at sqrts=7 TeV (supporting INT note)*, Tech. Rep. ATL-COM-PHYS-2010-1743, CERN, Geneva, March, 2012.

[10] A. Colaboration, *Search for mono-jet plus missing transverse energy in pp collisions at $\sqrt{s}$ = 7 TeV with the ATLAS detector*, Tech. Rep. ATL-COM-PHYS-2011-040, CERN, Geneva, June, 2011.

[11] T. A. collaboration, *Measurement of the cross section for jets produced in association with Z bosons*, Tech. Rep. ATL-COM-PHYS-2010-884, CERN, Geneva, December, 2010.

[12] T. A. collaboration, *Measurement of the production cross for W-bosons in association with jets in pp collisions at sqrts = 7 TeV with the ATLAS detector*, Tech. Rep. ATL-COM-PHYS-2010-883, CERN, Geneva, December, 2010.

[13] T. A. collaboration, *Jet energy scale and its systematic uncertainty for jets produced in proton-proton collisions at sqrt(s) = 7 TeV and measured with the ATLAS detector*, Tech. Rep. Tech. Rep. ATL-CONF-2010-056, CERN, Geneva, July, 2010.

[14] T. A. collaboration, *Supporting Document: Measurement of the W cross section and asymmetry in the electron and muon dacay channels at sqrts=7 TeV*, Tech. Rep. ATL-COM-PHYS-2010-447, CERN, Geneva, September, 2010.

[15] ATLAS Collaboration, D. Salek, D. Berge, J. Boyd, C. Chavez, L. Fiorini, and M. Huhtinen, *Beam background identification method*, 2012. ATLAS-COM-DAPR-2012-001.

1680 [16] R. Nisius, *Combination of ATLAS Results on the Mass of the Top-Quark*, Tech. Rep.
1681 ATL-COM-PHYS-2011-714, CERN, Geneva, Jun, 2011.

1682 [17] P. J. Fox, R. Harnik, J. Kopp, and Y. Tsai, *Missing Energy Signatures of Dark Matter at the LHC*,
1683 Phys.Rev. **D85** (2012) 056011, `arXiv:1109.4398 [hep-ph]`. 22 pages, 10 figures.

1684 [18] J. Goodman et al., *Constraints on Dark Matter from Colliders*, Phys. Rev. **D82** (2010) 116010,
1685 `arXiv:1008.1783 [hep-ph]`.

1686 [19] WMAP Collaboration Collaboration, E. Komatsu et al., *Seven-Year Wilkinson Microwave*
1687 *Anisotropy Probe (WMAP) Observations: Cosmological Interpretation*, Astrophys.J.Suppl. **192**
1688 (2011) 18, `arXiv:1001.4538 [astro-ph.CO]`.

1689 [20] Fermi-LAT collaboration Collaboration, M. Ackermann et al., *Constraining Dark Matter Models*
1690 *from a Combined Analysis of Milky Way Satellites with the Fermi Large Area Telescope*,
1691 Phys.Rev.Lett. **107** (2011) 241302, `arXiv:1108.3546 [astro-ph.HE]`. 6 pages, 2 figures/
1692 Contact authors: Johann Cohen-Tanugi, Jan Conrad, and Maja Llena Garde.